AD-A223 320

ARCCB-SP-90015

PROCEEDINGS OF THE

SIXTH U.S. ARMY SYMPOSIUM ON GUN DYNAMICS

VOLUME I OF II

TAMIMENT, PENNSYLVANIA

15-17 MAY 1990

SPONSORED BY

US ARMY ARMAMENT RESEARCH,
DEVELOPMENT AND ENGINEERING CENTER
CLOSE COMBAT ARMAMENTS CENTER
BENÉT LABORATORIES
WATERVLIET, N.Y. 12189-4050

DISCLAIMER

The findings in this report are not to be construed as an official Department of the Army position unless so designated by other authorized documents.

The use of trade name(s) and/or manufacturer(s) does not constitute an official indorsement or approval.

DESTRUCTION NOTICE

For classified documents, follow the procedures in DoD 5200.22-M, Industrial Security Manual, Section II-19 or DoD 5200.1-R, Information Security Program Regulation, Chapter IX.

For unclassified, limited documents, destroy by any method that will prevent disclosure of contents or reconstruction of the document.

For unclassified, unlimited documents, destroy when the report is no longer needed. Do not return it to the originator.

SECURITY CLASSIFICATION OF THIS PAGE (When Data Entered)

REPORT DOCUMENTATION PAGE		READ INSTRUCTIONS BEFORE COMPLETING FORM
1. REPORT NUMBER ARCCB-SP-90015	2. GOVT ACCESSION NO.	3. RECIPIENT'S CATALOG NUMBER
4. TITLE (and Subtitle) PROCEEDINGS OF THE SIXTH U.S. ARMY SYMPOSIUM ON GUN DYNAMICS VOLUME I OF II		5. TYPE OF REPORT & PERIOD COVERED Final 6. PERFORMING ORG. REPORT NUMBER
7. AUTHOR(s) Editor: Dr. Thomas E. Simkins		8. CONTRACT OR GRANT NUMBER(s)
9. PERFORMING ORGANIZATION NAME AND ADDRESS U.S. Army ARDEC Benet Laboratories, SMCAR-CCB-TL Watervliet, NY 12189-4050		10. PROGRAM ELEMENT, PROJECT, TASK AREA & WORK UNIT NUMBERS N/A
11. CONTROLLING OFFICE NAME AND ADDRESS U.S. Army ARDEC Close Combat Armaments Center Picatinny Arsenal, NJ 07806-5000		12. REPORT DATE May 1990 13. NUMBER OF PAGES 262
14. MONITORING AGENCY NAME & ADDRESS (if different from Controlling Office)		15. SECURITY CLASS. (of this report) UNCLASSIFIED 15a. DECLASSIFICATION/DOWNGRADING SCHEDULE

16. DISTRIBUTION STATEMENT (of this Report)

Approved for public release; distribution unlimited.

17. DISTRIBUTION STATEMENT (of the abstract entered in Block 20, if different from Report)

18. SUPPLEMENTARY NOTES

Presented at the Sixth U.S. Army Symposium on Gun Dynamics, Tamiment, Pennsylvania 15-17 May 1990

19. KEY WORDS (Continue on reverse side if necessary and identify by block number)

Ballistics	Precision
Barrel Vibration	Stabilization
Dynamics	Target Acquisition

20. ABSTRACT (Continue on reverse side if necessary and identify by block number)

This represents a compilation of technical papers concerning analyses, design, measurement, and automation of gun dynamics. The authors represent a cross-section of the scientific and technical community, including universities, industrial, and Government research laboratories.

DD FORM 1 JAN 73 1473 EDITION OF 1 NOV 65 IS OBSOLETE

UNCLASSIFIED

SECURITY CLASSIFICATION OF THIS PAGE (When Data Entered)

FOREWORD

The theme of the 1990 Symposium was Gun Dynamics. The Symposium was divided into six sessions: (I) Fluid Dynamics, (II) Experimental Work, (III) The Motion of Gun Tubes - Theory, (IV) The Motion of Gun Tubes - Measurement, (V) Modelling and Finite Element Simulation, and (VI) Projectiles and Projectile/Tube Interface.

During recent years, one has witnessed great strides in various branches of continuum mechanics, kinematic designs, and numerical and computer techniques for solving problems of great complexity as well as in the areas of experimental mechanics and instrumentation. Now more than ever it appears feasible to gain understanding and to improve the design of gun systems for greater accuracy by exploiting new technological advances. The Sixth Symposium represents the continuing interest of the United States Army in this direction.

The Proceedings of the Sixth U.S. Army Symposium on Gun Dynamics contains the technical papers presented at the Symposium held in Tamiment, Pennsylvania, 15-17 May 1990. The papers represent the current research efforts on gun dynamics and the effect on precision and design by industrial, university, and Department of the Army, Department of the Navy, and Department of Energy laboratories throughout the United States and the United Kingdom. In addition, papers not received in time for publication in the Proceedings of the Fifth Symposium are included herein.

I am grateful to everyone who submitted a paper for inclusion in the Proceedings. As in previous years, I am delighted by the number of scientific and technical people who have gathered to share their knowledge and experience.

Thomas E. Simkins, Chairman
Sixth U.S. Army Symposium on Gun Dynamics

CONTENTS

Page

SESSION II: EXPERIMENTAL WORK

Page

SESSION III: THE MOTION OF GUN TUBES - THEORY

Page

SESSION IV: THE MOTION OF GUN TUBES - MEASUREMENTS

Page

SESSION V: MODELLING AND FINITE ELEMENT SIMULATION

Page

SESSION VI: PROJECTILES AND PROJECTILE/TUBE INTERFACE

SESSION I:

FLUID DYNAMICS

CAROFANO

TITLE: A COMPARISON OF EXPERIMENTAL AND NUMERICAL BLAST DATA FOR PERFORATED MUZZLE BRAKES

G. C. CAROFANO
U.S. ARMY ARMAMENT RESEARCH, DEVELOPMENT, AND ENGINEERING CENTER
CLOSE COMBAT ARMAMENTS CENTER
BENET LABORATORIES
WATERVLIET, NY 12189-4050

ABSTRACT:

In an earlier study, a numerical model of the blast field produced by a cannon having a perforated muzzle brake was given. The results compared favorably with the near-field shadowgraph data of Dillon for a 20-mm cannon. This paper describes improvements to the model and compares the predictions with free-field blast data for small and large caliber cannon. The results show good agreement with data for a 20-mm cannon and satisfactory agreement with data for 105-mm and 120-mm cannon.

Some preliminary work on a method of reducing the blast levels near the breech using upstream venting is also presented. The scheme consists simply of moving one or two rows of vents about ten calibers upstream of the muzzle. The disturbance produced by the upstream vents interferes with that produced by the remainder of the brake such that the blast levels are reduced near the breech and increased somewhat near the muzzle.

BIOGRAPHY:

PRESENT ASSIGNMENT: Dr. Garry C. Carofano is a mechanical engineer in the Applied Mathematics and Mechanics Branch at Benet Laboratories. He is currently applying the methods of computational fluid dynamics to muzzle brake design.

PAST EXPERIENCE: Previously, he has done numerical and experimental research in areas such as blast produced by recoilless weapons and heat transfer from and stress analysis of finned mortar tubes.

DEGREES HELD: He received a B.M.E. degree from Clarkson University in 1961, and M.S. and Ph.D. degrees from Cornell University in 1964 and 1968, respectively.

A COMPARISON OF EXPERIMENTAL AND NUMERICAL BLAST DATA FOR PERFORATED MUZZLE BRAKES

G. C. Carofano
U.S. Army Armament Research, Development, and Engineering Center
Close Combat Armaments Center
Benet Laboratories
Watervliet, NY 12189-4050

INTRODUCTION

A perforated muzzle brake consists simply of a set of vents drilled through the wall of a cannon near the muzzle (see Figure 1). Venting reduces the axial thrust produced by the gas at the muzzle, thereby effecting a decrease in weapon impulse. However, the redirected exhaust increases the blast levels upstream of the muzzle. From a designer's perspective, the problem is to choose a cannon-brake system which yields specified values of muzzle velocity and weapon impulse but minimizes the blast increase.

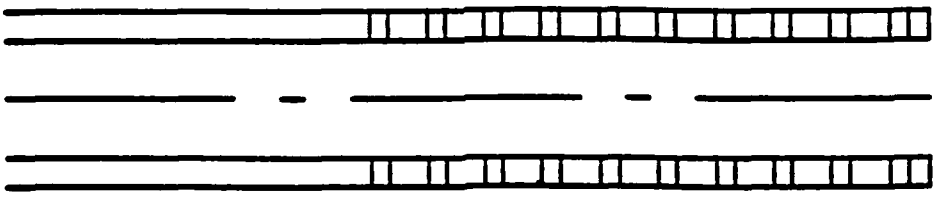

Figure 1. Schematic drawing of a perforated muzzle brake.

The magnitude of the weapon impulse was extensively studied by Dillon [1,2], Dillon and Nagamatsu [3-5], Nagamatsu et al. [6,7], and Carofano [8]. References 1 through 5 also contain shadowgraph and free-field overpressure data which characterize the blast field surrounding the cannon.

The computation of the blast field is challenging because the flow is transient, three-dimensional, and must be computed to distances considerably beyond the breech if realistic pressure histories near the breech are to be obtained for reasonable periods of time. The time requirement is necessary because the peak pressure at a particular location is not always achieved in the initial portion of the blast wave. To render the calculation tractable, Carofano [9] exploited a number of features of the flow. A brief description follows (see also References 6 and 8).

When the propellant gas expands through the brake, an asymmetric pressure distribution develops in each vent with the highest pressures acting on the

downstream surface. To calculate the blast field, the flow through each vent is required at each instant of time during tube blowdown. Because the flow is three-dimensional, it is not practical to obtain the complete solution with a transient calculation. Fortunately, the flow contains many features which permit a vigorous simplification of the problem.

First, because of the large volume of the gun tube, the blowdown process takes on the order of tens of milliseconds, while the three-dimensional calculations indicate that the flow in a vent is established in a fraction of a millisecond. Therefore, the latter can be treated as quasi-steady and only the flow inside and outside of the tube must be considered as time-dependent.

Secondly, in the applications of interest, the flow is supersonic as it enters the brake and, due to the venting, it expands to higher Mach numbers as it travels downstream. Also, because of the high tube pressures, the gas exits each hole at near sonic or supersonic velocities over most of the exit plane area. Experience has shown that the flow is rather insensitive to the outflow boundary condition over the remaining subsonic portion. Thus, the flow at a particular vent location is not influenced by events occurring farther downstream or outside of the tube. It depends solely on the conditions in the tube upstream of the vent. In particular, it was shown [6,8,9] that the flow is completely described by the upstream Mach number, the specific heat ratio and the covolume of the gas, and the vent geometry. One solution with these parameters specified is valid for all upstream pressures and densities. Thus, while a wide range of physical states are encountered during blowdown, only a few three-dimensional solutions are required to describe them.

Data from these solutions are used to obtain average values of density and pressure along with the mass and momentum fluxes in the exit plane of the vent. The averages are dimensionless functions of the parameters that appear in the three-dimensional solutions and are used to couple the interior and exterior flows.

The transient flow inside of the tube is calculated using the one-dimensional Euler equations with a source term included to represent the venting at the tube wall. This is constructed from the mass flux function and the local conditions prevailing in the tube at a given instant.

The transient flow outside of the tube is treated as axisymmetric. The large number of vents typical of such brakes and their symmetrical placement around the tube makes this feasible. Since the area of each vent represents only a portion of the local tube area, the averaged variables at the vent exit have to be adjusted to provide an appropriate boundary condition for the axisymmetric equations. A control volume approach to achieve this is described in Reference 9. The quantities at the vent exit are related to the interior flow through the averaged functions described above. Because the vent exit flow is supersonic, the exterior boundary condition is completely determined by the local conditions in the tube.

The model [9] produced results which compared favorably with previously unpublished shadowgraphs of the near-field obtained by Dillon in his 20-mm

experimental program. A quantitative comparison is made below of free-field overpressure data from that program taken at 30 calibers from the muzzle.

Some changes have been made in the original model to make it more generally applicable to cannon designs of current interest. For example, the perfect gas equation was replaced by the Abel equation of state to more adequately represent the gases at the pressure levels which prevail in large caliber cannon. Also, the projectile equation of motion was added to more realistically simulate the flow discharging to the environment. Previously, the projectile was restricted to move at a constant velocity.

Finally, a distribution of vents of variable diameter and spacing can now be accommodated. This is necessary in large caliber cannon analysis where the diameters of the vents near the brake entrance may have to be smaller than those near the muzzle to avoid exceeding allowable stress levels. It was also needed to simulate the upstream venting scheme discussed below.

INITIAL CONDITIONS

The starting configuration is shown in Figure 2. The initial projectile position is chosen such that the precursor shock is located just upstream of the vented region. The state of the air between the shock and the projectile is taken to be uniform and is computed from the projectile velocity at this instant. The latter is taken from the output of a standard ballistics solution.

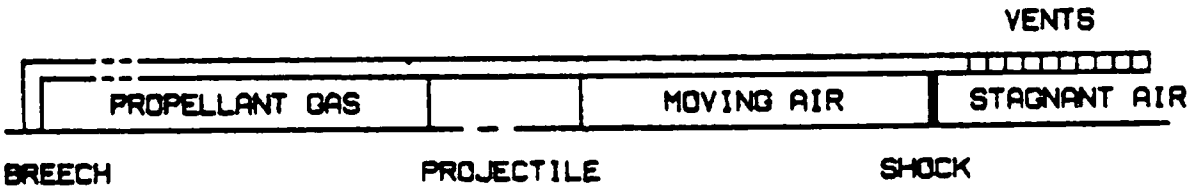

Figure 2. Starting configuration showing projectile pushing shock into the vented region.

The specification of the state of the propellant gas behind the projectile is delayed until its base reaches the vented region. During this interval, an analytical representation of the velocity and position time histories, taken from the ballistics solution, is used to advance the projectile and drive the numerical solution downstream of it. The propellant gas properties are then calculated from the Pidduck-Kent limiting solution for an Abel gas [10] using the ballistics data summarized in Table 1 (see References 6 and 8 for more details). In this manner, essentially all of the information generated by the ballistics solution relating to the combustion, friction, and heat transfer processes is included in the starting data behind the projectile.

TABLE 1. STARTING DATA FOR PROPELLANT GAS

Parameter/Cannon	20-mm	105-mm	120-mm
Propellant mass, kg	0.0389	5.92	6.26
Projectile mass, kg	0.0980	5.79	13.45
Projectile velocity, m/sec	1045.0	1466.1	1143.3
Projectile base pressure, atm	287.0	798.0	660.1
Projectile base position, cm	143.0	427.5	402.0
Projectile base travel, cm	154.84	475.0	485.1
Bore diameter, cm	2.0	10.5	12.0
Gun chamber volume, cm^3	41.7	6472.9	8749.9
Specific heat ratio	1.25	1.24	1.23
Covolume, cm^3/kg	982.0	1050.0	1035.0
Vent area ratio of brake	6.69	4.76	3.69

A comment is necessary regarding the starting data in Table 1 for the 20-mm cannon. The vents were actually part of an 11.84-cm extension rather than integral with the tube. In the bare muzzle case then, the projectile base travel was only 143.0 cm. The precursor shock was initially placed at the muzzle rather than upstream, as depicted in Figure 2, and the propellant gas properties were specified when the projectile base reached the muzzle.

VENT PATTERNS

Each brake had 12 columns of vents uniformly spaced around the tube circumference (columns run parallel to the tube axis). One column for each brake is shown schematically in Figure 3. All dimensions are scaled by the cannon bore diameter to facilitate comparison. The vent area ratio, defined as the ratio of the total vent area to the cannon bore area, is given as the last entry in Table 1.

In the 20-mm brake, every other hole was offset by 15 degrees in the circumferential direction to produce a staggered pattern. The code considers only the vent area per unit length of tube so the effect of staggering cannot be estimated. Presumably, this arrangement is more likely to produce the axisymmetric flow field assumed in the model than the straight patterns.

Vents of variable diameter and spacing were used in the 120-mm brake to avoid exceeding allowable stress levels. This feature is considered by the code.

A more complete description of the experimental setup for the 20-mm cannon, including a photograph of the brake, is given in Reference 1. Further details of the 105-mm and 120-mm tests are given in References 11 and 12, respectfully.

20-MM CANNON VENT PATTERN

105-MM CANNON VENT PATTERN

120-MM CANNON VENT PATTERN

Figure 3. Vent pattern for each cannon.

CALCULATIONS

Harten's Total Variation Diminishing scheme [13] was used in conjunction with a time-splitting algorithm [14] to solve the Euler equations. The calculations were performed on a Cray X-MP/48 computer using a single processor. A major effort was made to exploit the vector hardware wherever possible.

A uniform grid was employed over a rectangular region extending 60 calibers upstream from the muzzle, 110 calibers downstream, and 70 calibers radially outward from the tube axis. Beyond this region, a gradually expanding grid was used to limit memory requirements while still permitting the calculation to continue. Four cells were used across the tube radius, 800 in the axial direction and 350 in the radial direction. The program required 1.6 megawords of memory for these array sizes.

The size of the active grid is determined at the beginning of each time step to eliminate computation in the undisturbed environment. Run times for each configuration are given in Table 2. More time steps are required for the bare muzzle cases because the disturbance which propagates upstream takes longer to reach the pressure gages (see next section).

TABLE II. COMPUTATION TIMES

Cannon	Time Steps	CPU Minutes
20-mm, bare muzzle	1200	38.8
20-mm, with brake	1000	25.0
105-mm, bare muzzle	1200	38.6
105-mm, with brake	1000	28.5
120-mm, bare muzzle	1200	37.8
120-mm, with brake	1000	26.6

PRESSURE CONTOUR PLOTS

The blast fields produced by each cannon after 600 time steps are shown in Figures 4 through 6. Each plot is scaled by the respective cannon bore diameter to facilitate comparison. The small circles, located on a radius 30 calibers from the muzzle, indicate where pressure histories were stored in the calculations or measured in the experiments. Note in Figure 4, that when the brake extension was added in the 20-mm experiment, the gages were left at the positions they occupied in the bare muzzle case.

The principal effect of venting is seen to be the generation of a more uniform blast field around the cannon. The disturbance is diminished somewhat downstream of the muzzle and considerably strengthened upstream.

The 20-mm cannon had a significantly higher ratio of travel length to bore diameter than either large cannon. This produced a precursor flow of relatively long duration ahead of the projectile. In Figure 4, remnants of the precursor shock can be seen upstream of the muzzle and near the 60-degree gage position in the brake case. The precursor shock is completely overtaken by the main blast wave for both large cannon because of their relatively shorter barrels.

What other differences exist in the various blast fields are due mainly to the variations in projectile base pressure and velocity or the brake geometry. Some 20-mm experiments are planned that will employ brakes which are geometrically similar to those being used in ongoing 105-mm and 120-mm tests. The question of scaling the blast field will be addressed when those data become available.

OVERPRESSURE RESULTS

In Figure 7, experimental free-field overpressure data are given for the 20-mm cannon. Each cluster of data symbols is the result of four shots. The zero angle coincides with the projectile flight path.

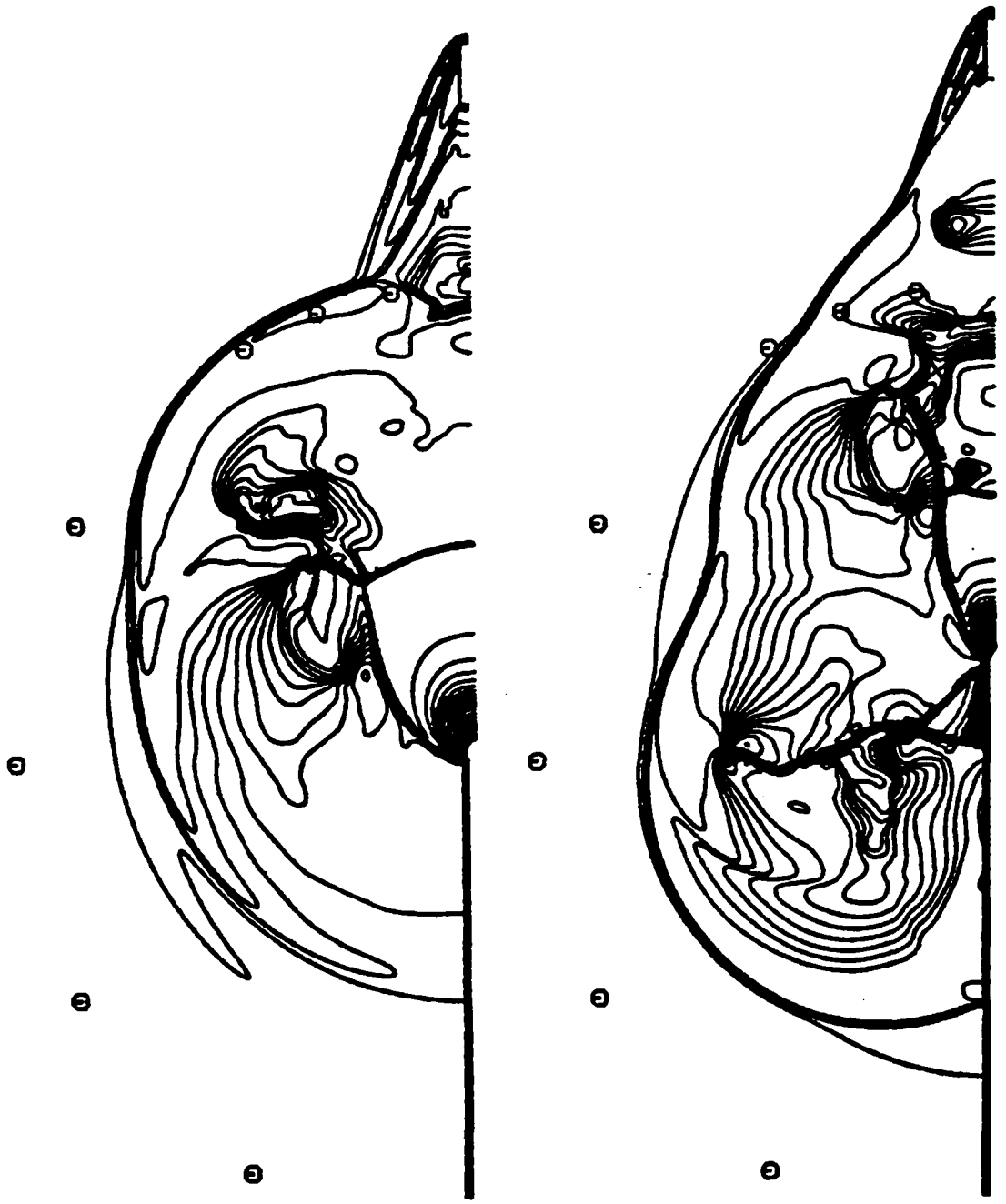

Figure 4. Pressure contour plots for the 20-mm cannon with and without venting.

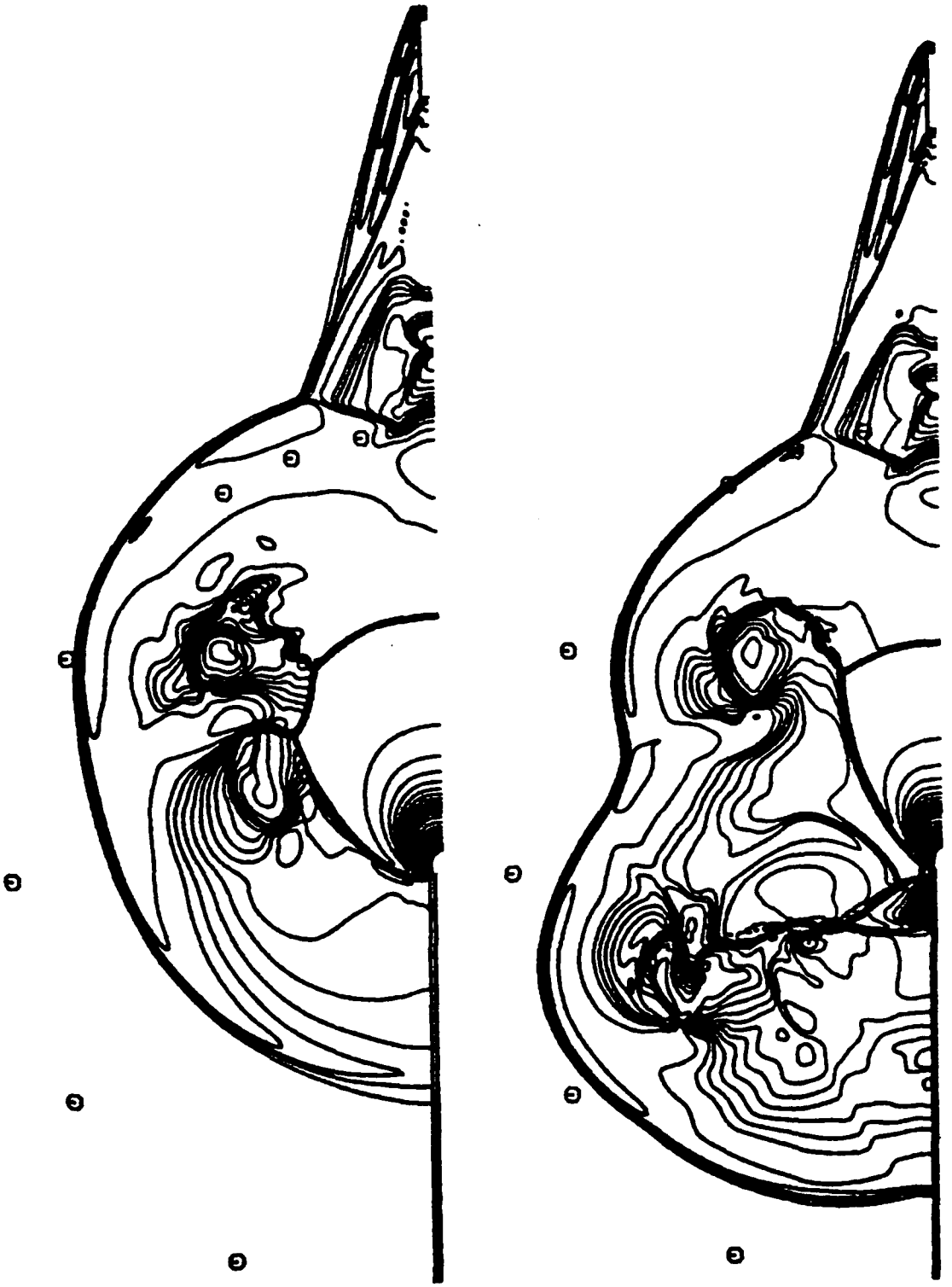

Figure 5. Pressure contour plots for the 105-mm cannon with and without venting.

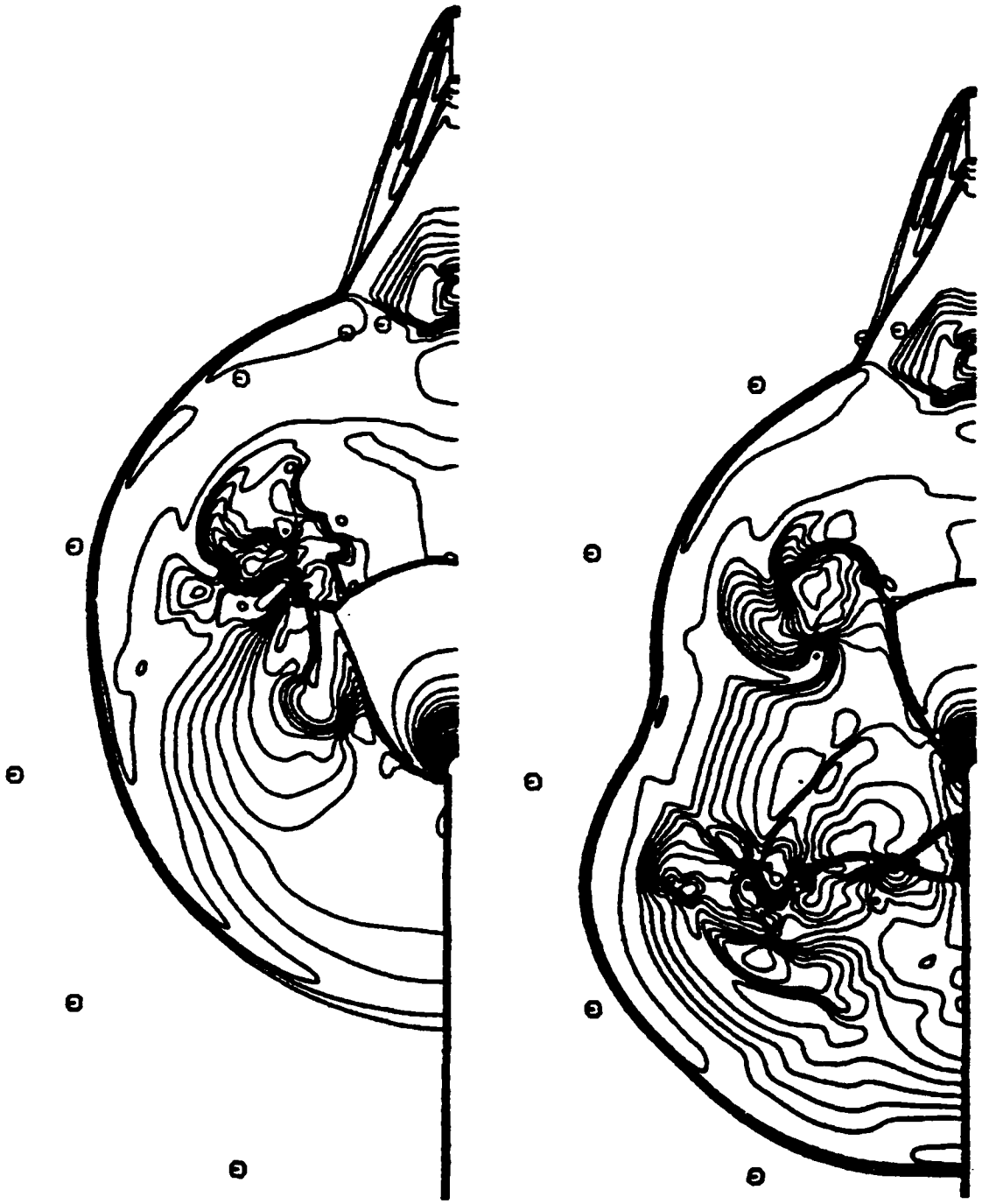

Figure 6. Pressure contour plots for the 120-mm cannon with and without venting.

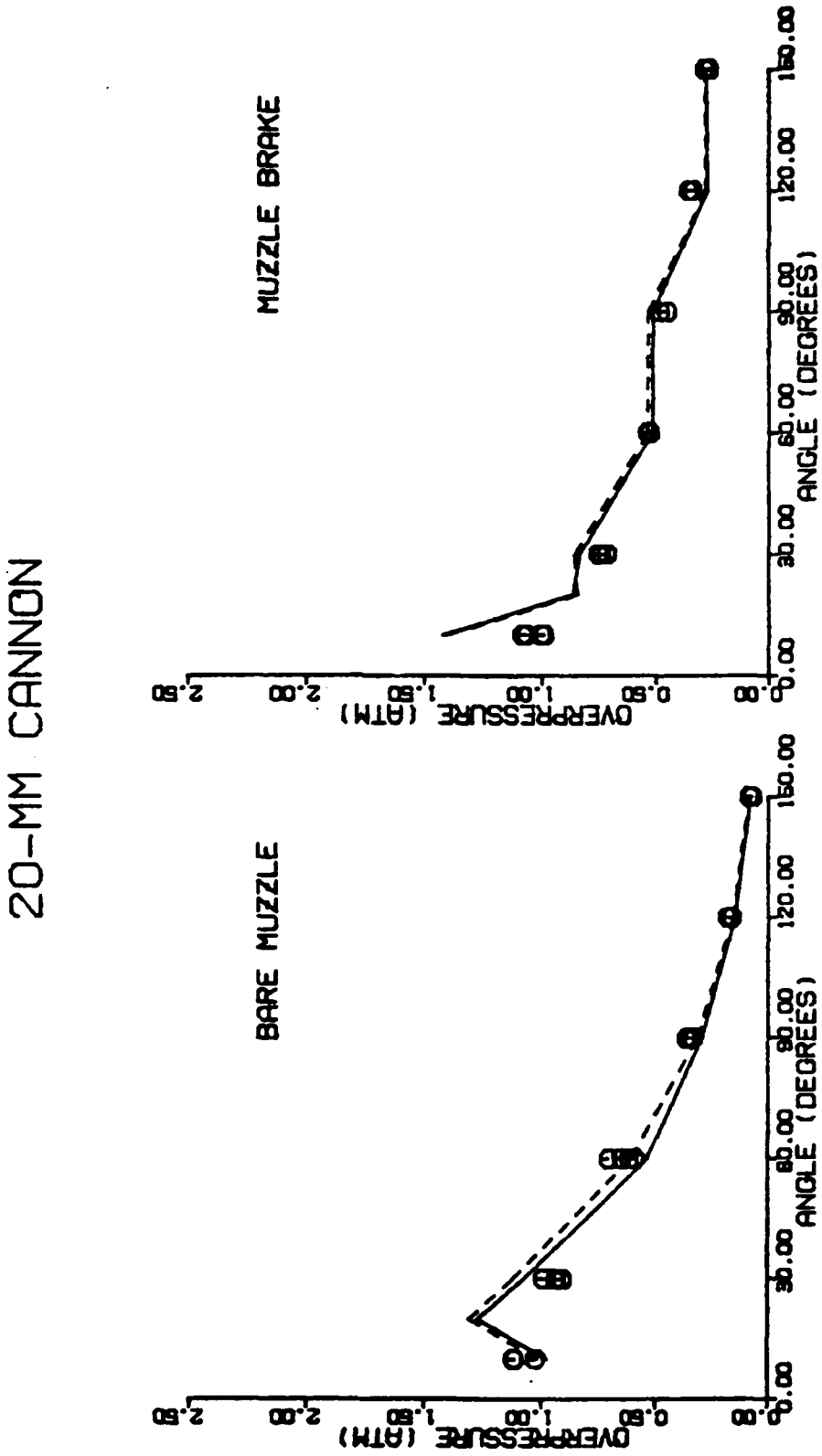

Figure 7. Comparison of model predictions with experimental free-field overpressure data for the 20-mm cannon.

The solid and dashed lines in the figure correspond to calculations made with the Abel and perfect gas equations, respectively. The projectile base pressure for this cannon is less than 300 atmospheres so the covolume term in the Abel equation had only a modest effect on the results. The predictions are generally in good agreement with the data. The only exception occurs at the 10-degree position with the brake in place.

The results in Figure 8 are for the 105-mm cannon. In this case, the base pressure is near 800 atmospheres and the value of using the Abel equation is evident. The predictions lie somewhat above the data forward of the muzzle, but this is not a characteristic of the model. The comparison in Figure 9 for the 120-mm cannon and a base pressure of 660 atmospheres, shows more satisfactory agreement at these locations.

Of some concern is the tendency of the model to underpredict the data at the 150-degree location for both large cannon. The experimental peak may be due to a wave reflected off the ground or the vehicle. The cause is being investigated.

Note that, in general, the peak overpressure is somewhat lower near the projectile flight path and rises to a maximum farther off axis. This can be explained by reference to the contour plots. Near the axis, the disturbance is influenced by the relatively weak projectile bow wave. Farther off axis, the disturbance is due to the strongest part of the main blast wave. The only exception occurs in the 20-mm brake case where the gage nearest the axis is struck directly by the main blast wave because of its position relative to the exit plane of the brake extension.

The overpressure plots for the large cannon indicate that venting decreases the strength of the blast wave downstream of the muzzle and increases it upstream. For the 20-mm cannon, the reduction downstream was not as pronounced, which is again associated with the brake extension. In a design situation, the tube will have to be lengthened somewhat to maintain the desired muzzle velocity, but the addition will be less than the vented length because the projectile continues to accelerate through this region. The trend of the overpressure measurements will then lie somewhat intermediate between the extremes observed here. In any event, the upstream pressure levels will increase. A method to limit the rise is discussed in the next section.

BLAST REDUCTION NEAR THE BREECH

In the experiments, all of the vents were located near the muzzle. The question arises, "Could another arrangement reduce the blast levels near the breech without producing significant changes in weapon impulse or projectile velocity?" Several patterns have been considered.

The obvious choice, increasing the vent spacing to spread the brake disturbance over a larger area, raised the pressure levels at the breech significantly. Displacing so many of the vents upstream simply moves the source of the disturbance closer to the area of concern.

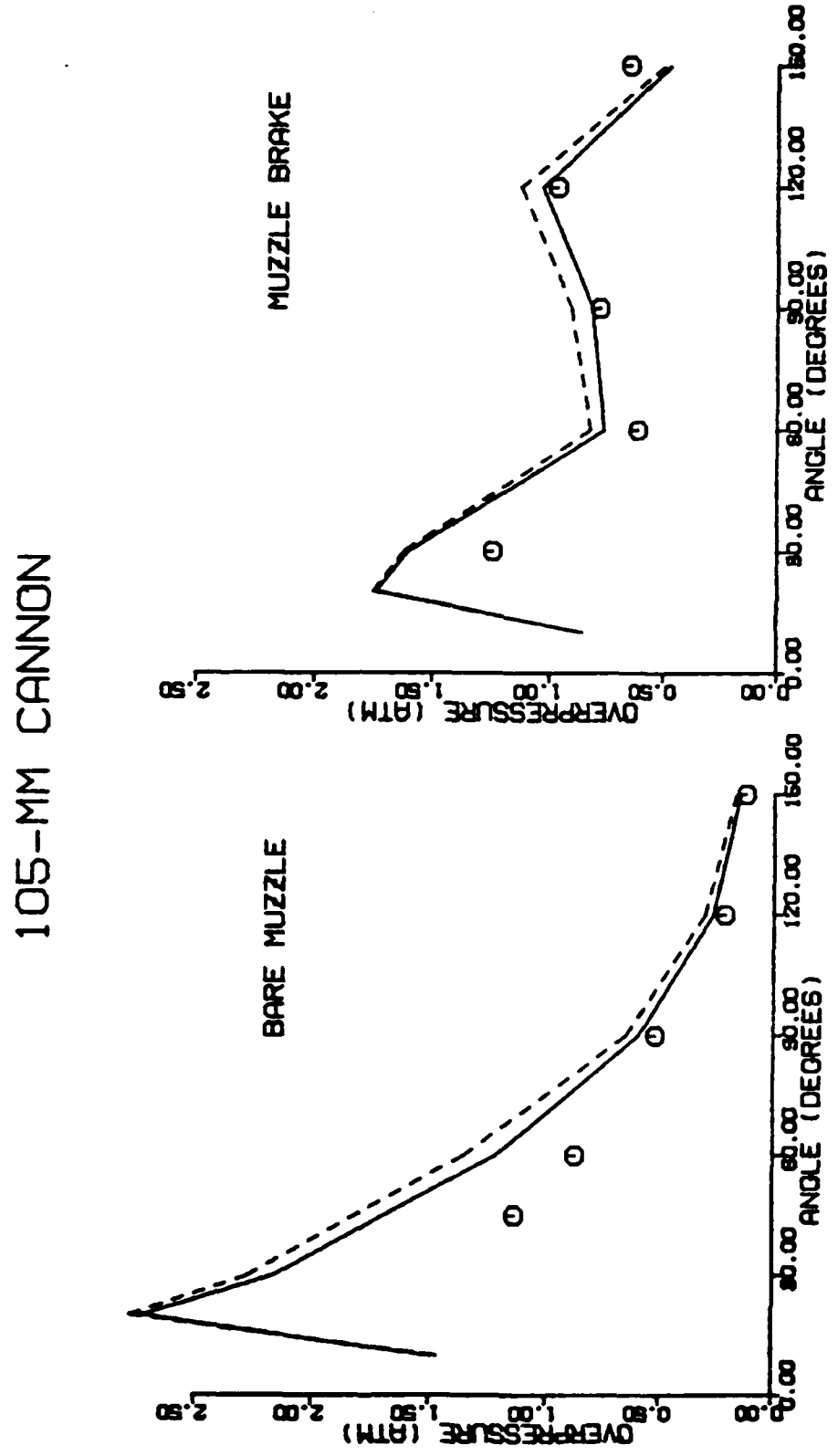

Figure 8. Comparison of model predictions with experimental free-field overpressure data for the 105-mm cannon.

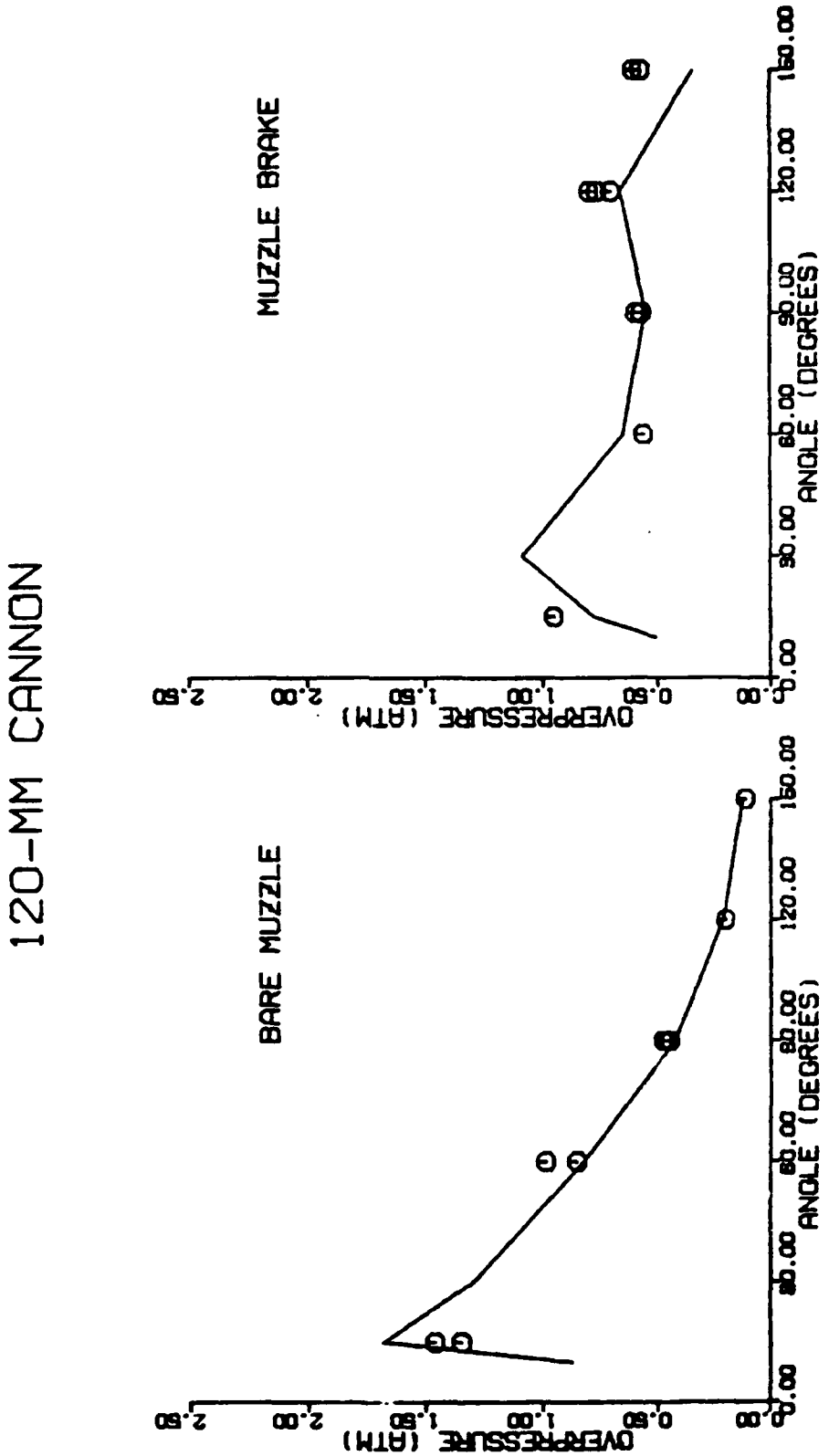

Figure 9. Comparison of model predictions with experimental free-field overpressure data for the 120-mm cannon.

The most successful change involved moving just one or two rows of vents upstream while leaving the remaining vents at the muzzle. Overpressure predictions are shown in Figure 10 for the region aft of the muzzle of a 105-mm cannon at a 50-caliber radius (a different round was used in these calculations than the one described above). The bare muzzle data, represented by the square symbols, decrease monotonically from muzzle to breech. Adding 12 rows of vents near the muzzle produces the opposite trend, as indicated by the circles. Displacing two of these rows ten calibers upstream from the muzzle produces a significant reduction in blast near the breech, as indicated by the triangles.

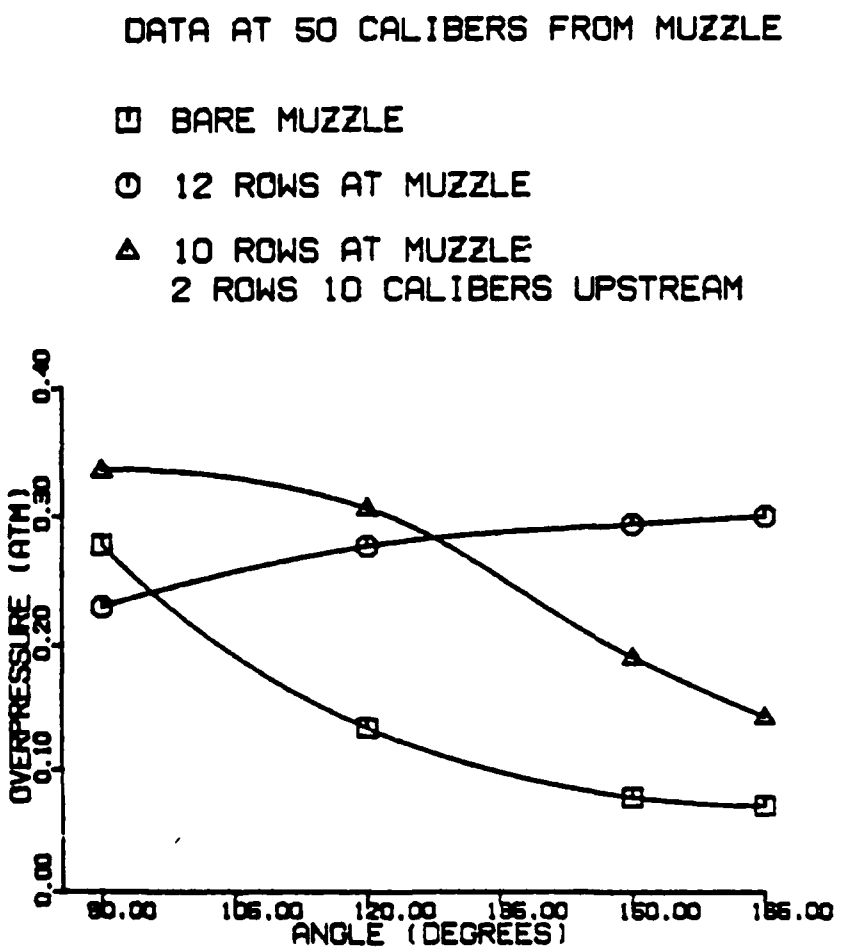

Figure 10. Overpressure predictions aft of the muzzle of a 105-mm cannon at a 50-caliber radius.

The scheme appears to work for two reasons. First, because only a small number of vents are moved upstream, the blast wave produced by them is relatively weak. Secondly, the flow field associated with them interferes with the propagation of the blast wave produced by the remaining vents. The result is

that two waves arrive at the breech rather than one. By moving the right number of vents the correct distance from the muzzle, the strength of each wave can be minimized.

As noted above, a vented tube must be somewhat longer to maintain the desired projectile velocity. Displacing some of the vents upstream adds another fraction of a caliber. However, because the upstream vents work at a higher pressure level, fewer vents are required to match the impulse reduction obtained with the unsplit design. In the example above, only 11 rows are needed rather than the original 12.

The scheme will be tested in the laboratory using a 20-mm cannon and in the field using a 105-mm cannon. More complete details of the calculations will be given in a future paper when the test results become available.

CONCLUSIONS

The model predictions are in satisfactory agreement with available overpressure data for small and large caliber cannon. The covolume correction in the Abel equation significantly improves the results for the latter. More data will be available in the near future for further comparison.

Upstream venting shows considerable promise as a method of reducing blast levels in the breech area while maintaining specified values of projectile velocity and weapon impulse. Laboratory and field testing of the scheme is planned.

REFERENCES

1. Dillon, R.E. Jr., "A Parametric Study of Perforated Muzzle Brakes," Technical Report ARLCB-TR-84015, Benet Weapons Laboratory, Watervliet, NY, May 1984.

2. Dillon, R.E. Jr., "Wall Thickness and Vent Area Effects on Perforated Muzzle Brake Performance," Technical Report ARLCB-TR-84020, Benet Weapons Laboratory, Watervliet, NY, May 1984.

3. Dillon, R.E. Jr. and Nagamatsu, H.T., "An Experimental Study of Perforated Muzzle Brakes," Technical Report ARLCB-TR-84004, Benet Weapons Laboratory, Watervliet, NY, February 1984.

4. Dillon, R.E. Jr. and Nagamatsu, H.T., "A Method of Analyzing Perforated Muzzle Brake Performance," Technical Report ARLCB-TR-84002, Benet Weapons Laboratory, Watervliet, NY, February 1984.

5. Dillon, R.E. Jr. and Nagamatsu, H.T., "An Experimental Study of Perforated Muzzle Brakes," AIAA Paper 84-1642, presented at the AIAA 17th Fluid Dynamics, Plasma Dynamics, and Lasers Conference, June 25-27, 1984, Snowmass, Colorado.

6. Nagamatsu, H.T., Choi, K.Y., Duffy, R.E., and Carofano, G.C., "An Experimental and Numerical Study of the Flow Through a Vent Hole in a Perforated Muzzle Brake," Technical Report ARCCB-TR-87016, Benet Laboratories, Watervliet, NY, June 1987.

7. Nagamatsu, H.T., Choi, K.Y., and Duffy, R.E., "Wall Thickness and Flow Mach Number Effects on Pressure Distribution in the Vent Hole for Perforated Muzzle Brakes," ARDEC Contractor Report ARCCB-CR-86038, Rensselaer Polytechnic Institute, Troy, NY, November 1986.

8. Carofano, G.C., "The Gasdynamics of Perforated Muzzle Brakes," Technical Report ARCCB-TR-88006, Benet Laboratories, Watervliet, NY, February 1988.

9. Carofano, G.C., "The Blast Field Produced by a Cannon Having a Perforated Muzzle Brake," Technical Report ARCCB-TR-88043, Benet Laboratories, Watervliet, NY, December 1988.

10. Corner, J., Theory of the Interior Ballistics of Guns, John Wiley and Sons, New York, 1950.

11. Plostins, P. and Clay, W.H., "Performance of Lightweight 105-mm Cannon Designs" (U), Technical Report BRL-TR-2749, Ballistic Research Laboratory, Aberdeen Proving Ground, MD, July 1986.

12. Baur, E.H. and Savick, D.S, "120-mm Perforated Muzzle Brake Performance," Ballistic Research Laboratory, Aberdeen Proving Ground, MD, technical report to be published.

13. Harten, A., "High Resolution Schemes for Hyperbolic Conservation Laws," J. Computational Physics, Vol. 49, No. 3, March 1983, pp. 357-393.

14. Carofano, G.C., "Blast Computation Using Harten's Total Variation Diminishing Scheme," Technical Report ARLCB-TR-84029, Benet Weapons Laboratory, Watervliet, NY, October 1984.

NAGAMATSU, DUFFY AND ANDRADE

TITLE: GENERIC GUN BORE EVACUATORS I. EXPERIMENTAL AND AERODYNAMIC INVESTIGATIONS

H. T. NAGAMATSU, R. E. DUFFY AND C. A. ANDRADE
RENSSELAER POLYTECHNIC INSTITUTE, TROY, NY AND
U.S. ARMY ARMAMENT RESEARCH, DEVELOPMENT, AND ENGINEERING CENTER
CLOSE COMBAT ARMAMENTS CENTER
BENET LABORATORIES
WATERVLIET, NY 12189-4050

ABSTRACT:

Gas dynamic processes for the gun bore evacuator are investigated analytically and experimentally with a 2-inch bore diameter model of the 120 mm cannon with room temperature air. Three breech and muzzle length-to-diameter ratios of 5, 10, and 20 and evacuator injection angles of 20, 30, 45 and 60 degrees were constructed and investigated for evacuator pressures of 16 to 82 psig.

For all barrel lengths and injection angles, the entrained breech airflow velocity increased as the evacuator reservoir pressure was increased. The maxima for breech flow velocity and mass-flow augmentation occurred for a muzzle length of 10. However, for all injection angles and gun configurations tested, augmentation decreases with reservoir pressure.

For a given reservoir pressure the maximum breech velocity and augmentation occur for an injection angle of 30° and for angles less and greater than 30° the breech velocity and augmentation are lower. Schlieren photographs of the jet plumes for injection angles of 20, 30, and 90° indicate that the jet plume for 20° inclination interacts with the wall, Coanda Effect, which causes the decrease in the breech velocity and augmentation from the values for 30° angle.

A one-dimensional compressible flow model of the steady-state evacuator discharge is used to calculate the performance of the evacuator for various reservoir pressures and injection angles and produces the trends of the experimental data for injection angles greater than 30°. The analysis did not predict the decrease in the breech velocity and augmentation for 20° injection angle because the Coanda Effect is not included.

BIOGRAPHY:

PRESENT ASSIGNMENT: Professor of Aeronautical Engineering, Rensselaer Polytechnic Institute, Troy, NY and Consultant Benet Laboratories, Watervliet, NY

PAST EXPERIENCE: Research in the areas of hypersonic gas dynamics, fluid mechanics, transonic flows, supersonic jet noise, arcs-in-nozzle flow, magnetohydrodynamics and heat transfer.

DEGREES HELD: B.S. in M. Eng., 1938; B.S. in Aero. Eng., 1939; M.S. in Aero. Eng., 1940 and Ph.D. in Aero, 1949, all from California Institute of Technology, Pasadena, CA.

GENERIC GUN BORE EVACUATORS I. EXPERIMENTAL AND AERODYNAMIC INVESTIGATIONS

H.T. Nagamatsu and R.E. Duffy
Rensselaer Polytechnic Institute, Troy, NY 12180-3590

and

C.A. Andrade
Benet Laboratories
Watervliet, NY 12189-4050

The evacuation of the propellant gas in the muzzle after the exiting of the projectile in modern large caliber cannons is accomplished by the injection of compressed propellant gas through the ports in the barrel wall from the evacuator cannister, which is charged with the hot gas. When the pressure in the barrel is below the level charged in the cannister, the high pressure gas flows into the barrel through the ejector ports distributed circumferentially around the barrel. The jet velocities can reach Mach 2 depending upon the peak reservoir charge level and the total pressure drop across the nozzle. During the evacuator discharge cycle the ejector nozzle mass flow rate reaches a steady state and induces a secondary mass flow that sweeps the residual gas out of the barrel before opening the breech to load the next round.

An investigation was conducted by Smith [1] with a gun barrel of 0.3-inch caliber and various injection angles relative to the axis of the muzzle. The amount of ambient mass flow induced by the injected air through the orifices for a reservoir pressure up to 6 atm was determined as functions of the injection port angle and pressure. The lengths of the barrel in front and downstream of the injection ports were 10 calibers. Attempts at solving the bore evacuator problem are presented in the Army sponsored projects [2,3]. These employed the Reynolds transport theorem which is the basis of steady state ejector theory.

Andrade et al. [4] used the Reynolds transport theorem to relate the mass, momentum, and energy flux for compressible flow at the simulated breech, muzzle, and ejector jet exit control surfaces to calculate the bore evacuator performances. This yields exact transcendental solutions for the induced velocities in the breech end as functions of reservoir pressure, nozzle angle, and nozzle to gun bore area ratio. From the induced velocities the induced mass flow rates were calculated to determine the augmentation, which is the ratio of the induced mass flow rate to the ejector mass flow rate. The calculated induced velocities and augementations were in approximate agreement with the experimental data [5]

A two-inch diameter bore evacuator model for the 120 mm gun barrel was constructed, Figs.1 and 2, to investigate the effects of injection angle, breech inlet and muzzle exit lengths on the performance of the bore evacuator with room temperature air [5]. Five constant 0.075-inch diameter injection holes of 20, 30, 45, and 60° from the barrel axis, Fig.1, were investigated for various ratios of breech to muzzle lengths and different evacuator reservoir pressures and head wind velocities. The entrained velocity distribution across the breech inlet was measured with the hot-wire probe and the mass flow rates for the evacuator ports were determined by the use of an orifice meter. The augmentations were determined for various model configurations and evacuator pressures. One-dimensional compressible ideal flow model of the steady-state generic bore evacuator results [4] were correlated with the experimental induced breech velocities and augmentations for various injection angles and evacuator pressures.

EXPERIMENTAL FACILITIES AND INSTRUMENTATION

Bore Evacuator Model

A bore evacuator model was constructed for steady-state operation for simulating the condition following the combustion of the propellant charge in the gun barrel. The model consists of a 12-inch pressure chamber surrounding the inner 2-inch diameter tube through which the ejector passages at various angles relative to the barrel axis were drilled, Figs.1 and 2. High pressure air is supplied to the pressure chamber by two flexible hoses and the pressure in the chamber is measured with a pressure gage attached to the evacuator, Fig.2. The breech and muzzle extensions of length-to-diameter ratios measured from the injection holes of 5, 10, and 20 were used to change the lengths of the breech and the muzzle, Figs.1 and 2.

Static pressure taps are placed along these extensions, Fig.1, and inside the evacuator chamber, Fig.2, to measure the static pressure distributions for various evacuator pressures, injection angles for the jets and breech and muzzle lengths. Ten static pressure taps are placed in the center bore at 1.125 in. interval location symmetrically about the axis of the injection holes.

Five injector ports were drilled so as to exit 0.25 inch off the center of the evacuator, Figs.1 and 2. Two evacuator center bore sections were constructed with the injection hole angles of 30° and 60° in one of the bore pieces and 20° and 45° in the other piece. The diameter of the injection holes was 0.075-inch with sharp corners at the entrance and exit of the constant diameter holes.

Air Supply to the Evacuator and Head Wind Simulation

A 110 psig compressor was used to supply the air to the evacuator at room temperature and a valve was installed ahead of the flexible inlet hoses to the bore evacuator, Fig.2b, to vary the pressure into the evacuator chamber. With this compressor it was possible to maintain steady flow

conditions in the bore evacuator for measuring the static pressures along the barrel and the induced flow velocity at the breech entrance. A bellmouth inlet was installed at the breech end to smooth the entrained room air into the barrel by the evacuator jets. To simulate the head wind for the gun barrel, a variable speed axial fan was placed in front of the muzzle exit, Fig.2b, and the head wind velocity was varied from 0 to 75 ft/sec. The effects of the head wind on the performance of the evacuator for various configurations were determined for a few injection angles.

Sharp-Edged Orifice to Measure Injector Mass Flow

The mass flow rate of air filling the reservoir was measured by a one-inch diameter sharp-edge orifice, utilizing flange taps located along the two-inch supply pipe, Fig.2. Measurements were made of the pressure drop across the orifice by a manometer filled with silicon oil. This data was reduced to give a value for the mass flow rate through the evacuator ejector nozzles.

Mass Flow Entrainment Measurements

Airflow entrained at the breech end of the model was measured by using a hot-wire anemometer lowered into the flow at the entrance to the barrel, Fig.2. This device makes use of electrical voltage measurements to determine the fluid velocity. The hot-wire was calibrated by using a small wind tunnel consisting of a fan, a laminar flow device and a manometer to measure the mass flow rate. A bell-mouth inlet was constructed and placed over the breech end of the model to prevent flow separation. Velocity profiles showed that no significant separation had occurred so that mass flow could be determined by this procedure.

EXPERIMENTAL RESULTS

Breech Induced Velocity as Functions of Breech and Muzzle Lengths, Injection Angle and Evacuator Pressure

The induced velocities at the breech entrance, Figs.1 and 2, as functions of the breech and muzzle lengths of 5, 10, 20, injection angles of 20, 30, 45, and 60° and evacuator pressures of 5 to 82 psig were determined and are presented in Ref.5. In Fig.3 the breech velocities produced with an injection angle of 30° for various muzzle lengths and evacuator pressures are presented for a breech length of 5. For these configurations the breech velocities increased monotonically with the evacuator pressure. A maximum entrained velocity of 370 ft/sec was produced for a muzzle length of 10 and a pressure of 82 psig. For muzzle lengths of 5 and 20 the increase in the breech velocities was about the same for all pressures.

Augmentation as Functions of Breech and Muzzle Lengths, Injection Angle and Evacuator Pressure

The augmentations as functions of the breech and muzzle lengths, injection angle and evacuator pressure were determined in Ref.5. From these

results the augmentation for an injection angle of 30° are presented in Fig.4 for a breech length of 5 and various muzzle lengths and evacuator pressures. The maximum augmentation is 17.8 for a muzzle length of 10 and a pressure of 27 psig. For muzzle lengths of 10 and 20 the augmentations were close and decreased only moderately with the evacuator pressure, but for a muzzle length of 5 the augmentation decreased more rapidly with the pressure because of a shorter muzzle length for the mixing of the jet flows with the entrained air.

Augmentation as Functions of Muzzle Length, Bore Evacuator Pressure and Breech Length for Injection Angle of 30°

The augmentation as functions of the muzzle length for various evacuator pressures for an injection angle of 30° is presented in Fig.5 for a breech length of 5. For evacuator pressures of 16 to 82 psig the augmentations were greatest for a muzzle length of 10 and the augmentations were less for muzzle lengths of 5 and 20. For a muzzle length of 5 the mixing of the evacuator jets with the entrained air through the breech end is not completed as indicated by the less than ambient static pressures over the muzzle length. The mixing of the jet flows with the entrained air is completed for the muzzle length of 20 but the viscous losses over the muzzle surface are greater than for the muzzle length of 10. Therefore, the augmentation for the muzzle length of 20 is lower than for a length of 10 for all evacuator pressures.

Breech Velocity as Functions of Injection Angle, Bore Evacuator Pressure, and Breech and Muzzle Lengths

The induced breech velocities at the entrance to the barrel as functions of the injection angle and bore evacuator pressure are presented in Fig.6 for the breech and muzzle lengths of 10. A breech velocity of 301 ft/sec was produced with an injection angle of 30° and evacuator pressure of 82 psig, and the maximum breech velocities occurred for an injection angle of 30° for all evacuator pressures. Similar variation of the breech velocity with the injection angle and evacuator pressure for other breech and muzzle lengths were observed [5].

The decrease in the induced breech velocity for an injection angle of 20° is caused by the jet flow from the ejector ports interacting with the barrel surface due to the Coanda Effect. The jet plume is partially attached to the wall so the entrainment of the ambient air through the breech by the jets is restricted. Therefore, an investigation was conducted with the ejector tubings cut at angles of 20, 30, and 90° with respect to the axis to observe the jet flow structure with the Schlieren photographs to confirm the existence of the Coanda Effect. This phenomenon is discussed later in the paper.

Augmentation as Functions of Injection Angle, Bore Evacuator Pressure, and Breech and Muzzle Lengths

The augmentations as functions of injection angle and bore evacuator pressure are presented in Fig.7 for breech and muzzle lengths of 10. The

maximum augmentations occurred for an injection angle of 30° for all evacuator pressures and the augmentation decreased with the evacuator pressure for all injection angles. As expected the augmentation decreased from the peak value for injection angles less and greater than 30° for all pressures. The augmentations for an injection angle of 60° were approximately one-third of the peak values for all pressures. The decrease in the augmentation for an injection angle of 20° is due to the interaction of the jets with the wall of the barrel, Coanda Effect, as discussed previously.

Augmentation as Functions of Head Wind Velocity, Bore Evacuator Pressure, and Breech and Muzzle Lengths for 45° Injection Angle

The effects of the head wind on the augmentation for various barrel configurations, injection angle, and bore evacuator pressure were studied using a blower ahead of the muzzle, Fig.2a. Since the head wind effects were similar for all barrel configurations and injection angles, the augmentation results for an injection angle of 45° were selected and are presented in Fig.8 for breech length of 5 and muzzle length of 20. For head wind velocities of 0 to 75 ft/sec the augmentation for evacuator pressures of 27 to 82 psig decreased only slightly with the velocity. This is due to the fact that the breech velocity varied from approximately 190 to 350 ft/sec for evacuator pressures of 27 to 82 psig, Fig.3. At the muzzle exit the velocity will be slightly greater than the breech velocity because of the additional mass flow rate from the evacuator.

Schlieren Photographs of Ejector Jets with Inclined Angles of 20, 30 and 90 Degrees

To study the interaction of the evacuator jet flows with the barrel wall, Coanda Effect, three tubings with an inside diameter of 0.178 inch were fabricated with exit angles of 20, 30 and 90° relative to the axis. These tubings were mounted on a flat plate to simulate the jet flow exiting from the evacuator ports, Fig.1. Static pressure taps were placed along the tube wall and the plate surface to determine the velocity distribution along the tube as well as the interaction of the jet plume with the plate surface.

Schlieren photographs of the jets inclined at angles of 20, 30 and 90° were taken for reservoir pressures of 5, 16, and 60 psig, and are presented in Fig.9. The corresponding nominal jet flow Mach numbers are 0.66, 1.09 and 1.71, respectively. For the 90° jet the shock bottles are present for 16 and 60 psig and the shock waves are normal to the axis. Also, for a Mach number of 1.71 the supersonic jet plume extends appreciable distance from the exit. Static pressure distribution along the tubing indicated near sonic velocity at the exit for pressures of 16 and 60 psig, and the static pressure at the exit was approximately 30 psig for a reservoir pressure of 60 psig.

For jet inclinations of 30 and 20° the shock bottles were inclined relative to the jet axis, Fig.9, and the jet plumes were broader compared to the 90° jet. The shock waves for the 20° jet with a pressure of 60 psig

and a nominal Mach number of 1.71 were inclined the greatest angle relative to the jet axis. Also, the jet plume is broad and does not extend as far as for the 90° jet. The static pressure distributions along the tubing for these inclination angles indicated that the sonic velocity existed ahead of the exit. Thus, the jet flows from these tubings were similar to the supersonic flow from a convergent-divergent nozzle. Static pressures at the exit of the tubing were close to the ambient pressure for reservoir pressures of 16 and 60 psig, indicating supersonic flows at the jet exit.

The static pressures on the plate surrounding the jet exit were close to the ambient pressure for inclination angles of 30 and 90° indicating that the jet plume is not affected by the plate surface. For these angles the jet plumes will entrain the ambient air through the breech without the influence of the wall surface. But for the 20° angle the static pressures on the plate surface adjacent to the jet exit were above the ambient pressure for supersonic jet flows. Thus, the jet plume is partially attached to the wall so the entrainment surface of the jet plume is less than for the 30° inclination. This Coanda Effect decreases the effectiveness of the evacuator jets in entraining the ambient air through the breech as shown in Figs.6 and 7.

THEORY OF ROOM TEMPERATURE AIR EVACUATORS

In the present work we model steady-state flow of a thermally perfect gas through the bore evacuator. The reservoir is annular, symmetric with the weapon axis. On any plane containing the axis, the nozzle angle, φ, is slanted up to 60° measured relative to the axis, Fig.10. Circular control surfaces labeled I and M, as shown on the figure, are placed at the inlet (breech-end of the evacuator) and at the outlet (muzzle-end) respectively; and an elliptical free-surface labeled N is placed at a uniform nozzle expansion flow area, that varies with supercritical reservoir pressure ratios, or is equal to the nozzle cross-section area at subcritical pressures.

Assumptions and Boundary Conditions

1) One-dimensional, compressible inviscid flow of a thermally perfect gas ($\gamma = 1.4$): Barrel extensions to the evacuator (connected at the evacuator breech and muzzle ends), the ejector nozzles, and nozzle jet "mixing" stream are assumed viscous-free and nonheat conducting.

2) Total enthalpy, H_I, at the inlet control surface, is equal to the ambient "freestream" total enthalpy, i.e.,

$$(\gamma - 1)H_I = a_I^2[1 + (\gamma - 1)M_I^2/2] = a_o^2 , \qquad (1)$$

where the unknown inlet Mach number, M_I, is an implicit function of reservoir pressure, i.e., $M_I = M_I(p_R)$, and γ is the ratio of specific heats for the gas under consideration. Assumptions 1) and 2) imply isentropic conditions at the inlet. In conformance with experimental observation, pressure at the inlet will fall below the ambient value, p_o, so that

3)

$$p_I = p_o/\{1 + (\gamma - 1)M_I^2/2\}^{\gamma/(\gamma-1)} . \tag{2}$$

As a consequence of these conditions the inlet flow variables are known as functions of the local Mach number, M_I.

4) Reservoir temperature equals the ambient room temperature, i.e., in conformance with the experimental procedure, $T_R = T_o$.

5) Nozzle exit total enthalpy equals the reservoir total enthalpy,

$$(\gamma - 1)H_N = a_R^2 = a_o^2 . \tag{3}$$

For internally shock-free nozzles, conditions 1 through 5 imply isentropic conditions at the nozzle expansion. Thus,

$$p_N = p_R/\{1 + (\gamma - 1)M_N^2/2\}^{\gamma/(\gamma-1)} . \tag{4}$$

6) Following the treatment of thrust ejectors designed for constant pressure mixing [6,7], we let the nozzle flow expansion pressure be equal to the inlet pressure, $p_N = p_I$. Thus, Eqs.(2) and (4) yield the nozzle flow expansion Mach number,

$$M_N = \{2[p_{RO}^{(\gamma-1)/\gamma}\{1 + (\gamma - 1))M_I^2/2\} - 1]/(\gamma - 1)\}^{1/2} \tag{5}$$

where M_I is an implicit function of the reservoir to ambient pressure ratio, $p_R/p_o = {}^{I}p_{Ro}$.

Equations to be Solved

Two state variables and the flow speed are to be determined at each of three control surfaces, I, N and M, amounting to nine flow quantities that may vary with the reservoir pressure gradient imposed through the nozzle. Reynolds' Transport Theorem [8] applied to these surfaces gives the outlet total mass flux,

$$\rho_M u_M = \rho_I u_I + \rho_N u_N \chi , \tag{6}$$

total momentum or impulse,

$$p_M + \rho_M u_M^2 = p_I + \rho_I u_I^2 + \{(p_N + \rho_N u_N^2)\cos\varphi\}\chi , \tag{7}$$

and total energy generated,

$$\rho_M u_M H_M = \rho_I u_I H_I + \rho_N u_N H_N \chi , \tag{8}$$

where the total nozzle expansion to gun bore area ratio is given by $\chi = A_N/A = (A_T/A)/(A^*/A)_N$, and $A_T = A^*$ at subcritical pressure ratios.

According to 6), the nozzle expansion pressure is a function of the inlet Mach number, i.e., $p_N = p_I$ is given by Eq.(2) and is thus eliminated from the set of unknowns. We use the conservation laws, Eqs.(6) - (8), three control surface state equations, written in the form $a^2 = \gamma p/\rho$, and Eq.(5) to solve for seven unknown quantities, after closing the system by assuming that the outlet pressure is equal to the ambient pressure, $p_M = p_o$. Note that this closure, together with Eq.(2), provides the pressure step function for the pump.

Mass flux through the nozzle is determined by reservoir and throat conditions:

$$\rho_N u_N = \rho^* a^* (A^*/A)_N = \rho_R a_R (A^*/A)_N / \{(\gamma+1)/2\}^{(\gamma+1)/2(\gamma-1)},$$

where $\{(\gamma+1)/2\}^{-(\gamma+1)/2(\gamma-1)} = 0.5787$ is the value for choked flow. Substituting the gas dynamic expression for A^*/A, using the equation of state for the reservoir, and considering assumption 4), gives

$$\rho_N u_N = \gamma p_o p_{Ro} M_N / \{1 + (\gamma - 1)M_N^2/2\}^{(\gamma+1)/2(\gamma-1)} a_o . \tag{9}$$

Since the nozzle expansion velocity is given by

$$u_N = M_N a_o / \{1 + (\gamma - 1)M_N^2/2\}^{1/2}, \tag{10}$$

where Eqs.(3) and (5) determine the local sound speed and Mach number, then the required nozzle expansion control surface variables are determined by Eqs.(5), (9) and (10), as functions of the inlet Mach number $M_I = M_I(p_{Ro})$. Thus, since the six variables at the inlet and nozzle exit control surfaces can be determined as functions of the inlet Mach number, the local equations can be used so that the three remaining variables on the left-hand sides of Eqs.(6) - (8) are also functions of MI, i.e., the conservation equations become:

$$\rho_M u_M = \rho_o a_o p_{Io} \eta , \tag{11}$$

$$p_M + \rho_M u_M^2 = p_I \zeta , \tag{12}$$

and

$$(\gamma - 1)\rho_M u_M H_M = (r + 1)\rho_N u_N a_o^2 \chi : \tag{13}$$

and where two auxiliary functions have been derived as listed:

1) The total mass flow function is

$$\eta(M_I, p_{Ro}, \chi) = M_I\{1 + (\gamma - 1)M_I^2/2\}^{1/2} + M_N\{1 + (\gamma - 1)M_N^2/2\}^{1/2}\chi \ ; \qquad (14)$$

2) the total impulse function is

$$\zeta(M_I, p_{Ro}, \varphi, \chi) = 1 + \gamma M_I^2 + \{(1 + \gamma M_N^2) \cos \varphi\}\chi \ . \qquad (15)$$

Flow Augmentation at the Breech

The frictionless breech mass flow augmentation ratio is defined as

$$r(M_I, p_{Ro}, \chi) = \rho_I u_I / \rho_N u_N \chi \ . \qquad (16)$$

Proceeding with mass flux derivations, e.g., Eq.(9), we obtain

$$r = (A^*/A)_I / (A^*/A)_N p_{Ro} \chi \ , \qquad (17)$$

that is, for fixed geometry, flow augmentation is a function of the reservoir pressure ratio and induced inlet Mach number, $M_I = M_I(p_{Ro})$.

Again, by using the local state equation and Mach number, Eq.(12) is rewritten as

$$p_M = \zeta p_I / (1 + \gamma M_M^2) \ . \qquad (18)$$

Thus, by examining the total impulse ratio, $p_M/p_I = p_o/p_I$, it is clear that the pumping action is given by momentum exchange, expressed as

$$\zeta(M_I)/(1 + \gamma M_M^2) = \{1 + (\gamma - 1)M_I^2/2\}^{\gamma/(\gamma-1)} \ . \qquad (19)$$

Induced velocity at the outlet, u_M, is calculated by transposing the pressure p_M to the right-hand side of Eq.(12), dividing the result by Eq.(11) and introducing Eq.(18) into the quotient. Thus,

$$u_M = a_o(\zeta/\eta)M_M^2/(1 + \gamma M_M^2) \ , \qquad (20)$$

which, substituted into Eq.(11) gives the remaining unknown, viz,

$$\rho_M = \rho_o p_{Io}(\eta^2/\zeta)(1 + \gamma M_M^2)/M_M^2 \ . \qquad (21)$$

Written as the usual product of Mach number with the local sound speed, $u_M = a_o M_M T_{Mo}^{1/2}$. Equating this to Eq.(20) gives the outlet to ambient temperature ratio, i.e., $T_{Mo} = [(\zeta/\eta)M_M/(1+\gamma M_M^2)]^2$. Rewriting the total mass flux, Eq.(6), in terms of the augmentation ratio allows us to eliminate mass flux from the energy equation. Thus, Eqs.(6), (8) and (16) give the expected isoenergetic result,

$$H_M = a_o^2/(\gamma - 1) ; \tag{22}$$

and using the definition of local total enthalpy, as in Eq.(1), we obtain the outlet to ambient temperature ratio as a function of M_M:

$$T_{Mo} = 1/\{1 + (\gamma - 1)M_M^2/2\} . \tag{23}$$

Equating the two expressions for T_{Mo} gives

$$(\eta/\zeta)^2 = M_M^2[1 + (\gamma - 1)M_M^2/2]/(1+\gamma M_M^2) , \tag{24}$$

where it is observed that the right-hand side is a function of the outlet Mach number alone, while the left-hand side is a function of the inlet Mach number and the given data. Thus, if $(\eta/\zeta)^2 = f(M_I, p_{Ro}, \varphi, \chi)$ is determined, M_M can be calculated from the implied biquadratic, Eq.(24). The combined mass, momentum and energy equations are then expressed by introducing Eq.(19) into (24):

$$\eta = \{1 + (\gamma - 1)M_I^2/2\}^{\gamma/(\gamma-1)} M_M \{1 + (\gamma - 1)M_M^2/2\}^{1/2} . \tag{25}$$

The iterative scheme used to find a unique variation of the inlet Mach number with the reservoir pressure ratio is obtained by forming a function difference oetween Eqs.(14) and (25), then proceeding with a root-finding routine until that difference is arbitrarily small. Note that for supercritical pressure ratios, p_{Ro}, the area ratio χ depends on A^*/A_N, a function of the nozzle expansion Mach number. All of the unknowns can now be determined by post iterative calculations in terms of the three Mach numbers at the control surfaces, for which there are two explicit Mach number equations, namely, Eqs.(5) and (24). Results are shown in Figures 11 - 14.

We also note that by Crocco's steady-state theorem, e.g., [8,9] an inviscid isoenergetic flow sustains vorticity, i.e., an exchange of linear to angular momentum within the control volume, thus producing a total pressure loss for the pump, which in the experimental case is augmented by the observed dissipation, so it is remarkable that the Reynolds control volume calculations have captured the essential trend and magnitude of that flow without requiring empirical evaluations.

Figure 11 gives the entrained breech velocity, u_I, as a function of the evacuator pressure, p_R (psig), at several nozzle injection angles. For all injection angles, the breech velocity increases monotonically with reservoir pressure. The greatest increase in the entrained velocity occurs between the injection angles of 75 and 60°. The velocity increase for injection angles between 30 and 20° is not appreciable. Figure 12 gives augmentation ratio, r, vs p_R at the same nozzle angles. Augmentation increases with decrease in the injection angle, and the maximum augmentation with respect to injection angle occurs at approximately 16 psig. As the evacuator pressure increases above this value the augmentation decreases for all injection angles. Generally, parametric trends displayed by these results follow that of the experimental observations shown in Figures 3 - 8.

The calculated nozzle jet and breech Mach numbers for two values of total nozzle expansion to bore area ratio, X, are presented in Figure 13 as a function of the reservoir pressure for a 30° injector inclination angle. At a given reservoir pressure, increasing the number of nozzles from 5 to 10 increases the injector jet Mach number in smaller proportion to corresponding increases in the breech Mach number [proportional derivative from Eq.(5)].

Figure 14 compares the theoretical and experimentally determined entrained breech velocity. Clearly, the experimental results indicate that a 30° nozzle angle gives the maximum entrained velocity over the entire reservoir pressure range. The decrease at 20° is attributed to the Coanda interaction of the jet Mach bottle with the barrel wall (Figure 10), not accounted for in the theory.

CONCLUSIONS

Gas dynamic processes that characterize the gun bore evacuators were investigated by using a model of the gun barrel with room temperature air as the working fluid. A one-dimensional compressible ideal flow model of the steady-state evacuator discharge was used to calculate the performance of the evacuator for various reservoir pressures, injection angles, and the results were correlated with the experimental data.

A 2-inch bore diameter model was designed and constructed to simulate nozzle-to-bore area ratio for generic 120 mm cannon. Three breech and nozzle lengths-to-diameter ratios of 5, 10, and 20 and evacuator injection angles of 20, 30, 45 and 60° were constructed and investigated for evacuator pressures of 16 to 82 psig.

The breech velocity was measured with a hot-wire anemometer and the mass flow rate for the ejector nozzles was determined by the sharp-edged orifice. Static pressures along the barrel were measured with a digital manometer.

The entrained breech velocity increases with the evacuator pressure for all barrel lengths and injection angles. The maximum breech velocities occurred for a muzzle length of 10 and for muzzle lengths of 5 and 20 the

velocities were lower. Ejector jet flows are mixed completely with the entrained flow for a muzzle length of 10, but for a muzzle length of 5 the mixing of the jet flow is not complete and for a length of 20 the friction losses in the muzzle decreases the pump action of the ejectors. The augmentation decreases with the evacuator pressure for all barrel configurations, and for a fixed injection angle the augmentation is a maximum for a muzzle length of 10 and decreases for lengths of 5 and 20.

Maximum breech velocity and augmentation occurred for an injection angle of 30° for constant reservoir pressures of 16 to 82 psig and breech and muzzle lengths of 10. For angles less and greater than 30° both breech velocity and augmentation decreased from the maximum values of 30°. Schlieren photographs of single tube mounted on a flat plate with the tube exit cut-off angles of 20, 30 and 90° confirmed the interaction of the jet plume for the 20° inclination with the plate surface, Coanda Effect, which caused the decrease in the breech velocity and augmentation from the maximum values for 30° ejector angle.

Head wind velocities of 0 to 75 ft/sec did not affect the augmentation within the experimental accuracy for reservoir pressures of 27 to 82 psig. The muzzle velocity for a pressure of 27 psig is approximately 175 ft/sec for an injection angle of 45°.

The breech velocities and the augmentations for various injection angles and evacuation pressures were calculated and the results produce the general trend of the experimental data for injection angles greater than 30°. The analysis did not produce the decrease in the breech velocity and the augmentation for an injection angle of 20° because the Coanda Effect was not considered in the analysis. To improve the correlation of the calculated results with the experimental data, the viscous losses in the breech and muzzle surfaces and the mixing phenomena of the jets with the entrained air must be included in the analysis.

Acknowledgements

Mr. F. Tesman contributed to the design and construction of the gun bore model and coordinated the tests. The authors acknowledge the support of Drs. J. Zweig and J. Santini, Messers. J. Allen and D. Jones.

REFERENCES

1. Smith, F., "Investigation of Fume Extraction Design," Royal Armament Research and Development Establishment, RARDE Memorandum 13167, 1967.
2. Fagen, W., "Bore Scavenging Study of Case-Loaded Cannon Mounted in Closed-Cab Vehicles," AMF Projects MR 1014 and 1030, Mechanics Research Department, American Machine and Foundry Co., September 1954 and June 1955.
3. Anon, "Bore Evacuators," Chapter 7 of Engineering Design Handbook, Gun Series, Muzzle Devices, U.S. Army Material Command AMC Pamphlet AMCP 706-251, May 1968.

4. Andrade, C., Nagamatsu, H. and Duffy, R., "Theoretical Compressible Flow in Generic Bore Evacuators and Experimental Verification," AIAA 89-0652, January 12, 1989.

5. Nagamatsu, H., Duffy, R. and Andrade, C., "Experimental and Theoretical Investigation of Generic Cannon Bore Evacuator," RPI Report to be published under Army Sponsorship. (In process.)

6. Keenan, J.H., Neumann, R.E. and Lustwerk, F., "An Investigation of Ejector Design by Analysis and Experiment," J. Appl. Mech., 17, 299-309, September 1950.

7. Alperin, J. and Wu, J., "Thrust Augmenting Ejectors, Part I," AIAA J., 21, 1428-1436, October 1983.

8. Thompson, P.A., Compressible Fluid Dynamics, p.16, McGraw-Hill, 1972.

9. Crocco, L., "One-Dimensional Treatment of Steady Gas Dynamics," in Fundamentals of Gas Dynamics, Princeton Univ. Press, 1958.

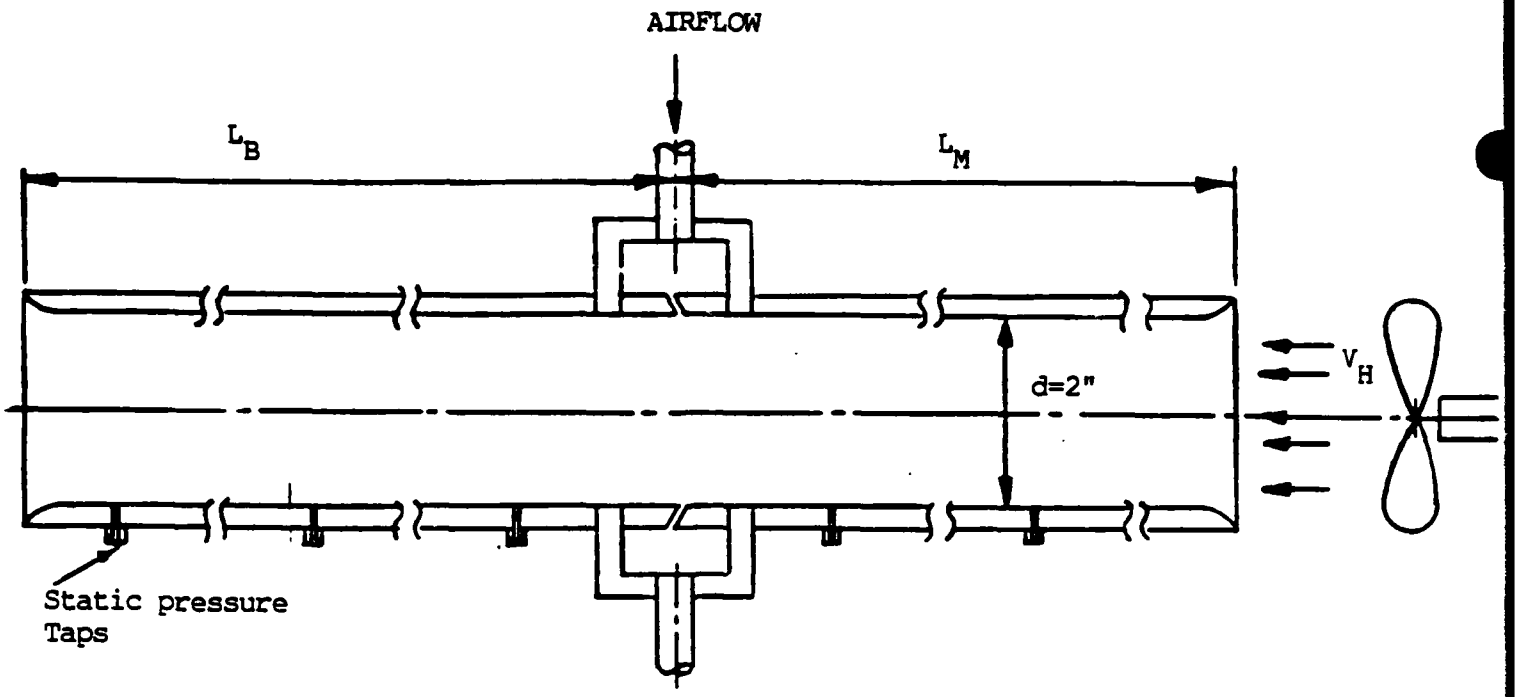

a. Barrel with Various Breech and Muzzle Length

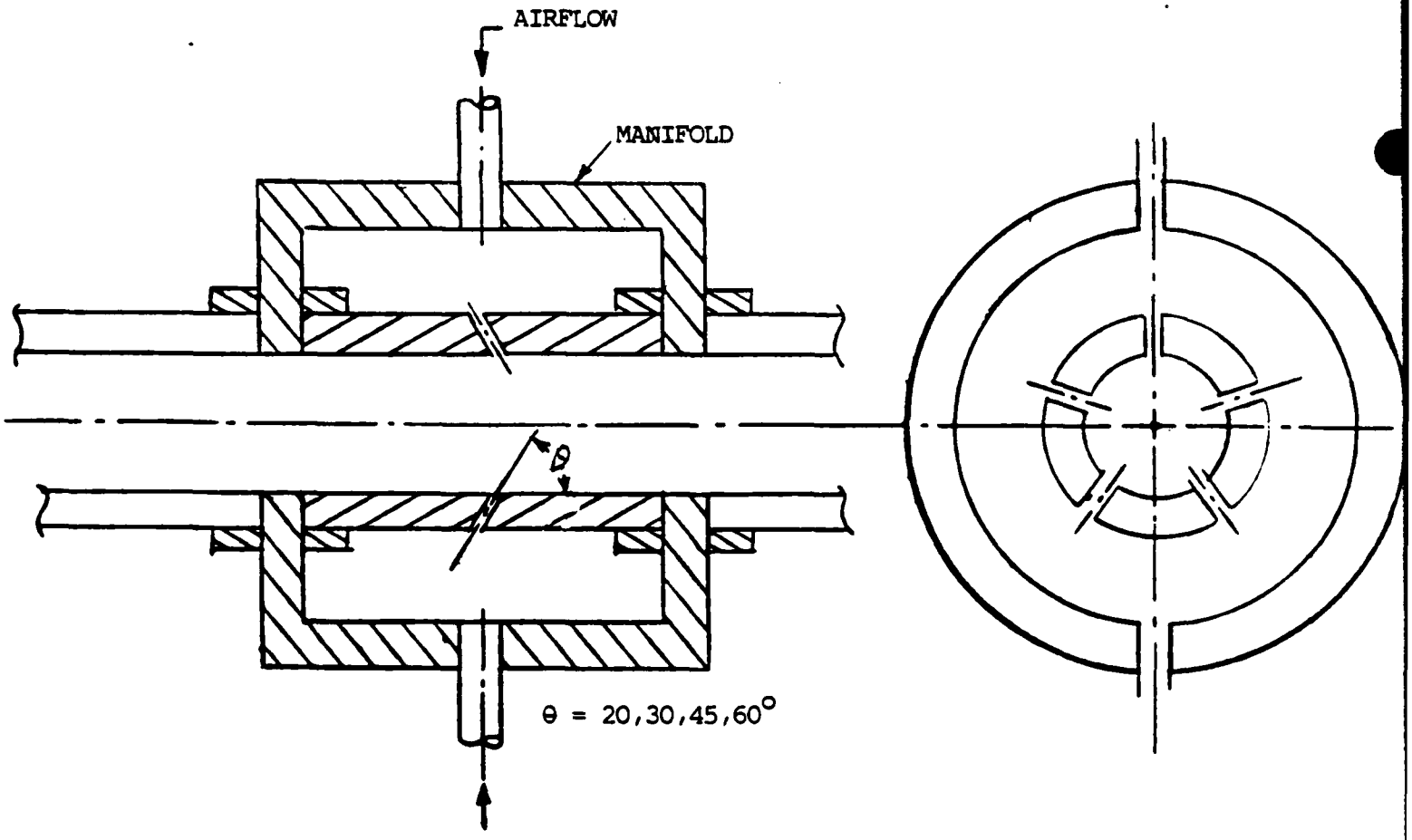

b. Detail of Bore Evacuator with Injection Holes

Figure 1 Barrel of Various Lengths for Bore Evacuator Model.

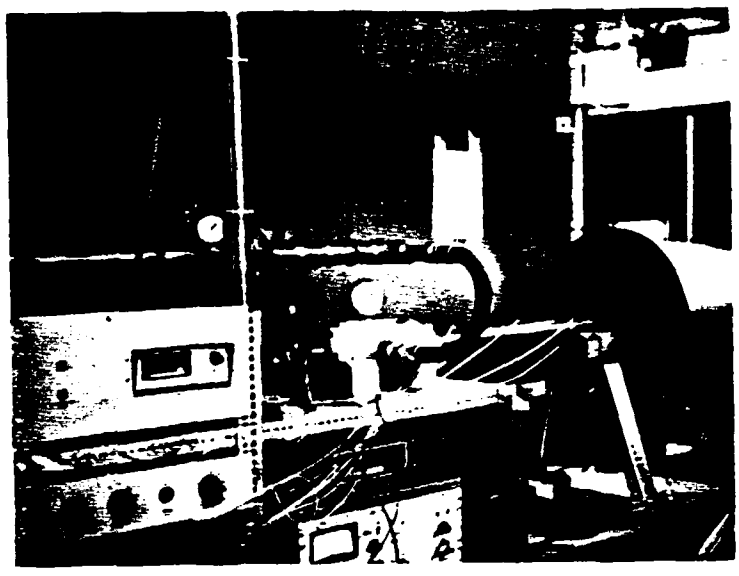

Figure 2a Experimental Fixture at R.P.I. Aerodynamics Laboratory

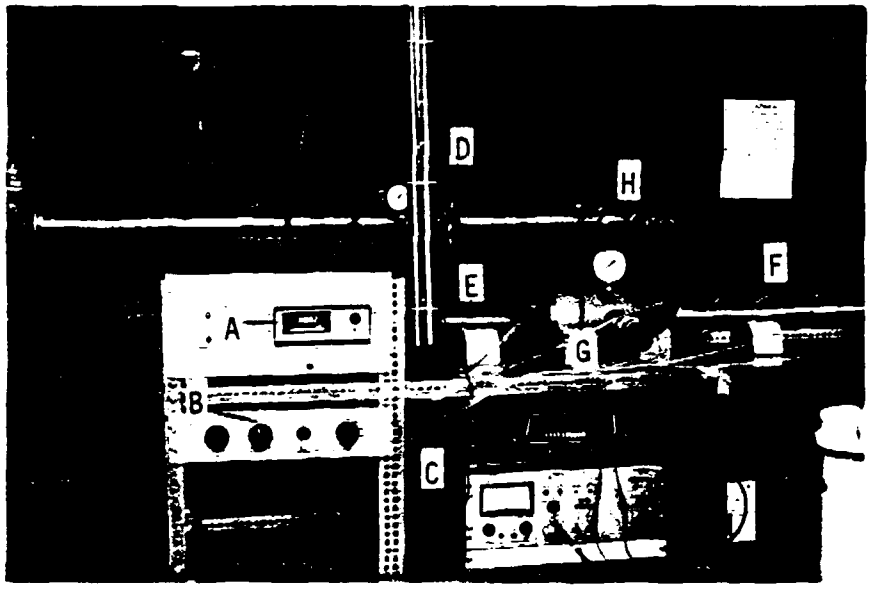

Figure 2b Experimental Set-up

A. Digital Manometer
B. Pressure Tap Dials
C. Hot Wire Equipment
D. Sharp-Edge Orifice
E. Breech End
F. Muzzle End
G. Bore Evacuator
H. Inlet Tubes

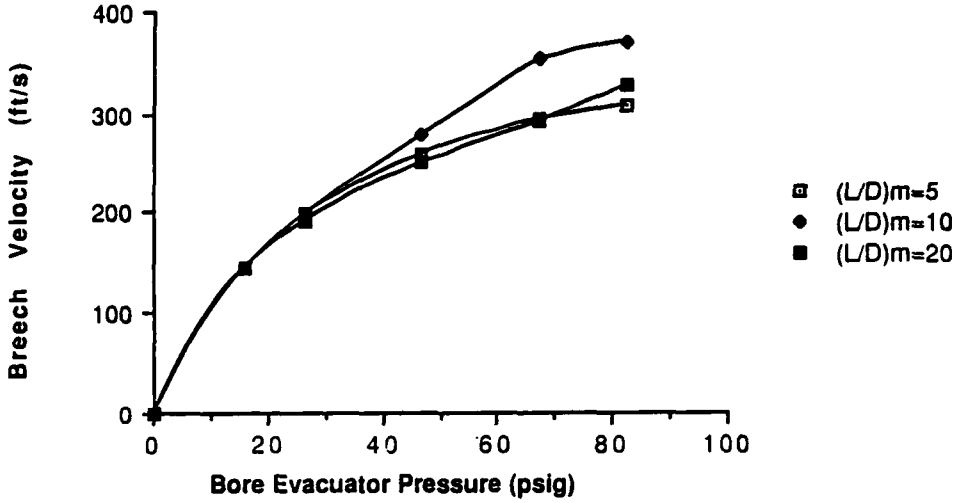

Figure 3 Breech Velocity as Functions of Bore Evacuator Pressure and (L/D)m for (L/D)b = 5 and $\theta = 30^{\circ}$

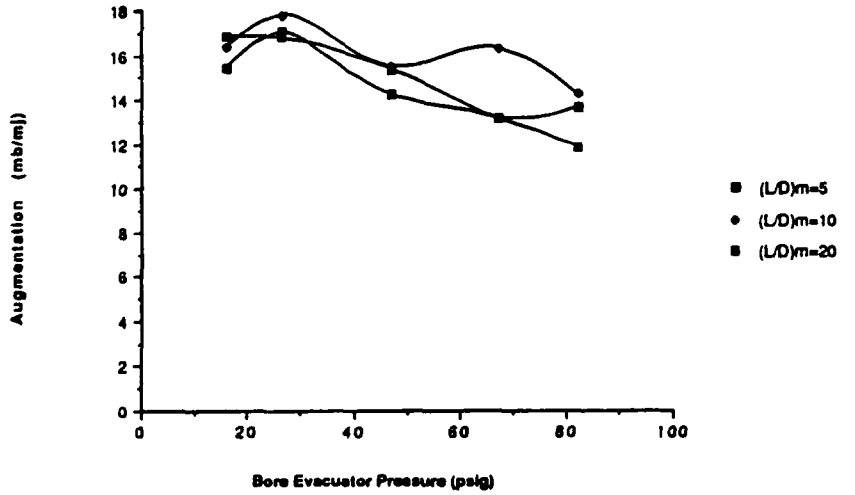

Figure 4 Augmentation as Functions of Bore Evacuator Pressure and (L/D)m for (L/D)b = 5 and $\theta = 30^{\circ}$

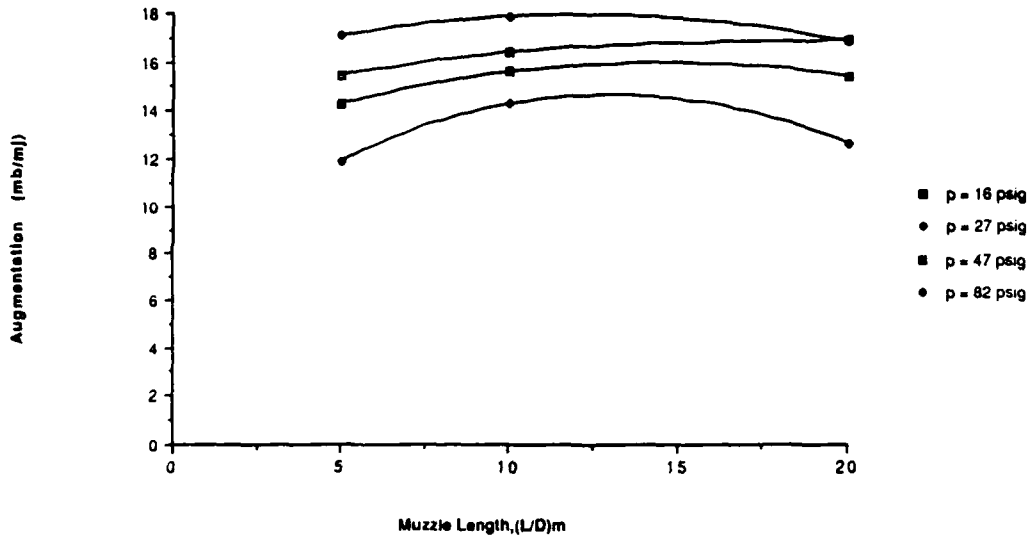

Figure 5 Augmentation as Functions of Muzzle Length, Bore Evacuator Pressure and $(L/D)b = 5$ for $\theta = 30°$

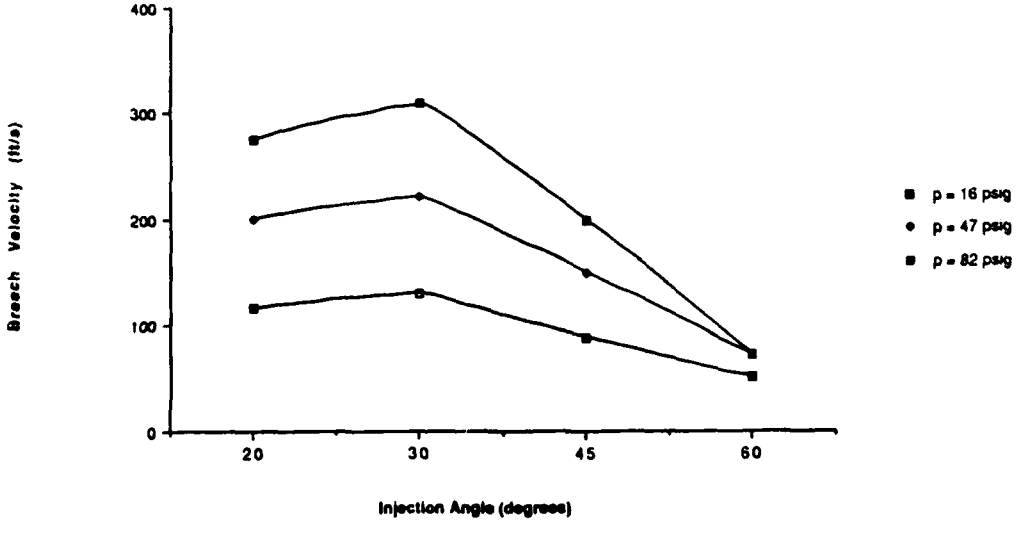

Figure 6 Breech Velocity as Functions of Injection Angle and Bore Evacuator Pressure for $(L/D)b = (L/D)m = 10$

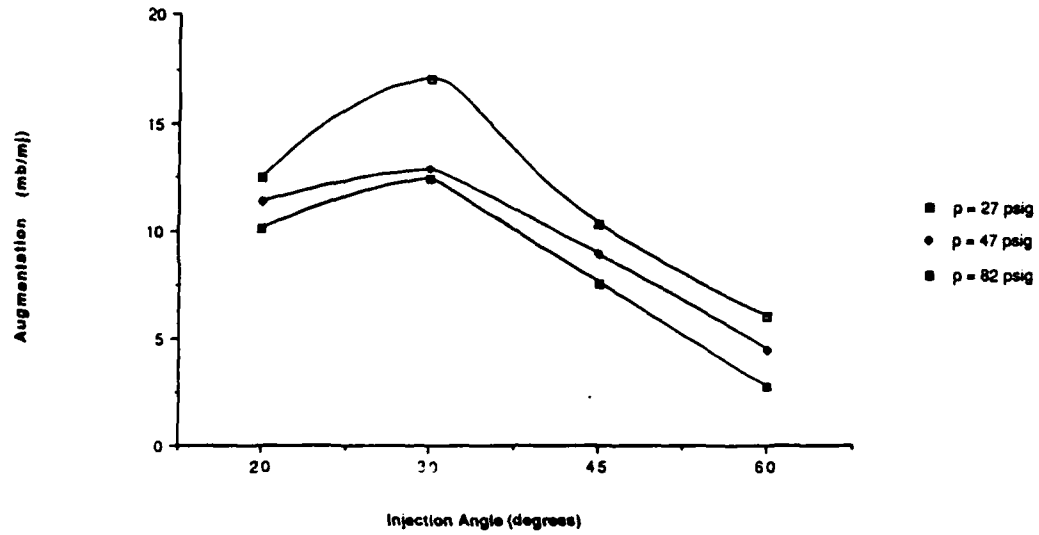

Figure 7 Augmentation as Functions of Injection Angle and Bore Evacuator Pressure for $(L/D)_b = (L/D)_m = 10$

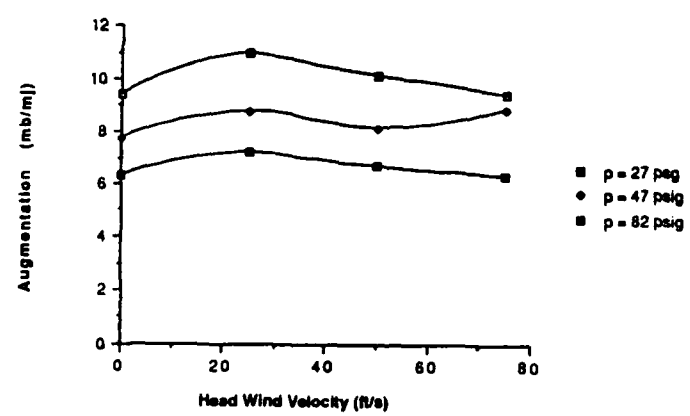

Figure 8 Augmentation as Functions of Head Wind Velocity and Bore Evacuator Pressure for $(L/D)_b = 5$, $(L/D)_m = 20$ and $\theta = 45°$

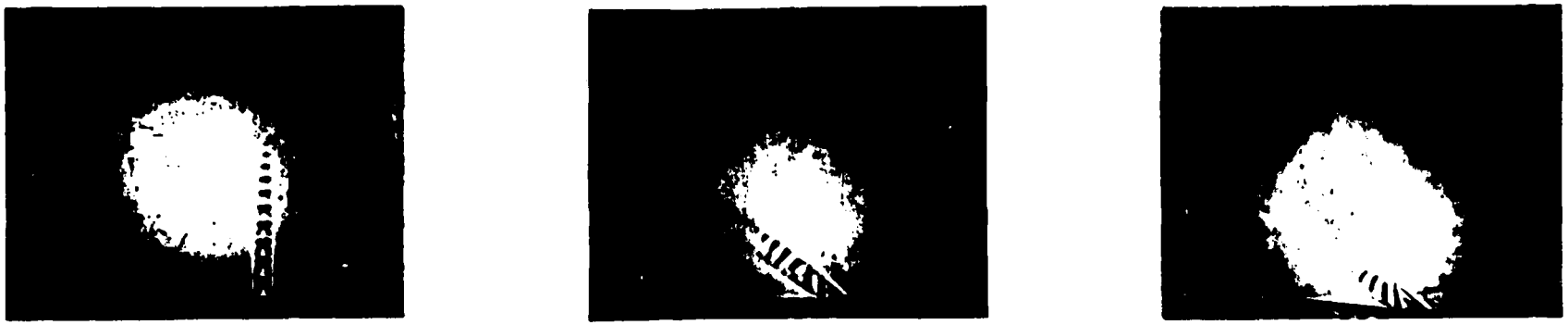

(a) 60 psig, p_o/p = 5.084, M = 1.71

(b) 16 psig, p_o/p = 2.089, M = 1.09

(c) 5 psig, p_o/p = 1.340, M = 0.66

FIGURE 9 NORMAL and INCLINED JETS with JET-SHEAR at BOUNDARY

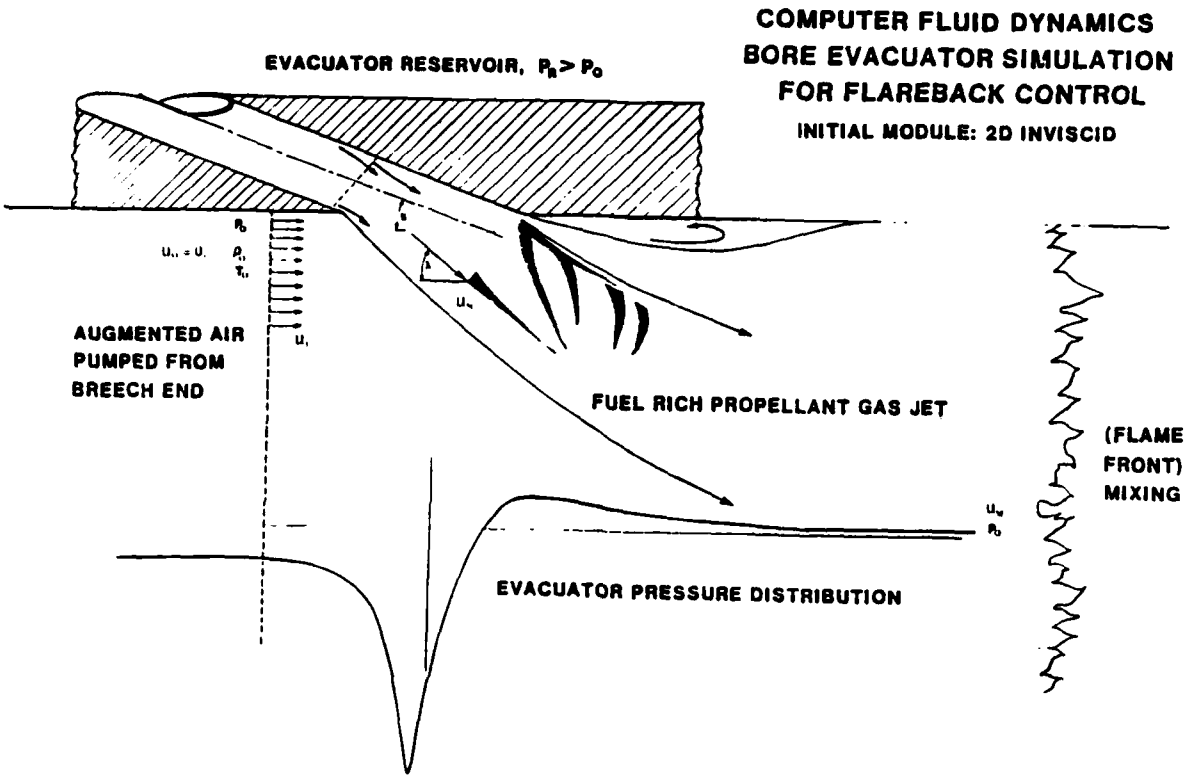

Figure 10 Theoretical Model of Flow Through Bore Evacuator

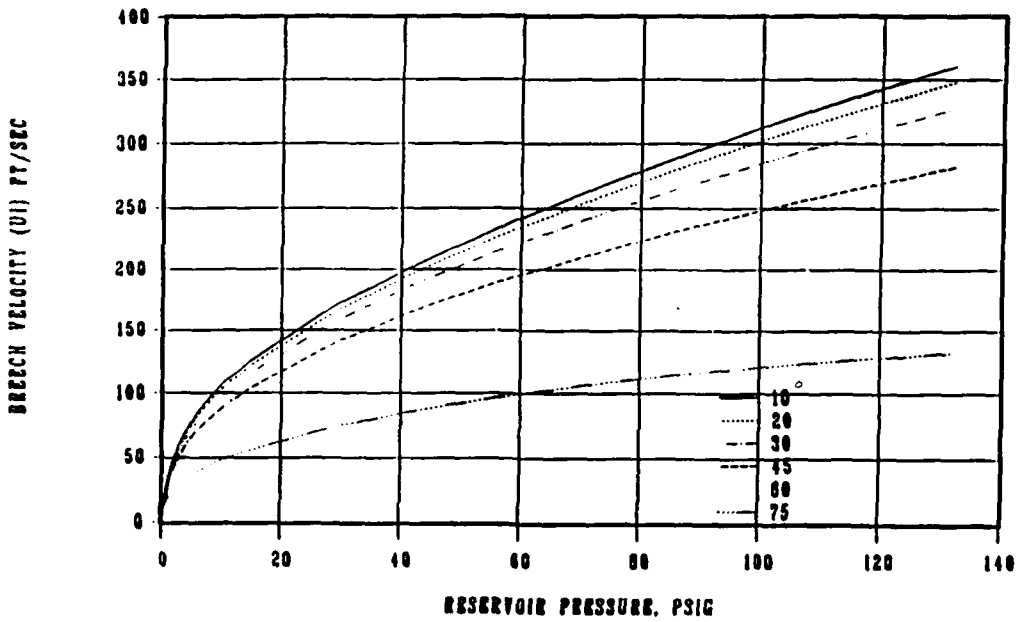

Figure 11 Theoretical Breech Velocity for Various Ejector Angles

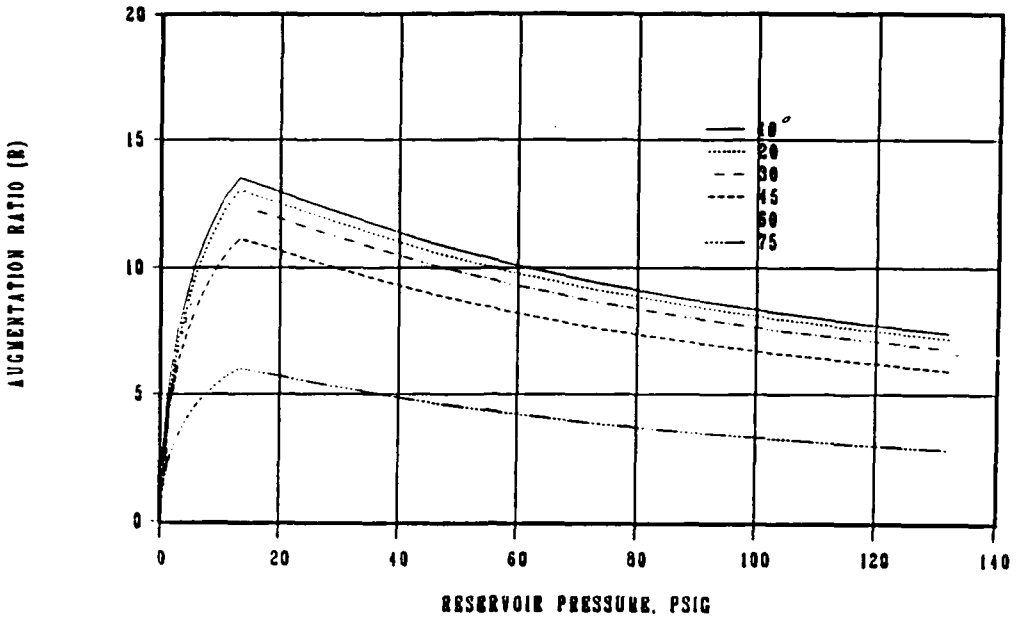

Figure 12 Theoretical Augmentation for Various Ejector Angles

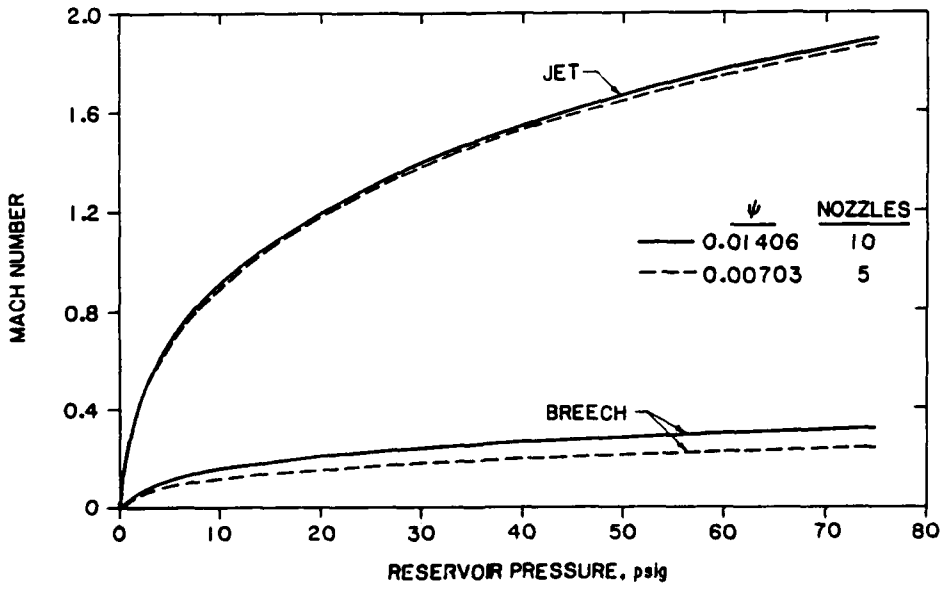

FIGURE 13 THEORETICAL JET & BREECH MACH NUMBERS. ϕ = 20°

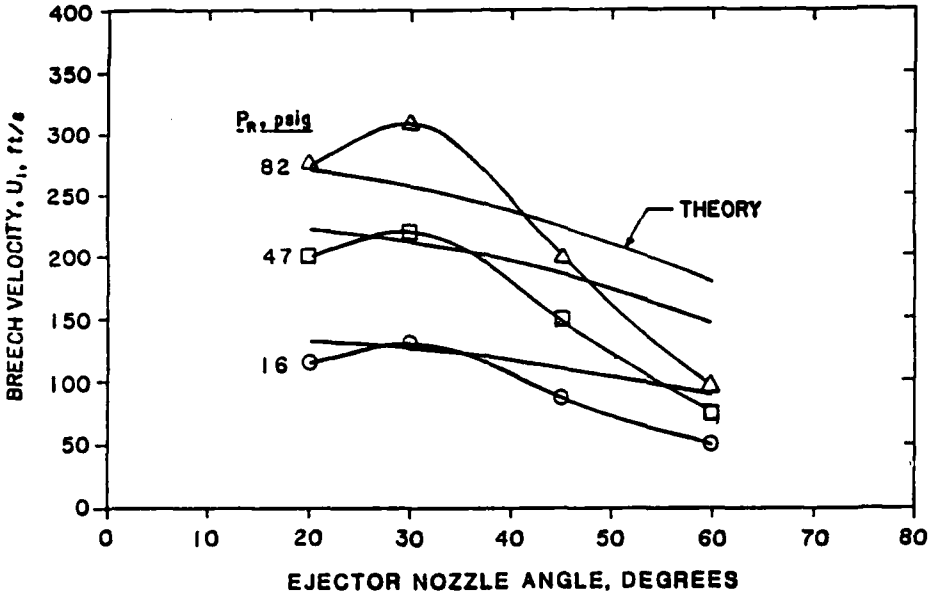

FIGURE 14 COMPARISON OF EXPERIMENTAL TO THEORETICAL BREECH VELOCITY. EXPERIMENTAL $(L/D)_{m,n} = 10$

ANDRADE, HAAS

TITLE: GENERIC GUN BORE EVACUATORS, II. IDEAL AND REAL PROPELLANT GAS TRANSIENTS

CHARLES A. ANDRADE AND JEFFREY W. HAAS
U.S. ARMY ARMAMENT RESEARCH, DEVELOPMENT, AND ENGINEERING CENTER
CLOSE COMBAT ARMAMENTS CENTER
BENET LABORATORIES
WATERVLIET, NY 12189-4050

ABSTRACT:

Propellant gas flow entering into, and discharging from, the bore evacuator reservoir has traditionally been treated as a one-dimensional, thermally and calorically perfect gas. However, increasing gun system performance prompts a new approach that, while incorporating a thermally perfect gas, for the first time attempts to account for the calorical imperfections of propellant gases by adopting thermochemical techniques. Two problems are defined and solved. First, the charge and discharge cycles for generic gun bore evacuators are calculated at quasi-steady operation. The calculation for a generic M256/M831 cannon configuration compared well with field test measurement when appropriate discharge coefficients were used. Second, the potential for shock ignition of fuel-rich propellant gas, entering the air-laden reservoir at first-round firing, is calculated for a generic M256/M829.

This work represents our collective progress reports on efforts to better understand the three-dimensional and calorically imperfect (real) gas dynamics of bore evacuators, with the purpose of improving pump characteristics by improved traditional approaches. Doing so lends insight to the eventual use of computational fluid dynamic methods, with which the non-adiabatic processes controlling flareback may be assessed.

BIOGRAPHY:

PRESENT ASSIGNMENT: Charles A. Andrade is a Mechanical Engineer in the Systems Engineering Branch at Benet Laboratories, assigned as Principal Investigator, "Gas Dynamics Of Bore Evacuators."

PAST EXPERIENCE: Blast overpressure reduction; emission spectroscopy of flames in a shock tube.

DEGREES HELD: Ph.D., Mechanical Engineering, Rensselaer Polytechnic Institute; M.S., Physics, Rollins College; B.S., Engineering Physics, University of California, Berkeley.

GENERIC GUN BORE EVACUATORS
II. IDEAL AND REAL PROPELLANT GAS TRANSIENTS

Charles A. Andrade and Jeffrey W. Haas
U.S. Army Armament Research, Development, and Engineering Center
Close Combat Armaments Center
Benet Laboratories
Watervliet, NY 12189-4050

INTRODUCTION

To solve the problem of toxic gases and to better understand how a flare-back event occurs, several aspects of the design of bore evacuators are being investigated. For tank systems and towed howitzers, the bore evacuator consists of a pressure reservoir located approximately at mid-length of the gun tube, Figure 1. The reservoir is tapped into the gun tube, by a circumferential array of ejector nozzles angled toward the muzzle, and thus is charged to peak pressure during gun blowdown. Since it is peak evacuator pressure that drives subsequent pressure history and evacuator performance, effective tailoring of the bore evacuator depends on proper modeling of the evacuator charge cycle.

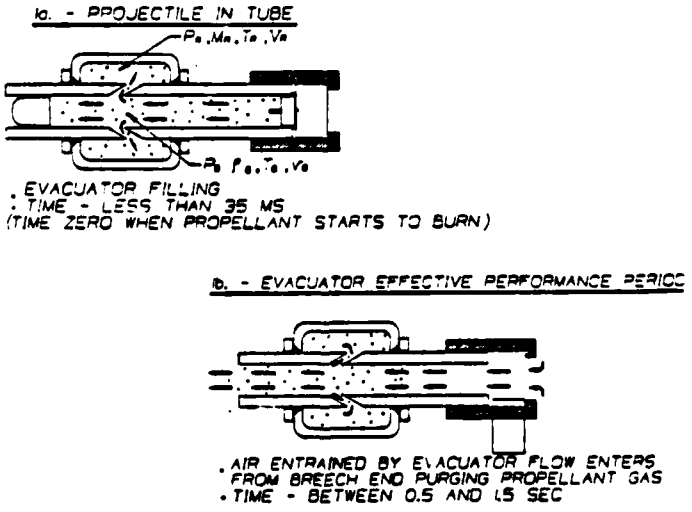

Figure 1. Bore evacuator operational sequencing.

Our approach is to model the charge and discharge cycles by one-dimensional methods, with initial values for the time-dependent charge algorithm, linked directly from an interior ballistics code. This approach yields peak pressures about the values measured during field tests, but it does not predict peak pressures for the "first" round, generally measured at about double that of the subsequent rounds. We define a first-round firing as one that occurs when the reservoir is filled with atmospheric air, either at normal temperature and pressure (NTP) or at elevated temperatures. Figure 2 compares reservoir pressure histories of first and subsequent round firings taken during a recent test of an M256/M831 system.

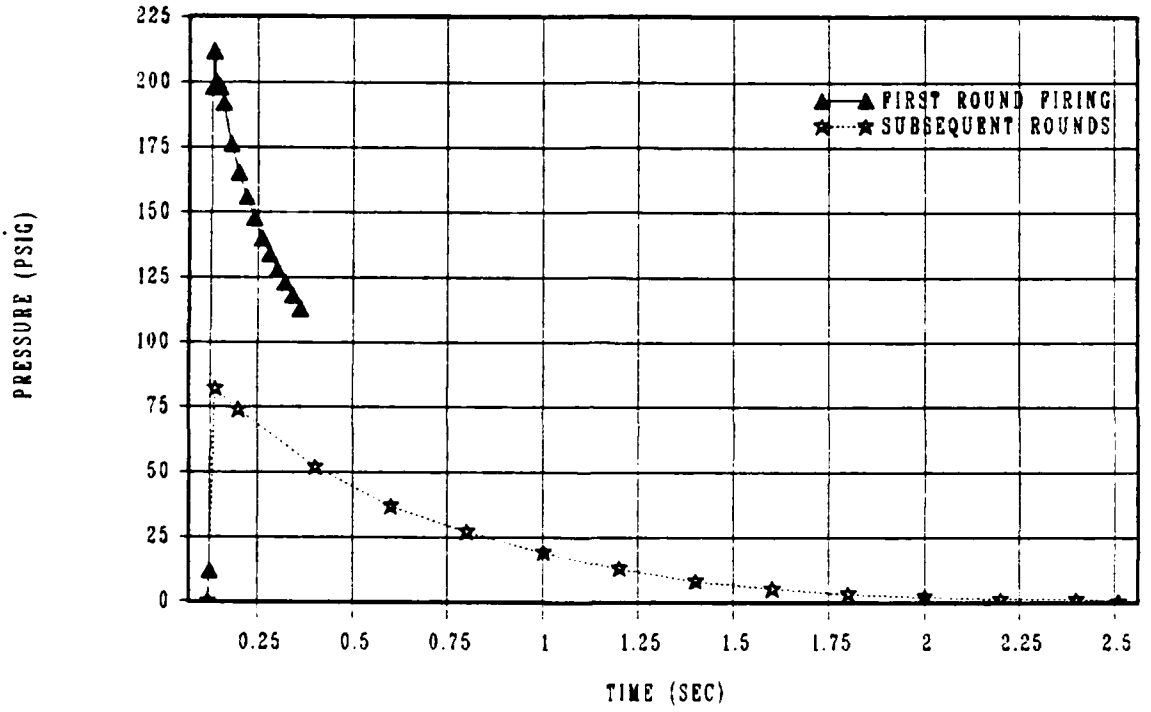

Figure 2. Evacuator pressures, measured M256/M831.

Our work is presented in two parts. In Part I, we describe our model charge/discharge method and, by applying the published [1,2] discharge coefficients, obtain good agreement with field test pressures for the M256/M831 system. For the rest of the paper, we focus attention on the M256/M829 system. To investigate relative effects of changing reservoir volume on bore evacuator performance, we use a discharge coefficient of unity for both charge and discharge, adapting the Reynolds control volume technique presented by Nagamatsu et al. [3] to calculate quasi-steady breech air entrainment characteristics for a generic M256/M829. The ballistic data bases for these calculations are shown in Table I.

In Part II, we apply the BRL/BLAKE and NASA/Lewis thermochemical codes [4,5] to investigate one possible source of ignition that may explain the observed high reservoir peak at first firing. We simulate ignition of JA2 propellant gas at the shocked air interface caused by propellant gas bursting through the ejector nozzles upon projectile arrival at the ports. Ignition by burning or thermally radiating particulates, which may be deflected 150 degrees from the mainstream as illustrated in Figure 1, is considered less likely to occur at the burst time.

TABLE I. GENERIC 120-MM CANNON BALLISTICS (IBHVG2.3)

PROJ	M831 (140)	M829 (145.4)	(F)
CHAM	533.95	595.0	cu.in.
PRWT	29.7	15.6	lbs.
PROP	Single Perf Stick	JA2 7 PERF	
CHWT	12.1	17.9	lbs.
RHO	0.05708	0.05780	lbs/cu.in.
GAMA	1.2335	1.2210	
COV	28.63	27.24	cu.in./lb.
TEMP	3141.0	3400.0	K
FORC	368300.0	376827.0	ft-lbf/lbm

	PMAX	MUZZ	PMAX	MUZZ	
t	4.623	8.750	3.140	5.810	ms
P	93686.0	9750.0	97022.0	10283.0	psi

Ejector Port, X. Parameters at projectile arrival:

t	6.9	4.9	ms
X	104.0	116.0	in.
P	16000.0	25400.0	psi
T	1655.0	2240.0	K

PART I

Background

After burst opening of the evacuator nozzles, an underexpanded quasi-steady jet is established which fills the reservoir to peak pressure. The approximate time to peak, following trigger, was 20 ms for the data shown in Figure 2. Reservoir peak must match the gun tube blowdown pressure, which rapidly drops below that of the reservoir pressure because of large impulse differences created by gun tube size, compared to that of total ejector nozzle size. The breech opens at $\leq$ 450 ms, after the gun tube pressure is at 1 atm; this, in principle, allows the reservoir gases to discharge back into the tube through the angled ports, such that air flow is entrained at the breech and the bore is purged of toxic gases.

Although bore evacuators have been studied for some time [1-3,6,7], this work attempts to improve on previous analyses and hopes to produce a more predictive model for use in design and development and to evaluate existing systems. In particular, we now examine the charge and discharge cycle of the reservoir.

Analysis

The model assumes that gas in the bore evacuator obeys the perfect gas law, i.e., the gas is thermally perfect. Moreover, processes are assumed to be quasi-steady and adiabatic. Gas flow through the ports was assumed to be choked throughout the cycle. That is, the mass flow through the ports is sonic, thus independent of downstream conditions. Finally, we seek thermodynamic improvements over traditional techniques while still considering a calorically perfect gas, i.e., gas properties such as the specific heats were assumed constant, independent of temperature.

1. The Charge Cycle. In the general case of the charge cycle it was assumed that gas initially in the reservoir (e.g., air) has different thermodynamic properties than the propellant gas. Using the law of partial pressures, the ideal gas law for the reservoir can be written

$$P_R = (m+\mu m_a)RT_R/V \tag{1}$$

where m, m_a, T_R, V, R and μ represent the gas mixture mass, the mass of air initially in the reservoir, gas temperature and volume, propellant ideal gas constant, and ratio of molecular weights of added gas to gas initially in the reservoir, respectively. Gun tube gas properties are those at the port location. Differentiating Eq. (1) with respect to time

$$dP_R/dt = R\{(dm/dt)_R T_R + (m+\mu m_a)(dT_R/dt)\}/V \tag{2}$$

where the reservoir mass balance is $dm_R/dt = dm/dt$, i.e., mass flow through the ports. Gas velocity at the evacuator ports is sonic when the ratio of gun tube pressure P_G to reservoir pressure P_R satisfies the condition

$$P_G/P_R \geq \{(\gamma+1)/2\}^{\gamma/(\gamma-1)} \tag{3}$$

where $\gamma = C_p/C_v$ is the ratio of specific heats. The energy equation for the reservoir can be written

$$C_p T_{GO} dm/dt = d\{(mC_v+m_a C_{va})T_R\}/dt \tag{4}$$

where T_{GO} is the in-bore stagnation temperature, obtained from interior ballistic data as a function of the local gas temperature T_G and flow Mach number M_G, viz., $T_{GO} = T_G\{1 + (\gamma-1)M_G^2/2\}$.

Equation (4) can be rewritten

$$\gamma T_{GO}(t)dm/dt = T_R dm/dt + (m+zm_a)dT_R/dt \tag{5}$$

where $z = C_{va}/C_v$. Combining Eqs. (1) and (5) into Eq. (2), the pressure equation can be written

$$dP_R/dt = \{[P_R/(m+\mu m_a)](1-y) + y\gamma RT_{GO}(t)/V\}dm/dt \quad (6)$$

where $y = (m+\mu m_a)/(m+zm_a)$.

Equation (6) represents the general rate of reservoir pressure increase for the case of a bore evacuator reservoir initially filled with air or with a mixture that differs appreciably from propellant gas entering the ports. A special case of Eq. (6) is obtained when residual propellant gas (with thermochemical properties nearly equal to that of the entering gas) accumulates in the reservoir from previous rounds, replacing air as the initial mass. Equation (6) then reduces to

$$VdP_R/dt = \gamma RT_{GO}(t)dm/dt \quad (6')$$

for propellant gas initially in the reservoir at frozen flow conditions, i.e., γ and molecular weights equal to the port values in-bore.

A general expression for mass flow rate into the reservoir, dm/dt, as a function of tube conditions, was obtained from Nagamatsu et al. [8] for the case of flow through ports at right angles to the gun bore, viz.,

$$dm/dt = K(M_G)A(P_G\rho_G)^{1/2} \quad (7)$$

where P_G and ρ_G are the tube pressure and density, respectively, obtained from the interior ballistic data, A is the total port cross section area, and $K(M_G)$ is a mass flow factor that depends on the tube Mach number, M_G. Sneck [9] has extended the use of Eq. (7) to two-dimensional (2-D) ports that intersect the gun tube at angles greater than 90 degrees with respect to the downstream flow. The 2-D analysis yields relatively constant values, $0.28 \leq K(M_G,\gamma) \leq 0.30$ over the expected range of Mach number and γ.

2. <u>The Discharge Cycle</u>. Maximum pressure in the reservoir occurs when tube and reservoir pressures equalize and the flow rate through the port drops to zero. As gun blowdown progresses, the tube pressure drops below the reservoir pressure, thus initiating discharge of the reservoir gases back through the ports into the gun bore. Sonic conditions at the ports are quickly established as the reservoir to bore pressure ratio becomes critical

$$P_R/P_G \geq \{(\gamma+1)/2\}^{\gamma/(\gamma-1)} \quad (8)$$

Gas in the reservoir is assumed to expand adiabatically, and isentropic relations for an ideal gas hold

$$P_R/P_{Ri} = (T_R/T_{Ri})^{\gamma/(\gamma-1)} \quad (9)$$

where the subscript i denotes initial (e.g., peak pressure) conditions and γ is the effective specific heat ratio of the gas in the reservoir. The problem of

the sonic discharge of a reservoir has been solved [1], and the solution is the Hugoniot equation

$$P_R/P_{Ri} = [1 + t/\phi]^{-2\gamma/(\gamma-1)} \qquad (10)$$

where

$$\phi = 2[\{(\gamma+1)/2\}^{(\gamma+1)/(\gamma-1)} m_{Ri} V/\gamma g_c P_{Ri}]^{1/2}/C_D A(\gamma-1)$$

Again, let the subscript i denote initial (maximum pressure) conditions in the reservoir and γ, the specific heat ratio of the gas. C_D is a discharge coefficient and A is the total cross-sectional port area.

3. Interior Ballistics Model. Equations (6) and (7) of the charge cycle are integrated numerically given tube conditions at the ports. IBHVG2.300, an interior ballistics code developed at the Ballistic Research Laboratory, is used to obtain tube properties at the port locations during the projectile in-bore time. After projectile exit, the analysis follows the treatment given by Corner [10]. In Corner's analysis, several simplifying assumptions are made to arrive at closed-form solutions. A primary assumption is that the square of the ratio C/W, charge weight to projectile weight, is much less than one. Since this is not generally the case, it remains to be determined experimentally how critical this assumption is to the analysis. Figure 3 gives the tube pressure at the port locations during the reservoir charge cycle. The round used in the analysis is an M831 training round with C/W of about 1/2. The discontinuity at the point of projectile exit is the expected result of using two separate treatments.

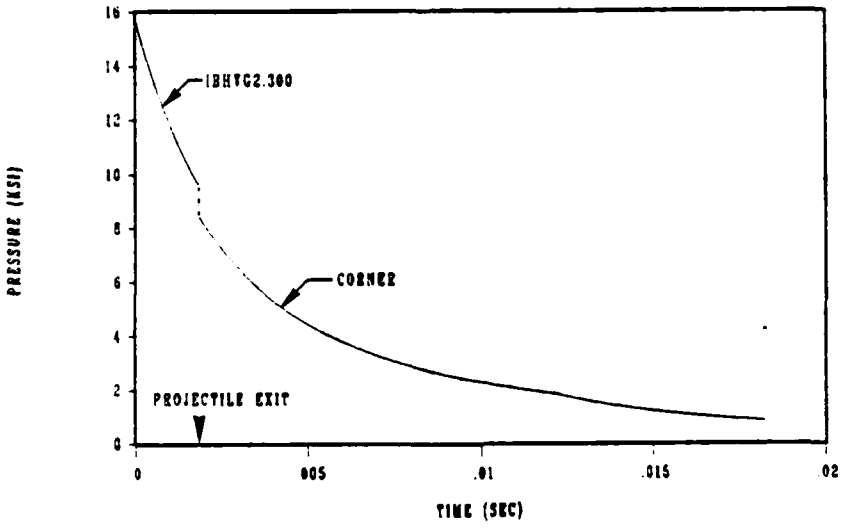

Figure 3. M256 tube pressures at nozzle location, M831 round.

4. Results. The model was compared with bore evacuator pressure data obtained from firing tests of the M256 cannon system. The initial case chosen was the particular case for an evacuator being initially filled with residual propellant gases from previous rounds. In assuming a value of $K(M_G) = 0.3$ for Eq. (7), it was found that the predicted values for the pressure gave about 60 percent of the actual measured value from the firing test. When $K(M_G)$ was assumed to be 0.48, very good agreement with the measured value was obtained, see Figure 4. For the discharge cycle, the discharge coefficient was assumed to be 0.85. The fact that a value of $K(M_G) = 0.48$ gave good agreement with experiment, compared to pressures calculated with $K(M_G) = 0.3$, may suggest differences in the 2-D analysis of nozzle flow and the actual three-dimensional (3-D) effects. However, the problem may lie in the assumptions made in the bore evacuator charge/discharge model itself; in particular, assumptions in the interior ballistic model mentioned above.

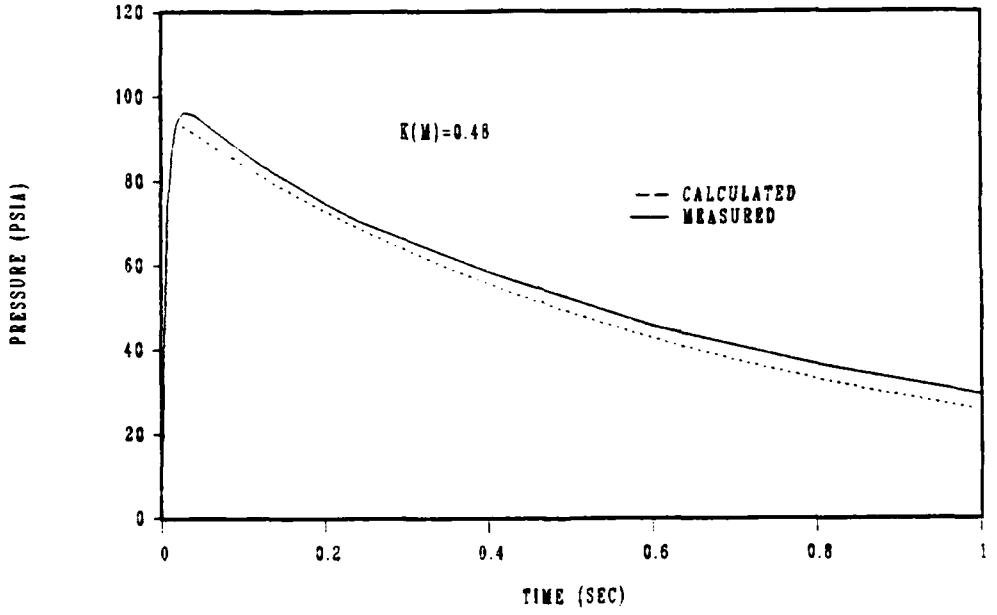

Figure 4. M256 reservoir pressure, M831 round.

Figure 5 represents the case for a bore evacuator initially filled with air (i.e., a first-round) rather than residual propellant gas. Here the agreement is less satisfactory. The model predicts a peak pressure of about 115 psia, while the pressure obtained from firing was over 210 psia. It should be noted that in subsequent rounds the peak pressures dropped to about 95 psia. This higher than normal first-round pressure peak (noted on other gun systems) strongly suggests secondary combustion of the propellant gas with air initially contained in the reservoir. In subsequent rounds, air in the reservoir has been depleted and replaced by burnt propellant gas. The initiation of first-round combustion is the subject of the second part of this paper.

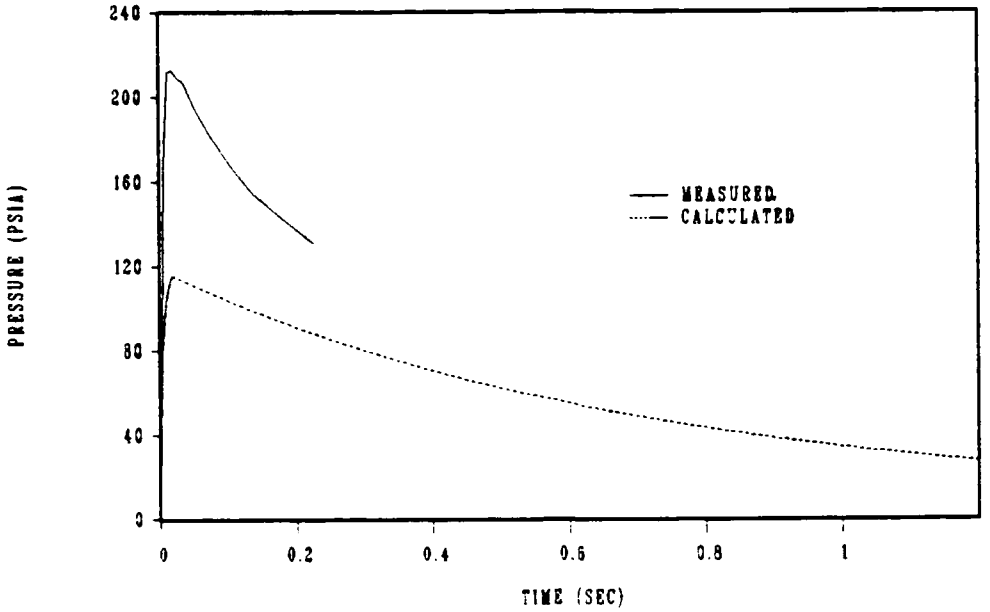

Figure 5. M256 reservoir pressure, M831 first-round.

We now turn attention to the M256/M829 cannon system, and compute the relative effects of changing reservoir volume on evacuator performance. In a departure from the model derived above, which incorporated Eq. (10) for the mass flow rate, another variant of Fliegner's formula [11] for propellant gases was used to derive a bore evacuator performance model. Here, the tube Mach number dependence is given by the total temperature, T_{GO}; but, instead of stagnation pressure, $P_{GO} = P_G(T_{GO}/T_G)^{\gamma/(\gamma-1)}$, the static pressure, P_G, is used. That is, the classically derived reference to stagnation conditions in a chamber, for the calculation of flow rates (dm/dt) through a sonic orifice, has been altered a priori to obtain the reservoir pressures shown in Figures 6 and 7. Since, in

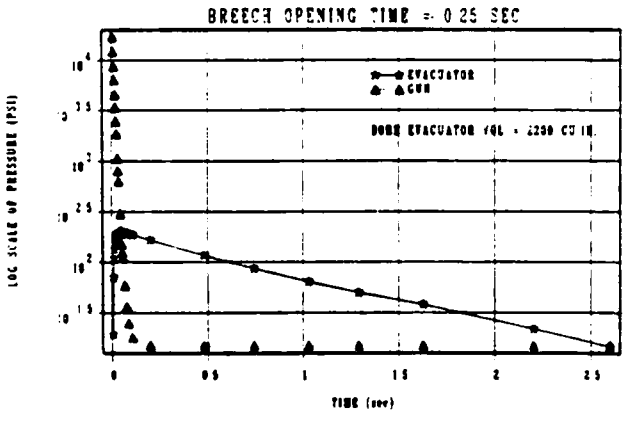

Figure 6. Gun and evacuator pressures.

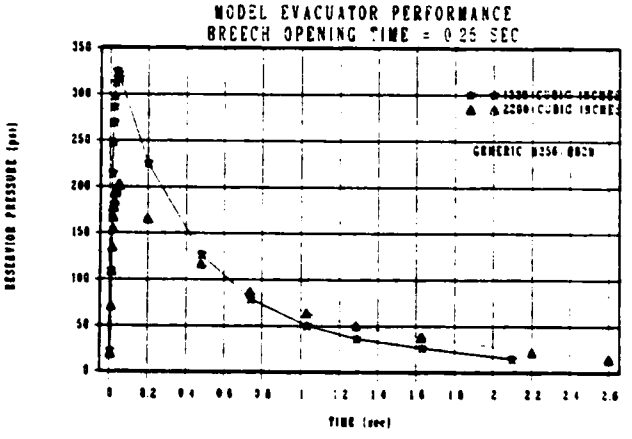

Figure 7. Effect of volume change.

further contrast to the above model a discharge coefficient of unity, $C_D = 1$, was used, these results show only the relative effect of reservoir size. To model the relative quasi-steady evacuator performance characteristics, shown in Figures 8 and 9, we adapt a Reynolds control volume method [3] for use with propellant gases. Note in Figure 9, the augmentation ratio is mass flow rate entrained at the breech to ejector nozzle flow rate. Vottis' interior ballistic model [12] was used with burn rate parameters altered to obtain results in close approximation to those presented in Table I. Corner's blowdown model yields the tube pressures, shown in Figure 6.

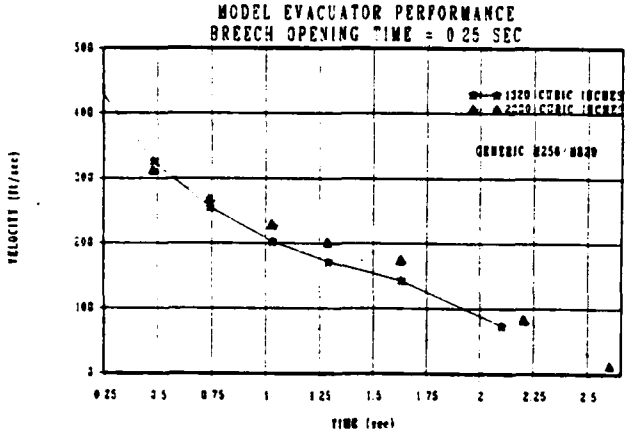

Figure 8. Entrained breech velocity.

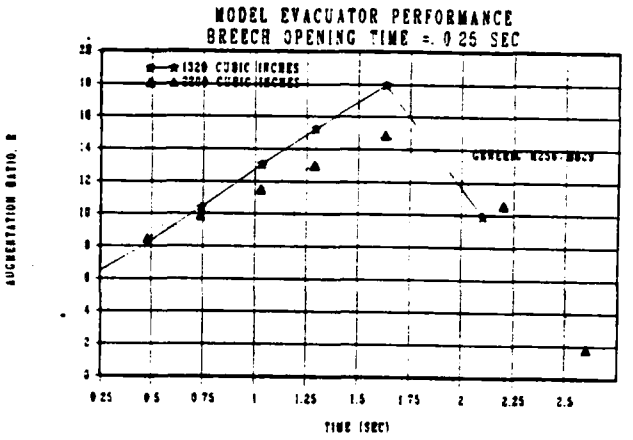

Figure 9. Augmentation ratio.

The calculations indicate that smaller reservoir capacity should give higher peak pressures, but that in this case, the pressures fall below that of the larger volume within 0.38 second after the breech is opened. The result is that air is entrained at the breech for a greater period of time due to the maintenance of a greater pump gradient with the larger reservoir capacity. Also note that the augmentation ratio is about the same as that for air [3].

PART II

Background

Examination of the first-round trace of Figure 2 at greater resolution shows oscillations superimposed on and about the peak, Figure 10. These oscillations and enhanced pressures have been observed with other system field tests and with shock-ignited flames [13], suggesting possible shock- or particle-ignited secondary combustion in the reservoir at first-round firing. Because the reservoir is air-laden, and since these peak levels and their superimposed oscillations exceed those of subsequent rounds, the evidence for enhanced combustion at first firing is compelling. Thus, a bulk energy balance, accounting for 59 kcal released per mole of H_2O formed by the stoichiometric reaction of H_2 with O_2 initially in a 30-ℓ air-laden reservoir, predicts the difference between pressure peaks shown in Figure 2, about 117 psia. This result was obtained with the JA2 gas compositions described below for the study of shock ignition when firing first-round M829 projectiles.

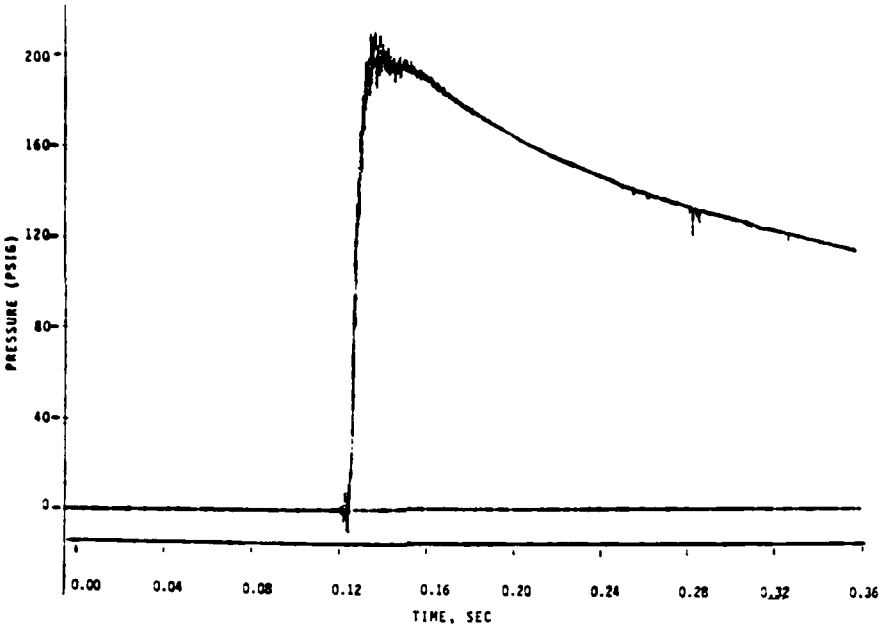

Figure 10. M256/M831 first-round.

Analysis

To investigate the feasibility of shock-ignited secondary combustion in the reservoir at first-round firings, we observe that the port opening time for an M829 projectile, about 5 μs, is the same order of diaphragm burst time that establishes a shock wave in a shock tube [14]. Figure 11 shows a sketch of projectile base at port opening, with a cross section sketch of the evacuator and reservoir [15]. By using the shock tube burst pressure equation linked to the NASA/Lewis Thermochemical Program [5], we compute the real gas temperature, pressure, and composition for shocked air, driven by JA2 propellant gas in the evacuator's jet nozzles. Diaphragm burst occurs when the projectile opens the jet nozzle ports at the pressure ratio $P_G/P_R = 1728$. The driver, JA2 propellant gas, is characterized by the tube temperature, pressure, specific heat ratio, and molecular weight obtained by using the isentropic expansion option of the BLAKE program, burning the solid propellant to match interior ballistic conditions at the port. The option used incorporates a Lennard-Jones potential model that accounts for intermolecular forces in the non-ideal propellant gas.

1. The Burst Pressure Equation. We assume that the Riemann invariant holds in an isentropic-centered-expansion-wave-region between driver gas at the opening (subscript G) and gas/air contact surface, (subscript 3)

$$v_3 + 2a_3/(\gamma_3-1) = v_G + 2a_G/(\gamma_G-1) \qquad (11)$$

where v is local gas velocity in the nozzle port and a is the local sound speed. We assume frozen flow in this process so that $\gamma_3 = \gamma_G = \gamma$. Since at port opening, the local flow velocity is instantaneously zero, $v_G = 0$, while at the contact boundary, $v_3 = v_2$, Eq. (11) becomes

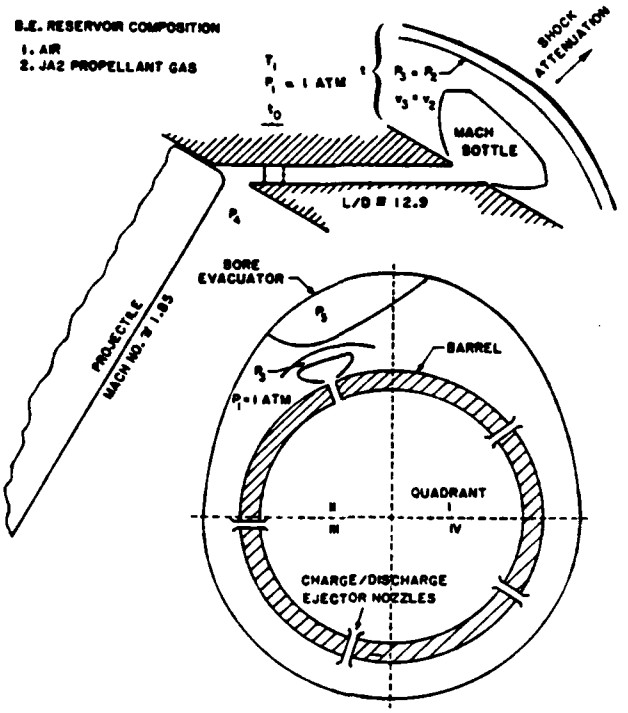

Figure 11. Evacuator cross section, $P_1 = P_R$ and $T_1 = T_R$.

$$a_{3G} = 1 - a_{1G}v_2(\gamma-1)/2a_1 \tag{12}$$

where $a_{3G} = a_3/a_G$ and $a_{1G} = a_1/a_G$, are local scnic speed ratios, and where conditions in the undisturbed stream ahead of the shock wave, i.e., in the reservoir (subscript R = 1), are given by

$$a_1 = (\gamma_1 R_U T_1/W_1)^{1/2}$$

i.e., the sonic speed, a function of γ_1, T_1, and W_1, the specific heat ratio, temperature, and molecular weight of the reservoir gas, respectively. Here, R_U is the universal gas constant. The velocity imparted to the thermally heated gas (e.g., air) by the shock wave is v_2, given by

$$v_2/a_1 = M_1(1-u_{21}) = K \tag{13}$$

where M_1 is the shock Mach number. By continuity, $u_{21} = u_2/u_1$ is the inverse density ratio across the shock wave, viz., $\rho_{21} = u_{21}^{-1}$, and is computed by subroutine SHOCK in the NASA code. We note that the shock density ratio for a calorically perfect gas is a function of shock Mach number, with an asymptotic limit equal to 6 for diatomic gases, while for the calorically imperfect gas it is much greater at the same shock Mach number, i.e., a greater compression of the reservoir gas results, albeit, locally and temporally. The expansion pressure ratio is

$$P_{3G} = T_{3G}^{\gamma/(\gamma-1)} = a_{3G}^{2\gamma/(\gamma-1)} \tag{14}$$

where $T_{3G} = T_3/T_G$ is the expansion temperature ratio.

Tautologically, the burst pressure ratio is $P_{G1} = P_{31}/P_{3G}$, so that combination of Eqs. (12) to (14) and the contact boundary condition, $P_3 = P_2$, gives

$$P_{G1} = P_{21}/[1-(\gamma-1)Ka_{1G}/2]^{2\gamma/(\gamma-1)} \qquad (15)$$

where $P_{21} = 1 + \gamma_1 M_1 K$ is the shock wave pressure rise. A subroutine was linked to the NASA program so that Eq. (15) is satisfied iteratively by the shock jump conditions for mole fractional compositions, up to 15 gaseous species, given at the equilibrium temperature and pressure ahead of the shock wave, i.e., in the bore evacuator reservoir.

2. Results Computed for Shocked Air in the Evacuator Nozzle Ports. The ports at projectile opening illustrated in Figure 11 have an L/D = 12.9, which is comparable to many shock tubes. Thus, a shock wave created at the burst pressure ratio of 1728 (and at the tube temperature of 2240 K) would not be expected to attenuate appreciably before it reaches the bore evacuator reservoir. Figure 12 gives the postshock elevated pressure P_3 and temperature T_3 downstream of the incident shock wave, assuming air in the reservoir is at 1 atm, and further assuming various selected temperatures T_1, indicated on the abscissa. The corresponding shock Mach number variation ranged from 7.79 at T_1 = 300 K to 4.03 at T_1 = 2000 K.

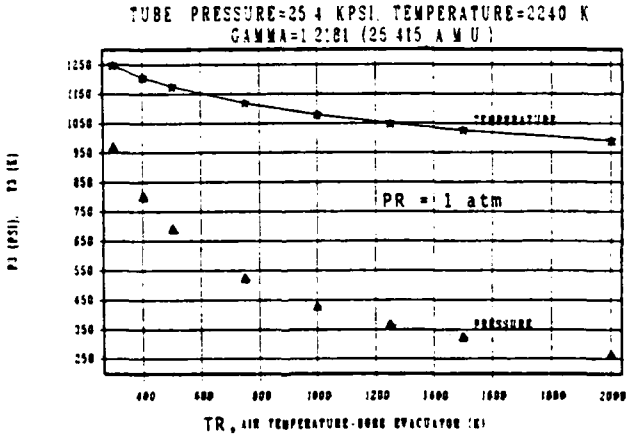

Figure 12. Bore evacuator initial transient postshock states.

3. Ignition. An examination of postshock ignition delay measurements for stoichiometric hydrogen-air mixtures, published in the review by Schott and Getzinger [16], shows that ignition initiates in less than 1 μs as temperatures exceed 1429 K and pressures exceed 35 psi in the postshock region. Consider a first-round burst opening of the ports, with air in the reservoir at NTP (1 atm and 300 K). The shock wave produced at M_1 = 7.79, corresponding to a shock velocity u_1 = 2.719 km/s, creates a postshock environment in which ignition could initiate in about 0.1 of the time that it takes the shock wave to traverse the port. These postshock conditions are well within the third explosion limit for stoichiometric H_2/O_2 mixtures [16,17], where branching chain kinetics mechanisms are known to support shock-ignited detonation waves in a Chapman-Jouguet

mode [17]. It is convenient to use the detonation option available in the NASA/Lewis thermochemical code. This requires the equilibrium propellant gas composition at the postshock state, P_3 and T_3, and at an appropriate mix ratio with the equilibrium air composition for each calculated state. Results of the BLAKE code computations discussed above are shown as isentropes in Figure 13 and as crossplot isochoric curves in Figure 14.

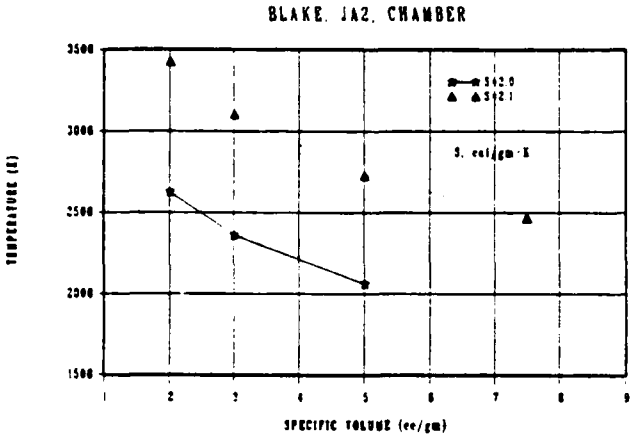

Figure 13. Isentropes, JA2 gas.

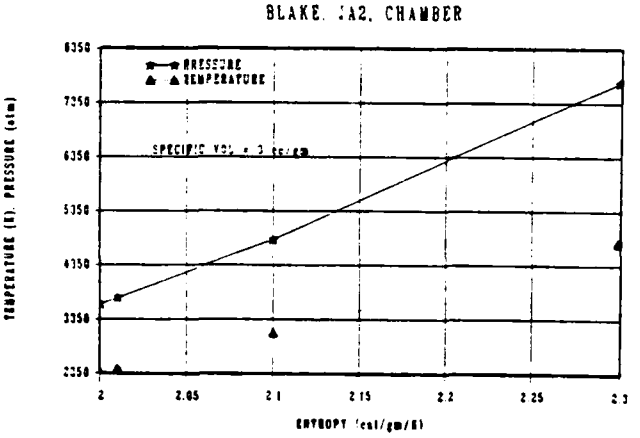

Figure 14. Isochores, JA2 gas.

Data shown apply at the chamber; furthermore, the option used also performed isentropic expansion calculations for each trial chamber point shown. The purpose of these thermodynamic crossplots is to select the entropy level that most closely matches interior ballistic conditions for the M256/M829 system in Table I. It was decided that the appropriate level is about 2.1 cal/gm/K for a specific volume between 2 and 3 cc/g. The expanded gas composition was selected that most closely matched the port conditions. Figure 15 shows postshock end-point equilibrium state compositions derived from the port state; but the maximum entropy level obtained, 2.035 cal/g/K, was too low for the process.

Instead of end-point composition mixing, the unmixed postshock state was composed of the port state composition at contact interface pressure, P_3. Since shocked air computations resulted in different compositions as T_1 was varied, the mole fraction composition of heated air added to fixed mole fraction composition of heated gas at one mole each, resulted in a different file for each detonation initiated at the postshock state (P_3, T_3). A summary of these computations is given in Table II for a fuel to oxygen mix ratio of unity, E = 1, and for the case of a reservoir initially filled with air at 1 atm and 750 K. The process entropy level is acceptable.

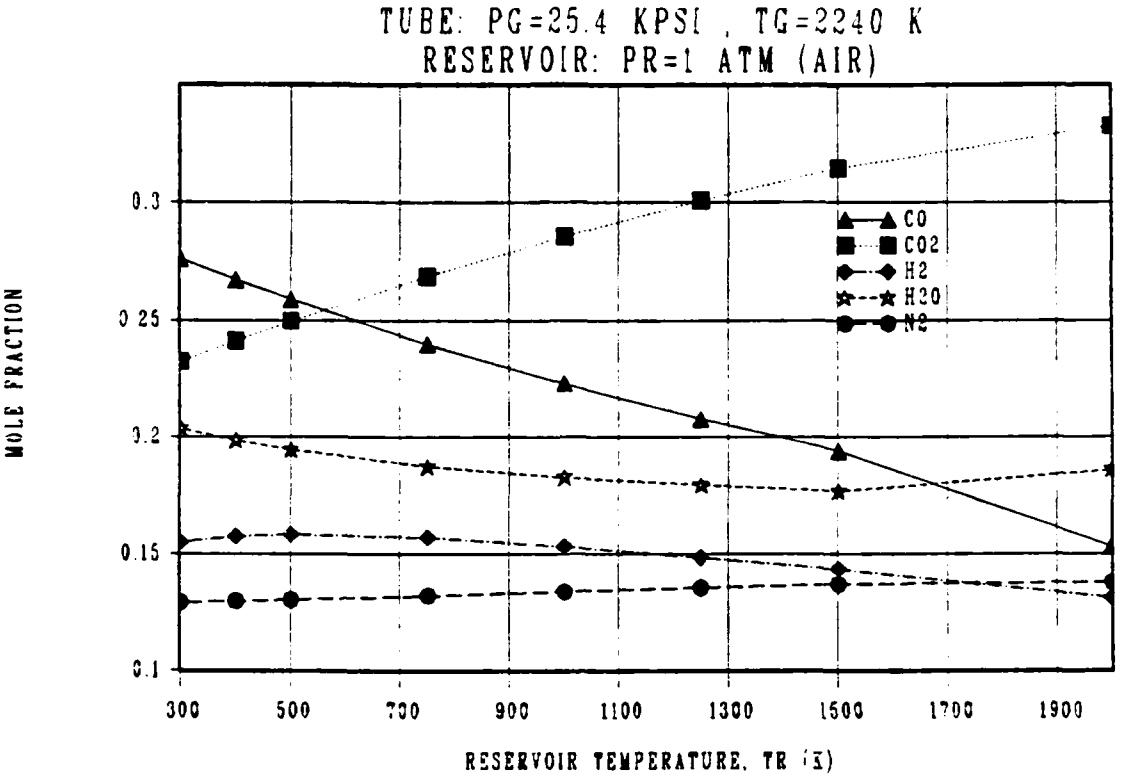

Figure 15. Postshock equilibrium composition of JA2 gas before mixing.

Figure 16 presents a summary of detonation wave properties and burned gas composition as a function of E, the unburned fuel/oxygen mix ratio. As E was varied from 0.4 to 1.2, corresponding to increasing fuel from about 5 to 95 percent, the entropy level for the process increases to about 2.1 cal/gm/K as the mix ratio approaches unity. At that point, the amount of oxygen initially available has diminished to a small fraction of a mole, see also Table II. Figure 17 presents the detonation wave properties at a mix value of E = 1 for all the postshock points of Figure 12. Reading off these charts, for a reservoir at NTP, the combined transient pressure rise due to shock followed by the detonation is 950 times 3.7 or 3515 psi; the corresponding temperature rise is 3125 K. It is interesting to note that the calculated Chapman-Jouguet wave speed of about 1.7 km/s, for the case of the first-round with reservoir air at NTP, would accelerate a shock wave moving initially at 2.719 km/s. As the shock wave emerges into the reservoir, the detonative impulse may tend to compensate for shock dissipation sufficient to cause further heating of the gas by strong reflection at the wall. The possibility of asymmetric heating by reflections has been suggested as a contributing factor in muzzle droop [15].

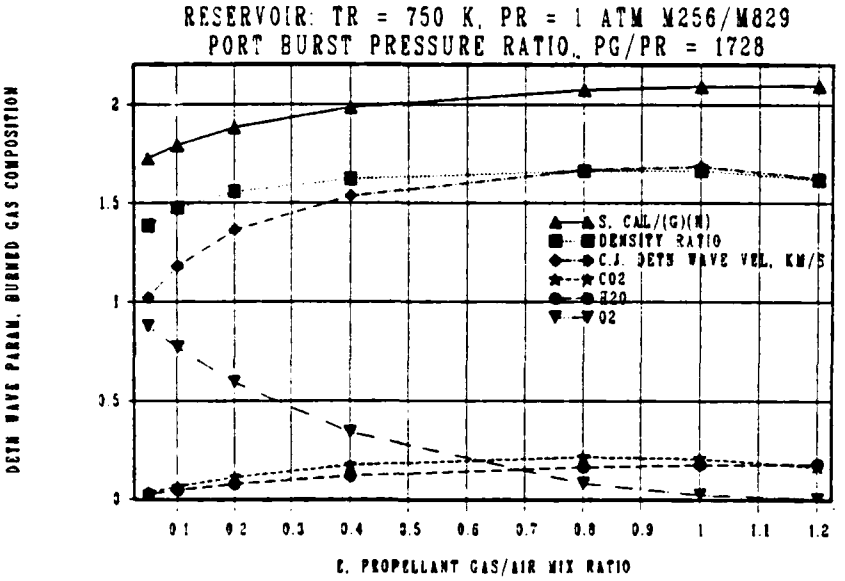

Figure 16. Ignition potential at evacuator opening, M256/M829 first-round.

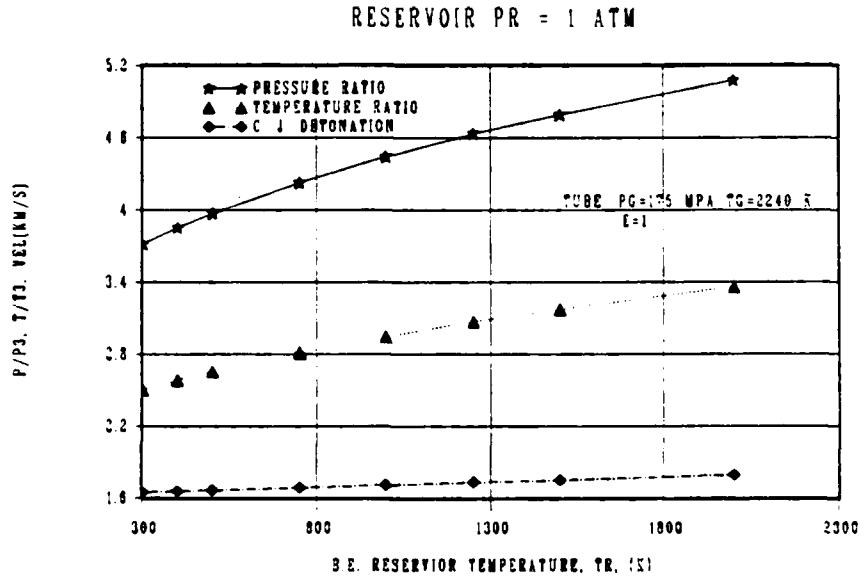

Figure 17. JA2 gas/air detonation properties at reservoir postshock state.

TABLE II. NASA I/O FOR DETONATION PROPERTIES OF AN IDEAL REACTING GAS (Port Burst Pressure Ratio, PGR = 1728, TGR = 2.987, E = 1)

Mole Fraction Compositions

Species	Unburned 2 moles	Burned 1 mole
CO	0.37113	0.06134
CO2	0.11761	0.20623
H	0.01557	0.00163
HCN	0.00017	
HCO	0.00100	
HO2	0.00029	0.00007
H2	0.08415	0.00694
H2O	0.24022	0.17574
H2O2		0.00001
HNO		0.00001
NH3	0.24022	
NO	0.08183	0.01451
NO2		0.00003
N2	0.86895	0.48975
N2O		0.00001
O	0.04750	0.00220
OH	0.03449	0.01571
O2	0.13020	0.02217
AR	0.00668	0.00365

Gas Dynamics

Unburned (at postshock interface)		
P3	35.7301	atm
T3	1118.50	K
W3	26.435	mol wt
GA3	1.3064	
Burned (Chapman-Jouguet)		
P	151.03	atm
T	3146.4	K
W	29.293	mol wt
RHO	0.0171	g/cc
S	2.0932	cal/g/K
CP	0.7670	cal/g/K
GA	1.1479	
Sonic Velocity	1012.5	m/sec
Detonation Parameters		
P/P3	227	
T/T3	2.813	
W/W3	1.1081	
RHO/RHO3	1.6651	
Detonation Vel.	1685.8	m/sec

CONCLUSIONS

Considerable experimental and analytical work remains to be done. In summary, results of the present work suggest that the use of calorically perfect gas methods and other simplifications, such as neglect of terms of order $(C/W)^2$ used in the interior ballistics of gun "blowdown," and neglect of multiple reflections of the rarefaction wave in traditional bore evacuator design, do not properly account for the observed pressure peaks during the critical charge cycle.

In Part I we presented computed results of a quasi-steady, thermally perfect flow model used to predict the charge and discharge pressures in the reservoir of a gun bore evacuator. Comparison of these results to measurement showed good prediction for the firing of a generic M256/M831 cannon system, provided it was not a "first"-round firing. That is, by using results from the NASA thermochemical code, we show that charge pressure does tend to increase when the molecular energy of formation in reaching end-point compositions is accounted for, but the prediction fell short of the mark (Figure 5). Although ideal (thermally perfect gas flow) performance of bore evacuator pumps has been verified with steady-state laboratory experiments using room temperature air [3,7], the use of ideal propellant gas methods in the reciprocal, charge-up,

process shows such methods fail to predict peak evacuator pressure in a consistent way from one gun system to another. Our calculations also show that discharge coefficients, extrapolated from experimental data by ideal gas methods, claim excessive penalties on the charge pressure. Ideal or real, i.e., calorically imperfect, in either case there will be entropic losses during the charge cycle, resulting in charge, K(MG), and discharge, CD, coefficients that should be verified experimentally.

In Part II we presented a first-round study of the transient expansion shock processes that can occur in the initial stages of evacuator charge at port opening. The initial shock transient represents a region of increased gas density where molecular collision energies are transformed into elevated internal energy states of the molecules at the equilibrium temperature. We assume that fuel-rich propellant combustibles mix with air in the propellant gas/air postshock interface, with sufficient ignition delay to promote a detonative acceleration of the shock wave. If so, then secondary combustion of propellant gases in the air-laden reservoir at the first-round may explain the high pressures measured compared to the subsequent firings. Likewise, anomalous high reservoir pressures may be observed at subsequent firings if sufficient time elapses between firings for the equilibrium mixing of residual propellant gases in the reservoir with air diffusing in through the ports. Since the mutual H_2/O_2 diffusion at NTP for a distance equal to the port length is the order of one minute, calculations pertinent to this argument were carried out by shocking premixed compositions in the reservoir, rather than air, obtaining similar results.

These combined studies suggest that our modeling techniques could be improved by considering the real gas properties associated with changes of thermochemical state of the propellant gas through the nozzles and in the evacuator's reservoir, i.e., accounting for calorical imperfections due to the processes. Such changes may be due to shock and/or particle-induced combustion in the reservoir at first firing, and possibly due to combustion and/or thermochemical elevation of the gas state due to expansion and mixing processes (turbulence) in the reservoir during subsequent firings. Thus, field tests to assess combustion are planned.

Finally, much incentive for this work is generated by difficulties in the interpretation of field data, or the lack of it. The need for more and reliable data to guide our modeling efforts is paramount.

REFERENCES

1. Fagen, W. and Henry, L.R., "Bore Scavenging Study for Case-Loaded Cannon Mounted in Closed Cab Vehicles," Am. Machine & Foundry Co., Chicago, IL, 1954.

2. Sneck, H.J., "Gas Flows Through Small Holes In Gun Tube Walls," in: Proceedings of the Fifth U.S. Army Symposium on Gun Dynamics, ARCCB-SP-87023, Benet Laboratories, Watervliet, NY, 23-25 September 1987, pp. 30-43.

3. Nagamatsu, H.T., Duffy, R.E., and Andrade, C., "Generic Bore Evacuators, I. Experimental and Aerodynamic Investigations," in: Proceedings of the Sixth U.S. Army Symposium on Gun Dynamics, ARCCB-SP-90015, Benet Laboratories, Watervliet, NY, 15-17 May 1990, pp. 18-40.

4. Freedman, E., "BLAKE - A Thermodynamic Code Based on TIGER: Users' Guide and Manual," ARBRL-TR-02411, Ballistic Research Laboratory, Aberdeen Proving Ground, MD, July 1982.

5. Gordon, S. and McBride, B.J., NASA SP-273, 1971.

6. Smith, F., "Investigation of Fume Extractor Design by Model Techniques," RARDE Memo. 13/67, Fort Halstead, U.K., 1967.

7. Andrade, C.A., Nagamatsu, H.T., and Duffy, R.E., "Theoretical Compressible Flow in Generic Bore Evacuators and Experimental Verification," AIAA 89-0652, January 1989.

8. Nagamatsu, H.T., Choi, K.Y., Duffy, R.E., Carofano, G.C., "An Experimental and Numerical Study of the Flow Through a Vent Hole in a Perforated Muzzle Brake," ARCCB-TR-87016, Benet Laboratories, Watervliet, NY, June 1987.

9. Sneck, H.J. and Witting, P., "Bore Evacuator Hole Flows," in: Proceedings of the Sixth U.S. Army Symposium on Gun Dynamics, ARCCB-SP-90015, Benet Laboratories, Watervliet, NY, 15-17 May 1990, pp. 61-75.

10. Corner, J., Theory of Internal Ballistics of Guns, Wiley, New York, 1950.

11. Shapiro, A.H., The Dynamics and Thermodynamics of Compressible Fluid Flow, Vol. I, Ronald Press, New York, 1953, p. 85.

12. Vottis, P.M., "Digital Computer Simulation of the Interior Ballistic Process in Guns," WVT-6615, Benet Weapons Laboratory, Watervliet Arsenal, Watervliet, NY, October 1966.

13. Andrade, C.A., "Final Scientific Report on Combustion Chemistry of High Energy Pyrophoric Fuels," Martin Marietta Report OR 10119, Orlando Division, Orlando, FL, 26 May 1969; also "Emission Spectroscopy of Shock Ignited Diborane Flames," M.S. Thesis, Rollins College, Winter Park, FL, September 22, 1969.

14. White, D.R., "Influence of Diaphragm Opening Time on Shock Tube Flows," J. Fluid Mech., Vol. 4, 1958, p. 585.

15. Bundy, M.L., "Analysis of Thermally Induced Barrel Distortion From Firing," in: Proceedings of the Fifth U. S. Army Symposium on Gun Dynamics, ARCCB-SP-87023, Benet Laboratories, Watervliet, NY, 23-25 September 1987, pp. 80-94.

16. Schott, G.L. and Getzinger, R.W., "Shock Tube Studies of the Hydrogen-Oxygen Reaction System," in: Physical Chemistry of Fast Reactions, Volume I: Gas Phase Reactions of Small Molecules (B.P. Levitt, ed.), Plenum Press, New York, 1973, Chapter 2.

17. Lewis, B. and von Elbe, G., Combustion, Flames and Explosions of Gases, 2nd Edition, Academic Press, New York, 1961, Chapters II and VIII.

TITLE: Bore Evacuator Hole Flows

H.J. Sneck
U.S. Army Armament Research, Development, and Engineering Center
Close Combat Armaments Center, Benet Laboratories
Watervliet, NY 12189-4050
also
Professor of Mechanical Engineering
Rensselaer Polytechnic Institute
Troy, New York
and
Peter Witting
SUNY, Buffalo

ABSTRACT:

The flows from the bore of a gun tube through its bore evacuator holes are re-examined for subsonic and supersonic tube flows. The two-dimensional analytic/graphical methods presented at a previous conference are refined and the computations computerized. Empirical incompressible correlations are extended to low subsonic Mach number tube and hole flows. The state-of-the-art of hole-flow correlations based on these results and the work of others are assessed, and design methods recommended.

BIOGRAPHY:

PRESENT ASSIGNMENT: Mechanical Engineer - Benet Laboratories (WAE), Watervliet, NY.

PAST EXPERIENCE: Professor of Mechanical Engineering - 1953 to present, consultant.

DEGREES HELD: B.M.E., Rensselaer Polytechnic Institute, Troy, NY, 1951; M. Eng., Yale University, New Haven, CT, 1952; Ph.D., Rensselaer Polytechnic Institute, Troy, NY, 1961.

BORE EVACUATOR HOLE FLOWS

H.J. Sneck
U.S. Army Armament Research, Development, and Engineering Center
Watervliet, NY 12189-4050
and
Peter Witting
SUNY, Buffalo
Buffalo, NY

INTRODUCTION

The work presented here is a refinement of the results presented in an earlier work [1]. A method for extending incompressible hole flow correlations to compressible fluids has been developed for subsonic tube flows. Computational methods for two-dimensional hole flows have also been developed for supersonic tube flows. The predicted hole flows are compared with prior experimental and theoretical results.

SUBSONIC TUBE FLOW

In the previous work on this subject the empirical correlation [2] shown in Table 1 was used in conjunction with a momentum balance to estimate the hole flow coefficient, K, for subsonic flow in holes normal to the tube centerline. Down-hole velocities were obtained from a formula which accompanied Table 1 in [2].

TABLE 1 DISCHARGE COEFFICIENTS, C_D

$R^2 = \frac{\rho U_t^2/2}{P - P_e + \rho U_t^2/2}$	0.0	0.1	0.2	0.3	0.4	0.5	0.6	0.7	0.8	0.9	1.0
C_D	0.68	0.64	0.61	0.58	0.55	0.51	0.46	0.39	0.29	0.16	0.0

In this paper a logical extension of the incompressible formulations to compressible flows is proposed, and the predictions of the resulting correlation reexamined.

The flow equation of [2] can be written in the form

$$\left(P_t + \frac{\rho U_t^2}{2}\right) - \left(P_e + \frac{\rho U_e^2}{2}\right) = \left(\frac{1}{C_D^2} - 1\right)\frac{\rho U_e^2}{2} \tag{1}$$

This equation equates the difference in the tube and hole stagnation pressures on the left side to a hole dissipation on the right. In terms of the stagnation pressures Eq.(1) becomes

$$C_D^2 = \frac{P_e^o - P_e}{P_t^o - P_e} \tag{2}$$

A logical extension of this equation to compressible flow is

$$C_D^2 = \frac{\left[1 + \left(\frac{\gamma - 1}{2}\right) M_e^2\right]^{\gamma/\gamma-1} - 1}{\frac{P_t}{P_e}\left[1 + \left(\frac{\gamma - 1}{2}\right) M_t^2\right]^{\gamma/\gamma-1} - 1} \tag{3}$$

which is obtained from Eq.(2) using $P^o = P\left[1 + \left(\frac{\gamma - 1}{2}\right) M^2\right]^{\gamma/\gamma-1}$. For isentropic flows $C_D = 1.0$. The loss of stagnation pressure due to the nonisentropic flow from the tube through the hole is reflected in the C_D values of Table 1, all of which are less than unity.

The coefficients C_D are correlated with a dimensionless parameter, R^2. The compressible flow version of this parameter is

$$\frac{1}{R^2} = \frac{P_t^o - P_e}{P_t^o - P_t} \tag{4}$$

Compressible flow through radial holes has been correlated by Carofano [3] using a flow coefficient K defined by

$$K = \frac{\dot{m}}{a\sqrt{gP_tP_t}} = \sqrt{\gamma}\left(\frac{P_e}{P_t}\right) M_e \sqrt{\frac{1 + \left(\frac{\gamma - 1}{2}\right) M_e^2}{1 + \left(\frac{\gamma - 1}{2}\right) M_t^2}} \tag{5}$$

The pressure ratio required in Eq.(5) can be obtained from Eq.(4) and takes the form

$$\frac{P_e}{P_t} = \left[1 + \left(\frac{\gamma - 1}{2}\right) M_t^2\right]^{\frac{\gamma-1}{\gamma}} \left(1 - \frac{1}{R^2}\right) + \frac{1}{R^2} \qquad (6)$$

The computation of K for 90° holes is now a straightforward procedure. For a constant γ it begins by selecting C_D and R^2 combinations from Table 1. Then $\frac{P_e}{P_t}$ is found from Eq.(6) for selected values of $0 < M_t < 1.0$, and the corresponding M_e found from Eq.(3). Inserting the results into Eq.(5) yields K.

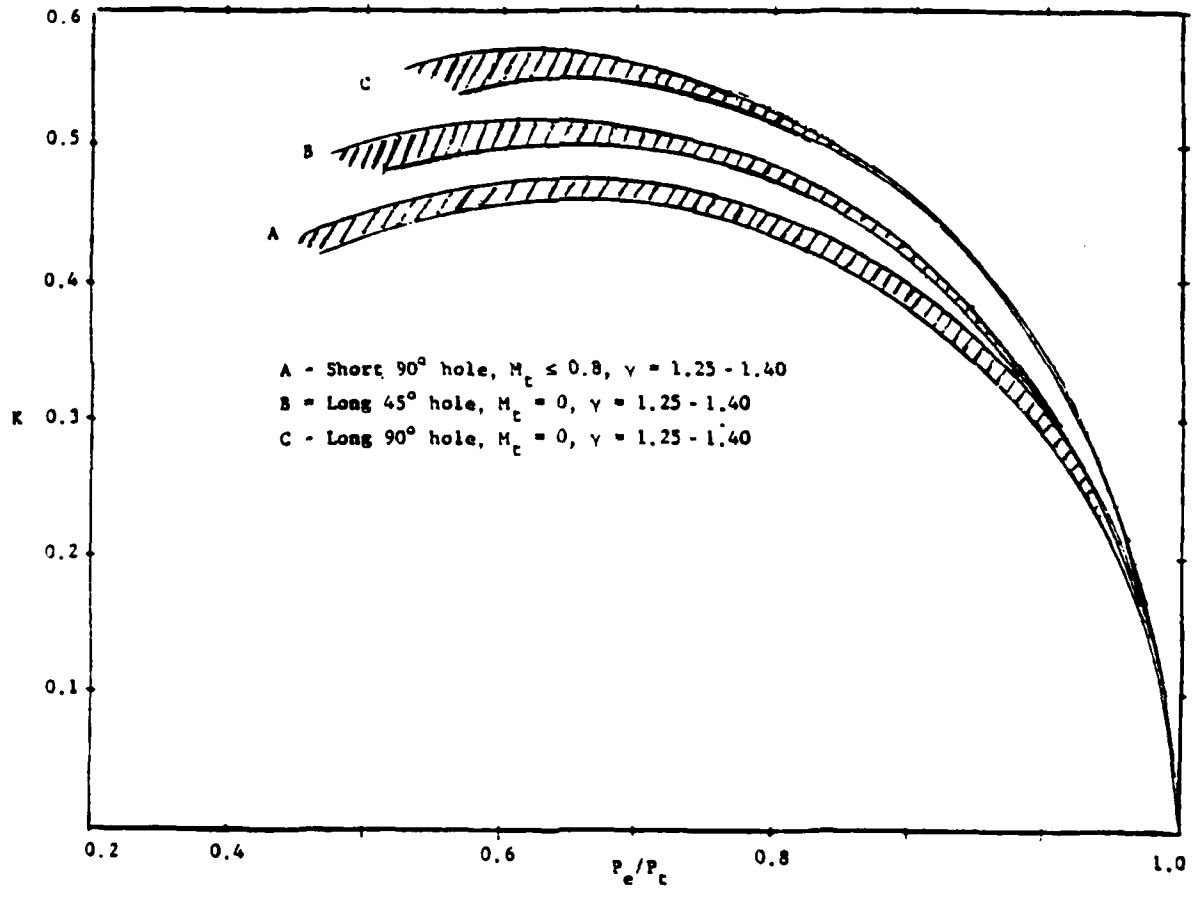

Figure 1 Subsonic Flow Coefficient

Figure 1 shows the results obtained using the "short hole" correlation of Table 1 for $0 \leq M_t \leq 0.8$ with γ = 1.25 and 1.4. Despite the wide range of C_D - R^2 combinations, Figure 1 indicates that K changes little with the choice of γ and is insensitive to $M_t \leq 0.8$ over the range of P_e/P_t which yield

$M_e \leq 1.0$. When $\gamma = 1.25$ choking occurs for $0.36 \leq P_e/P_t \leq 0.39$. For $\gamma = 1.4$ it occurs when $0.34 \leq P_e/P_t \leq 0.37$.

When the applied pressure ratio P_e/P_t is less than the critical P_e/P_t, K is independent of the applied pressure ratio and the gas enters the reservoir underexpanded.

The calculated K for $M_t = 0.9$ are slightly less than those for $M_t \leq 0.8$, indicating that for higher P_e/P_t the coefficient K tends to decrease somewhat as M_t approaches unity. Most of the tube Mach number range is quite accurately predicted by the $M_t = 0$ calculations, i.e., $R^2 = 0$, $C_D = 0.68$. For longer 90° holes ($\ell/d > 3$) [2] gives $C_D = 0.82$. This is the same value which is obtained using an entrance loss coefficient of $k_{ent} = 0.5$ and zero friction loss $f \frac{L}{D}$ in the relation

$$C_D \equiv \frac{1}{\sqrt{1 + k_{ent} + f \frac{L}{D}}} \tag{7}$$

The results for 90° "long" holes using $\gamma = 1.25$ and 1.40, $C_D = 0.82$, and $M_t = 0$ are plotted in Figure 1 and are presumably applicable for $M_t \geq 0.8$. The increase in K relative to the "short" holes is probably a result of the pressure recovery afforded by the longer hole. For P_e/P_t less than about 0.44 K is approximately 0.55.

Bore evacuator holes are typically inclined toward the breech and not a 90° to the bore axis. Reference [2] gives the $M_t = 0$ entrance coefficient for angled holes as

$$k_{ent} = 0.5 + 0.3 \cos \theta + 0.2 \cos^2\theta \tag{8}$$

At $\theta = 45°$, $k_{ent} = 0.812$ and $C_D = 0.743$. The computed flow coefficients for $M_t = 0$ are also plotted in Figure 1 for $\gamma = 1.25$ and 1.4. The lower flow coefficients and critical pressure ratios which result are as expected.

If angled bore evacuator hole coefficients are as insensitive to M_t and γ as the 90° holes are then the $M_t = 0$ results shown in Figure 1 should be representative of the subsonic range $0 \leq M_t < 0.8$. For unchoked flows the $M_t = 0$ curves in Figure 2 are accurately approximated by the modified isentropic nozzle flow coefficient

$$K = C_D \sqrt{\frac{2\gamma}{\gamma - 1}\left[\left(\frac{P_e}{P_t}\right)^{2/\gamma} - \left(\frac{P_e}{P_t}\right)^{\frac{\gamma+1}{\gamma}}\right]} \tag{9}$$

SUPERSONIC TUBE FLOW

When $M_t \geq 1.0$ the flow through the hole is complicated by the formation of a nearly straight detached shock [3] in the hole entrance as illustrated in Figure 2a. To estimate the flow coefficient this flow will be modelled as

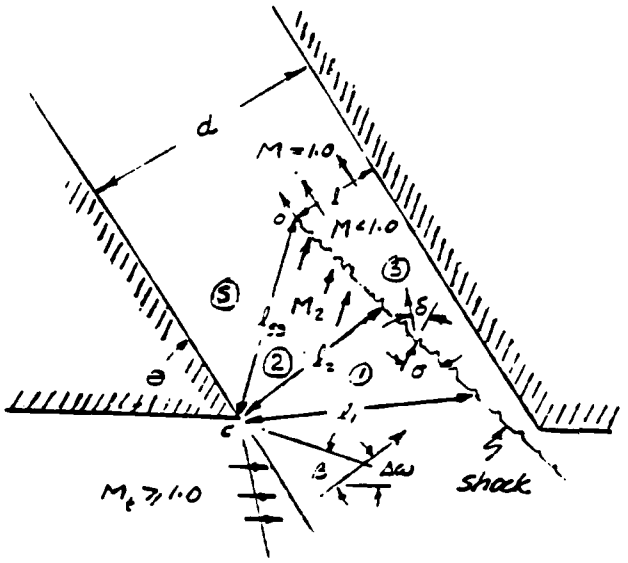

Figure 2a Hole Entrance

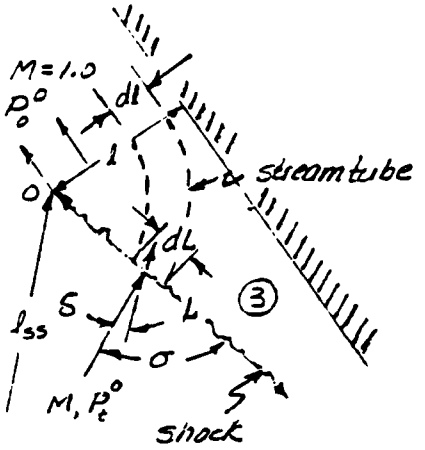

Figure 2b Detail of Region 3

two-dimensional. The approach to the shock will be assumed to be via a Prandtl-Meyer expansion fan (region 1) which terminates in a uniform flow (region 2) bounding the stagnant separated region 5. The hole-end of the shock lies on the separation streamline ℓ_{ss}. The flow direction and Mach number in the uniform flow region are related by the expression

$$\Delta\omega_2 = \left[\sqrt{\frac{\gamma+1}{\gamma-1}}\tan^{-1}\sqrt{\frac{\gamma-1}{\gamma+1}(M_2^2 - 1)} - \tan^{-1}\sqrt{M_t^2 - 1}\right]$$
$$-\left[\sqrt{\frac{\gamma+1}{\gamma-1}}\tan^{-1}\sqrt{\frac{\gamma-1}{\gamma+1}(M_t^2 - 1)} - \tan^{-1}\sqrt{M_t^2 - 1}\right] \tag{10}$$

Carofano [3] shows the flow exits the post-shock subsonic region 3 at approximately sonic velocity parallel to the downstream wall. To satisfy this condition the approach and deflection angles θ_2 and δ_2, for the oblique shock at this point must satisfy the condition

$$\Delta\omega_2 + \sigma_2 + \delta_2 = 180 \tag{11}$$

where

$$\delta_2 = \sigma_2 - \tan^{-1}\left[\frac{\gamma - 1}{\gamma + 1} + \left(\frac{2}{\gamma + 1}\right)\frac{1}{(M_2 \sin\theta_2)^2}\right] \tag{12}$$

The post-shock sonic velocity is described by the oblique shock relation

$$\sqrt{\frac{(M_2 \sin\sigma_2)^2 + \frac{2}{\gamma+1}}{\frac{2\gamma}{\gamma+1}(M_2 \sin\sigma_2)^2 - 1}} = \sin(\sigma_2 - \delta_2) \tag{13}$$

Equations (10) - (13) containing the four unknowns M_2, δ_2, σ_2, $\Delta\omega_2$ uniquely determine the orientation of the shock at 0.

The portion of the shock front which supplies the down-hole flow is related to the length of the sonic exit from the subsonic region 3 by the conservation of mass principle. Figure 2b is a detail of region 3 showing a typical streamtube connecting the boundaries. Streamtube continuity is given by

$$\frac{d\ell}{\ell} = \frac{P_t^o}{P_o^o}\frac{D(M)}{D(1)}\sin\sigma\,\frac{dL}{\ell} \tag{14}$$

where

$$D(M) = \left[1 + \left(\frac{\gamma - 1}{2}\right)M^2\right]^{\frac{\gamma+1}{2(\gamma-1)}} \tag{15a}$$

and the stagnation pressure ratio is

$$\frac{P_t^o}{P_o^o} = \left[\left(\frac{2}{\gamma+1}\right)\frac{1}{(M\sin\sigma)^2} + \frac{\gamma-1}{\gamma+1}\right]^{\frac{\gamma}{\gamma-1}} \cdot \left[\left(\frac{2\gamma}{\gamma+1}\right)(M\sin\sigma)^2 - \frac{\gamma-1}{\gamma+1}\right]^{\frac{1}{\gamma-1}} \tag{15b}$$

The ratio $d\ell/dL$ is constant for flow from region 2 since M_2 and σ_2 are constant. The flow from the expansion-fan region intersects the shock with

varying M_1 and σ_1. Because the shock is assumed to be straight $\sigma_2 + \Delta\omega_2 = \sigma + \Delta\omega$ at every point along the shock so that $d\ell/dL$ is only a function of M.

Integration of Eq.(14) along the ℓ and L boundaries starting at 0 establishes the relative lengths of the inlet and outlet boundaries of the subsonic region. Two lengths are needed to insure that the shock fits into the hole since geometry requires that

$$\frac{d}{\ell_2} = \frac{\ell}{\ell_2} + \frac{\ell_{ss}}{\ell_2} \cos(\Delta\omega_2 + \theta - 90) \tag{16}$$

where ℓ_{ss} is the length of the separation streamline from C to 0 in Figure 2a.

Since energy concepts have been embodied in the assumption of homentropic flows in regions 1 and 2, and isentropic flow in region 3, we must look to momentum to complete closure. Figure 3 shows the control volume for the

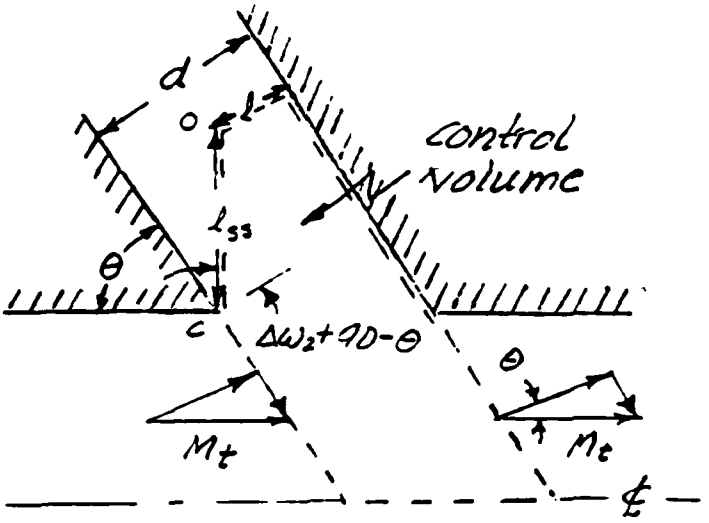

Figure 3 Momentum Control Volume

momentum balance reaching from the tube centerline to the separating streamline, ℓ_{ss}, and the subsonic region exit boundary, ℓ. Neglecting wall friction and assuming that M_t remains unchanged across the control volume, the momentum balance along the hole axis is

$$P_t d - \frac{\dot{m}}{g} M_t \sqrt{\gamma g R T_t} \cos\theta = P_2 \ell_{ss} \cos(\Delta\omega_2 + 90 - \theta) + \int_0^{\ell} P_o^o G(M_o) d\ell \tag{17}$$

where $P_o^o G(M_o)$ is the force per unit length at the exit boundary of the subsonic region and

$$G(M_o) = \frac{1+\gamma M_o^2}{\left[1+\left(\frac{\gamma-1}{2}\right)M_o^2\right]^{\frac{\gamma}{\gamma-1}}} \tag{18a}$$

Since it is assumed that $M_o = 1.0$, $G(M_o) = G(1)$

$$G(M_o) = G(1) = \frac{1+\gamma}{\left(\frac{\gamma+1}{2}\right)^{\frac{\gamma}{\gamma-1}}} \tag{18b}$$

The mass flow rate through the hole is given by Eq.(5), which for the two-dimensional hole of unit depth becomes

$$\dot{m} = Kd\sqrt{gP_t\rho_t} \tag{19}$$

Combining Eqs.(17) and (19) and normalizing yields

$$\frac{d}{\ell_2} = K\left(\frac{d}{\ell_2}\right)\sqrt{\gamma}\,M_t\cos\theta + \left(\frac{P_2}{P_t}\right)\left(\frac{\ell_{ss}}{\ell_2}\right)\cos(\Delta\omega_2 + 90 - \theta) + G(1)\int_o^{\ell}\frac{P_o^o}{P_t}\frac{d\ell}{\ell_2} \tag{20}$$

The terms on the right-hand side of this equation are not in a form convenient for computation. More useful forms will be developed in the paragraphs to follow.

Figure 4 shows a detail of regions 1 and 2. The geometry of region 1 is described by the law of sines, i.e.,

$$\frac{\ell_1}{d} = \frac{\ell_2}{d}\,\frac{\sin(\sigma_2+\beta_2)}{\sin(\sigma_1+\beta_1)} \tag{21}$$

where ℓ_1, ℓ_{n-0}, ℓ_{n-1}, ℓ_2 are Mach lines. Since the down-hole flow crosses ℓ_1 it is a simple matter to show that in the first right-hand side term of Eq.(20)

$$K\frac{d}{\ell_2}\sqrt{\gamma} = \gamma\left[\frac{1+\left(\frac{\gamma-1}{2}\right)M_t^2}{1+\left(\frac{\gamma-1}{2}\right)M_1^2}\right]^{\frac{\gamma+1}{2(\gamma-1)}}\left[\frac{\sin(\sigma_2+\beta_2)}{\sin(\sigma_1+\beta_1)}\right] \tag{22}$$

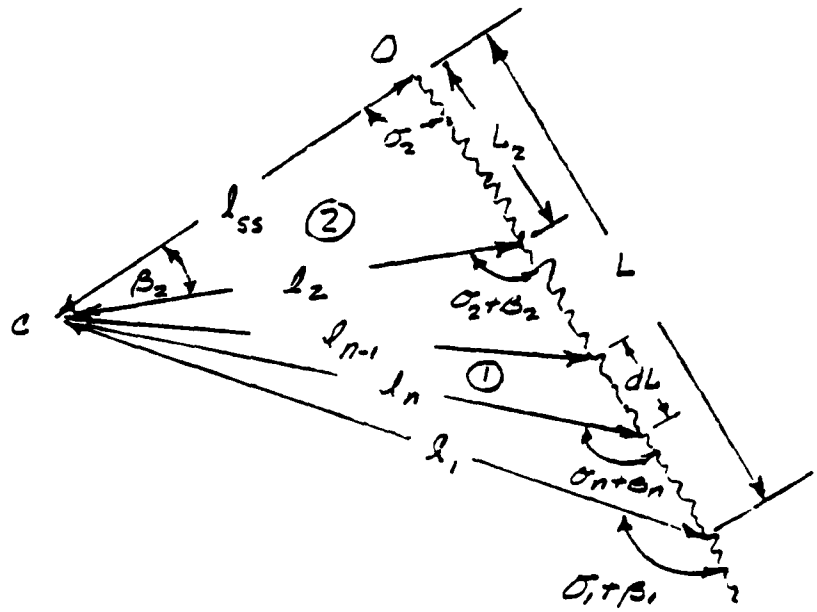

Figure 4 Geometry of Regions 1 and 2

The law of sines applied to the uniform flow region 2 gives

$$\frac{\ell_{ss}}{\ell_2} = \frac{\sin(\sigma_2 + \beta_2)}{\sin \sigma_2} \tag{23}$$

Since regions 1 and 2 are homentropic

$$\frac{P_2}{P_t} = \left[\frac{1 + \left(\frac{\gamma - 1}{2}\right) M_t^2}{1 + \left(\frac{\gamma - 1}{2}\right) M_2^2}\right]^{\frac{\gamma}{\gamma-1}} \tag{24}$$

These two terms appear in the second right-hand side term of Eq.(20).

In the last term of Eq.(20)

$$\frac{1}{P_t} = \frac{\left[1 + \left(\frac{\gamma - 1}{2}\right) M_t^2\right]^{\frac{\gamma}{\gamma-1}}}{P_t^o} \tag{25}$$

From the continuity equation (4)

$$\frac{d\ell}{\ell_2} = \frac{P_t^o}{P_o^o} \frac{D(M)}{D(1)} \sin \sigma \frac{dL}{\ell_2} \tag{26}$$

As a consequence the integrand of the last term becomes

$$\frac{P_o^o}{P_t}\frac{d\ell}{\ell_2} = \frac{D(M)}{D(1)}\left[1 + \left(\frac{\gamma-1}{2}\right)M_t^2\right]^{\frac{\gamma}{\gamma-1}} \sin\sigma\,\frac{dL}{\ell_2} \tag{27}$$

The integral term in Eq.(20) now becomes

$$G(1)\int_o^{\ell}\frac{P_o^o}{P_t}\frac{d\ell}{\ell_2} = \frac{G(1)}{D(1)}\left[1 + \left(\frac{\gamma-1}{2}\right)M_t^2\right]^{\frac{\gamma}{\gamma-1}}\int_o^{L} D(M)\sin\sigma\,\frac{dL}{\ell_2} \tag{28}$$

In the uniform region 2 M_2 and σ_2 are constant so that for that portion of the shock, L_2,

$$\int_o^{L_2} D(M)\sin\sigma\,\frac{dL}{\ell_2} = D(M_2)\sin\sigma_2\,\frac{L_2}{\ell_2} \tag{29}$$

From the law of sines for region 2

$$\frac{L_2}{\ell_2} = \frac{\sin\beta_2}{\sin\sigma_2} \tag{30}$$

so that

$$\int_o^{L_2} D(M)\sin\sigma\,\frac{dL}{\ell_2} = D(M_2)\sin\beta_2 \tag{31}$$

Returning to the dimensionless momentum expression (20) and inserting Eqs.(22), (23), (24), (28), and (31) yields

$$\begin{aligned}\frac{d}{\ell_2} = \gamma&\left[\frac{1 + \left(\frac{\gamma-1}{2}\right)M_t^2}{1 + \left(\frac{\gamma-1}{2}\right)M_1^2}\right]^{\frac{\gamma+1}{2(\gamma-1)}}\left[\frac{\sin(\sigma_2+\beta_2)}{\sin(\sigma_1+\beta_1)}\right]M_t\cos\theta\\ &+\left[\frac{1 + \left(\frac{\gamma-1}{2}\right)M_t^2}{1 + \left(\frac{\gamma-1}{2}\right)M_2^2}\right]^{\frac{\gamma}{\gamma-1}}\left[\frac{\sin(\sigma_2+\beta_2)}{\sin\sigma_2}\right]\cos(\Delta\omega_2 - 90 + \theta)\\ &+\frac{G(1)}{D(1)}\left[1 + \left(\frac{\gamma-1}{2}\right)M_t^2\right]^{\frac{\gamma}{\gamma-1}}\left[D(M_2)\sin\sigma_2 + \int_{L_2}^{L} D(M)\sin\theta\,\frac{dL}{\ell_2}\right]\end{aligned} \tag{32}$$

Equation (16) also calculates the ratio d/ℓ_2. Inserting Eq.(23) it becomes

$$\frac{d}{\ell_2} = \int_o^{\ell} \frac{d\ell}{\ell_2} + \left[\frac{\sin(\sigma_2 + \beta_2)}{\sin \sigma_2}\right] \cos(\Delta\omega_2 - 90 + \theta) \tag{33}$$

Using Eq.(26) the first term can be written

$$\int_o^{\ell} \frac{d\ell}{\ell_2} = \int_o^{L} \frac{P_t^o}{P_o^o} \frac{D(M)}{D(1)} \sin \sigma \frac{dL}{\ell_2} = \int_o^{L_2} \frac{P_t^o}{P_o^o} \frac{D(M_2)}{D(1)} \sin \sigma_2 \frac{dL}{\ell_2} + \int_{L_2}^{L} \frac{P_t^o}{P_o^o} \frac{D(M_1)}{D(1)} \sin \sigma_1 \frac{dL}{\ell_2} \tag{34}$$

Over the shock length L_2 of uniform region 2,

$$\int_o^{L_2} \frac{P_t^o}{P_o^o} \frac{D(M_2)}{D(1)} \sin \sigma_2 \frac{dL}{\ell_2} = \left.\frac{P_t^o}{P_o^o}\right|_{L_2} \frac{D(M_2)}{D(1)} \sin \sigma_2 \frac{L_2}{\ell_2} = \left.\frac{P_t^o}{P_o^o}\right|_{L_2} \frac{D(M_2)}{D(1)} \sin \beta_2 \tag{35}$$

Equation (33) can now be written

$$\frac{d}{\ell_2} = \left.\frac{P_t^o}{P_o^o}\right|_{L_2} \frac{D(M_2)}{D(1)} \sin \beta_2 + \int_{L_2}^{L} \frac{P_t^o}{P_o^o} \frac{D(M)}{D(1)} \sin \sigma \frac{dL}{\ell_2} + \left[\frac{\sin(\sigma_2 + \beta_2)}{\sin \sigma_2}\right] \cos(\Delta\omega_2 - 90 + \theta) \tag{36}$$

The stagnation pressure ratio and D(M) are given by Eqs.(15).

Equations (32) and (36) are two independent expressions for d/ℓ_2 which depend on L for a given M_t. The location and length of the shock is found by integrating along the shock boundary region 1 until Eqs.(32) and (36) yield the same d/ℓ_2 which then locates ℓ_1. The flow coefficient can then be found from

Figure 5 also shows the results computed by Carofano [3] for $\theta = 90^\circ$ and the experimental result of Smith [4]. The two-dimensional results obtained here and the three-dimensional results of Carofano indicate that K is relatively insensitive to M_t. The two-dimensional model yields flow coefficients about one and one-half times the round hole results for 90° holes. Larger coefficients are not unreasonable for the less complex slot flows modelled by the two-dimensional flows.

OBSERVATIONS

The available analytical results suggest the following generalities concerning the hole flow coefficients:

1. They are relatively insensitive to the tube Mach number.
2. For subsonic flows they are strongly dependent on the pressure ratio across the hole when the hole is not choked.
3. The effect of hole angle is more significant for supersonic tube flows than for subsonic.
4. They do not exceed 0.5.

The work presented here is an attempt to estimate flow coefficients using formulations based on existing data or simplified models. Experimental measurements are necessary before undertaking more elaborate and expensive analyses.

NOMENCLATURE

a	hole area
C_D	discharge coefficient
d	slot width
k_{ent}	entrance coefficient
K	flow coefficient
ℓ, L	lengths
$\dot{m}$	hole mass flow rate
M	Mach number
P	pressure
P^o	stagnation pressure
R	gas constant
T	temperature
U	velocity
β	Mach angle

$$K = \sqrt{\gamma}\left[\frac{1 + \left(\frac{\gamma - 1}{2}\right) M_t^2}{1 + \left(\frac{\gamma - 1}{2}\right) M_1^2}\right]^{\frac{\gamma+1}{2(\gamma-1)}} \frac{\sin(\sigma_2 + \beta_2)}{\sin(\sigma_1 + \beta_1)} \left(\frac{\ell_2}{d}\right) \tag{37}$$

From the law of sines it can be shown that

$$\frac{dL}{\ell_2} = \left[\frac{\sin[(\sigma_n + \beta_n) - (\sigma_{n-1} + \beta_{n-1})]}{\sin(\sigma_{n-1} + \beta_{n-1})}\right] \frac{\sin(\sigma_2 + \beta_2)}{\sin(\sigma_n + \beta_n)} \tag{38}$$

Equation (38) provides a means of incrementing along the shock in Eqs.(32) and (36) starting at L_s. Agreement is established when the difference between the two computed d/ℓ_2 is within a prescribed convergence error.

Once Eqs.(32) and (36) agree the geometry of regions 2 and 3 are established and K can be computed. The results of these computations are shown in Figure 5.

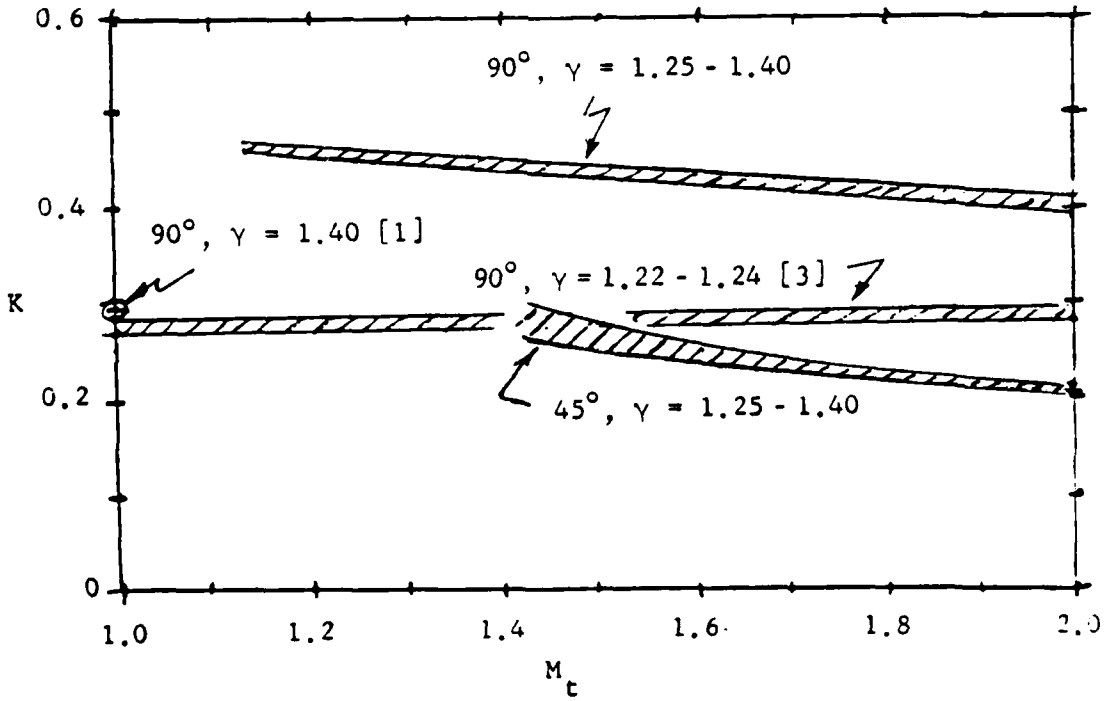

Figure 5 Supersonic Flow Coefficient

γ	specific heat ratio
δ	deflection angle
θ	hole angle
ρ	density
$\Delta\omega$	Prandtl-Meyer angle

Subscripts

e	hole exit
o	exit subsonic region
ss	separating streamline
t	tube

REFERENCES

1. Sneck, H.J., "Gas Flows Through Small Holes in Gun Tube Walls," Proc. Fifth U.S. Army Symposium on Gun Dynamics, Sept. 1987, pp. 30-44.

2. Blevins, R.F., Applied Fluid Dynamics Handbook, Van Nostrand, 1984, pp.94-95.

3. Carofano, G.C., "The Gas Dynamics of Perforated Muzzle Brakes," Proc. Fifth U.S. Army Symposium on Gun Dynamics, Sept. 1987, pp.10-29, 141, 72.

4. Smith, F., "Investigation of Fume Extractor Design by Model Techniques," RARDE Memo. 13/67, Fort Halstead, U.K., 1967.

TITLE: STATISTICAL ANALYSIS OF 16-IN. GUN BLAST

JON J. YAGLA AND MICHEAL M. KORDICH
NAVAL SURFACE WARFARE CENTER, DAHLGREN, VA 22448

ABSTRACT:

The reactivation of the four U.S.S. IOWA class battleships with modern weapons and electronics equipment has led to an extensive study of the blast overpressure from 16-in. gun firings. The experimental database incorporates data taken from land and ship firings beginning in 1981 through the present time. All 16-in. gun firings in which blast overpressures were measured were carefully designed so that the data could be systematically analyzed and used to enlarge the database.

The analysis of the data has been accomplished through the use of formal statistical methods. The approach has been to store the overpressure data according to azimuth and distance. The data at fixed points are then analyzed by computing the mean, variance, and standard deviation. Any new data being considered for inclusion in the database are analyzed by computing the mean and variance at each point in the field. The sample means and variances are then tested with the "T" test and "F" test of mathematical statistics.

Regression analysis with exponential expressions has been used to provide expressions for the decay of overpressure along the standardized azimuths. The parameters of the regression analysis depend mainly on azimuth, and this dependency has been studied to provide complete analytical description of the blast overpressure field.

BIOGRAPHY: Dr. Yagla has done experimental and analytical research in the field of weapons blast and dynamical response since 1965 at the Dahlgren Laboratory.

PRESENT ASSIGNMENT: Chief Engineer for Surface Weapons.

PAST EXPERIENCE: Test Conductor for the gun and missile structural test firings in IOWA class battleships. Consultant to Battleship Combat System Engineer and Cruise Missiles Project. Presently in structural design, test, and manufacturing of Standard Missile.

DEGREES HELD: Bachelor of Arts (Science), State College of Iowa, Master of Science (Engineering Mechanics), Arizona State University, Doctor of Philosophy (Aerospace Engineering and Engineering Science), Arizona State University.

STATISTICAL ANALYSIS OF 16-IN. GUN BLAST

Jon J. Yagla* and Micheal M. Kordich
Naval Surface Warfare Center
Dahlgren, Virginia 22448

INTRODUCTION

Gun blast has been a critical issue in the modernization and reintroduction of the IOWA class battleship into the U.S. fleet. The modernized battleships include many new elements in their combat systems. New weapons include the Close-In Weapons System, and Tomahawk and Harpoon cruise missiles. New radars and the SLQ-32 electronics countermeasures sets are also included. New munitions and fire control systems are also under development [Reference 1].

The 16-in. gun blast is so powerful that there is no place outside the ship that is completely free from the effects of blast. Figure 1 shows the locations of the new equipment on the modernized battleships. The effect of 16-in. gun blast on the stowed Tomahawk missiles was a critical safety issue [Reference 2], and led to a very careful examination of the gun blast data. The impact on the Tomahawk equipment also must be thoroughly analyzed for any changes in the 16-in. gun or munitions.

Because of the serious engineering and safety issues of the 16-in. gun blast, a thorough and mathematically rigorous statistical analysis was required. The database now contains over 1100 data points. This paper presents the analysis that was used and the results.

BLAST OVERPRESSURE DATABASE

The Ship Engineering Branch has established a database of blast overpressure data from 16-in. gun firings. The database primarily consists of service round firings that are either 1900- or 2700-lb projectiles propelled by up to a 700-lb charge. The database contains over 1100 pressure measurements recorded beginning in November 1981 prior to the recommissioning of the U.S.S. NEW JERSEY (BB-62) and presently extending through November 1988. All the data were recorded by H13 personnel at one of three different locations. The first location was the NSWC Main Range where reactivation and proofing tests were conducted [References 3 and 4]. The other two test locations were at sea aboard the U.S.S. NEW JERSEY and U.S.S. IOWA as part of the structural test firing program [References 5, 6, and 7].

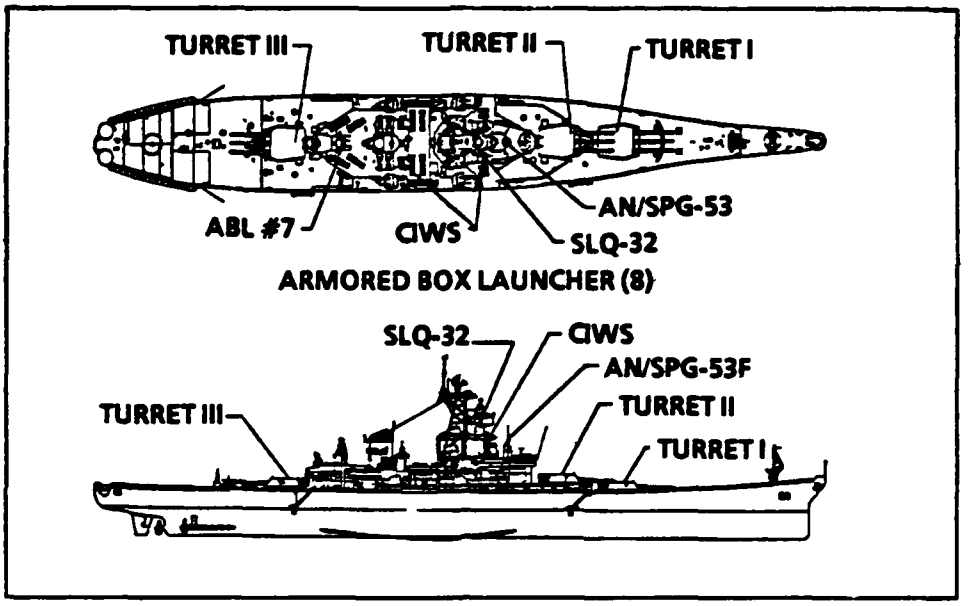

FIGURE 1. BATTLESHIP SHOWING LOCATIONS OF VARIOUS EQUIPMENTS

The blast overpressure database is divided into two general categories. The somewhat arbitrary division point is set with respect to 1 psi. Data with peak pressure readings below 1 psi are generally associated with noise levels rather than blast. At large distances from the gun, the pressure pulse is normally acoustic in nature, consisting of an oscillating wave rather than a shock front. This category of data, referred to as far field propagation, is not applicable to this report but has been documented [Reference 8].

The free-air blast data are characterized by a shockwave that results in a step pressure rise to a peak value followed by an exponential decay (Friedlander) of the pressure to ambient conditions (Figure 2). The peak blast overpressure for a gun is a function of the azimuth off of the line of fire and the distance between the muzzle of the gun and the point of interest. This relationship was originally documented by Walther [Reference 9].

The peak overpressure is given analytically by the following equation:

$$P_{R,\phi} = A_{\phi} R^{N} \qquad (1)$$

where

P = peak free-air pressure (psi)
R = radial distance from the muzzle (ft)
ϕ = angle off the line of fire (deg)
A,N = coefficients determined through least-squares curve fitting routines (functions of ϕ)

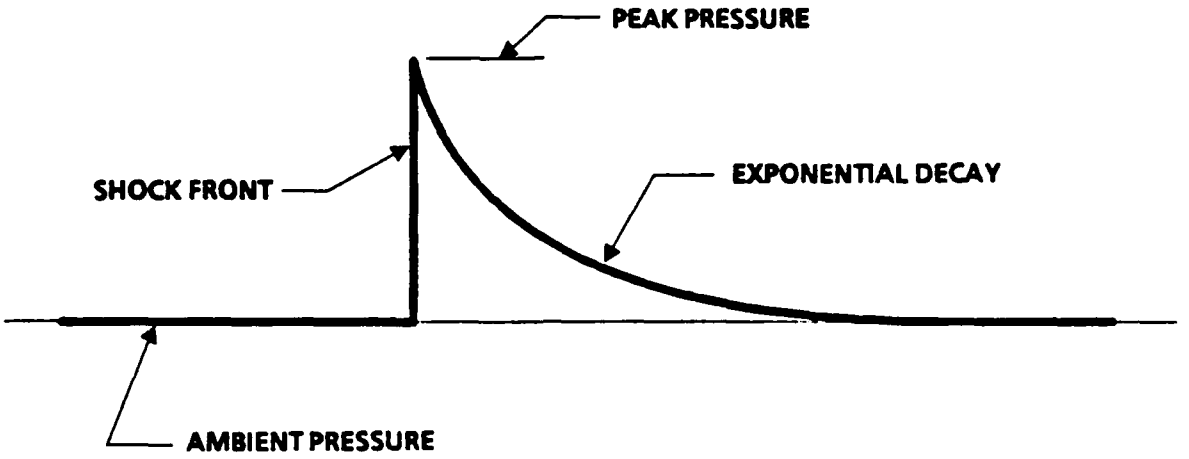

FIGURE 2. TYPICAL FREE-AIR BLAST PROFILE

A graphical representation of the coordinate system showing how the azimuth (ϕ) and the radial distance (R) are measured is shown in Figure 3.

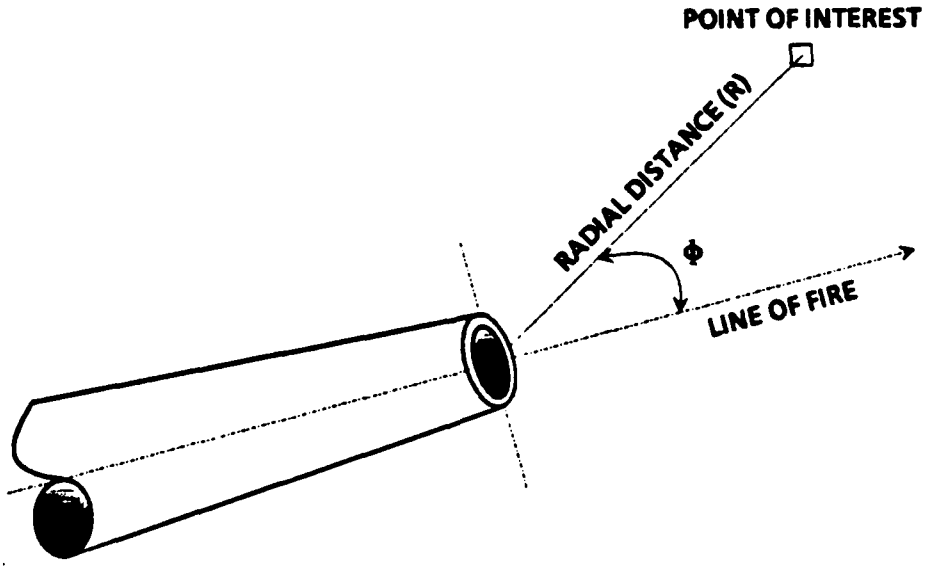

FIGURE 3. COORDINATE SYSTEM FOR FREE-AIR GUN BLAST EQUATIONS

DATA ANALYSIS

There is round-to-round variation in the overpressure observed at any given point. This round-to-round variation is a significant fraction of the peak overpressure. Therefore, statistical methods are required to analyze the data. The analysis of the blast data took the form of a sequential

operation. The first set of experiments consisted of firing 36 rounds of ammunition with various propellant weights, two projectile weights, and 32 instrument locations. A rigorous statistical analysis showed that the blast data was not changed significantly, in the statistical sense, by the changes in propellant or projectiles. The data set from these experiments formed the baseline data, and were the basis for analysis and design of the shipboard equipment installations and further experiments. The data set has been subsequently greatly enlarged, and now contains data from other propelling charges and projectiles.

Processing the raw data involved digitizing the recorded analog data and determining the peak pressure value for each of these records. The analog-to-digital conversion was accomplished using a Data Precision DATA 6000 waveform analyzer. The waveform analyzer also performed the tasks of scaling the data (magnitude and engineering units) and determining the peak pressure. After the peak pressures had been calculated, they were incorporated into the database so that comparisons could be made. The database consists of data recorded over a period of approximately seven years with more data to be incorporated when available. Data recorded over this length of time can yield numerous data points at any given location. Therefore, the data was indexed by the azimuth and distance between the muzzle and the transducer.

The data comparisons were accomplished by statistical analysis. This approach examined the relationships between the mean pressure value and variance of those values of each set of test data to determine if they were compatible. A test data set was defined as the free-air overpressure for a given location (angle and distance) recorded during a firing exercise for a given round (projectile and charge weight). With the database being indexed to angle and distance, the test date was employed to complete the definition of a data set. A complete listing of the data as defined by the test data set is contained in Reference 10.

The equations of Table 1 were set forth by Steel and Torrie [Reference 11]. The calculations denoted as sample mean and sample variance were associated with the data points of the individual test data sets. This was the basic calculation upon which all comparisons were based. After the statistical data for the individual tests had been calculated, a cumulative type of comparison began. The data sets that were employed in the statistical analyses are contained in Appendix A. The comparison is described as cumulative because each test was compared against the population developed by the previous comparison. This concept is shown schematically in Figure 4. Each new data set was compared to the population from the previous data sets by means of the *f* and *t* tests of statistics.

The first calculation performed was the analysis of variances or *f* test. This calculation was performed to determine if the sample variances from two independent test data sets, s_1^2 and s_2^2, are from a single population. The test is based upon the null hypothesis that the independent sample variances are equal ($s_1^2=s_2^2$). The level of significance or probability of erroneous rejection for the analysis was set at $\alpha=0.10$. This setting provides the two standards for the test. The first is the value of *f*, which is used to

determine whether to accept or reject the null hypothesis. The second is the value of α which is the probability of rejecting the null hypothesis even if it were true. For this calculation, the larger of the two values between s_1^2 and s_2^2 was always employed as the numerator of the ratio

TABLE 1. STATISTICAL FORMULAS FOR THE 16-IN.GUN BLAST ANALYSIS

Calculation	Equation	Remarks
sample mean		
sample variance	$s_1^2 = \frac{[n\Sigma(x_2^2)-(\Sigma x_1)^2]}{n(n-1)}$	calculated for each set of test data
analysis of variance null hypothesis (variances are equal)	$f = s_1^2/s_2^2$ $\beta_1 = n_1-1$ $\beta_2 = n_2-1$	$f<F_{\alpha(\beta1,\beta2)}$ $\alpha=.10$
estimated population variance	$\sigma^2 = \frac{(n_1-1)(s_1^2)+(n_2-1)(s_2^2)}{(n_1+n_2-2)}$	weighted average of sample variances
standard deviation for the difference of two random means	$\sigma^2 = \frac{(n_1-1)(s_1^2)+(n_2-1)(s_2^2)}{(n_1+n_2-2)}$	
analysis of means null hypothesis (means are equal)	$t=(\mu_1-\mu_2)/S_d$	$t<T_{\alpha(\beta1+\beta2)}$ $\alpha=.40$
population mean	$\mu_0=(\mu_1*n_1+\mu_2*n_2)/(n_1+n_2)$	
population standard deviation	$\sigma=[\sigma2]^{1/2}$	

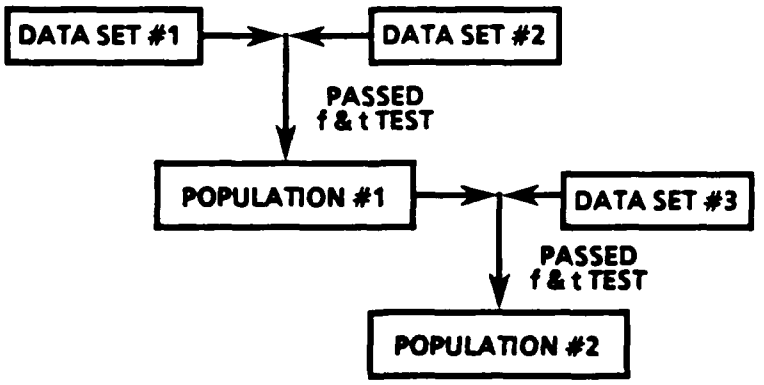

FIGURE 4. CUMULATIVE STATISTICAL APPROACH SCHEMATIC

$$f = s^2_{large} / s^2_{small} \tag{2}$$

By determining the value of f in the above manner, the analysis is described as two-tailed. By employing a two-tailed analysis, the probability of erroneous rejection (P_α) of the null hypothesis is divided in half ($P_\alpha/2$) and relegated to either end of a normal distribution. This means that the analysis was employed solely to determine if the null hypothesis was true or not; on which side of the center the value of f fell was not important. The concept of a two-tailed analysis is shown graphically in Figure 5 and is stated mathematically as:

$$P_\alpha \equiv P_{\alpha/2} \; that \; F_{-\alpha/2} < s_1^2/s_2^2 \; or \; s_1^2/s_2^2 > F_{\alpha/2}, \tag{3}$$

where f is a tabulated value dependent on the degree of freedom of each of the two samples. The degree of freedom is defined as the number of events in a sample minus one ($\Sigma n_1 - 1$). For this analysis, the degree of freedom for a data set was the number of rounds fired for the exercise minus one.

The operations in performing the f test at a given point (angle, distance) were done with the aid of a spreadsheet computer program as follows: first the variance of the overpressure was calculated for the previous population at the point (Figure 4). Then the variance of the data set in question was calculated. The ratio of the two variances was calculated such that the ratio was greater than unity. This ratio is the value f. The next step was to enter published tables [Reference 11] of the distribution of f. f is a statistic that relates the variances of samples drawn from a large population of data with a normal distribution. The tables have three parameters that must be specified to obtain f. These are the confidence (taken as 90%; i.e., $\alpha = 0.1$), the degrees of freedom of the sample, the degrees of freedom of the population. The result is the value f. If $f \leq F$, then it is 90% certain, from the standpoint of statistical variance, that the sample can be taken as a subset of the population. If $f > F$, then the test failed, and the sample cannot be assumed to be from the population.

The hypothesis that the samples were from a single population was not rejected solely on the basis of the f test. An additional calculation, the analysis of two means or t test was also performed. This calculation is normally used to determine if two random sample means are from the same population defined by a normal distribution. For this analysis, the calculation was employed as a confirmation of the results of the analysis of variances. The t test performed is described as a two-tailed analysis of unmatched observations with equal variances. The test was two-tailed because, as was the case in the f test, the alternate hypothesis was that the means were not equal. The level of significance for this calculation was set at $\alpha = 0.40$. By setting the level of significance to a higher percentage, a small acceptance region was produced. The small acceptance region provided greater confidence in the results of the f test when both tests accepted the null hypothesis.

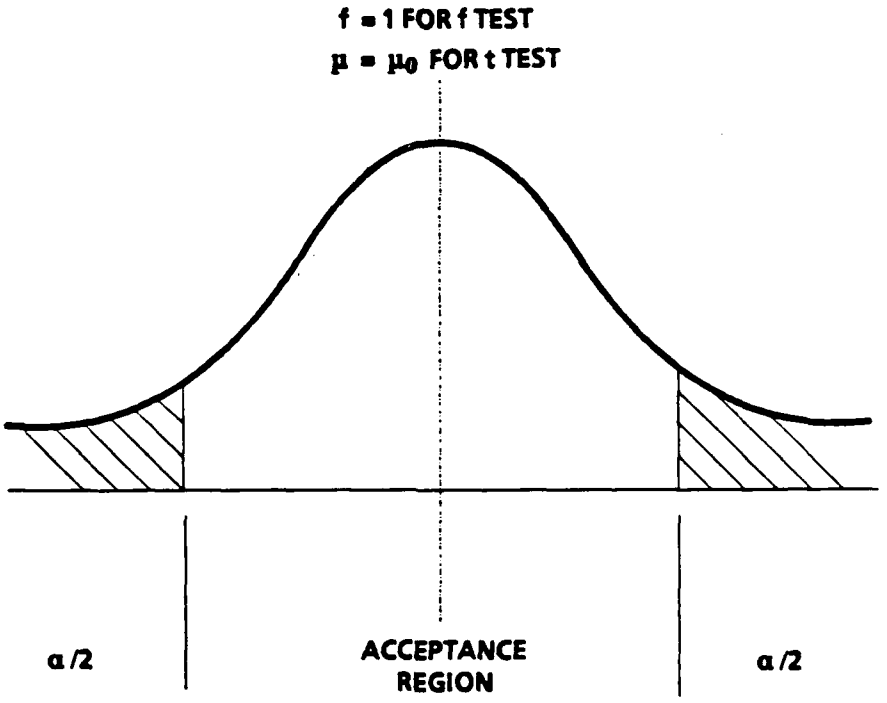

FIGURE 5. ACCEPTANCE REGION FOR A TWO-TAILED *f* OR *t* TEST

The *t* test uses standardized tables of the statistic T, which is a tabulated function of the number of degrees of freedom of the sample in question and the probability that $t \leq T$. The calculations provide a formal means of determining whether or not the mean of the data sample in question is sufficiently close to the mean of the population. The calculations were performed on a spreadsheet. The first step was to form the estimated population variance, σ^2, from the sample variances. Then the standard deviation, S_d, was computed. The quantity *t*, which compares the difference between the two means to the estimated standard deviation, was then computed. The quantity *t* should then be less than T for the test to pass. Samples that pass both the T and the F tests are then deemed to be statistically equivalent to the population and are then included in the database.

ANALYSIS RESULTS

For the most part, the decision on whether to accept or reject the null hypothesis for each data set was clear cut. As stated previously, the criteria employed to assure that the data sets were from the same population was that both the *f* and *t* tests had to accept the null hypothesis. The calculated values of *f* were either well within or very far outside of the acceptance region. The calculated values of *t* were usually closer to the critical portion of the acceptance region, but this was a result of the higher level of significance ($\alpha = .40$). There were, however, a few locations where the calculated values of *f* or *t* fell outside of the acceptance region

and the data sets were combined anyway. This occurred when there was a large disparity between the variances of the two samples as on the 90 deg radial. Tables showing all of the calculated values of the analyses are contained in Appendix B.

The analysis showed that the blast overpressures associated with firing all the 16-in. service rounds tested thus far are from the same parent population with four exceptions. These exceptions occurred on the radials between 60 and 90 deg and at distances of 20 to 30 ft. Upon investigation of the firing data, it was discovered that the baseline blast data was generated by 1900 lb. projectiles propelled by charges certified for the 2700 lb. projectile. It is felt that this charge/projectile combination produced blast overpressures that were higher than normal because the gun chamber pressures would be significantly greater than with the service charge of the 1900 lb. projectile.

For the most part, the 2240-lb projectile fell within the acceptance region and can be considered as part of the same parent population. Therefore, the 2240-lb. projectile blast data has been included in the service round database and will be part of any future analyses. The general tendency for the data was that as the projectile weight decreased the mean of the data set tended to move away from the mean of the parent population.

REGRESSION ANALYSIS

As in previous blast analyses of land-based test data, pressure measurements made in the mach reflection region were plotted employing a distance correction factor before the regression analysis was conducted. This correction factor is volumetrically defined and produces a scaled distance $R_S=R/2^{1/3}$. Discussions of how the mach region scaling factor was derived are presented in References 2 and 4. The mach region scaling factor was only applied to the land-based data at distances in excess of 75 ft; it was not applied to any data recorded during at-sea testing. The regression analysis curves for the conventional rounds are in Appendix B.

SUMMARY AND CONCLUSIONS

The 16-in. gun blast pressure wave is characterized by a discontinuous increase in pressure followed by an exponential decay. The pressure field exhibits round-to-round variations that are a significant fraction of the peak pressure. Formal statistical methods have been used to analyze the database, which consists of over 1100 experimental pressure versus time records. The analysis showed that the blast overpressure from the 2240-lb projectile firings are not significantly different from the main database obtained from 1900- and 2700-lb projectiles. The data from the 2240-lb projectile firings have, therefore, been included in the database.

The statistical methods provide a means of comparing the blast from new ammunition types to conventional types, even when there is a large round-to-round variation in overpressure.

REFERENCES

1. White, R. W. and Antoniuk, T. H., "The Improved 16-In. Gun Weapon System," Naval Engineers Journal, March 1988.

2. Yagla, J. J., "16-In. Gun Blast and The Battleship Reactivation Program," Naval Engineers Journal, May 1987.

3. Lord, Susan, 16-In. Gun Blast Data Analysis Report, Vitro Corporation, Dahlgren, Virginia, 17 August 1982.

4. Yagla, J. J., 16-In. Gun Blast Experiments, International Conference on Ballistics, Nanjing, Peoples Republic of China, 25-28 October, 1988. Reprinted as NSWC TR 88-407, Naval Surface Warfare Center, Dahlgren, Virginia.

5. Yagla, J. J., "Phase II Structural Test Firings on USS NEW JERSEY," NSWC N43:JJY:plt 8800/bb-62-4 of 22 June 1983.

6. Yagla, J. J., "Firing Arc Enlargement Structural Test Firings on NEW JERSEY," NSWC E53-JJY 8800.1 of 11 October 1984.

7. Gloyna, F. L., Tomahawk Environment Induced by Sixteen Inch Gun Blast, Report GDC-SLCM-85-120, General Dynamics, Convair Division, 3C September 1985.

8. Yagla, J. J., Far Propagation of Blast from the 16-Inch Naval Gun, Naval Surface Warfare Center TR 86-191, February 1987.

9. M. F. Walther, Gun Blast From Naval Guns, Naval Surface Warfare Center NWL TR-2733, August 1972.

10. Steel, Robert G.D. and Torrie, James H., Principles and Procedures of Statistics, McGraw-Hill Book Company, Inc., 1960.

TABLE A-1. STATISTICAL ANALYSIS TABLE FOR 45 DEGREE RADIAL

DISTANCE FEET	ROUNDS FIRED	SAMPLE PRESSURE	PROJECTILE WEIGHT	POPULATION MEAN	POPULATION DEVIATION	POPULATION VARIANCE	SAMPLE MEAN	SAMPLE VARIANCE	CALCULATED f	F(table) α = .10	STD DEV Sd	CALCULATED t	T(table) α=0.4	REMARKS
20	1	34.24												
30	10						17.90	1.72						
30	1	16.43	1900											
30	1	18.18	1900											
30	1	18.22	1900											
30	1	16.22	1900	17.72	1.26	1.58	17.24	1.18	1.45	5.24	0.74	0.86	0.87	JOIN
30	1	19.14												
30	1	15.53	2700											
30	1	15.51	2700											
30	1	18.08	2700	17.57	1.38	1.92	17.07	3.37	2.13	2.56	0.79	0.83	0.86	JOIN
30	1	16.62	2240											
30	1	20.64	2240											
30	1	20.11	2240											
30	1	21.19	2240											
30	1	23.19	2240											
30	1	18.89	2240											
30	1	19.93	2240											
30	1	22.25	2240			2.73	20.35	4.11	2.14	2.06	0.66	-4.28	0.86	NO JOIN
30	1	21.20	1332											
30	1	23.87	1336											
30	1	23.85	1341											
30	1	24.57	1342											
30	1	22.58	1343											
30	1	23.65	1346											
30	1	21.29	1349											
30	1	23.15	1350											
30	1	23.60	1350											
30	1	23.58	1355											
30	1	22.19	1355	21.48	1.61	1.65	23.04	1.20	1.60	2.22	0.49	-11.12	0.86	NO JOIN
50	12	0.00					0.64	0.38						
50	1	0.64		0.64	0.62									
70	1	3.64												
70	1	3.29												
70	1	2.06												
70	1	3.00		3.00	0.68									
71	1	3.10												
71	1	5.96												
71	1	4.53		4.53	1.43									
72	1	3.56												
73	1	3.08												

TABLE A-2. STATISTICAL ANALYSIS TABLE FOR 60 DEGREE RADIAL

DISTANCE FEET	ROUNDS FIRED	SAMPLE PRESSURE	PROJECTILE WEIGHT	POPULATION MEAN	POPULATION DEVIATION	POPULATION VARIANCE	SAMPLE MEAN	SAMPLE VARIANCE	CALCULATED f	F(table) " =0.1"	STD DEV Sd	CALCULATED t	T(table) "=0.4"	REMARKS
20	12	0.00					34.27	13.25						
20	1	35.69												
20	1	31.81												
20	1	26.45												
20	1	29.34												
20	1	31.81												
20	1	39.13												
20	1	34.47												
20	1	35.69												
20	1	35.69												
20	1	35.69												
20	1	36.94		34.08	3.65	13.35	33.88	13.47	1.02	2.25	1.53	-0.25	0.86	JOIN
20	1	33.72	1900											
20	1	38.12	1900											
20	1	34.71	1900											
20	1	32.34	1900	34.18	3.53	12.48	34.72	6.07	2.20	5.18	1.91	-0.33	0.86	JOIN
20	1	35.99	2700											
20	1	32.58	2700											
20	1	36.11	2700											
20	1	39.06	2700	34.41	3.45	11.91	35.94	7.02	1.78	5,18	1.85	-0.95	0.85	JOIN
20	1	28.82	2240											
20	1	38.11	2240											
20	1	32.42	2240											
20	1	33.38	2240											
20	1	34.32	2240											
20	1	30.00	2240											
20	1	35.62	2240											
20	1	36.41	2240											
20	1	30.92	2240											
20	1	34.24	2240	34.25	3.34	11.14	33.44	8.56	1.39	3.17	1.21	0.79	0.85	JOIN
20	1	25.56	1332											
20	1	26.88	1336											
20	1	27.12	1341											
20	1	22.48	1342											
20	1	26.97	1343											
20	1	32.72	1349											
20	1	37.77	1350											
20	1	49.26	1350											
20	1	47.33	1355				32.90	95.86	8.61	1.83				NO JOIN
20	1	13.43												

TABLE A-2. STATISTICAL ANALYSIS TABLE FOR 60 DEGREE RADIAL (CONTINUED)

DISTANCE FEET	ROUNDS FIRED	SAMPLE PRESSURE	PROJECTILE WEIGHT	POPULATION MEAN	POPULATION DEVIATION	POPULATION VARIANCE	SAMPLE MEAN	SAMPLE VARIANCE	CALCULATED f	F(table) = 0.1	STD DEV Sd	CALCULATED t	T(table) =0.4	REMARKS
31	1	7.02												
37	1	9.16												
41	1	6.88												
41	1	6.85		6.87	0.02									
44	1	5.29												
44	1	5.07												
50	12						8.32	0.29						
50	1	8.41	2700											
50	1	7.99	2700											
50	1	8.15	2700											
50	1	8.25	2700	8.29	0.49	0.24	8.20	0.03	9.39	5.23	0.28	0.43	0.07	JOIN
50	1	8.03	1900											
50	1	8.42	1900											
50	1	9.18	1900	8.61	0.50	0.25	8.54	0.34	1.45	2.49	0.31	-0.81	0.06	JOIN
50	1	8.86	2240											
50	1	8.70	2240											
50	1	8.92	2240											
50	1	8.78	2240											
50	1	8.00	2240											
50	1	8.60	2240	8.47	0.47	0.22	8.63	0.11	2.28	2.42	0.22	-0.99	0.06	JOIN
50	1	9.09	1332											
50	1	8.71	1336											
50	1	8.81	1341											
50	1	9.75	1342											
50	1	9.36	1343											
50	1	9.20	1344											
50	1	9.36	1349											
50	1	8.07	1350											
50	1	8.29	1350											
50	1	8.13	1355											
50	1	9.37	1355	8.65	0.50	0.25	8.92	0.32	1.46	1.88	0.18	-2.53	0.05	NO JOIN

DISTANCE FEET	ROUNDS FIRED	SAMPLE PRESSURE	PROJECTILE WEIGHT	POPULATION MEAN	POPULATION DEVIATION	POPULATION VARIENCE	SAMPLE MEAN	SAMPLE VARIANCE	CALCULATED f	F(table) =.1	STD DEV Sd	CALCULATED t	T(table) =0.4	REMARKS
127	1	2.08												
128	1	1.90												
129	1	1.96												
134	1	1.94												
135	1	1.65												
135	1	1.79		1.72	0.18									
136	1	1.95												
136	1	1.98		1.97	0.02									
139	1	1.73												
141	1	2.05												
149	1	1.52												
161	1	1.73												
161	1	1.83												
161	1	1.79												
161	1	1.65												
161	1	1.58												
161	1	1.59		1.69	0.18									
165	1	1.47												
200	12	0.00		1.69	0.18									

TABLE A-3. STATISTICAL ANALYSIS TABLE FOR 75 DEGREE RADIAL

DISTANCE FEET	ROUNDS FIRED	SAMPLE PRESSURE	PROJECTILE WEIGHT	POPULATION MEAN	POPULATION DEVIATION	POPULATION VARIANCE	SAMPLE MEAN	SAMPLE VARIANCE	CALCULATED f	F(table) =.1	STD DEV Sd	CALCULATED t	T(table) =±0.4°	REMARKS
30	1	9.35	2700											
30	1	11.72	2700											
30	1	9.51	2700											
30	1	11.29	2700				10.47	1.47						
30	1	11.50	2240											
30	1	11.38	2240											
30	1	10.14	2240											
30	1	9.68	2240											
30	1	9.55	2240											
30	1	10.79	2240											
30	1	11.19	2240											
30	1	11.40	2240											
30	1	11.38	2240	10.68	0.92	0.85	10.78	0.62	2.39	2.92	0.55	-0.56	0.86	JOIN
30	1	10.29	1900											
30	1	10.78	1900											
30	1	9.79	1900	10.55	0.75	0.56	10.29	0.25	3.46	9.41	0.58	0.79	0.87	JOIN
30	1	9.83												
30	1	11.28												
30	1	10.78												
30	1	11.13		10.64	0.79	0.53	10.76	0.42	1.33	2.23	0.37	-0.59	0.86	JOIN
30	1	14.87	1332											
30	1	16.56	1336											
30	1	17.53	1342											
30	1	17.68	1343											
30	1	17.22	1346	12.05	0.59	0.54	17.81	0.46	1.22	3.87	0.38	-17.19	0.86	NO JOIN
31	1	16.21												
32	1	12.81												
32	1	8.34		10.18	2.60									
33	1	10.29												
38	1	5.78												
39	1	7.65												
40	1	4.87												
47	1	5.38												
48	1	4.83												
48	1	5.55												
48	1	4.86												
48	1	4.99												
48	1	4.51		4.95	0.38									
49	1	4.65												
49	1	5.13		4.89	0.34									

TABLE A-3. STATISTICAL ANALYSIS TABLE FOR 75 DEGREE RADIAL (CONTINUED)

DISTANCE FEET	ROUNDS FIRED	SAMPLE PRESSURE	PROJECTILE WEIGHT	POPULATION MEAN	POPULATION DEVIATION	POPULATION VARIANCE	SAMPLE MEAN	SAMPLE VARIANCE	CALCULATED f	F(table) =.1	STD DEV Sd	CALCULATED t	T(table) =0.4	REMARKS
73	1	5.98												
73	1	6.56												
73	1	6.17		6.15	0.30									
75	1	2.80												
76	1	3.09												
77	1	3.49												
80	1	4.49												
81	1	3.41												
81	1	3.29		3.35	0.08									
82	1	3.69												
85	1	2.10												
85	1	2.50												
85	1	3.07												
85	1	3.00		2.67	0.46									
86	1	1.93												
86	1	3.20		2.57	0.90									
87	1	3.41												
88	1	2.50												
88	1	2.87		2.69	0.26									
89	1	3.41												
89	1	2.54		2.98	0.62									
90	1	2.65												
94	1	2.72												
94	1	1.85		2.29	0.62									
95	1	2.36												
98	1	2.57												
102	1	3.08												
105	1	2.18												
105	1	1.61		1.86	0.35									
106	1	2.54												
109	1	1.77												
113	1	2.06												
122	1	1.77												
122	1	1.61		1.69	0.11									
127	1	1.61												
127	1	1.67		1.64	0.04									
128	1	1.73												
131	1	1.69												
134	1	1.71												
147	1	1.88												
150	1	2.01												
150	1	1.98												
150	1	1.87												

TABLE B-1. STATISTICAL DATA SUMMARY FOR 16-IN. GUN BLAST ANALYSIS

DISTANCE FEET	ROUNDS FIRED	SAMPLE PRESSURE	PROJECTILE WEIGHT	POPULATION MEAN	POPULATION DEVIATION	POPULATION VARIANCE	SAMPLE MEAN	SAMPLE VARIANCE	CALCULATED F	F(table) α =0.1	STD DEV Sd	CALCULATED t	T(table) α=0.4	REMARKS
20	9	15.45					15.45	1.59						
20	1	15.14	1900											
20	1	17.71	1900											
20	1	16.74	1900											
20	1	12.41	1900	15.47	1.62	2.62	15.50	5.37	3.38	2.92	0.97	-0.05	0.87	JOIN
20	1	15.57	2700											
20	1	16.99	2700											
20	1	16.68	2700											
20	1	17.52	2700	15.78	1.49	2.23	16.69	0.68	3.86	5.22	0.85	-1.43	0.87	NO JOIN
20	1	17.74	2240											
20	1	15.10	2240											
20	1	17.80	2240											
20	1	18.25	2240											
20	1	17.41	2240											
20	1	20.29	2240											
20	1	15.97	2240											
20	1	18.02	2240											
20	1	15.78	2240											
20	1	15.33	2240	16.89	1.70	2.89	16.97	3.62	1.62	5.24	1.01	-0.28	0.87	JOIN
20	1	13.55	1355											2240 & 2700
20	1	15.38	1355											
20	1	14.72	1350											
20	1	13.77	1350											
20	1	14.32	1349											
20	1	15.08	1346											
20	1	15.87	1343											
20	1	14.59	1342											
20	1	14.59	1341											
20	1	14.86	1336											
20	1	15.63	1332			1.66	14.76	0.52	5.05	2.28	0.53	1.33	0.86	NO JOIN
27	1	12.49												

TABLE B-1. STATISTICAL DATA SUMMARY FOR 16-IN. GUN BLAST ANALYSIS (CONTINUED)

DISTANCE FEET	ROUNDS FIRED	SAMPLE PRESSURE	PROJECTILE WEIGHT	POPULATION MEAN	POPULATION DEVIATION	POPULATION VARIANCE	SAMPLE MEAN	SAMPLE VARIANCE	CALCULATED f	F(table) α =0.1%	STD DEV Sd	CALCULATED t	T(table) α=0.4%	REMARKS
46	1	5.73												
50	12			5.22	0.35	0.12	5.05	0.14						
50	1	5.26	2700											
50	1	5.25	2700											
50	1	5.57	2700											
50	1	5.41	2700			0.12	5.37	0.02	5.91	5.22	0.20	-1.60	0.87	NO JOIN
50	1	4.17	1900											
50	1	5.45	1900											
50	1	5.36	1900											
50	1	5.26	1900	5.46	0.31	0.10	5.56	0.17	7.02	2.73	0.22	0.87	0.90	JOIN
50	1	5.62	2240											1900 & 2700
50	1	5.95	2240											
50	1	6.73	2240											
50	1	5.86	2240											
50	1	6.13	2240											
50	1	7.00	2240											
50	1	6.27	2240	5.89	0.61	0.19	6.32	0.29	2.91	2.78	0.22	-3.92	0.86	NOT JOINED
50	1	7.02	2240											
50	1	5.40	1332											
50	1	5.66	1336											
50	1	5.27	1341											
50	1	5.29	1342											
50	1	6.02	1343											
50	1	5.99	1346											
50	1	5.30	1349											
50	1	5.64	1350											
50	1	6.86	1350											
50	1	5.51	1355											
50	1	5.63	1355			0.12	5.47	0.09	1.63	2.25	0.14	-2.93	0.86	NO JOIN
51	1	4.22												
54	1	3.85												
56	1	3.95		3.90	0.07									
66	1	2.55												
66	1	2.39		2.47	0.11									
73	1	5.14												
73	1	5.84		5.49	0.49									
75	1	5.06												
75	1	5.32		5.19	0.18									
77	1	4.13												
79	1	1.93												
79	1	3.44	2.80	1.22										
80	1	2.52												
80	1	2.38												

TABLE B-1. STATISTICAL DATA SUMMARY FOR 16-IN. GUN BLAST ANALYSIS (CONTINUED)

ANGLE	DISTANCE FEET	PLOT DISTANCE	ROUNDS FIRED	MEAN PRESSURE	STD DEVIATION	% DEVIATION	
15	50	50.00	8	11.34	1.42	12.52	
15	80	63.64	11	9.54	0.77	8.07	
15	120	95.46	12	6.99	0.30	6.01	
ANGLE	DISTANCE FEET	PLOT DISTANCE	ROUNDS FIRED	MEAN PRESSURE	STD DEVIATION	% DEVIATION	
30	50	50.00	13	10.25	0.77	7.47%	
30	80	63.64	13	9.73	0.48	4.92%	
30	120	95.46	12	5.22	0.20	3.84%	
30	200	159.11	13	2.42	0.12	5.14%	
ANGLE	DISTANCE FEET	PLOT DISTANCE	ROUNDS FIRED	MEAN PRESSURE	STD DEVIATION	% DEVIATION	PROJECTILE WEIGHT
45	20	20.00	1	34.23			
45	30	30.00	18	17.57	1.38	7.88%	
45	30	30.00	10	21.19	2.51	11.86%	2240
45	30	30.00	11	23.04	1.09	4.73%	1350
45	50	50.00	13	8.64	0.62	7.18%	
45	70	70.00	4	3.00	0.68	22.61%	
45	71	71.00	3	4.53	1.43	31.57%	
45	72	72.00	1	3.56			
45	73	73.00	1	3.08			
45	80	63.64	28	8.93	0.99	11.08%	
45	80	63.64	11	7.97	0.38	4.73%	1350
45	83	66.03	1	2.53			
45	93	73.98	1	3.20			
45	94	74.78	1	2.40			
45	120	95.46	13	6.90	0.41	5.97%	
45	123	97.85	1	2.13			
45	133	105.81	1	2.55			
45	144	114.56	1	2.80			
45	200	159.11	12	1.92	0.10	5.46%	

TABLE A-4. STATISTICAL ANALYSIS TABLE FOR 90 DEGREE RADIAL

ANGLE	DISTANCE FEET	PLOT DISTANCE	ROUNDS FIRED	MEAN PRESSURE	STD DEVIATION	% DEVIATION	PROJECTILE WEIGHT
75	20	20.00	12	22.84	1.79	7.84%	ORIGINAL
75	20	20.00	9	24.93	3.06	12.27%	
75	20	20.00	18	17.61	1.59	9.03%	19/27/2240
75	20	20.00	11	19.51	2.82	14.45%	1350
75	21	21.00	1	16.56	0.00	0.00%	
75	23	23.00	1	12.95	0.00	0.00%	
75	26	26.00	1	10.64	0.00	0.00%	
75	29	29.00	1	5.66	0.00	0.00%	
75	30	30.00	20	10.64	0.79	7.42%	
75	30	30.00	5	17.01	0.68	4.00%	1350
75	31	31.00	1	16.21	0.00	0.00%	
75	32	32.00	2	10.18	2.60	25.50%	
75	33	33.00	1	10.29	0.00	0.00%	
75	38	38.00	1	5.70	0.00	0.00%	
75	39	39.00	1	7.03	0.00	0.00%	
75	40	40.00	1	4.87	0.00	0.00%	
75	47	47.00	1	5.38	0.00	0.00%	
75	48	48.00	5	4.95	0.38	7.68%	
75	49	49.00	2	4.89	0.34	6.94%	
75	50	50.00	27	7.02	0.65	9.26%	
75	50	50.00	10	7.72	0.87	11.27%	2240
75	50	50.00	7	6.93	0.94	13.56%	1350
75	52	52.00	1	3.62		0.00%	
75	53	53.00	1	3.89		0.00%	
75	56	56.00	1	6.65		0.00%	
75	57	57.00	1	4.43		0.00%	
75	67	67.00	1	3.29		0.00%	
75	70	70.00	3	3.31	1.34	40.42%	
75	73	73.00	4	6.15	0.30	4.88%	
75	76	76.00	1	3.09			
75	77	77.00	1	3.49			
75	80	80.00	1	4.49			
75	81	81.00	2	3.35	0.08	2.53%	
75	82	82.00	1	3.69			
75	85	85.00	3	2.67	0.46	17.08%	
75	86	86.00	2	2.57	0.90	35.01%	
75	87	87.00	1	3.41			
75	88	88.00	2	2.69	0.26	9.76%	
75	89	89.00	2	2.98	0.62	20.68%	
75	90	90.00	1	2.65			
75	94	94.00	2	2.29	0.62	26.92%	
75	95	95.00	1	2.36			
75	98	98.00	1	2.57			
75	102	102.00	1	3.08			
75	105	105.00	2	1.86	0.35	18.68%	
75	106	106.00	1	2.54			
75	109	109.00	1	1.77			
75	113	113.00	1	2.04			
75	122	122.00	2	1.69	0.11	6.69%	
75	127	127.00	2	1.64	0.04	2.59%	
75	128	128.00	1	1.73			
75	131	131.00	1	1.69			
75	134	134.00	1	1.71			
75	147	147.00	1	1.80			
75	150	119.06	7	1.86	0.10	5.25%	
75	151	151.00	1	1.72			
75	153	153.00	1	1.63			
75	155	155.00	1	1.70			
75	159	159.00	2	1.49	0.01	0.48%	
75	162	162.00	1	1.85			
75	172	172.00	1	1.77			
75	182	182.00	1	1.65			
75	185	146.83	12	1.85	0.09	4.86%	

TABLE A-4. STATISTICAL ANALYSIS TABLE FOR 90 DEGREE RADIAL (CONTINUED)

ANGLE	DISTANCE FEET	PLOT DISTANCE	ROUNDS FIRED	MEAN PRESSURE	STD DEVIATION	% DEVIATION	
105	20	20.00	12	10.37	0.76	7.33%	
105	30	30.00	12	8.03	0.85	10.59%	
105	49	49.00	1	3.25			
105	50	50.00	10	3.94	0.45	11.42%	
105	55	55.00	1	2.93			
105	59	59.00	1	2.48			
105	60	60.00	1	2.91			
105	68	68.00	1	1.72			
105	69	69.00	1	2.09			
105	87	87.00	1	2.09			
105	95	95.00	1	2.29			
105	96	96.00	1	1.69			
105	117	117.00	1	0.81			
105	122	122.00	1	1.11			
105	126	126.00	3	0.97	0.03	2.97%	
105	131	131.00	3	0.97	0.03	2.97%	

ANGLE	DISTANCE FEET	PLOT DISTANCE	ROUNDS FIRED	MEAN PRESSURE	STD DEVIATION	% DEVIATION	
120	20	20.00	11	6.54	0.47	7.19%	
120	30	30.00	12	4.72	0.70	14.83%	
120	41	41.00	1	2.82			
120	43	43.00	1	2.18			
120	46	46.00	1	2.39			
120	50	50.00	13	2.61	0.24	9.34%	
120	59	59.00	1	1.78			
120	110	110.00	1	0.89			
120	119	119.00	3	0.98	0.06	5.87%	
120	154	154.00	3	1.77	0.10	5.65%	

ANGLE	DISTANCE FEET	PLOT DISTANCE	ROUNDS FIRED	MEAN PRESSURE	STD DEVIATION	% DEVIATION	
135	25	25.00	1	1.72			
135	29	29.00	1	2.22			
135	30	30.00	1	2.69			
135	32	32.00	1	2.71			
135	38	38.00	1	2.43			
135	41	41.00	1	2.47			
135	77	77.00	1	1.12			

ANGLE	DISTANCE FEET	PLOT DISTANCE	ROUNDS FIRED	MEAN PRESSURE	STD DEVIATION	% DEVIATION	
150	20	20.00	8	3.52	0.43	12.22%	
150	25	25.00	1	2.18			
150	30	30.00	11	1.93	0.25	12.90%	
150	50	50.00	11	1.40	0.12	8.57%	
152	23	22.74	1	1.89			
157	20	20.43	1	1.02			
160	20	19.56	1	1.18			

TABLE C-2. 16-IN. GUN BLAST REGRESSION
45 DEGREE RADIAL

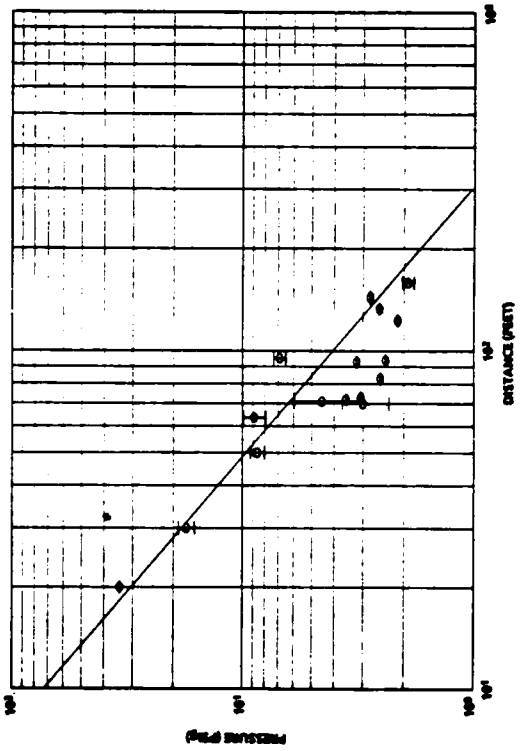

TABLE C-4. 16-IN. GUN BLAST REGRESSION
105 DEGREE RADIAL

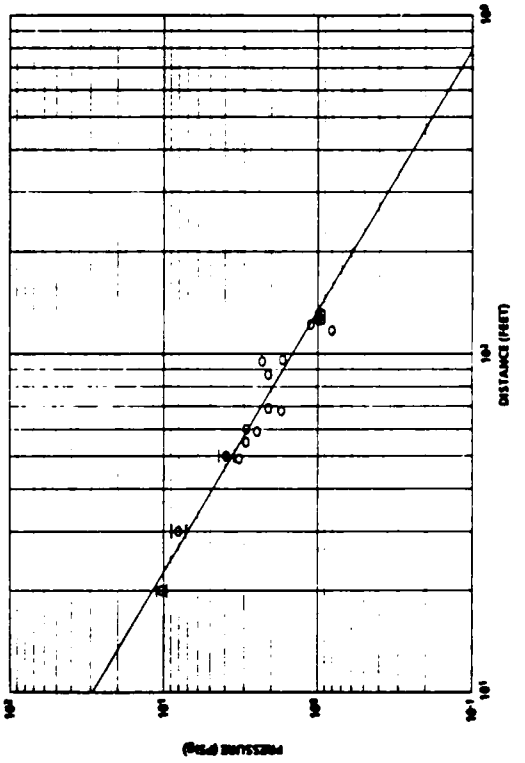

TABLE C-1. 16-IN. GUN BLAST REGRESSION
15 DEGREE RADIAL

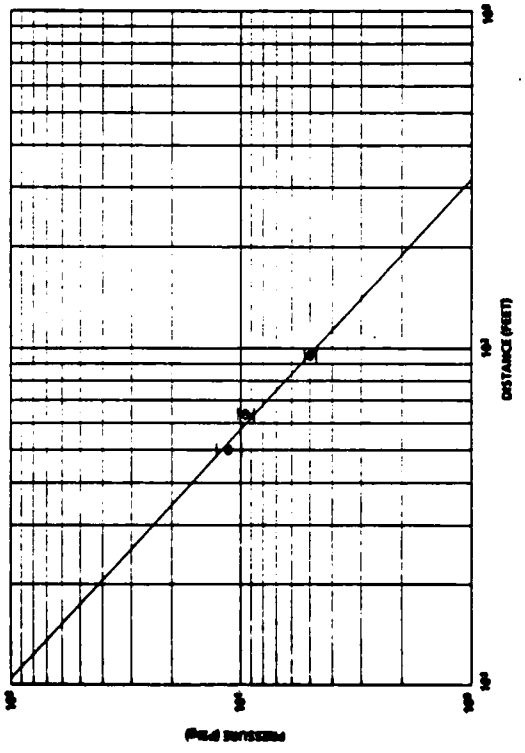

TABLE C-3. 16-IN. GUN BLAST REGRESSION
75 DEGREE RADIAL

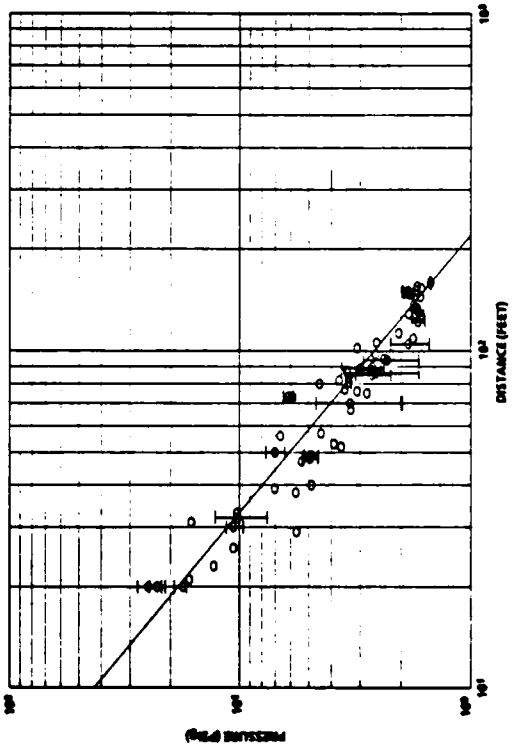

TABLE C-5. 16-IN. GUN BLAST REGRESSION
135 DEGREE RADIAL

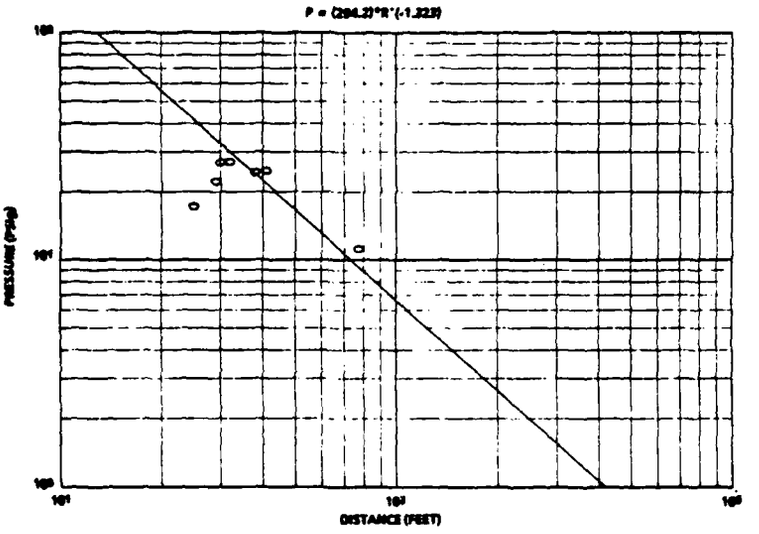

ZEPP

TITLE: A VARIABLE DISCHARGE COEFFICIENT FUNCTION FOR HEAVY ARTILLERY GUN MOUNT ANALYSIS AND DESIGN

WILLIAM T. ZEPP
U.S. ARMY ARMAMENT RESEARCH, DEVELOPMENT, AND ENGINEERING CENTER
FIRE SUPPORT ARMAMENTS CENTER
PICATINNY ARSENAL, NJ 07806-5000

ABSTRACT

Requirements for ever greater range and projectile lethality continue unabated for cannon artillery. The new projectiles, charges, and cannons proposed to meet these requirements must be mated to a weapon system through a suitable gun mount. This gun mount may be an existing model, an enhanced version of an existing model, or a newly developed model. System requirements place increasing limits and restrictions on size, weight, recoil distance, RAM, etc., on it. Determining the ability of a given gun mount, or development of a compatible improved or new gun mount, within these limits and restrictions of handling a new combination of projectile/cannon/charge without trial firings, requires numerical computer models.

Development of computer models began in the mid-1970s with a code modeling the M127 gun mount. It was used to develop an improved version, the M178 gun mount, capable of firing the M203 charge (extended range) and the M712 (increased lethality). The code accurately predicted the performance of the weapon system, but only when firing maximum impulse projectile/charge combinations and in the short recoil mode (above 800 mils quadrant elevation, QE). At lower charges and QE's, the accuracy fell drastically to a level of dubious use. The code utilized constant discharge coefficients throughout the recoil cycle.

At the same time, a code modeling the M158 gun mount to support the upgunning of the M110 8-inch self-propelled howitzer with a new longer cannon, top charge, and projectiles was developed. The new gun mount was the M174. This code, as with the code for the M127/M178 gun mounts, was usable for modeling maximum impulse/high QE combinations only. Again, constant discharge coefficients were used throughout.

In the late 1970s, the M178 and M174 codes were improved in their numerical routines and recoil orifice system modeling technique. The improvements increased the accuracy of the models but still only for the high impulse/high QE situations. They still utilized constant discharge coefficients.

In 1983, a requirement for extended range, accuracy, and lethality was established. This required a new cannon/charge/projectile/gun mount system be developed. A code to support the new gun mount (XM183) was developed. It again improved on the M178 and M174 codes in numerical speed, accuracy, and control rod fabrication support, but again only for high impulse/QE situations. As before, it utilized constant discharge coefficients.

ZEPP

During the 1980s, attempts were made to develop variable discharge coefficient functions expanding modeling capabilities to low QE's and lower charges. The attempts were limited in scope and failed to bear fruit. In 1989, a variable discharge coefficient function for the Schneider type recoil mechanism was formulated improving the accuracy of an improved version of the XM183 gun mount code at impulse levels and QE's that are not near the system maximums.

The function uses a series of fluid parameters at the start of each time step as inputs to calculate a "constant" discharge coefficient for that time step for each of the orifices in the hydraulic recoil brake. As the numerical integration of the model progresses, the discharge coefficients are discreetly varied throughout the recoil cycle. This variation allows the simulation of impulse levels less than the maximum and for QE's ranging down from the howitzer/mortar realm to the direct fire realm with meaningful accuracy.

Efforts are underway to adopt the function, modify the function, or develop a similar function for the Filloux type recoil brakes used in the M178 and M182 gun mounts. This improvement in modeling the M178/M182 gun mount will support the continued life of the M109 family of weapon systems through the 1990s as new 155-mm cargo rounds are developed.

This paper was not available for printing in this publication.

SESSION II:

EXPERIMENTAL WORK

BARKER, BULMAN, CHAMBERS.

TITLE: AN ACCELEROMETER TECHNIQUE FOR THE MEASUREMENT OF GUN MUZZLE MOTION

BARKER G
BULMAN D N
CHAMBERS A E

THE ROYAL MILITARY COLLEGE OF SCIENCE
SCHOOL OF MECHANICAL, MATERIALS AND CIVIL ENGINEERING
LAND SYSTEMS GROUP
SHRIVENHAM, SWINDON, SN7 7HU, ENGLAND.

ABSTRACT:

A technique for measuring the motion of a 120mm gun barrel during the firing cycle has been developed at RMCS. Accelerometers, mounted on specially designed elastomeric mounts, were fitted to the muzzle. The acceleration signals during the firing cycle were captured on a high speed analogue to digitial converter. These signals were then intergrated to give the velocity and displacement history of the muzzle.

This technique has been used on a number of accuracy firing trials. The results showed that small changes in shot design can produce recognisable changes in muzzle motion. Also when using tweleve round serials, there was some correlation between shot dispersion and the variations in muzzle displacement. Differences between barrels could also be observed.

Comparision with theoretical predictions using the gun dynamics simulation package, SIMBAD, have been shown to be good. Furthermore, although muzzle motion is shown not to be an indication of the final fall of shot, the theoretical analysis, has given shot launch conditions which go a long way to the final predication of gun accuracy.

This paper describes in detail the measurement technique which has been develeoped, and the factors which have influenced measuring accuracy and consistency. It then presents a number of the results showing muzzle transvers motion from shot initiation to shot exit. Some of the theoretical predictions are also shown for comparison.

BIOGRAPHY : BARKER G

PRESENT ASSIGNMENT : Research scientist, RMCS investigating the dynamics of gun barrel vibration and evaluating different measuring techniques for muzzle motion.

PAST EXPERIENCE : The study of in-bore yaw using the RMCS air powered gun, and the analysis of a semi-automatic breech opening mechanism.

DEGREES HELD : 2:1 Honours BSc.

AN ACCELEROMETER TECHNIQUE FOR THE MEASUREMENT OF GUN MUZZLE MOTION

G Barker, D N Bulman, A E Chambers

The Royal Military College of Science
School of Mechanical, Materials and Civil Engineering
Land Systems Goup
Shrivenham, Swindon, SN6 8LA, England.

1.0 Introduction

In modern tank warfare the requirement for greater range and improved accuracy has resulted in the need to fully understand and quantify the critical gun system parameters that affect gun accuracy and consistency. The performance of a gun system can now be predicted using advanced mathematical models such as SIMBAD [1]. In order to help validate such models experimental data is required from full size firings. One of the most important parameters to be measured is the motion of the gun muzzle during the firing cycle. This paper describes the development of a technique which enabled the motion of a 120mm tank gun to be measured easily and reliably. The results obtained were used to assist in the validation of results from the gun dynamics simulation package SIMBAD.

2.0 The problems of measuring muzzle displacement

The harsh environment present around the muzzle of the gun during the firing cycle makes it very difficult to measure the displacement of the gun barrel. A number of techniques have been tried in the past but none have proved to be reliable or easy to operate for a large number of firings. Optical and other techniques have generally required the equipment to be re-aligned carefully between each firing . Proximity probes and rings have been tried but problems have been found in reliably moving the probes out of

the way before the barrel strikes them on run out. It is also possible that the passage of the round past the tip of the probe, may cause an error in the measurement.

In the late seventies an alternative technique was developed using accelerometers mounted onto the barrel near to the muzzle by Bulman [2]. When accelerometers were mounted directly on the barrel, the level of acceleration measured were far greater than expected. Accelerometers which could withstand 10,000g were destroyed after one firing. This was later found to be due to very high frequency stress waves which travel down the barrel in front of the shot. When accelerometers which could withstand these high acceleration levels were used, the signal due to the main barrel motion could not be distinguished from the noise created by the material stress waves. Attempts were made to separate the required signal by filtering either electrically or digitally but little success was achieved. The problem was overcome by mounting the accelerometers on elastomeric mounts, to effectively modify the frequency response characteristics of the transducer. These filtered out the high frequency, high acceleration, signals and allowed much more sensitive accelerometers to be used without damage. However, problems were still found when the signal was integrated to determine the velocity and displacement. This was mainly caused by zero errors producing drift and the requirement for high digitisation accuracy. These problems have been solved and a reliable system has been developed which is in regular use on trials.

3.0 Development of experimental technique

The technique depends upon the mechanical filtering provided by the elastomeric mount, which protects the accelerometer from the high frequency, high accelerations. The earlier experiments and the mathematical simulations showed that the frequency of the whole barrel motion of a 120mm gun is normally less than 1KHz if the stress waves are ignored. The level of acceleration seen at the muzzle should also be no greater than 10,000 m/s^2. The mechanical filter must therefore have a flat frequency response up to at least 1KHz and not give too high a gain at its resonant frequency. The accelerometer requires a range up to 1000g, and a considerable overload capability is desirable.

Kyowa AS-1000A accelerometers were selected, with a measuring range of $\pm$ 1000g and a 300% overload capability. They are of the strain gauge type, with a frequency response from 0 to 7.5 KHz. The full specification of these accelerometers is given in Appendix 1.

The design of the accelerometer mount is shown in Fig 1, the accelerometer is clamped between two pieces of polymer rubber. The type of rubber, the thickness and the clamping force was determined from a series of experiments. The accelerometer had to be clamped by the mount sufficently to prevent it sliding or rotating under the action of recoil, and the clamping preload had an effect on the frequency response of the mounted transducer. The accelerometers were placed very close to the muzzle of the barrel, and therefore a small shield was attached to the front face of the mounting to protect the accelerometer from the effects of the charge gas. Finally the mount was completed by adding an extension to support the accelerometer cable

so that no strain would be imposed on the accelerometer from its cable, either during firing, or from mishandling.

The accelerometer mount needed to be easily attached to the barrel, without the barrel having to be machined or altered in any way. This was achieved by placing a thin steel band around the muzzle and holding it in place with a clamping bolt. The ring is shown in fig 2. Mounting blocks were welded to the ring to allow accelerometers to be placed at the required positions around the barrel. The ring design was such that the centre of gravity of the final assembly was on the axes of the barrel. This ensured that it would not add any out of balance moment during recoil.

Strain gauges were bonded to the ring so that the barrel expansion could be detected and used to indicate the time of shot exit. The attachment of the strain gauges to the ring was improved over a number of trials, and the current method, which uses a combination of a thin layer of epoxy and a small metal blast shield, has now withstood many serials without damage.

4.0 Data capture and analysis

The accuracy to which the acceleration signal could be captured was very important. Studies into the differences between digitising at 10,12, 14 and 16 Bit accuracy had been shown by Bulman and Storey [3], that digitising with less than 12 bits would give significant rounding errors during the integration to obtain displacement.

A "CIL Electronics" analogue to digital converter which digitises to an accuracy of 16 Bits and at a rate of 50 KHz was purchased. This instrument can have up to 15 separate channels which will each sample at the same rate and at the same time, thus allowing fifteen channels of data to be captured

simultaneously. Each channel has 64K of memory and so 32K points of data can be stored in real time. The full specifications are given in appendix 1.

The CIL instrument was controlled by a Hewlett Packard 9816 Computer using a program written at RMCS and using the IEEE 488 interface. The program initially arms the A to D and waits for a trigger pulse to initiate data capture. The firing pulse used to initiate the charge is used for this purpose. Once the data has been captured, it is transfered to the computer for processing. The data is displayed on a simple set of axes and the desired section for analysis is selected manually and is stored onto disc.

The data can be analysed a channel at a time, and the shot exit pulse is used as a datum to align the records as required. This makes it easier to compare the results from round to round.

An error correction for any zero drift is made as follows. The raw data of acceleration for the desired time interval is displayed on a calibrated set of axes, and the integral of this graph is calculated using the trapezoidal technique. This is also displayed on the screen. Any velocity drift prior to shot start is then used to calculate a constant error correction to the acceleration signal. The corrected acceleration data is then integrated twice to give the velocity and displacement. The program is arranged so that all the produced data can be plotted as required and the necessary comparisons made.

The instrumentation system allows (depending on the rate of fire) all of the graphs to be plotted out between firings. This is very useful as the trends can be seen as the trial progresses and any failure of the transducers or cables can be corrected before the next firing.

5.0 Experimental Results

The system has been used on a number of trials and has allowed results to be taken from many firings of APFSDS type rounds in different barrels and mountings. The majority of these firings have been of experimental rounds and so the results are classified. However some typical results are given in Appendix 2 for both Vertical and Horizontal muzzle displacement.

6.0 Discussion of Experimental Results

From theoretical analysis it was not expected that barrel motion could be directly related to the fall of shot, and this was proved in practise. It was considered more important to use the data for comparison with theoretical models such as SIMBAD, and to see if any correlation could be obtained between muzzle motion and shot dispersion.

It has been found on more than one trial that a relationship exists between the standard deviation of the displacement of the muzzle at shot exit and the standard deviation of the fall of shot. Recent trials, in which different designs of sabot were fired have shown that the serial with the smallest standard deviation of muzzle displacement also gave the smallest standard deviation of the fall of shot.

Of particular interest were the effects that different shot designs had on muzzle motion. A number of different shot designs were tested, and each has shown a particular characteristic of muzzle displacement. Small changes to the design have changed the muzzle motion. This has been quantified for serials of 12 rounds by taking the mean and standard deviation of muzzle displacement at shot exit.

The theoretical modelling for each type of shot has also given similar results, although the variations within a serial has not been attempted because of the lack of data.

The results have also indicated occasion to occasion variations which were similarly related to the fall of shot.

7.0 Comparison of experimental and Theoretical Results

A considerable number of theoretical simulations have been produced using the well proven gun dynamics simulation program SIMBAD. This is a commercial code simulating barrel, shot and mounting dynamics.

Each barrel was simulated using actual measured data. All of the additional masses were included in the data, including the breech, fume extractor and muzzle reference sight. Any offsets were also added.

The cradle was simulated in both rigid and flexible form, although it was concluded that the flexure was negligible in this case and the rigid cradle was sufficent. Bearing clearance, elevation gear stiffness and backlash was also included. The buffer and recuperator characteristics were modelled, along with the barrel expansion on the bearings.

The shots were modelled in both rigid and flexible form, contacting the barrel at the rear band and front bourrelet. The required band stiffness and damping were obtained from experiments, by Barker and Chambers [4]. Clearance around the front bourellet was also simulated. The barrel was rifled, and a slipping band simulated for the rigid shot. In the case of the flexible shot a smooth bore case was simulated.

An internal ballistics model was used to obtain the pressure at the breech face and the front of the chamber. The derived shot acceleration was applied directly to the shot.

8.0 Conclusion

A system has been developed at RMCS for measuring the muzzle displacement of gun barrels during the firing cycle. It has proved to be robust, reliable and give good round to round repeatability. The results obtained agreed well with those predicted by the mathematical model SIMBAD. The variation between rounds of muzzle displacement at shot exit provides a good indicator of the shot performance.

9.0 Acknowledgements

The authors would like to acknowledge the support given to this research by Royal Ordnance UK.

10.0 References

1 SIMBAD (A computer program)
A computer program for the simulation of Gun System Dynamics.
Danby Engineering (Cirencester) Ltd, Eastleach, Cirencester, GL7 3NQ, UK
Copyright 1985-90.

2 BULMAN D.N.
The use of accelerometers for the measurement of gun barrel transverse motion. Preliminary report
Test note E/67/1/69/01 RMCS October 1980

3 BULMAN D.N. and STOREY S.F.
An experimental investigation to compare various techniques which are used in measuring the motion of a gun barrel during firing.
Tech note AM 107 RMCS October 1980

4 BARKER G. and CHAMBERS A.E.
An experimental technique for measurement of shot parameters used in gun dynamics modelling.
RMCS Land systems Group report No SMMCE/LS/104 March 1990
for presentation at the Sixth U.S. Army Symposium on Gun Dynamics, Tamiment, Pennsylvania, May 1990.

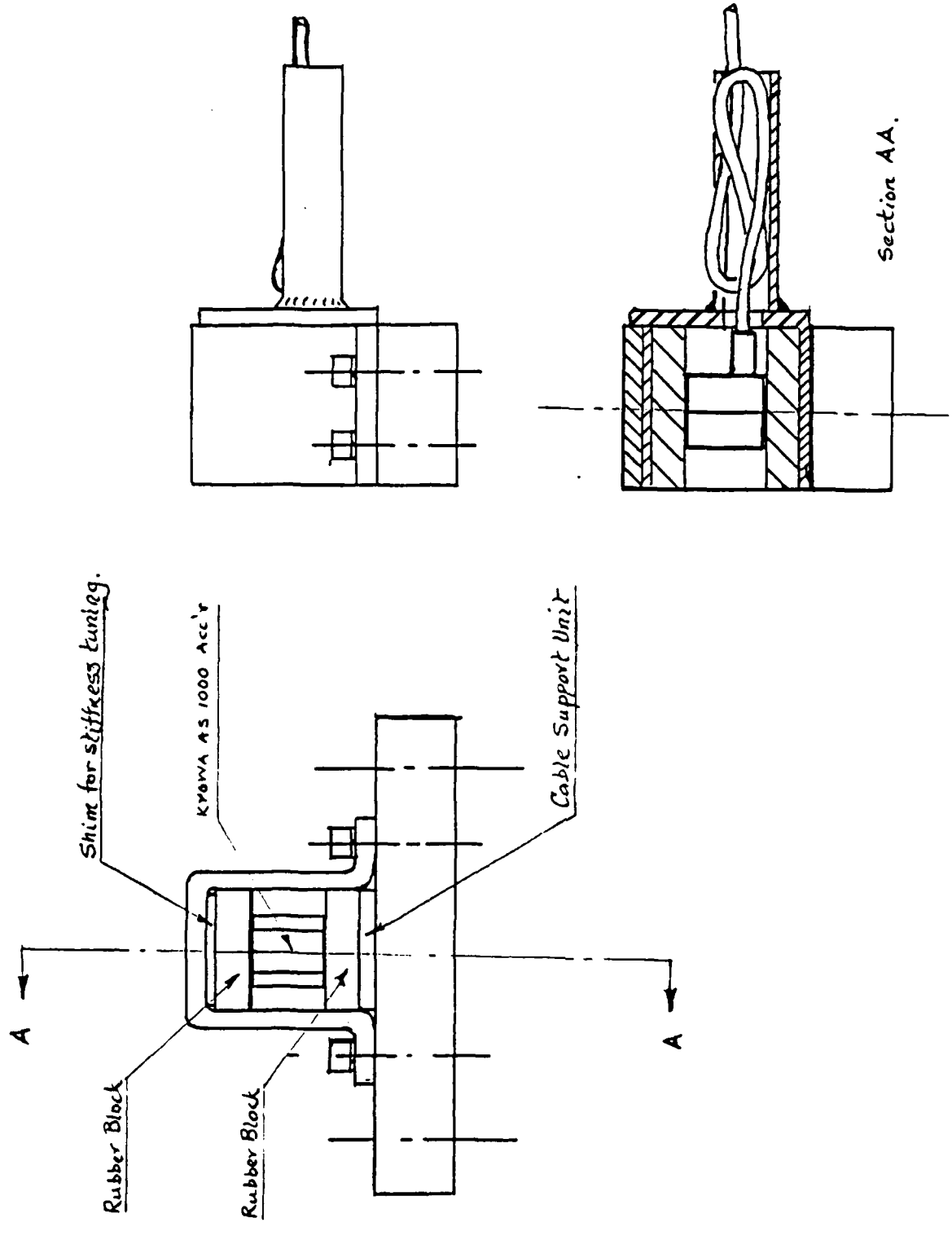

Elastomeric Accelerometer Mount.

Fig 1.

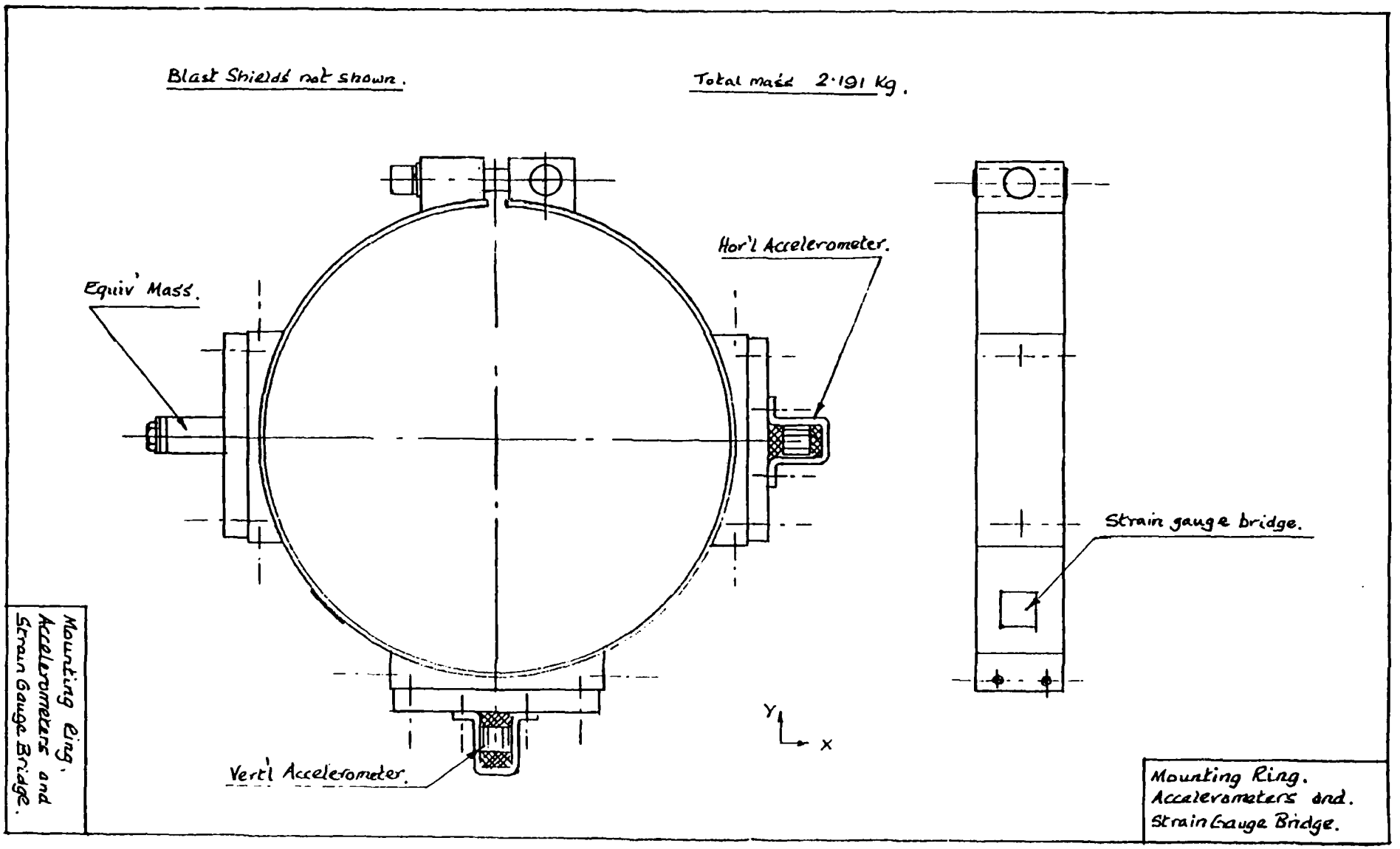
Blast Shields not shown.
Total mass 2·191 kg.
Equiv' Mass.
Hor'l Accelerometer.
Strain gauge bridge.
Vert'l Accelerometer.
Y
X
Mounting Ring, Accelerometers and Strain Gauge Bridge.
Mounting Ring.
Accelerometers and.
Strain Gauge Bridge.

Fig 2

APPENDIX 1

Instrumentation specification

Accelerometer specification

Manufacturer:		Kyowa Instruments Co Ltd Japan. British agent (Graham and White Instruments)
Type	:	AS - 1000A (Strain gauge type)
Range	:	±1000 g. (300 % Overload permited)
Sensitivity	:	600 uV/V/g
Frequency Response	:	0 - 7.5 KHz

Signal conditioning specification

Manufacturer:		CIL Microsystems Ltd, England.
Type	:	Strain gauge amplifier SGA 111 AT
Band with	:	2.5 MHz
Gain	:	5 to 10,000

Data capture specification

Manufacturer:		CIL Microystems Ltd, England.
Type	:	Multi channel analogue to digital converter designated Alpha blocks.
Preformance	:	F Block 16 Bit 20 uS (50Khz) conversion time, 64K Bytes of buffer memory per channel.

APPENDIX 2

Experimental results obtained from a 120mm gun trial, with two different designs of shot in which slight alterations had been made to the sabbot.

The rounds are given as A and B and the results from three typical firings for each round are given, overlaid for easy comparison.

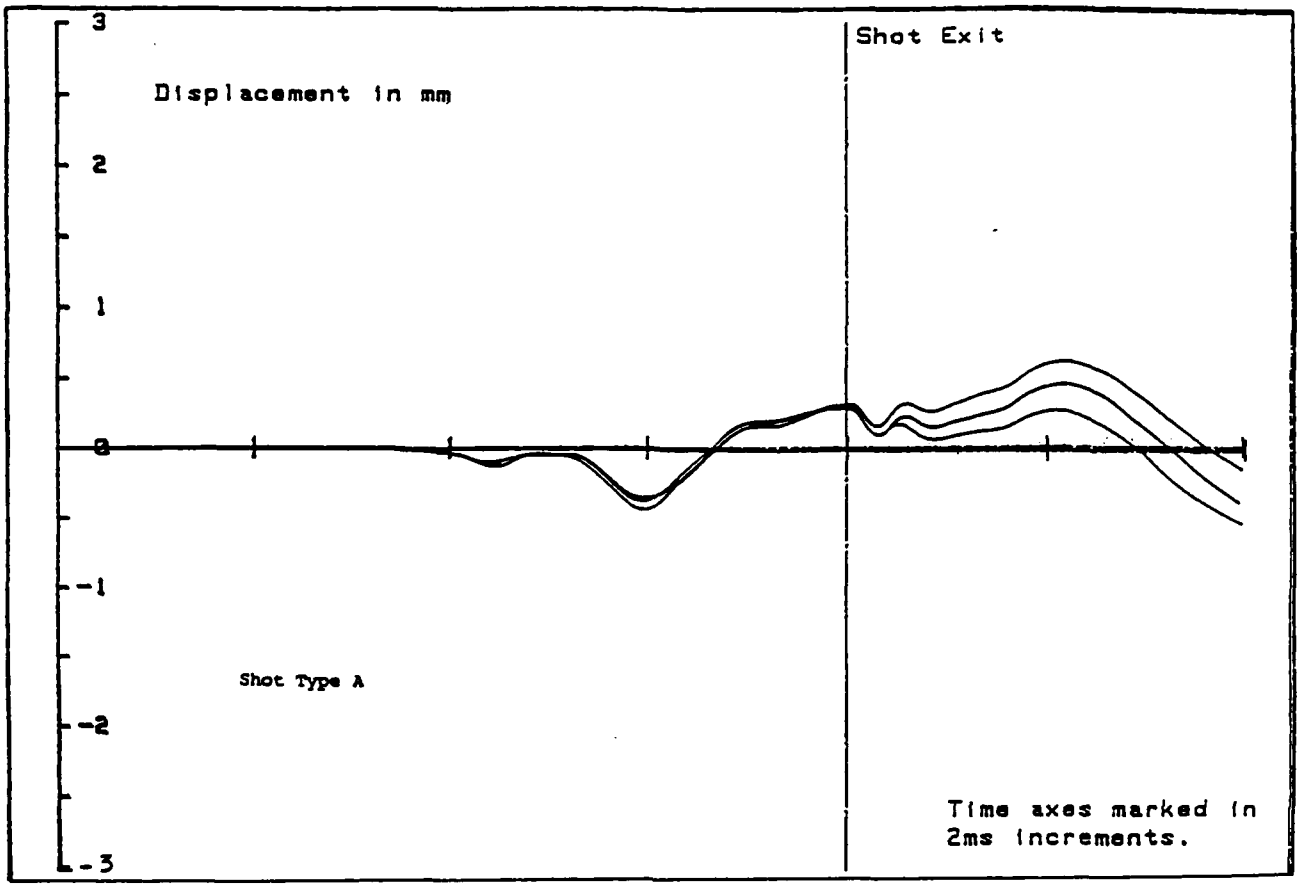

Vertical displacement of the muzzle

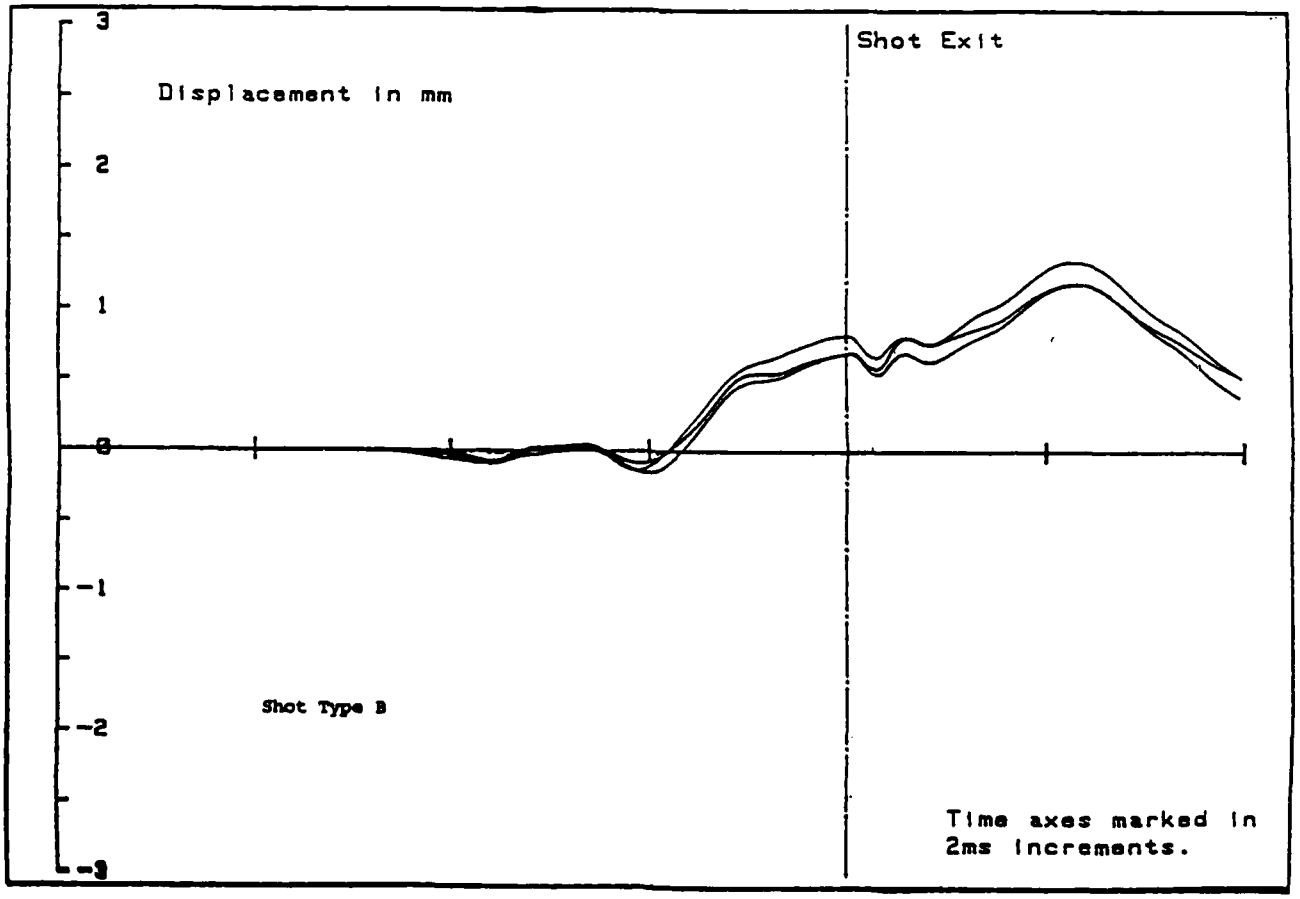

Vertical displacement of the muzzle

BARKER, CHAMBERS

TITLE: AN EXPERIMENTAL TECHNIQUE FOR MEASUREMENT OF SHOT PARAMETERS USED IN GUN DYNAMICS MODELLING

G. BARKER AND A.E. CHAMBERS
THE ROYAL MILITARY COLLEGE OF SCIENCE
SCHOOL OF MECHANICAL, MATERIALS AND CIVIL ENGINEERING
LAND SYSTEMS GROUP
SHRIVENHAM, SWINDON, SN6 8LA, ENGLAND

ABSTRACT

One of the problems of gun dynamics modelling is that the shot parameters are not accurately known, and estimates have to be used in the simulations. In particular, it has been shown that incorrect values for the shot band stiffness can dramatically modify the predicted launch conditions of the shot, and hence the final jump figures. If non-straight barrels are being simulated, then accurate data becomes even more critical.

This paper gives details of a purpose-built rig used to obtain the shot natural frequencies and damping characteristics. The results are then used to find representative shot band stiffnesses and damping values for inclusion in a gun dynamics modelling package. Results have been obtained from a number of shot designs, and small differences in sabot profile have produced significant effects on the measured parameters.

This paper was not available for printing in this publication.

EXELL

TITLE: THE USE OF A 30MM RESEARCH GUN TO TEST THE VALIDITY OF THE RAMA GUN DYNAMICS COMPUTER SIMULATION

ALAN EXELL
ROYAL ARMAMENT RESEARCH AND DEVELOPMENT ESTABLISHMENT
VT3 DIVISION
CHOBHAM LANE, CHERTSEY, SURREY KT16 OEE
UNITED KINGDOM

ABSTRACT

This paper gives details of the initial firing trials on a gun dynamics test rig to validate the gun dynamics computer simulations currently being used at RARDE(Ch). It aims to describe the use of proximity gauges for gun dynamics measurements, and also to show a validation exercise for the RAMA computer simulation.

The gun rig was designed around a "heavy" 30mm RARDEN barrel, and mimics the format of the current generation of tank gun systems, i.e., a twin plain bearing type mounting. A modular design was chosen so that various system parameters could be easily varied, to give a more comprehensive validation of the computer simulation.

The transient behaviour of the muzzle and cradle was measured by eddy-current proximity gauges. These have the advantages of being non-contacting and unaffected by the heat and light produced in the muzzle region during firing. However, their use has attracted some criticism both due to the difficulties in rigidly mounting the gauges, and their large diameter introducing some ambiguity into the displacement measurement. These questions were investigated using a series of dynamic laboratory experiments (to compare the displacement registered by the proximity gauges with accelerometers mounted on the barrel), and secondary measurements during the trials themselves (using accelerometers to show the movement of the stand prior to shot exit). The results in both cases reassured us of their validity for such small calibre gun trials.

The RAMA Gun Dynamics Computer Simulation has been developed under contract to RARDE(Ch) by RMCS, Shrivenham, details of which have been presented previously. Calculation of the model input parameters was by a combination of simple finite element techniques and empirical measurement. The predicted muzzle and cradle motions from the simulation were compared with the measured displacements and a good correlation was found between the two.

This paper was not available for printing in this publication.

HOYLE

TITLE: THE DEVELOPMENT OF AN EXPERIMENTAL FACILITY FOR STUDYING THE EFFECTS OF CRADLE DESIGN ON BARREL MOTION

HOYLE, J.B.

THE ROYAL MILITARY COLLEGE OF SCIENCE
SCHOOL OF MECHANICAL,MATERIALS AND CIVIL ENGINEERING
LAND SYSTEMS GROUP
SHRIVENHAM, SWINDON, SN6 8LA, ENGLAND

ABSTRACT:

The continuing requirement for greater range and accuracy of gun systems has led to the study of certain aspects of gun dynamics as a means of understanding the critical factors of design that affect accuracy. This is particularly relevant for the modern tank gun.

One way of quantifying the effects of gun and shot design on gun accuracy is to develop mathematical models that simulate real guns. The development of these theoretical simulation packages has led to the requirement for validation data from experimental test firings. Due to the extreme cost and great difficulties associated with attempts to conduct experimental work in these areas, there exists a need for some alternative to firing real guns in order to aquire the necessary data. Specially designed smaller scale experimental guns can offer solutions to the problems of cost and experimental difficulties. They will allow relevant simulation as well as the large data acquisition necessary for validating mathematical models. This paper describes the apparatus used in an investigation into gun cradle design using this technique, together with an indication of its effects on barrel and shot motion.

BIOGRAPHY : HOYLE J.B.

PRESENT ASSIGNMENT: Research Engineer, RMCS, conducting research in to gun,shot and cradle dynamics.

PAST EXPERIENCE : Engineer in a small manufacturing company.

DEGREES HELD : BSc Degree Mechanical Engineering.

THE DEVELOPMENT OF AN EXPERIMENTAL FACILITY FOR STUDYING THE EFFECTS OF CRADLE DESIGN ON BARREL MOTION

HOYLE, J.B.

THE ROYAL MILITARY COLLEGE OF SCIENCE
SCHOOL OF MECHANICAL,MATERIALS AND CIVIL ENGINEERING
LAND SYSTEMS GROUP
SHRIVENHAM, SWINDON, SN6 8LA, ENGLAND

1. INTRODUCTION :

Gun accuracy has long been of great importance in warfare, particularly if a modern tank battle is considered, and this has led to a continuing requirement for longer range and greater accuracy. One of the contributing factors to round to round dispersion is the yawing motion of the shot due to the interaction of the shot with the barrel, and a considerable amount of work has been carried out in to this phenomenon. Another contributing factor to the motion of the barrel (and therefore, shot) is the flexing of the gun cradle.

In order to quantify the effects of gun, cradle and shot design on gun accuracy, the problem can be approached both theoreticaly and experimentaly, the former leading to the development of a number of gun dynamics simulation packages. Due to the versatility of some of these theoretical simulation packages, the ability to vary certain parameters of the gun design within the simulation is readily achieved, and the effects of these changes on gun and shot motion can be demonstrated. However, an experimental rig designed to study the effects of these parameters is more difficult to achieve, primarily due to the need to vary them. The effect of unbalanced rounds on gun accuracy, for instance, has been successfully carried out using the RMCS 30 mm Air Powered Gun, but it has become necessary to investigate some of the other variable parameters affecting gun and shot motion.

A special gun cradle has been developed at the Royal Military College of Science to be used in conjunction with an improved version of an existing air powered gun. The design requirement for the gun cradle was that it must be able to simulate, both easily and cheaply, any existing and forseeable gun cradle configuration, whilst at the same time allowing many of the parameters of a real gun cradle to be varied. Suitable measuring techniques have also been developed for the measurement of specified parameters and motions.

A short experimental test firing programme was conducted to commission the new gun cradle and to establish that the various variable parameters did have an effect on barrel motion, and that these effects could be measured.

2. CRADLE DESIGN SPECIFICATION :

In order to study experimentaly the effects of cradle design on barrel and shot motion, a cradle had to be designed and built that would enable all of the numerous design parameters of a real gun cradle to be varied while at the same time allowing certain barrel and cradle motions to be measured. This would enable a systematic investigation to be carried out in to the effects on barrel motion of changes in these parameters. The cradle design specification required that the following parameters be readily varied:
total mass, inertia, bearing spacing, bearing elasticity, bearing clearance, width of bearing, multiple bearings, trunnion position, elevation gear stiffness and cradle flexibility,

and that the following motions be measured:
relative barrel/bearing motion, relative bearing/cradle motion, cradle motion at the bearing positions, and barrel (muzzle) motion.
The breech pressure/time history was also to be measured

It was thus intended that the cradle would be able to experimentally simulate any of the existing and forseeable cradle configurations, including the two commonly found on modern tank guns, ie. those similar to the Chieftain and Abrams gun mounts respectively (Fig. 1 shows some examples).

3. DESCRIPTION OF AIR GUN AND CRADLE :

The latest development of the RMCS 30mm Air Powered Gun and Cradle (Fig. 9) consists of two basic sub-assemblies, namely the gun (barrel and breech) and the gun cradle (cradle, elevation gear and recoil buffers).

The Gun.

The gun consists of two main parts - barrel and breech

Barrel. There are a number of barrels, all of which have a bore of 30mm and are either rifled or smoothbore. Existing barrels include one light weight aluminium smoothbore barrel, one heavy inflexible smooth bore barrel and one specially adapted RARDEN Cannon rifled barrel and are all approximately 50 calibres long. A new rifled cannon barrel has been adapted to fit the breech and is 75 calibres long. This latter barrel can be used in conjunction with the very large breech for studying fairly heavy shots at high velocities.

Breech. A third generation development of the existing RMCS Air Powered Gun has been built for the attainment of very high velocities, up to and exceeding Mach 1, especially when used in conjunction with the 75 calibre barrel. The principal improvements on previous breech generations are the much larger charge volume and the firing mechanism. The firing mechanism operates on a rapid release poppet valve

arrangement as opposed to the bursting diaphragm of that previously used. It can also be operated at much higher pressures (of the order of 2000 psi) and is far easier and more reliable to operate (a detailed description of the workings of the breech can be found in Appendix 1). The breech also has provision for the addition of off-axis masses to enable the simulation of unbalanced breeches.

3.2 The Cradle

The cradle consists of a number of different parts specially designed to achieve the variability of parameters, and the measurement of the various motions, as laid out in the specifications. The cradle is made up of the front and rear bearing housings attached via stiffening rods to the bearing housing box to form the cradle "tube". This is then attached to the trunnions as shown in Fig. 2 (see Ref. 1 and 2)

Bearing housings. The bearings housings serve three primary functions, namely - location of the bearing outer casing, the attachment of the stiffening rods and the positioning of the proximity transducers for the measurement of the relative bearing/cradle motions.

The bearing outer casing is located within the bearing housing via a location fit and is bolted in place to prevent axial movement. Between 4 and 28 stiffening rods can be attached in place around the sides of the bearing housing by the use of 8 seperate bolt-on clamping pieces. The two proximity transducers for the measurement of relative bearing/cradle motions in both the horizontal and vertical planes screw in to the bearing housing, are held by locking nuts, and protrude through the bearing outer casing to the vicinity of the bearing inner casing. The rear bearing housing also has a plate bolted to it to which are attached the recoil buffers and the elevation gear stiffness simulation rods.

Bearing housing box. Two of the above bearing housings are bolted together to form the bearing housing box and are attached to the stiffening rods in the same way. This box is then attached to two brackets, one on each side, that are themselves attached to two trunnion rods. This arrangement will allow the positioning of the gun trunnions away from the bearing housing box (see Fig. 2) and will enable cradle configurations where the trunnions are in front of the front bearings to be investigated. Both bearing housings that make up the box can accept a standard bearing.

Stiffening rods. The cradle has been designed to accept any number of stiffening rods between 4 and 28, although in practise they should be applied in multiples of four. They are each 8 mm in diameter, of any length, and can be made of any material. The stiffness of the cradle is altered by changing the number of stiffening rods.

Bearings. The bearings are each made up of four parts, - the bearing hub, bearing inner casing, bearing spring medium and the bearing outer casing (see bearing section on Fig. 2). The bearing hub is located

within the bearing inner casing by a location fit and is bolted in place to prevent axial movement. The inner casing is then suspended within the bearing outer casing by the bearing spring medium. The spring medium consists of a cylinder with its walls machined away in such a fashion as to leave three rings joined by eight small webs. The two outer rings are attached to the bearing outer casing whilst the middle ring is attached to the bearing casing. This allows the eight small webs joining the rings together to flex, thus producing a "flexible" bearing.

Barrel/bearing clearance is altered by replacing the bearing hub with a different unit with a different clearance. The bearing stiffness is altered by changing the spring medium for one with larger or smaller webs. Rigid bearings can be made by changing the spring medium for a solid walled cylinder of the same dimensions. The bearing hubs have each been machined to accept two proximity transducer sleeves which in turn hold proximity transducers. These will enable the measurement of the motion of the barrel within the bearing, in both the horizontal and the vertical planes.

Elevation gear stiffness simulation rods. These consist of two rods that are effectively built in to each side of the rear bearing housing and are used to simulate the flexibility of the elevation gear. The stiffness of these rods is changed by altering the position at which they are clamped by the elevation gear bracket, the longer the rod the greater the elevation gear flexibility. Clamping the rod at the rear bearing housing has the effect of making the elevation gear rigid.

Recoil buffers. Two recoil buffers are located on each side of the breech, the pistons of which are attached to the rear bearing housing. Both recoil buffer cylinders consequently recoil with the breech. As these recoil buffers are rather small, they have been augmented by the addition of extra recoil cylinders at a set distance behind the breech, thus allowing the breech to initialy recoil with no additional recoil action until well after shot exit.

Other cradle parameters can be varied in the following ways - the total mass of the cradle can be altered by attaching extra masses where required, the bearing spacing can be adjusted by moving and reclamping the bearing housings along the stiffening rods, and the placing of bearings within the bearing housing box or the addition of extra bearing housings will satisfy the requirement for multiple bearings.

4. INITIAL INSTRUMENTATION :

For the measurement of all displacements, small inductive proximity transducers are used. These are placed in strategic positions to enable the measurement of all the relative motions within the bearings and the barrel and cradle motions, the outputs being sent via signal conditioners to A/D transient recorders. The raw data is then processed on a computer and stored on disc for further processing and plotting.

5. FIRING PROGRAMME :

The new cradle, having been completed and undergone initial test firings, required validation trials. A test firing programme was devised with a view to establishing that the variable parameters of the cradle had an effect on barrel motion, and then of carrying out further trials in greater depth in to specific areas of cradle design.

The firing programme was arranged such that one variable parameter was changed after each group of firings, a group of firings being the number necessary to ensure consistency.

The firings carried out were as follows :

1. Rigid bearings with clearance, rigid cradle, rigid elevation gear.

2. Rigid bearings without clearance, rigid cradle, rigid elevation gear.

3. Flexible bearings with clearance, rigid cradle, rigid elevation gear.

4. Flexible bearings without clearance, rigid cradle, rigid elevation gear.
5. Rigid bearings without clearance, flexible cradle, rigid elevation gear.
6. Rigid bearings without clearance, flexible cradle, flexible elevation gear.
7. 5. repeated with different trunnion position.

8. Rigid bearings without clearance, rigid cradle, flexible elevation gear.

For the firings a "rigid" cradle had all the stiffening rods in place and a "flexible" cradle had only 3 stiffening rods in place.

All the cradle configurations apart from 7 above had the following dimensions - 580 mm between front and rear bearings, 350 mm between the front bearing trunnions, and the trunnions were positioned at the bearing housing brackets. In the case of the flexible elevation gear, the elevation gear bracket was situated 70 mm from the cradle recoil bracket.

6. RESULTS :

The data from the validation firing programme was processed in to a graphical form showing various displacements against time, some of which are shown in Figs.3 to 8. Each different cradle configuration was employed with three breech balance conditions :- breech centre of gravity above, balanced, and below the axis of the barrel.

Figs. 3 to 5 show the 3 motions :- barrel motion within the bearing, cradle motion at the front bearing, and muzzle motion for each of the three breech balance conditions. Figs. 6 to 8 show the same motions

but with the addition of bearing motion within the cradle due to this cradle configuration having flexible bearings.

A brief examination of the results shows that it was an off-axis breech that produced the largest response from the barrel and cradle, the basic motion trends due to the breech being only modified by the variable parameters of the cradle. It must also be noted that barrel expansion due to charge pressure cannot be simulated as the relatively low breech pressure used in the firing programme produced no significant barrel expansion.

As only the results from two different cradle configurations (Figs. 3 to 8) are shown, these will be discussed briefly,but they are sufficient to show that the main motion forcing component is due to the off-axis centre of gravity of the breech, and also that the cradle has only secondary effects on these motions.

A comparison of Figs. 3,4 & 5 shows the effects of the different breech balance conditions, and it is clear that the breech forces the muzzle in the opposite direction to the breech centre of gravity. Figs. 6,7 & 8 show the same trends, but are slightly modified by the flexible bearings, the motions being more pronounced.

The data acquired from the other cradle configurations that were investigated was also analysed to enable similar comparisons to be made. Although not discussed here, the conclusions are given below.

7. DISCUSSION OF RESULTS :

The results are discussed seperately under each parameter heading.

Bearing clearances. It would appear from the results that bearing clearance has an effect on cradle motion, but its effect on muzzle motion is less obvious, and depends on bearing stiffness. For the specific cradle configurations with rigid bearings, bearing clearance appears to have no effect on muzzle motion, a trend which is reinforced by the observed lack of barrel motion within the bearings.

It must be remembered, however, that there is no simulation of barrel expansion, and that the overall centre of gravity of the barrel and breech is located between the two bearings, thus the barrel sits down on both.

Bearing stiffness. Flexible bearings appear to have a detrimental effect on cradle motion but not a significant effect on muzzle motion as compared to rigid bearings when the bearing clearance is quite large. This was found to be accentuated in the case where there was very little bearing clearance although the muzzle motion was not greatly affected. It would appear that having very stiff bearings is marginally superior to flexible bearings in that muzzle motion is reduced.

Cradle stiffness. A comparison between the rigid and flexible cradle configurations tends to indicate that cradle stiffness has little or no effect on cradle and barrel motion.

Elevation gear stiffness. Increasing the flexibility of the elevation gear appears to have a large effect on both cradle and muzzle motion as compared to the rigid elevation gear, especially in the case where the breech centre of gravity is below the barrel axis. The similarities between the motion curves seems to depend on the breech out of balance, but in both cases where the breech is unbalanced, there is a much larger cradle and muzzle deflection at shot exit. In general, it is believed that flexible elevation gears are detrimental to gun accuracy.

Trunnion position. Moving the front bearing towards the rear so that the bearings are closer together has the effect of shortening the cradle, of making it stiffer, and of moving the trunnion in relation to the two bearings. A study of the results indicates that the shorter and stiffer cradle shows exactly the same trends as the longer and more flexible cradle but has a considerably reduced amplitude of motion. When considering the effects of the other stiffer cradles, it would appear that it is the position of the bearings that is responsible for the reduction in cradle and muzzle motion.

8. CONCLUSIONS :

The RMCS 30 mm Air Powered Gun has been developed successfully to include a flexible gun cradle, and a short firing programme has been carried out to obtain validation data. Results clearly show that the systematic variation of certain gun and cradle parameters does have an effect on barrel (and hence shot launch) motion, and that these effects can be consistently measured.

8. ACKNOWLEDGEMENTS :

This research is funded by the Royal Armament Research and Development Establishment (Fort Halstead).

9. REFERENCES :

1. HOYLE J.B.
RMCS Air Powered Gun - Proposed Cradle Design
RMCS Report LS/059/1327. October 1987

2. HOYLE J.B
Design details of a Cradle for the RMCS Air Powered Gun.
RMCS Report LS/069/1327. February 1988

HOYLE

POSSIBLE CRADLE CONFIGURATIONS - PLAN VIEWS

1/.

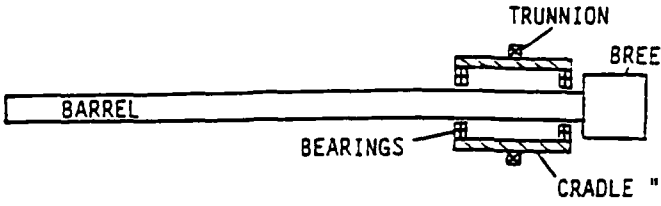

(M1 / LEOPARD 2)

2/.

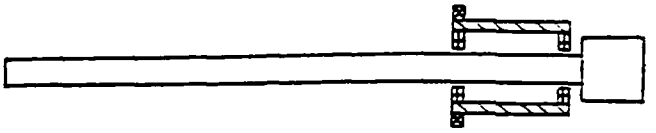

3/.

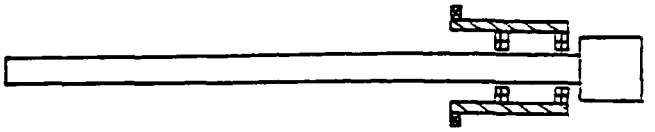

(CHIEFTAIN)

4/.

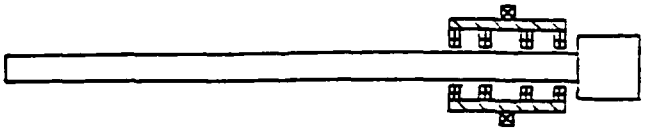

5/.

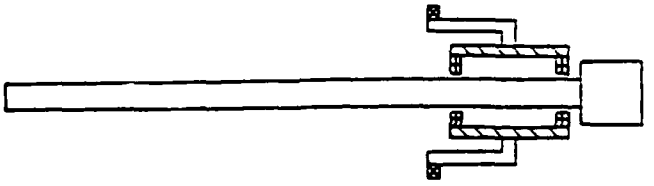

6/. ANY COMBINATION OF THE ABOVE.

Fig. 1

Fig. 2

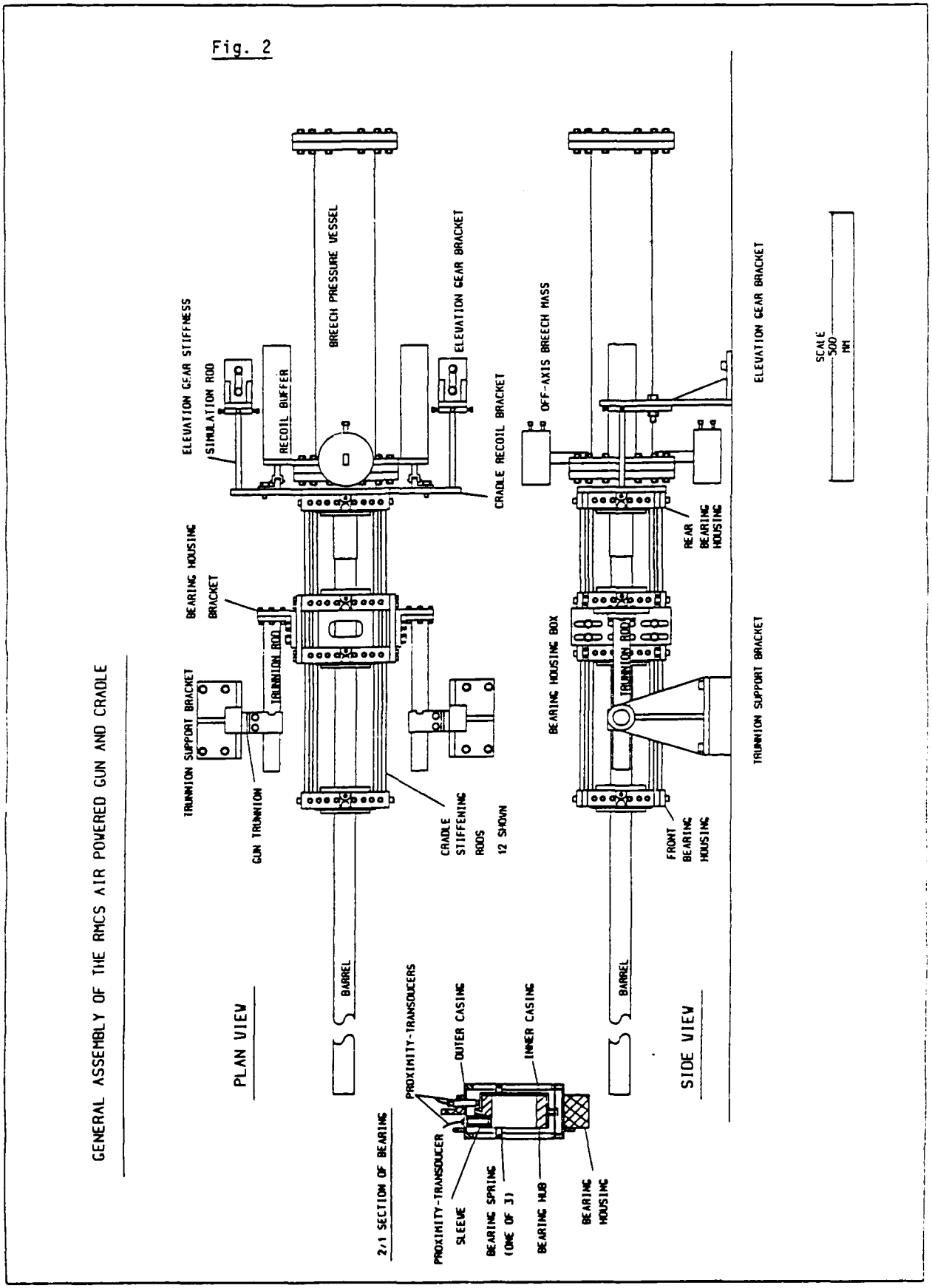
GENERAL ASSEMBLY OF THE RMCS AIR POWERED GUN AND CRADLE
PLAN VIEW
SIDE VIEW
2/1 SECTION OF BEARING
ELEVATION GEAR STIFFNESS SIMULATION ROD
RECOIL BUFFER
BREECH PRESSURE VESSEL
ELEVATION GEAR BRACKET
CRADLE RECOIL BRACKET
BEARING HOUSING BRACKET
TRUNNION SUPPORT BRACKET
TRUNNION ROD
GUN TRUNNION
CRADLE STIFFENING RODS 12 SHOWN
BARREL
OFF-AXIS BREECH MASS
REAR BEARING HOUSING
BEARING HOUSING BOX
FRONT BEARING HOUSING
TRUNNION SUPPORT BRACKET
SCALE 500 MM
PROXIMITY-TRANSDUCERS
OUTER CASING
INNER CASING
PROXIMITY-TRANSDUCER
SLEEVE
BEARING SPRING (ONE OF 3)
BEARING HUB
BEARING HOUSING

HOYLE

Fig. 3

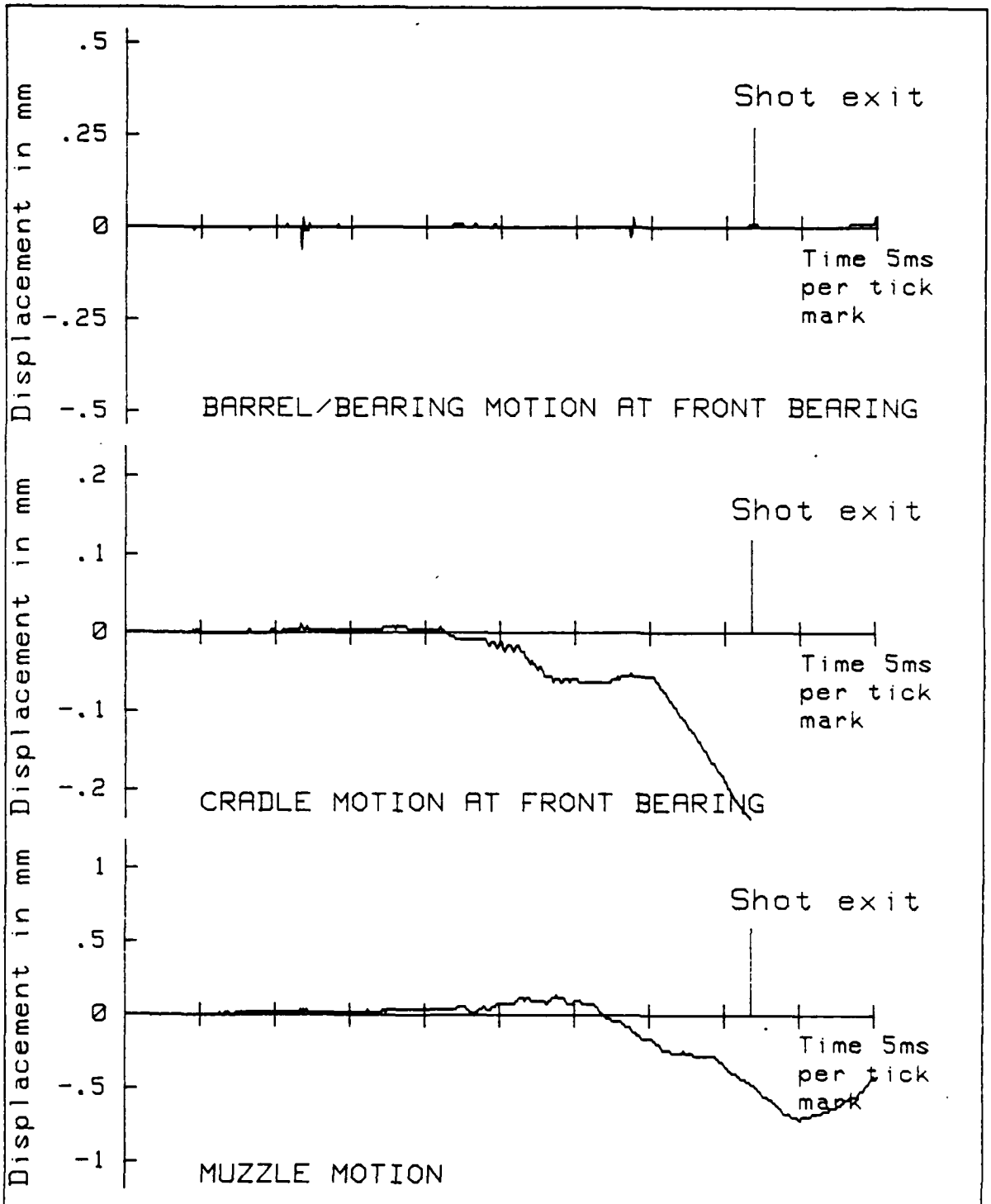

CRADLE CONFIGURATION 1 BEARING CLEARANCE .5 mm

Initial breech pressure 2.67 MN/m^2 Shot mass .326 Kg Muzzle vel 122 m/s Breech c.of g. above axis	Firing No. 57

HOYLE

Fig. 4

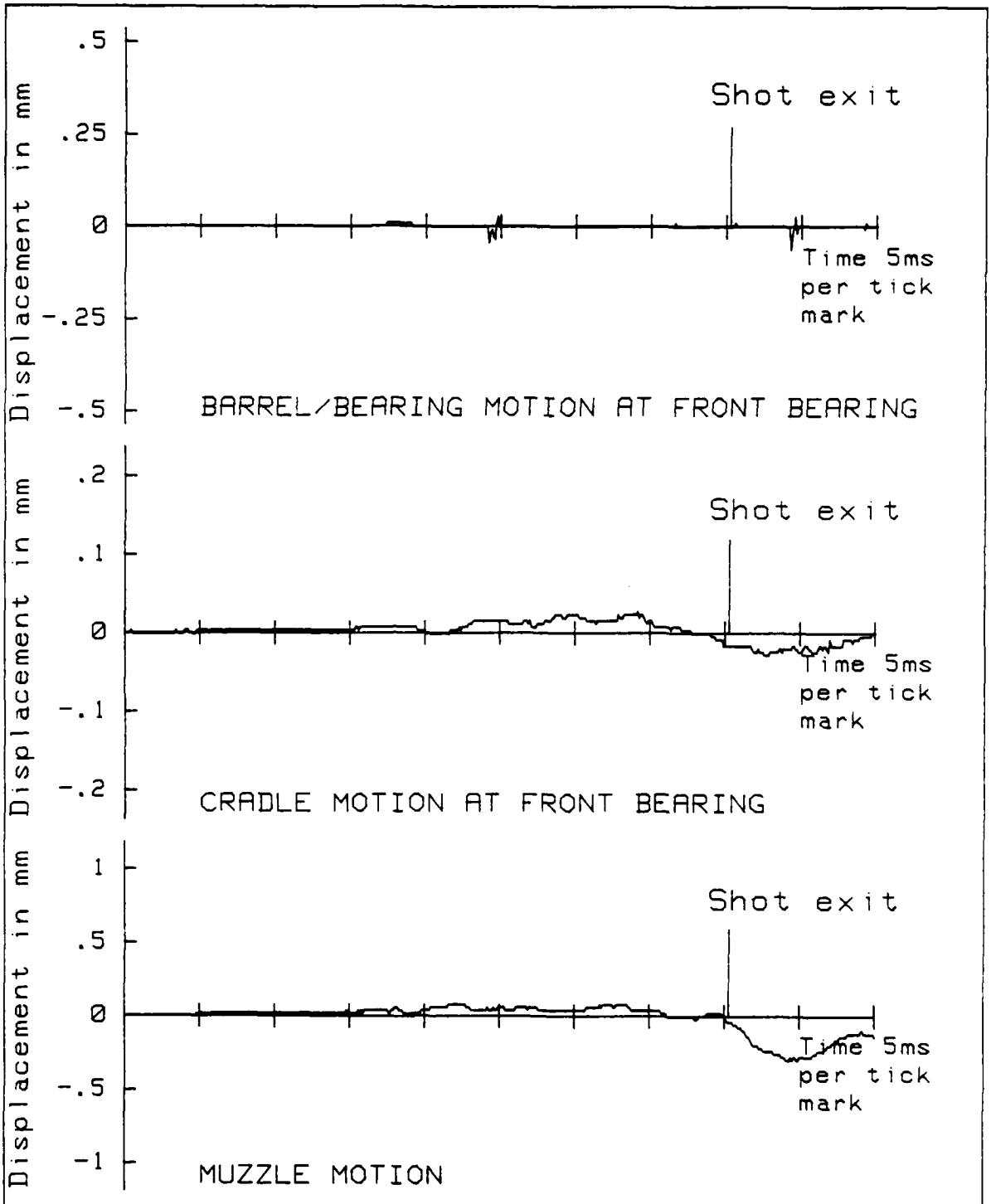

CRADLE CONFIGURATION 1 BEARING CLEARANCE .5 mm

Initial breech pressure 2.67 MN/m^2 Shot mass .326 Kg Muzzle vel 122 m/s Breech c.of g. balanced	Firing No. 48

HOYLE

Fig. 5

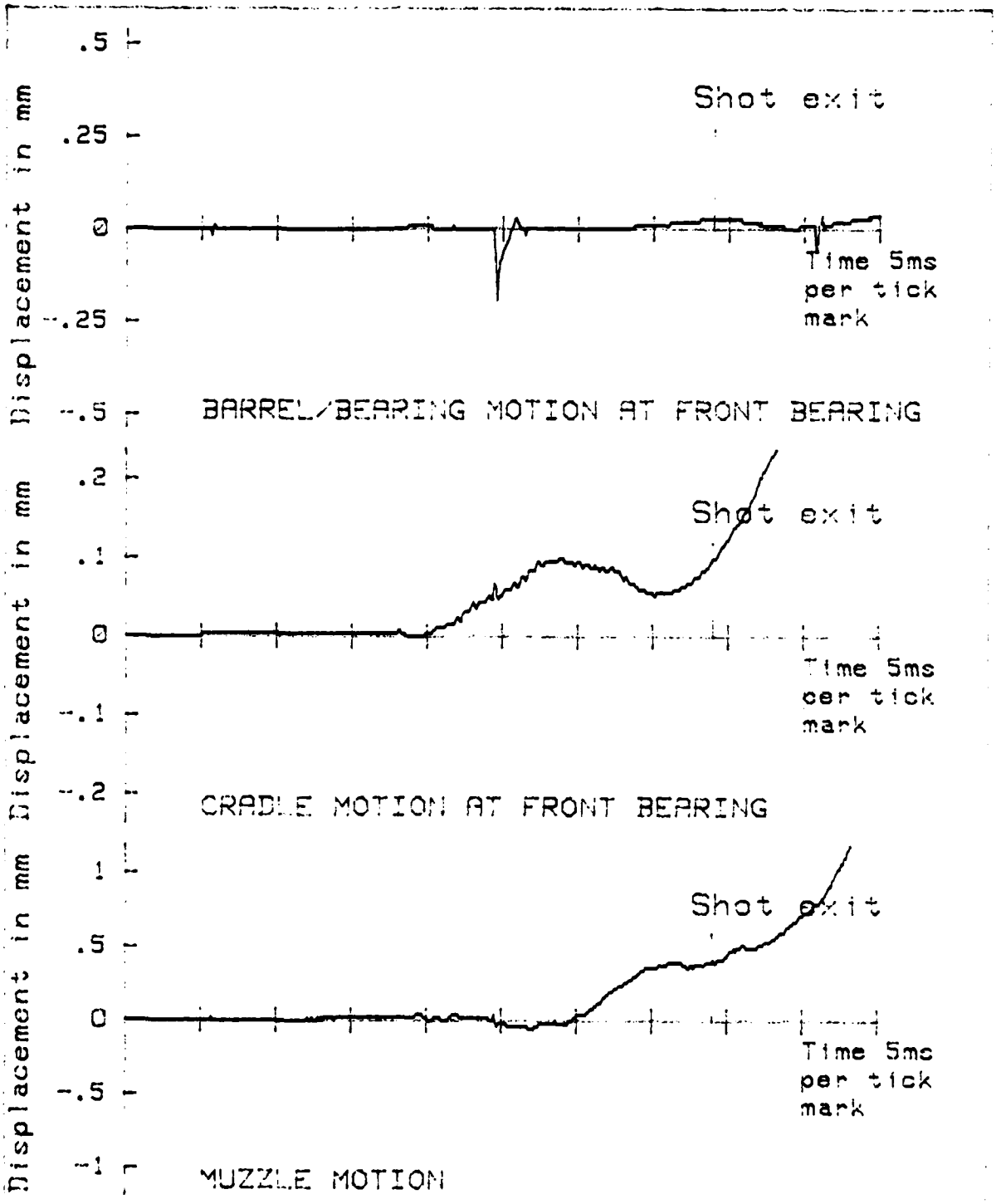

CRADLE CONFIGURATION 1 BEARING CLEARANCE .5 mm

Initial breech pressure 2.67 MN/m^2
Shot mass .326 Kg Muzzle vel 122 m/s
Breech c.of g. below axis

Firing No. 44

Fig. 6

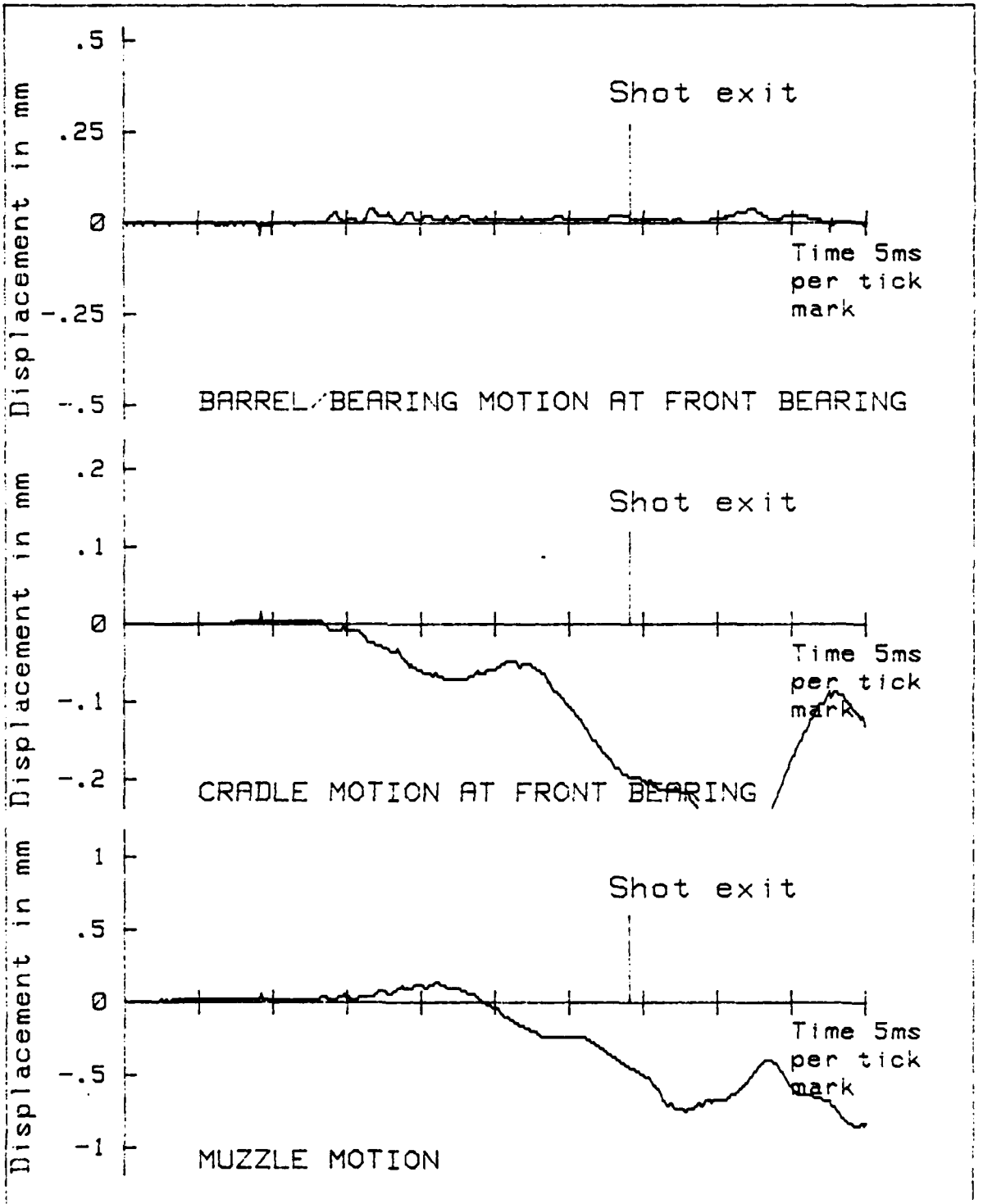

CRADLE CONFIGURATION 2 BEARING CLEARANCE .05 mm

Initial breech pressure 2.67 MN/m^2 Shot mass .326 Kg Muzzle vel 122 m/s Breech c.of g. above axis	Firing No. 70

Fig. 7

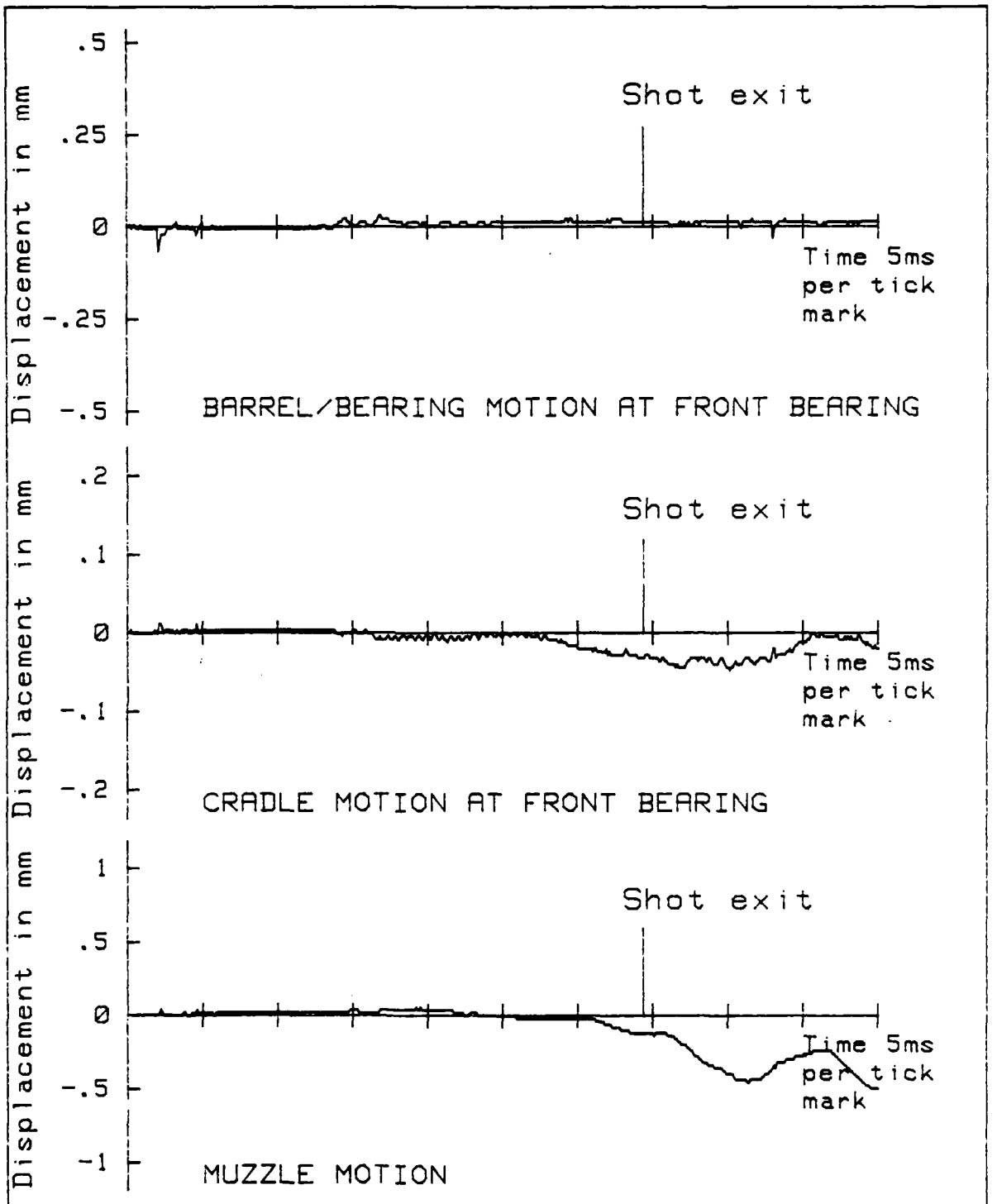

CRADLE CONFIGURATION 2 BEARING CLEARANCE .05 mm

Initial breech pressure 2.67 MN/m^2 Shot mass .326 Kg Muzzle vel 122 m/s Breech c.of g. balanced	Firing No. 60

Fig. 8

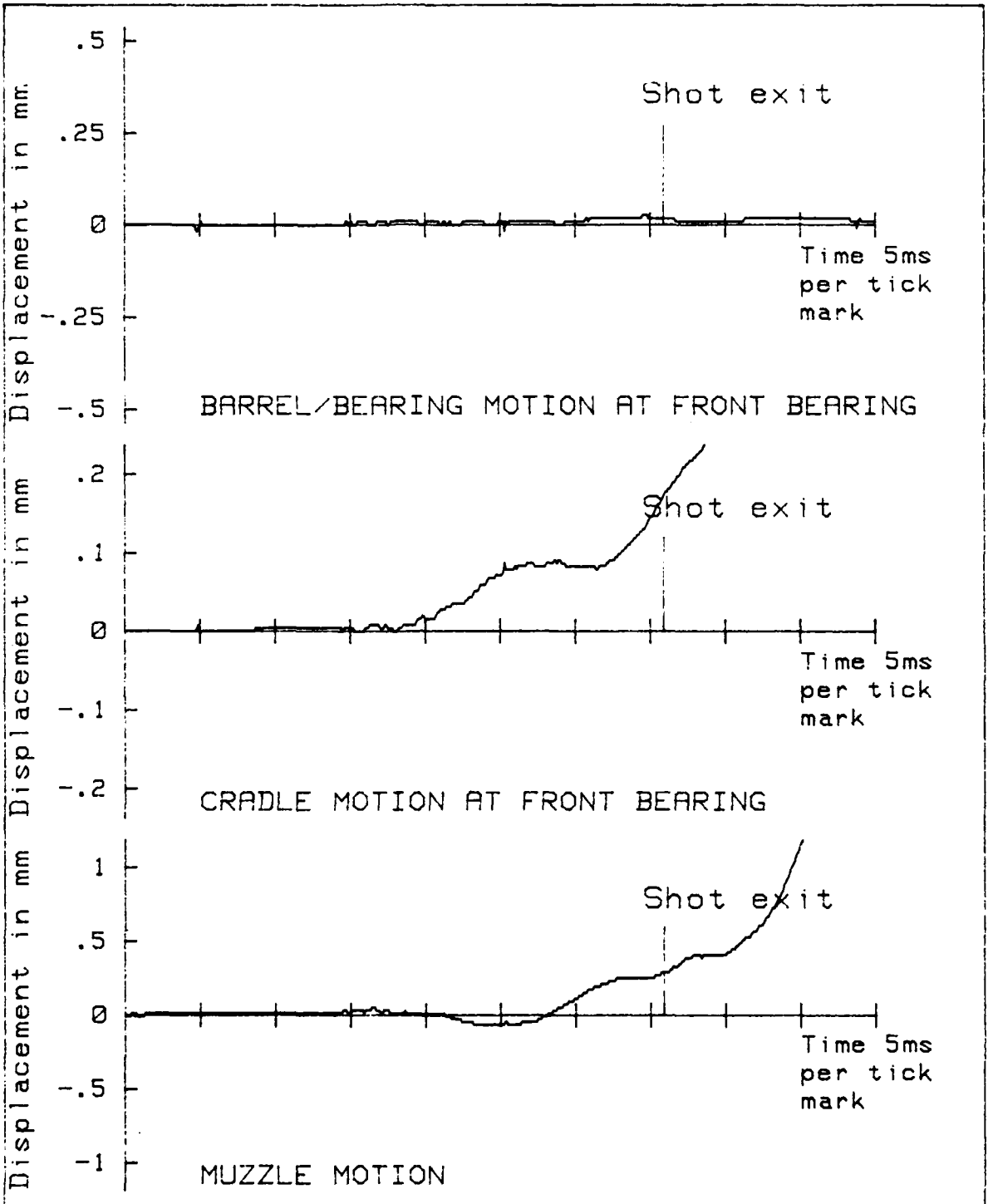

CRADLE CONFIGURATION 2 BEARING CLEARANCE .05 mm

Initial breech pressure 2.67 MN/m^2 Shot mass .326 Kg Muzzle vel 122 m/s Breech c.of g. below axis	Firing No. 125

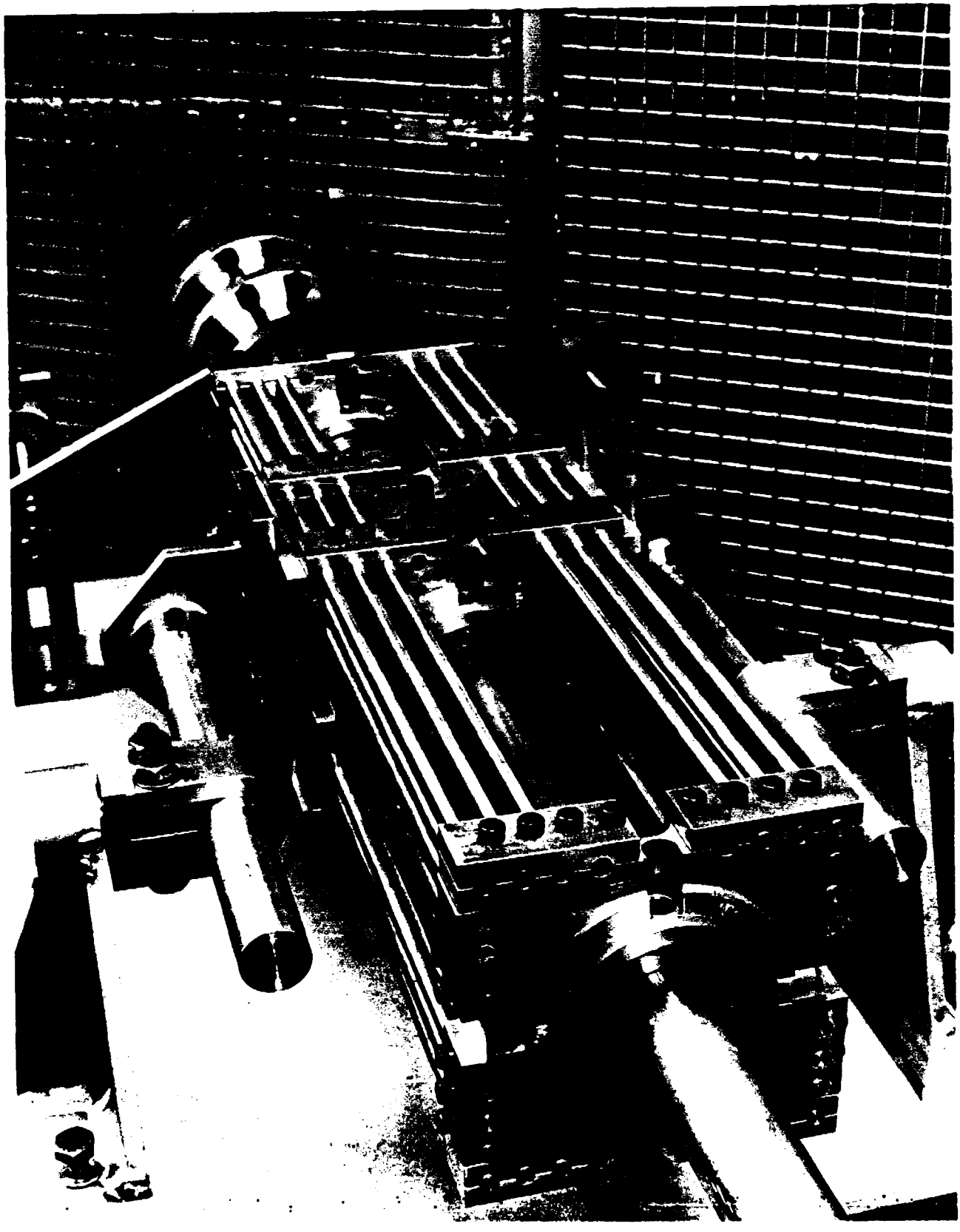

GUN CRADLE & SECOND GENERATION BREECH

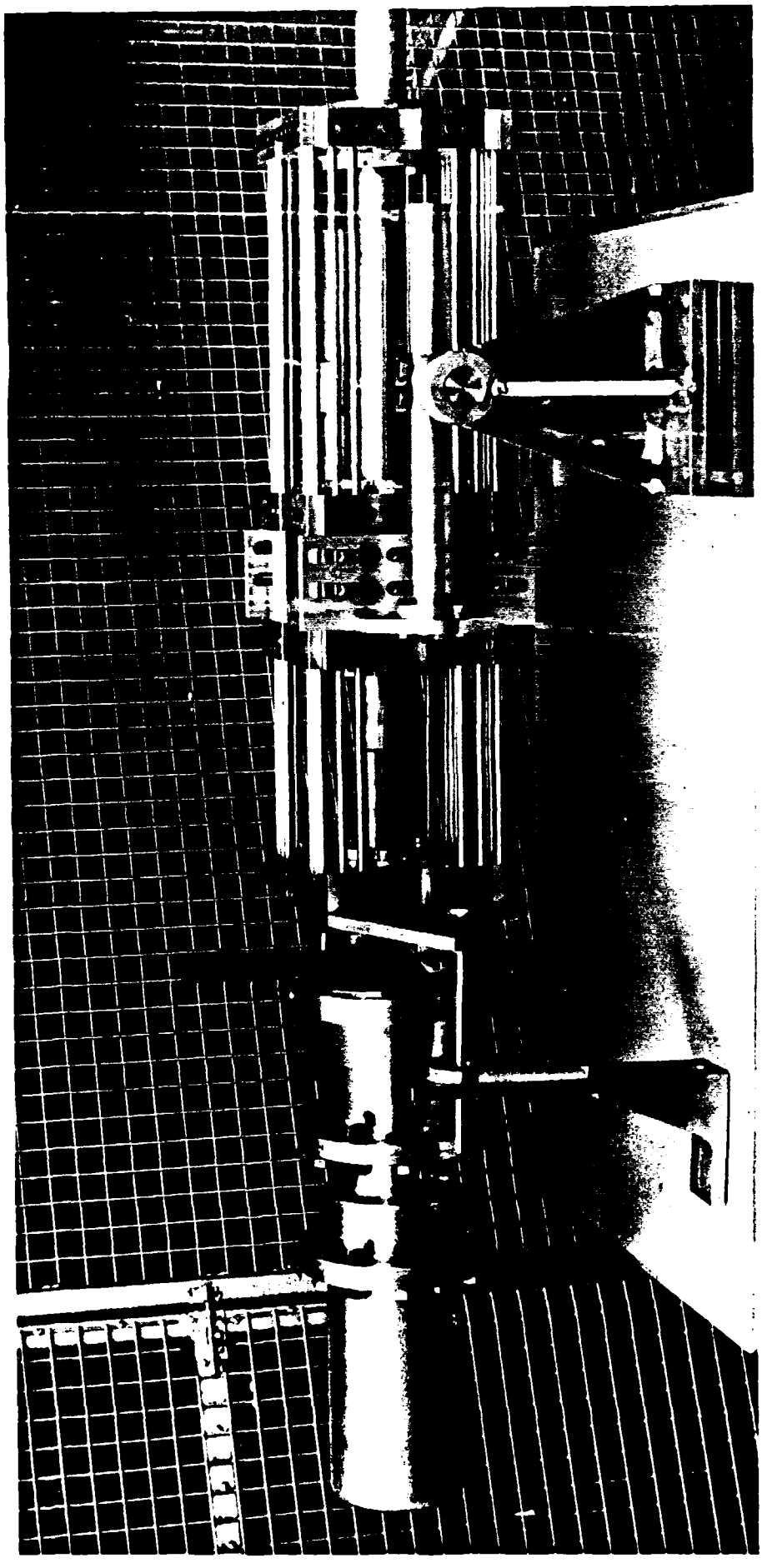

GUN CRADLE & SECOND GENERATION BREECH

Appendix 1

The accompanying diagram shows a cross section of the breech pressure vessel. When the pressure vessel is charged, compressed air is allowed to flow through the small bleed-hole in to the small cylinder at the back of the vessel, such that pressure P1 = pressure P2. The nett pressure difference across the piston is therefore zero and the nett force on the poppet valve is such as to keep it closed (as the pressure in the barrel is atmospheric).

When the gun is fired, however, air is dumped from the small cylinder at the back of the vessel, through a rapid release valve to atmosphere. This causes a pressure difference across the piston which can not be equalised by air flowing through the bleed hole as it is so small. The piston area being greater than the poppet valve area leads to a greater force on the piston trying to open the poppet valve than the force on the poppet valve trying to close it, the result being that the poppet valve opens very rapidly, dumping the main compressed air charge in the breech to the barrel. The shot is then propelled down the barrel.

When the main air charge has left the breech pressure vessel, pressure P1 = pressure P2 and the small return spring pushes the poppet valve shut ready for the next charge of compressed air. The rapid release valve is remote from the breech (being joined by pressure hose) and is solenoid operated.

The operation of the air gun is very simple, (only manual loading of the shot is required) has proved extremely reliable (to date, no failure to fire), and reqiures little or no maintenance.

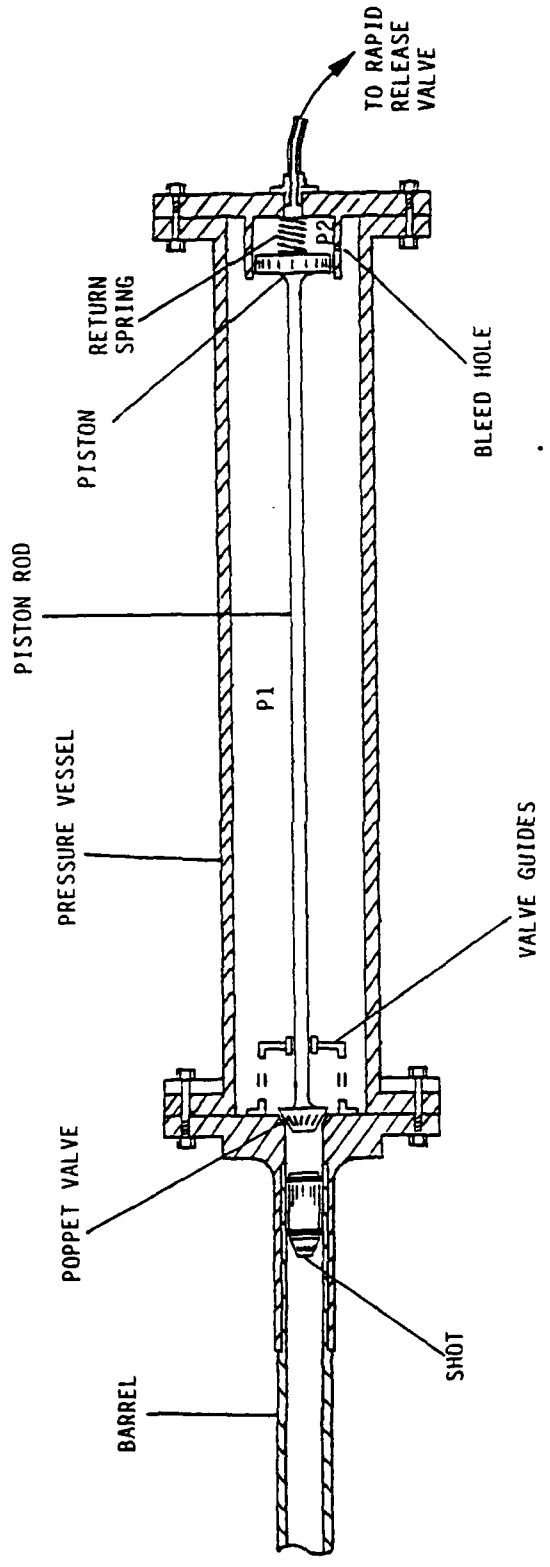

RMCS AIR POWERED GUN - BREECH PRESSURE VESSEL SECTION.

Brosseau, Kregel, Baran

TITLE: AUTONOMOUS ACCURACY ENHANCEMENT SYSTEM

T. L. Brosseau, M.D. Kregel, A.F. Baran
U.S.Army Ballistic Research Laboratory
Aberdeen Proving Ground, MD 21005-5066

ABSTRACT:

This paper provides a description of how one would automatically position the muzzle of the 120-mm main gun on the M1A1 tank to improve the pointing accuracy. After determining the static and dynamic sources that produce errors in pointing accuracy an exploratory research program was designed to correct these errors by the use of mathematical algorithms, electronic sensors, and electronic controls. The integration of these algorithms, sensors, and controls along with signals from the azimuth and elevation sensors in the tank, produced an excellent combination to improve the pointing of the tank gun muzzle. The Autonomous Accuracy Enhancement System is discussed and data from successful firing-on-the-move tests are presented.

BIOGRAPHY: T. L. Brosseau
PRESENT ASSIGNMENT: Senior Engineer Weapons Control Systems and Weapon Dynamics & Accuracy Programs
PAST EXPERIENCE: Weapons Design Engineer, Interior Ballistician, Weapon Dynamics, Heat Transfer, High Pressure Gages, Weapons Control Systems, and Wear Reducing Additives for Large and Small Caliber Weapons.
DEGREES HELD: BSME University of Vermont
MSME University of Vermont

BIOGRAPHY: M. D. Kregel
PRESENT ASSIGNMENT: Research Physicist at the BRL. Weapon Accuracy Enhancement Techniques and Modeling of Projectile / Barrel In-bore Dynamics.
PAST EXPERIENCE: Weapon Accuracy Enhancement Techniques and Modeling of Projectile / Barrel In-bore Dynamics for Large and Small Caliber weapons.
DEGREES HELD: BS North State Texas University
MS North State Texas University
PhD New Mexico State University

BIOGRAPHY: A. F. Baran
PRESENT ASSIGNMENT: Leader, Weapons Systems Team and BRL POC for Robotics and Small Arms.
PAST EXPERIENCE: Small Arms, Automatic Cannon Systems, Simulation Modeling, Weapon Dynamics, Control, and Accuracy.
DEGREES HELD: BSME University of Massachusetts
MBA Florida Institute of Technology

AUTONOMOUS ACCURACY ENHANCEMENT SYSTEM

T. L. Brosseau, M. D. Kregel, A. F. Baran
U.S. Army Ballistic Research Laboratory
Aberdeen Proving Ground, Maryland

I. INTRODUCTION

Motion of the muzzle of a tank gun tube exists whether due to static conditions, such as uneven heating caused by the sun or the rapid firing of ammunition, or dynamic conditions, such as vibrations when firing on the move caused by the tank treads or the terrain. This motion can have adverse effects on the probability of a weapon system to hit a target. One such weapon system having this accuracy problem, due to motion of the muzzle of the gun tube, is the M1A1 tank using an experimental gun tube. To improve the accuracy of this modified M1A1 tank when firing either stationary or on the move, BRL has developed an Autonomous Accuracy Enhancement System that is easily interfaced to the existing weapon system without major modifications.

II. ANGULAR POSITION IN THE ELEVATION DIRECTION

The angular position of a tank gun tube in the elevation direction was broken up into three angular components as shown in Figure 1. The first angular component, p, was the angular position of the gun shield relative to the line of sight in the elevation direction. The second angular component, d, was the angular difference between the angular position of the gun shield in the elevation direction and the angular position of the breech end of the gun tube in the elevation direction. This angular difference was caused by the clearance between the gun shield and the breech end of the gun tube since the breech end of the gun tube recoiled within the gun shield. The third angular component, b, was the angular position of the muzzle of the gun tube relative to the breech end of the gun tube in the elevation direction. The sum of these three angular components, m, made up the angular position of the muzzle relative to the line of sight in the elevation direction.

III. MEASUREMENT OF ANGULAR COMPONENTS IN THE ELEVATION DIRECTION

The continuous measurement of the three angular components of gun tube angular position in the elevation direction, which were required as inputs to the Autonomous Accuracy Enhancement

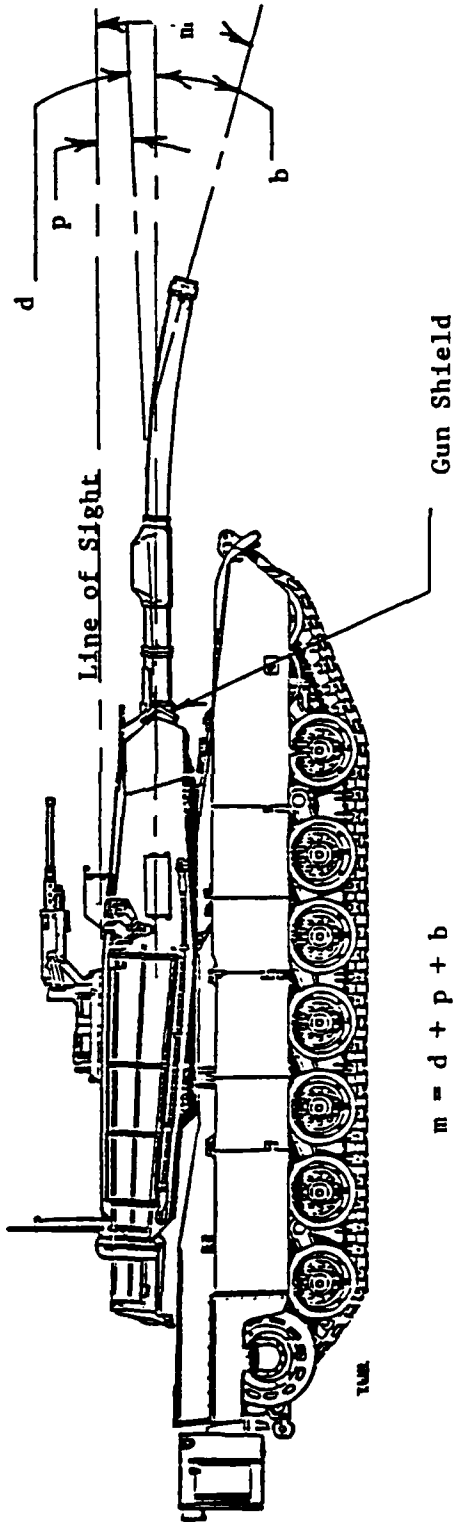

Figure 1. (U) Components Of The Angular Position Of The Gun Tube In The Elevation Direction

System, was accomplished by using three different measuring techniques. The first angular component, p, in the elevation direction was measured using a continuous analog output signal from the elevation servo control system of the tank. This signal called DCT was essentially an error signal between where the sight was pointing in elevation and where the gun shield was pointing in elevation. So whenever this signal was zero the gun shield was pointing in elevation to where the sight was pointing in elevation. The sum of the second and the third angular components, d+b, in the elevation direction was measured using a Tadiran muzzle reference system. The Tadiran was an electro-optical automated collimation system consisting of a transceiver and a mirror. The transceiver was mounted on the gun shield while the mirror was mounted on the muzzle. A collimated infrared light beam was emitted by the transmitter onto the mirror, which reflected it back to the receiver. However since the infrared light source could not be pulsed at a very high rate the output from the Tadiran was not sufficient for firing on the move. Therefore a third continuous measurement of the third angular component, b, in the elevation direction was required for firing on the move. This continuous measurement of the third angular component, b, in the elevation direction was accomplished by spot welding special high temperature strain patches to the top and the bottom of the gun tube as sensors for gun tube bending in the elevation direction. Two sets of strain patches were spot welded to the gun tube at positions in front of and behind the bore evacuator. The outputs from the two sets of patches were summed and averaged to give a single output that was used as a continuous measurement of the angular position of the muzzle of the gun tube relative to the breech end of the gun tube in the elevation direction. Examples of the continuous measurements made while firing on the move are shown in Figures 2 and 3. Figure 2 shows the measurements made prior to firing the first round in a five round run and Figure 3 shows the measurements made prior to firing the fifth round in a five round run. Figure 2 shows that the measurements of the elevation Tadiran and the strain agreed very well at each sample point of the Tadiran before the first round was fired. However Figure 3 shows that the elevation Tadiran measurement had a large downward offset when compared to the strain measurement even though the dynamic response agreed very well at each sample point of the Tadiran. This downward offset was caused by a change in the difference angle, d, which was included in the elevation Tadiran measurement but not in the strain measurement. In order to obtain a continuous measurement of the angular position of the muzzle relative to the gun shield, d+b, in the elevation direction, the elevation Tadiran measurement was repetitively sampled, read, and averaged to obtain a static reference which was then used as a static reference for the strain measurement. The sampling, reading, and averaging was done using the same Pro-Log computer that was used to control the Tadiran pulse laser and the Precision Aim Technique (PAT) firing predictor algorithms.

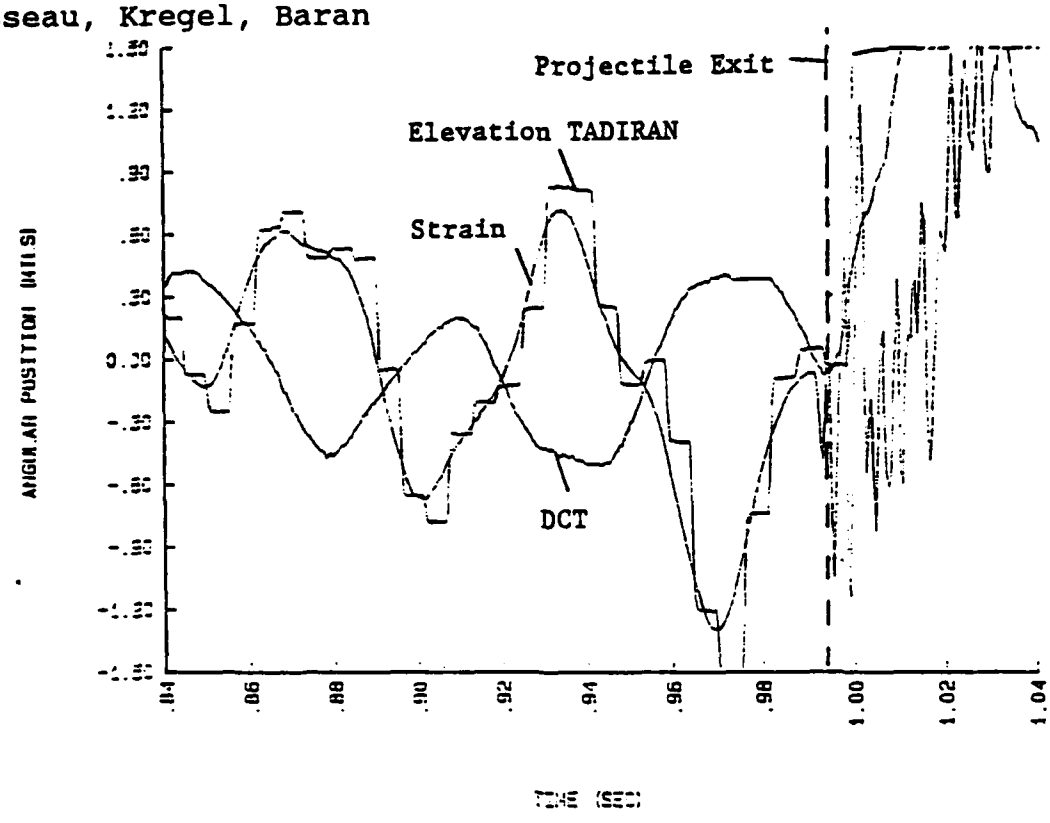

Figure 2. (U) Angular Position For First Round Fired In Run

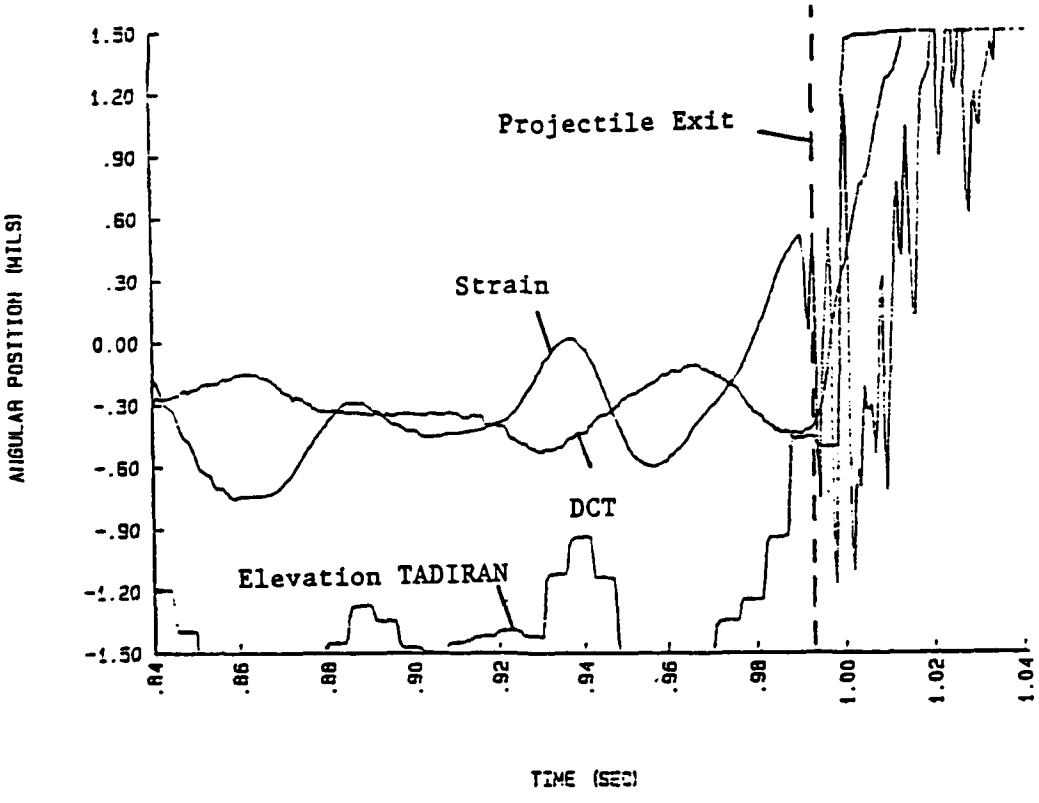

Figure 3. (U) Angular Position For Fifth Round Fired In Run

IV. REPOSITIONING MUZZLE BACK ONTO ELEVATION AIM POINT

Even though a continuous measurement of the angular position of the muzzle relative to the gun shield in the elevation direction was obtained the muzzle of the gun tube was no longer pointing at the elevation aim point, and the PAT elevation firing predictor algorithm might not allow the gun to fire. To move the muzzle of the gun tube back onto the elevation aim point the elevation Tadiran measurement was filtered very heavily to obtain the static offset component of the measurement and this was fed into the DCT circuitry of the tank. This was done with no modifications to the tank circuitry by making a short jumper harness to fit between the turret networks box and the cable that connected to the turret networks box. The measurement of the angular position of the gun shield relative to the line of sight in the elevation direction, the DCT signal, was increased the same amount as the static offset component of the elevation Tadiran measurement was decreased. This made the DCT signal no longer equal to zero and caused the gun tube to elevate until the DCT signal became zero again. This upward elevation of the gun tube repositioned the muzzle back onto the elevation aim point. Once the system was installed, calibrated, and the initial offset taken out of the elevation Tadiran measurement the system essentially became an automatic bore-sight retention system in the elevation direction.

V. PAT ELEVATION FIRING PREDICTOR ALGORITHM

To improve the accuracy of the modified M1A1 tank while firing on the move the PAT elevation firing predictor algorithm was interfaced into the Autonomous Accuracy Enhancement System. The PAT elevation firing predictor algorithm is a computer controlled electronic firing circuit that uses continuous measurement of the elevation angular position of the muzzle relative to the line of sight to control the precise firing time to ensure that the launch of the projectile occurs when the muzzle of the gun tube is at the elevation aim point. A new firing circuit was also used because of an inherent delay between the time when the trigger was depressed to the time when the primer was energized. This was determined to be caused by a relay used in the M1A1 firing circuit. To eliminate this delay a solid state relay was designed that reduced the delay to microseconds. Measurements taken of projectile exit showed that the time measured from the PAT fire pulse to projectile exit was about 10.0 msec for the DM13 round when fired with the new firing circuit.

Results of the previous tests with the M1A1 tank using this experimental gun tube showed that the gun tube experienced higher modes of vibration in the elevation direction that were not seen in the previous tests with the M1 and the M1A1 tanks. These

higher modes of vibrations were not constant over the entire run of the bump course but came and went as the gun tube resonated while the tank was traversing the bump course. The amplitude of these higher mode vibrations were seen to be in excess of +1.0 or -1.0 mil and the combination of the higher mode and high amplitude caused the elevation predictor algorithm to become unacceptable because of the excessive noise levels in the second derivative term of the elevation predictor algorithm. Because of these higher mode, high amplitude vibrations the second derivative term of the elevation predictor algorithm was removed and an additional check was placed in the fire control loop of the elevation predictor algorithm. The additional check did not allow the gun to fire whenever the gun tube was experiencing the higher mode vibration in excess of +0.4 or -0.4 mil in amplitude. This check was accomplished by continually monitoring the derivative of the combined DCT signal and the strain signals. Since the higher mode, high amplitude vibrations came and went at such a rapid rate there was no noticable delay in the firing of the round by the gunner. By using only the first derivative term in the elevation predictor algorithm the maximum prediction time interval was limited to about 5.0 msec at 20.0 Hz instead of the projectile inbore time of about 10.0 msec. However with the additional check required to fire the gun, the error that occurred, by not having the predictor time interval of 10.0 msec, was kept to between +0.2 or -0.2 mil which was well below the ammunition error or the error in trying to hold the sight on target. Examples of the continuous measurements made while firing on the move using the PAT elevation firing predictor algorithm with the additional check in the fire control loop are shown in Figure 4. Shown in Figure 4 are the elevation angular position of the muzzle relative to the line of sight, the PAT predicted elevation angular position of the muzzle relative to the line of sight, and the additional check in the fire control loop prior to firing the second round in a five round run. Figure 4 shows that the additional circuitry functioned properly in not allowing the gun to be fired when the gun tube was experiencing higher mode, high amplitude vibrations.

VI. ANGULAR POSITION IN THE AZIMUTH DIRECTION

The angular position of a tank gun tube in the azimuth direction was broken up into three angular components as shown in Figure 5. The first angular component, p, was the angular position of the gun shield or turret, since they are pinned together, relative to the line of sight in the azimuth direction. The second angular component, d, was the angular difference between the angular position of the gun shield in the azimuth direction and the angular position of the breech end of the gun tube in the azimuth direction. This angular difference was caused by the clearance between the gun shield and the breech end of the gun tube since the breech end of the gun tube recoiled within the gun shield. The third angular component, b, was the

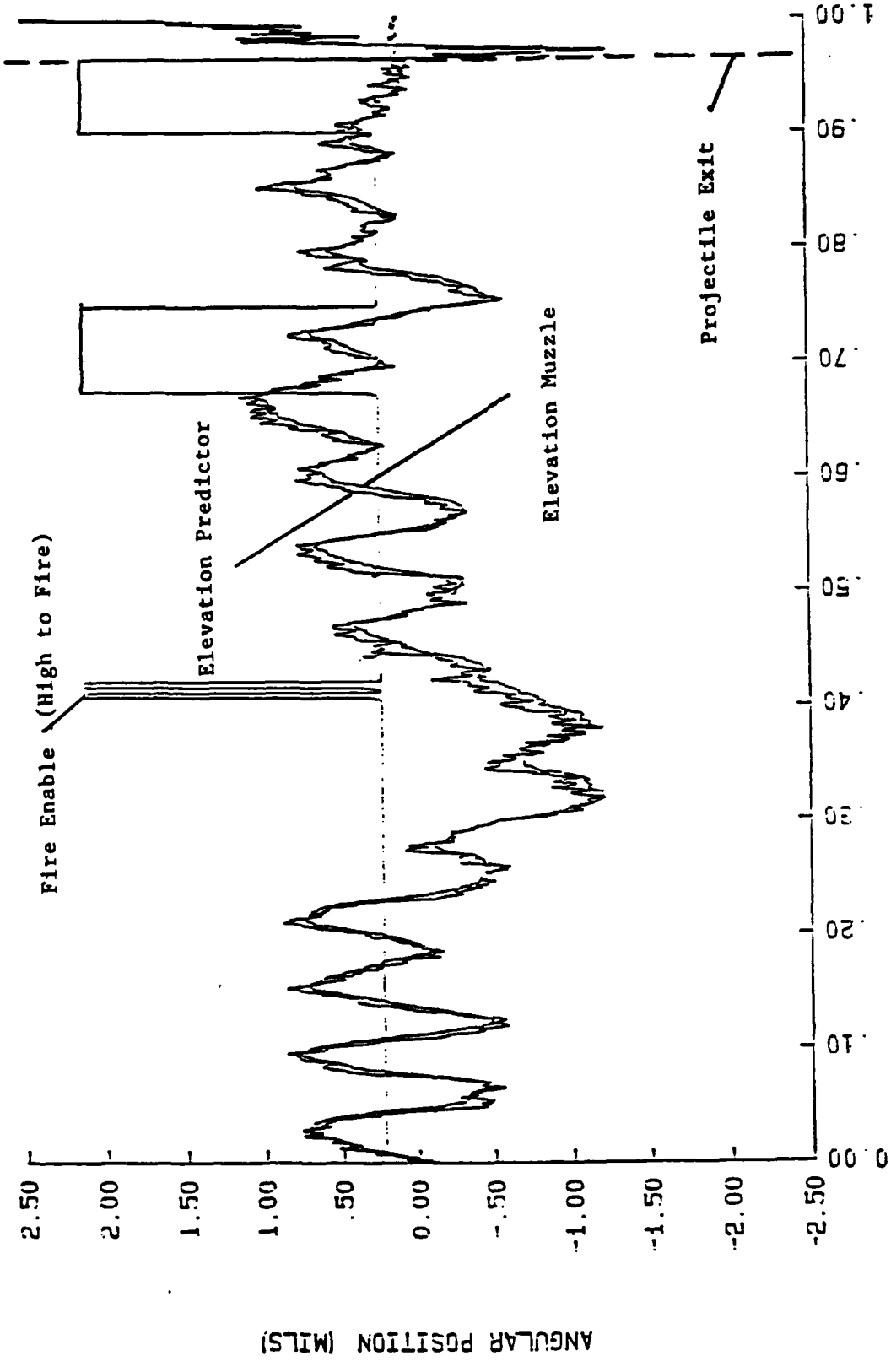

Figure 4. (U) Angular Position For Second Round Fired In Run

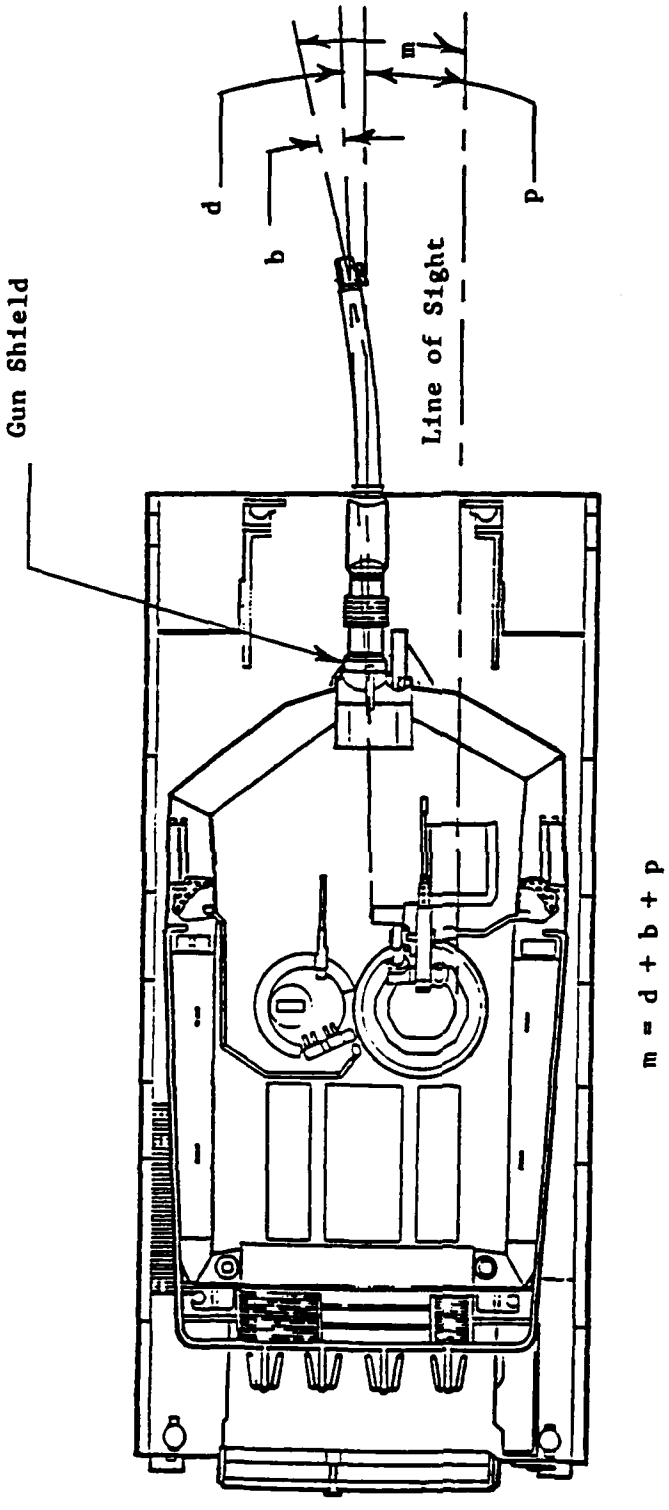

Figure 5. (U) Components Of The Angular Position Of The Gun Tube In The Azimuth Direction

angular position of the muzzle of the gun tube relative to the breech end of the gun tube in the azimuth direction. The sum of these three angular components, m, made up the angular position of the muzzle relative to the line of sight in the azimuth direction.

VII. MEASUREMEN OF ANGULAR COMPONENTS IN THE AZIMUTH DIRECTION

The continuous measurement of the three angular components of gun tube angular position in the azimuth direction, which were required as inputs to the Autonomous Accuracy Enhancement System, was accomplished by using the same measuring techniques that were used in making the measurements in the elevation direction. Since the only component that was stabalized in the azimuth direction was the reticle in the primary sight the first angular component, p, in the azimuth direction was measured using a continuous analog output signal from the azimuth reticle control in the primary sight. This signal called GRC was essentially an error signal between where the azimuth reticle in the primary sight was pointing in azimuth and where the gun turret was pointing in azimuth. So whenever this signal was zero the gun turret was pointing in azimuth to where the azimuth reticle in the primary sight was pointing in azimuth. The sum of the second and the third angular components, d+b, in the azimuth direction was measured using the Tadiran muzzle reference system described previously in the measurements for the components in the elevation direction. Since there was no significant bending of the gun tube in the azimuth direction while firing on the move, the third continuous measurement of the third angular component, b, was not required and therefore the strain patches were not used in the azimuth direction. Examples of the continuous measurements made while firing on the move are shown in Figure 6 and 7. Figure 6 shows the measurements prior to firing the first round in a five round run, and Figure 7 shows the measurements prior to firing the fifth round in a five round run. The GRC measurements shown in Figure 6 and 7 show that the frequency of the angular position of the turret relative to the line of sight in the azimuth direction was very low because of the massive turret through which the motion had to be transmitted. The azimuth Tadiran measurements shown in Figures 6 and 7 show that there was no significant bending of the gun tube in the azimuth direction while firing on the move. However the azimuth Tadiran measurements also show that there was a significant change in the azimuth angular position of the muzzle relative to the turret, d+b, between the firing of the first round and the firing of the fifth round.

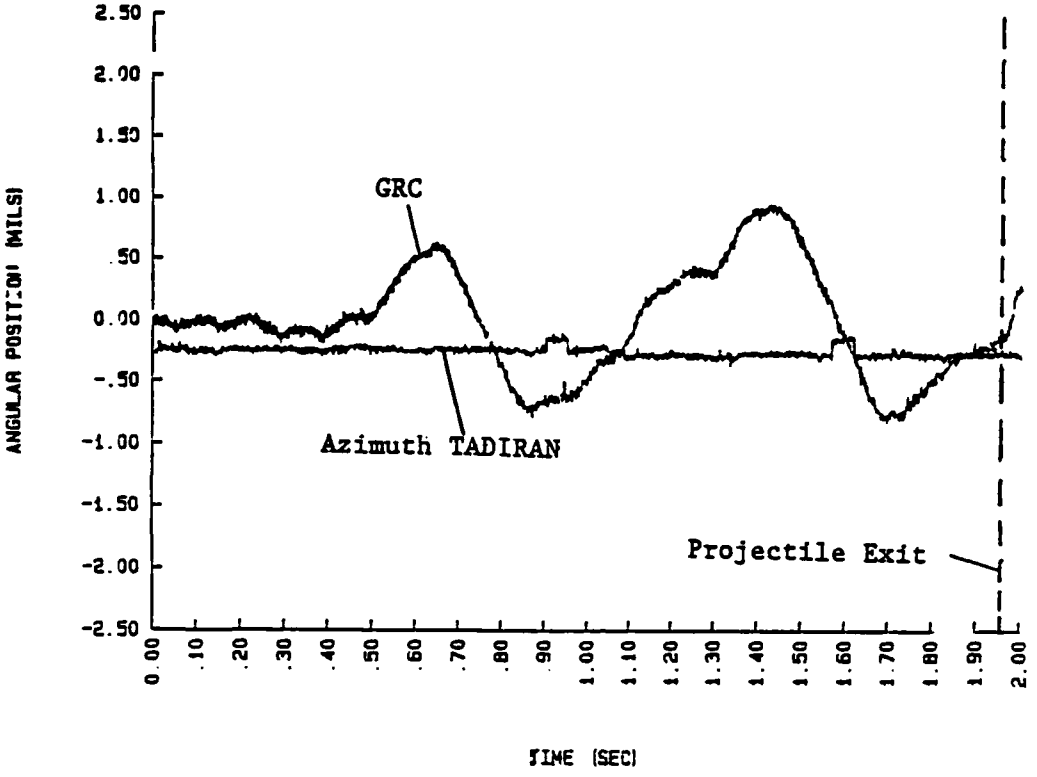

Figure 6. (U) Angular Position For First Round Fired In Run

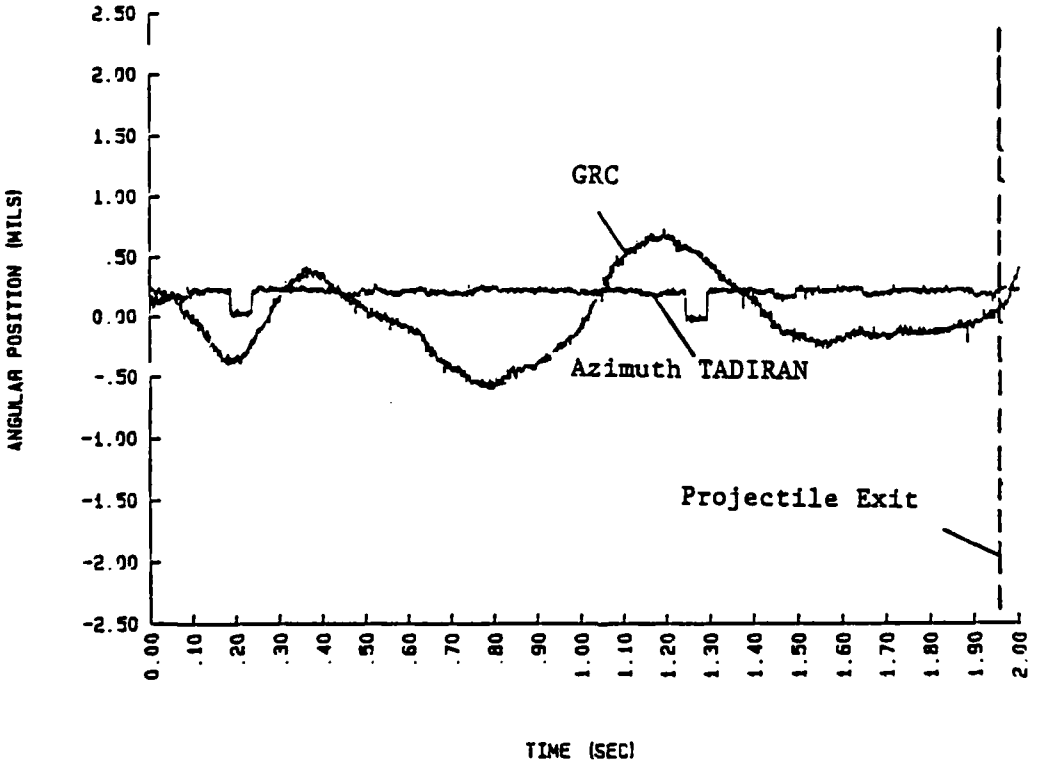

Figure 7. (U) Angular Position For Fifth Round Fired In Run

VIII. REPOSITIONING MUZZLE BACK ONTO AZIMUTH AIM POINT

Even though a continuous measurement of the angular position of the muzzle relative to the gun shield in the azimuth direction was obtained the muzzle of the gun tube was no longer pointing at the azimuth aim point, and the PAT azimuth firing predictor algorithm might not allow the gun to fire. To move the muzzle of the gun tube back onto the azimuth aim point the azimuth Tadiran measurement was filtered very heavily to obtain the static offset component of the measurement and this was fed into the GRC circuitry of the tank. This was done with no modifications to the tank circuitry by using the same short jumper harness to fit between the turret networks box and the cable connected to the turret networks box that was made for the elevation repositioning circuitry. The measurement of the angular position of the gun turret relative to the line of sight in the azimuth direction, the GRC signal, was increased the same amount as the static offset component of the azimuth Tadiran measurement was increased. This made the GRC signal no longer equal to zero and caused the reticle in the primary sight to move to the left until the GRC signal became zero again. The gunner then simply and unknowingly repositioned the reticle back onto the azimuth aim point which in turn moved the muzzle of the gun tube back onto the aim point. Once the system was installed, calibrated, and the initial offset taken out of the azimuth Tadiran measurement the system essentially became an automatic bore-sight retention system in the azimuth direction.

IX. PAT AZIMUTH FIRING PREDICTOR ALGORITHM

To improve the accuracy of the modified M1A1 tank while firing on the move the PAT azimuth firing predictor algorithm was interfaced into the Autonomous Accuracy Enhancement System. The PAT azimuth firing predictor algorithm is a computer controlled electronic firing circuit that uses continuous measurement of the azimuth angular position of the muzzle relative to the line of sight to control the precise firing time to ensure that the launch of the projectile occurs when the muzzle of the gun tube is at the azimuth aim point. Since there was no significant bending of the gun tube in the azimuth direction while firing on the move, the only continuous measurement that was required for the PAT azimuth firing predictor algorithm was the azimuth angular position of the turret relative to the line of sight, the GRC signal. Since the turret was so massive the frequency of the GRC signal while firing on the move was very low. Therefore only one derivative term was required in the PAT azimuth firing predictor algorithm to predict over the full 10.0 msec of the projectile inbore time. However because the frequency of the GRC signal was so low the firing window of the azimuth predictor had to be increased from the +0.05 or -0.05 mil of the elevation

predictor to +0.2 or -0.2 mil because there would be noticable delays in firing of the round by the gunner due to only a few zero crossings of the muzzle. This larger firing window in azimuth was still well below the ammunition error or the error in trying to hold the sight on target.

X. FIRING TESTS WITH DM13 AMMUNITION

Firing on the move tests were conducted at the TECOM, H-Field facility at APG-EA. Before the on the move tests were started the gun tube was bore-sighted using a muzzle scope, and the Tadiran signals in both elevation and azimuth were zeroed. Once the Tadiran signals had been zeroed no further bore scoping, zeroing, or other adjustments were made throughout the tests. The on the move tests were started with the M1A1 tank using the experimental gun tube positioned 1500.0 meters from the target. The tank was then driven over the bump course at a constant velocity of 11.0 mph, and five rounds were fired approximately 10.0 seconds apart while the tank was traversing the bump course. Two runs were made with the M1A1 tank using this experimental gun tube interfaced with the PAT electronics, the Tadiran system, and the additional circuitry. The impact of each round was recorded on a target downrange.

XI. CONCLUSIONS

Measurements of the impacts on target indicated that the accuracy of the M1A1 tank using this experimental gun tube, while firing on the move, with the Autonomous Accuracy Enhancement System, had been improved to equal the accuracy of the M1A1 tank using the standard gun tube while firing bore-sighted stationary shots.

BUNDY

TITLE: THERMAL DISTORTION IN CONVENTIONAL RECOIL MOUNTS

MARK L. BUNDY
U.S. ARMY BALLISTIC RESEARCH LABORATORY
ABERDEEN PROVING GROUND, MD 21005-5066

ABSTRACT:

Conventional gun barrel recoil mounts support the weight of the gun barrel from below, at either end of the mount. The heat transfer rate through the lower, load bearing surface in these areas is much greater than through the upper contact surface, which is separated from the barrel by the diametrical tolerance necessary to remove the barrel from the mount. The uneven cooling that takes place in these regions (after firing) gives rise to cross-barrel and cross-mount temperature differences, which in turn leads to uneven thermal expansion, and hence distortion of the barrel and mount.

This paper reports the temperature and displacement measurements that were taken along an M256, 120 mm tank gun barrel and mount as they cooled. A finite element thermal expansion model was created, using the measured temperatures, to estimate the local barrel bending in areas not accessible to displacement measurement. The experiment and model agree fairly well where they overlap. The most notable change was in the breech angle, which dropped -0.2 milliradians. The use of a gunner's quadrant (which rests on the breech) under these conditions, would introduce a similar angular error into the gun elevation measurement. Furthermore, the curvature of the barrel centerline was found to change by 0.25-0.30 mils in the region from the breech to the thrust nut. In general, such a centerline change will affect projectile jump, and thus "fall of shot." A thermally symmetric mount would eliminate these adverse effects.

BIOGRAPHY:

PRESENT ASSIGNMENT: Research Physicist, Fluid Physics Branch, Launch and Flight Division, Ballistic Research Laboratory, Aberdeen Proving Ground, MD., 21005-5066.

PAST EXPERIENCE: Eight years experience at U.S. Army BRL, expertise in gun barrel heating and thermal distortion.

DEGREES HELD: B.A. in Math & Physics, Augsburg College, Mpls., MN. (1972) / M.S. in Physics, Drake Univ., Des Moines, IA. (1975) / Ph.D. in Physics, Univ. of Maine, Orono, ME. (1980).

THERMAL DISTORTION IN CONVENTIONAL RECOIL MOUNTS

MARK L. BUNDY
U.S. ARMY BALLISTIC RESEARCH LABORATORY
ABERDEEN PROVING GROUND, MD 21005-5066

INTRODUCTION

As the barrel temperature rises from firing, air convection currents flow into and out of the barrel through the muzzle, as well as recirculate from the bottom of the bore to the top. Such a flow pattern cools the bottom of the barrel faster than the top, which is found to be the primary cause of tank gun thermal droop, Bundy (1).

The results of laboratory heating and cooling experiments show that the top-minus-bottom barrel temperature difference generally diminishes in going from the muzzle to the recoil mount. It was therefore a surprise to find an increase in this temperature difference when it was measured (inside the recoil) during the cool down phase of a live fire test, Fig. 1. At the same time, further probing revealed a large reverse temperature gradient across the recoil mount in the forward load bearing region.

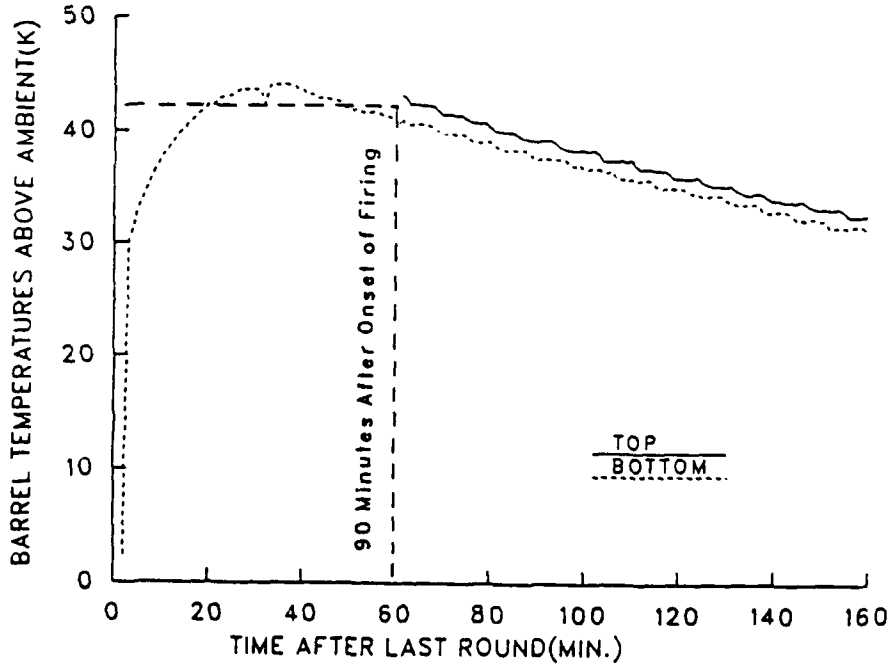

Figure 1. In-Bore Surface Temperatures (Top & Bottom) at 1.0 m from Breech.

This paper will present temperature and displacement measurements, as well as finite element thermal modeling, which leads to the conclusion that uneven barrel cooling is due to asymmetric heat conduction, not convection, within the recoil mount. Moreover, these temperature differences produce substantial distortion of the barrel centerline and breech. Even the recoil mount undergoes thermal distortion, particularly near the front, load bearing region.

EXPERIMENTAL MEASUREMENTS

To study cross-barrel temperature differences over the 1.9 m portion of the M256, 120 mm gun barrel which extends inside the recoil mount, a 1.7 m long internal barrel heater was used, Bundy (2). After 20 minutes of heating, followed by 45 minutes of cooling (to dissipate transient temperature gradients created by the presence, and subsequent removal, of the barrel heater), the barrel and mount temperatures were roughly the same as those measured (Fig. 1) 60 minutes after the last of a 25 round group was fired. Viewed in another context, it is estimated (using a barrel heating model, Bundy (3)) that this barrel temperature could also to be reached and maintained by firing 1 round every 15 minutes, see Fig. 2. Barrel temperature measurements were recorded in the recoil section of the barrel by sliding a spring loaded, two-ended, thermocouple device down the bore. External temperatures on the mount were also recorded.

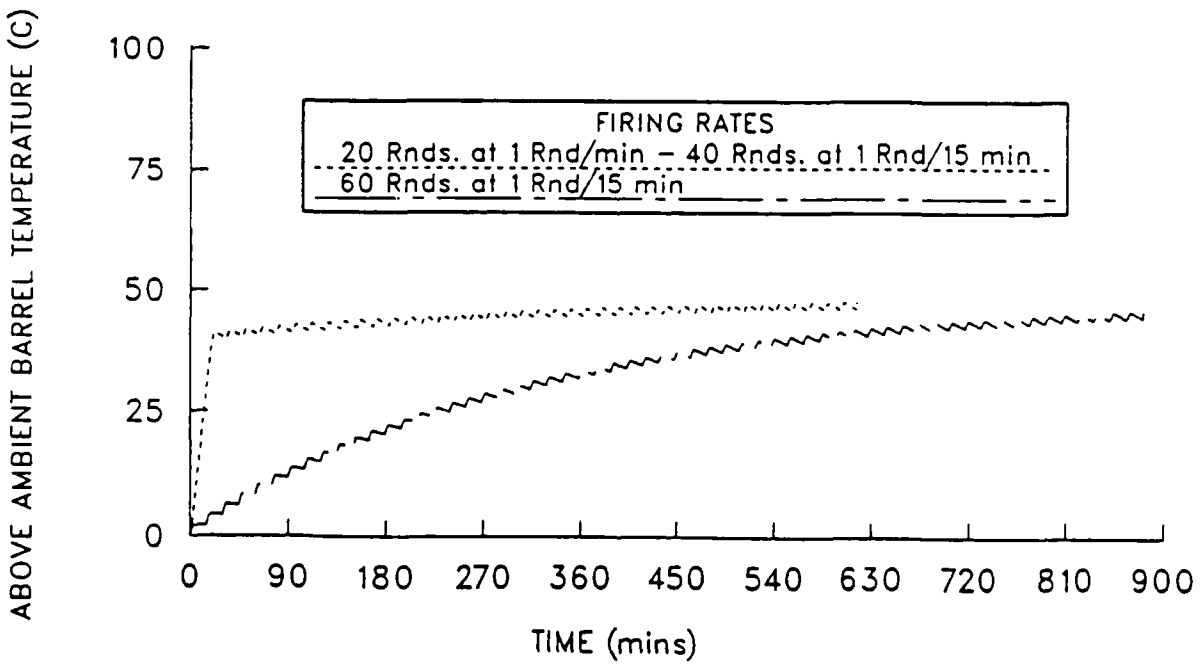

Figure 2. Estimated Barrel Temperature (from Bundy (3)), at 1.0 m from Breech, for Sustained Firing Rates (Two Cases) of One Round Every Fifteen Minutes.

To obtain information on the thermal distortion, (two) 20 power scopes were affixed to the recoil mount and (one) to the breech; also, one 8 power scope was placed in the bore at the muzzle;, and one (displacement) dial indicator was positioned to measure the vertical movement of the mount in the forward load bearing region. This instrumentation is diagramed in Fig. 3.

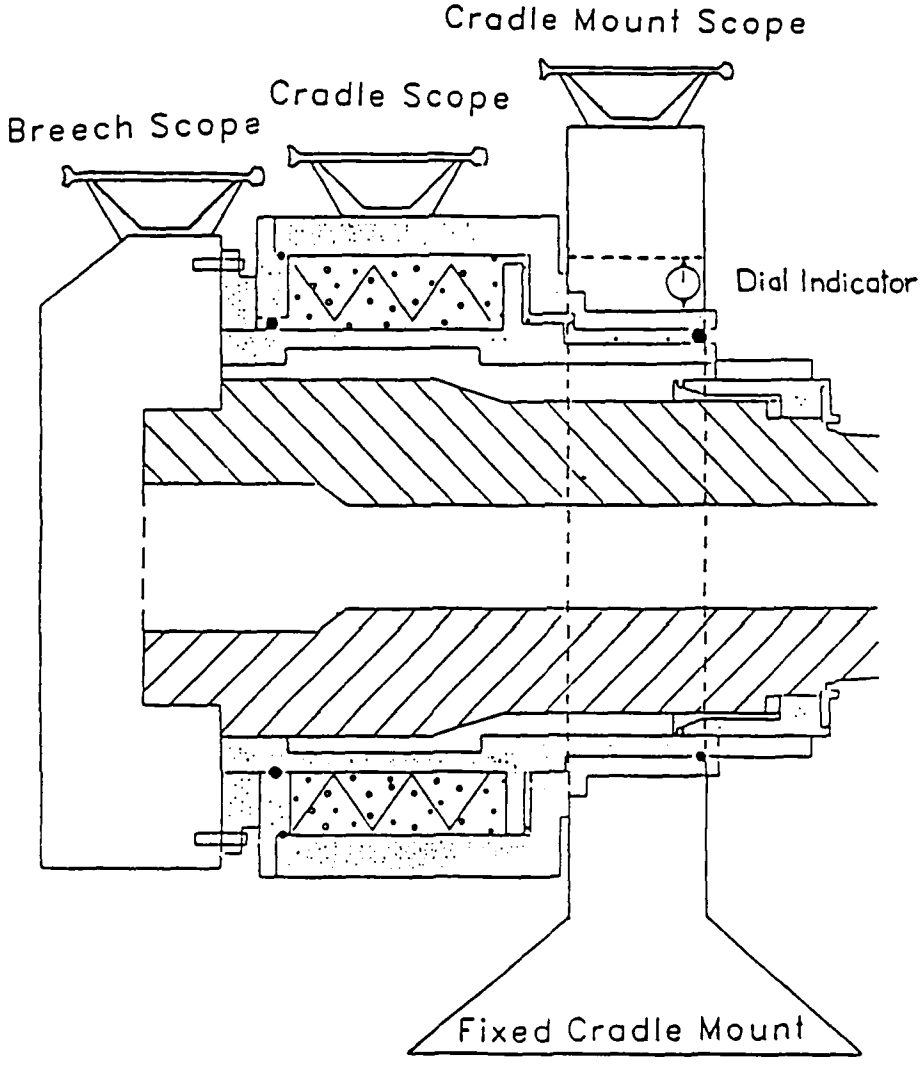

Figure 3. Positioning of Angular Distortion Instrumentation.

For comparison purposes the experiment was repeated, but this time the entire barrel was heated. The same temperature and displacement measurements were taken 45 minutes after the heater was removed. To maintain consistancy, the heater was applied along the entire barrel so as to create (after a 45 minute cool down phase) a barrel temperature that closely matched the asymptotic predictions of the (aforementioned) barrel heating model for a firing rate of 1 round every 15 minutes, see Fig. 4.

BUNDY

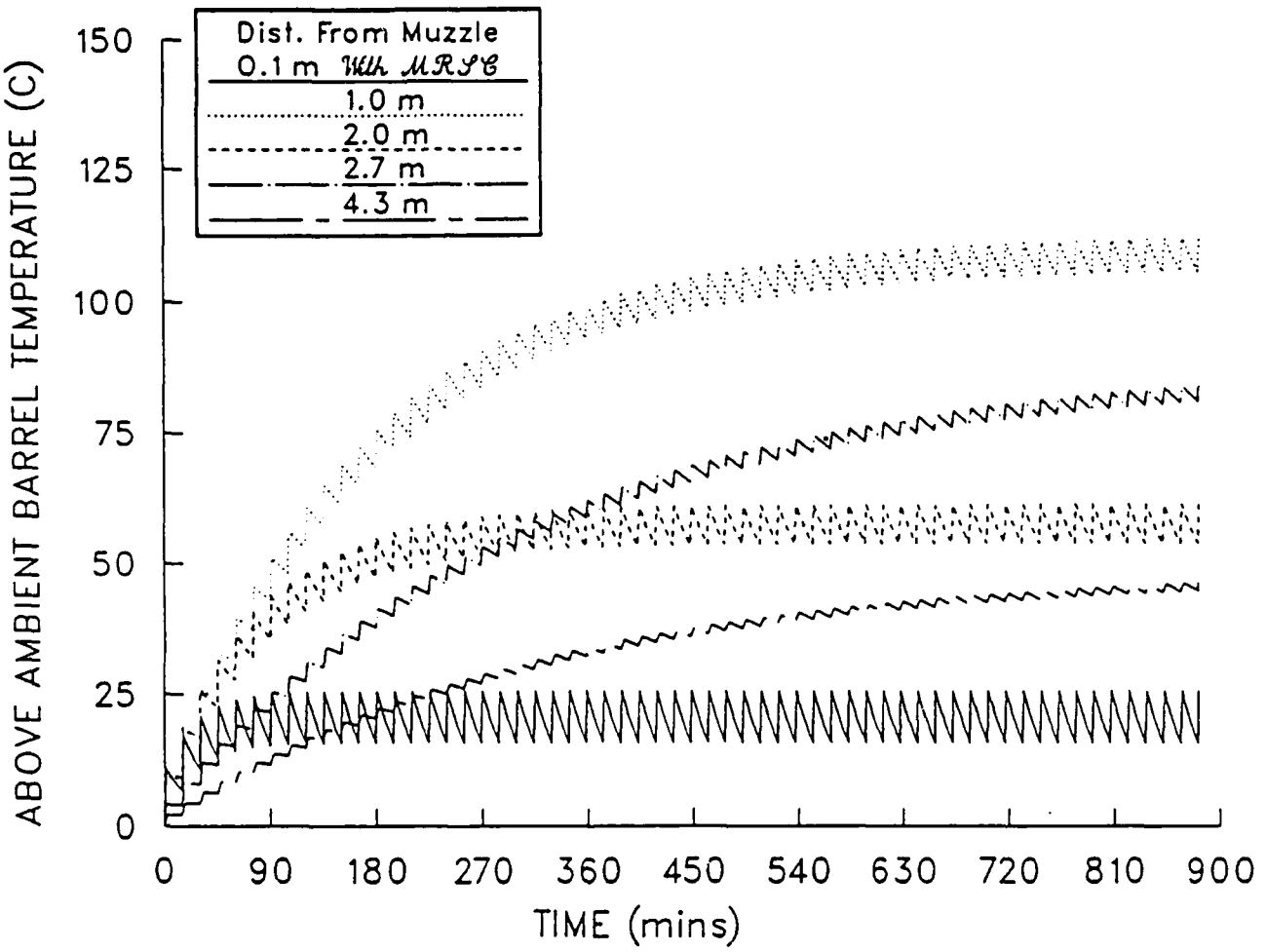

Figure 4. Estimated Barrel Temperatures (from Bundy (3)), at Five Locations, for Firing One Round Every Fifteen Minutes.

EXPERIMENTAL RESULTS

The vertical cross-barrel temperature difference measured along the entire bore length, Fig. 5, reveals that cooling asymmetries in the recoil region are as large, or larger, than anywhere else along the barrel. Moreover, they peak in the two load bearing regions. At the same time, the temperature difference across the mount is reversed, being hotter on the bottom than the top, at least in the load bearing areas.

When the heat was applied only in the recoil portion of the barrel, the breech angle dropped -0.2 (+/- 0.02) mils, and the muzzle angle dropped -0.08 (+/- 0.05) mils. The recoil mount elevated +0.05 (+/- 0.02) mils behind the trunnions, and +0.3 (+/- 0.03) mils ahead of the trunnions, Fig. 6. On the other hand, when the entire barrel was heated, the only notable difference occurred in the muzzle angle, which dropped to -0.81 mils.

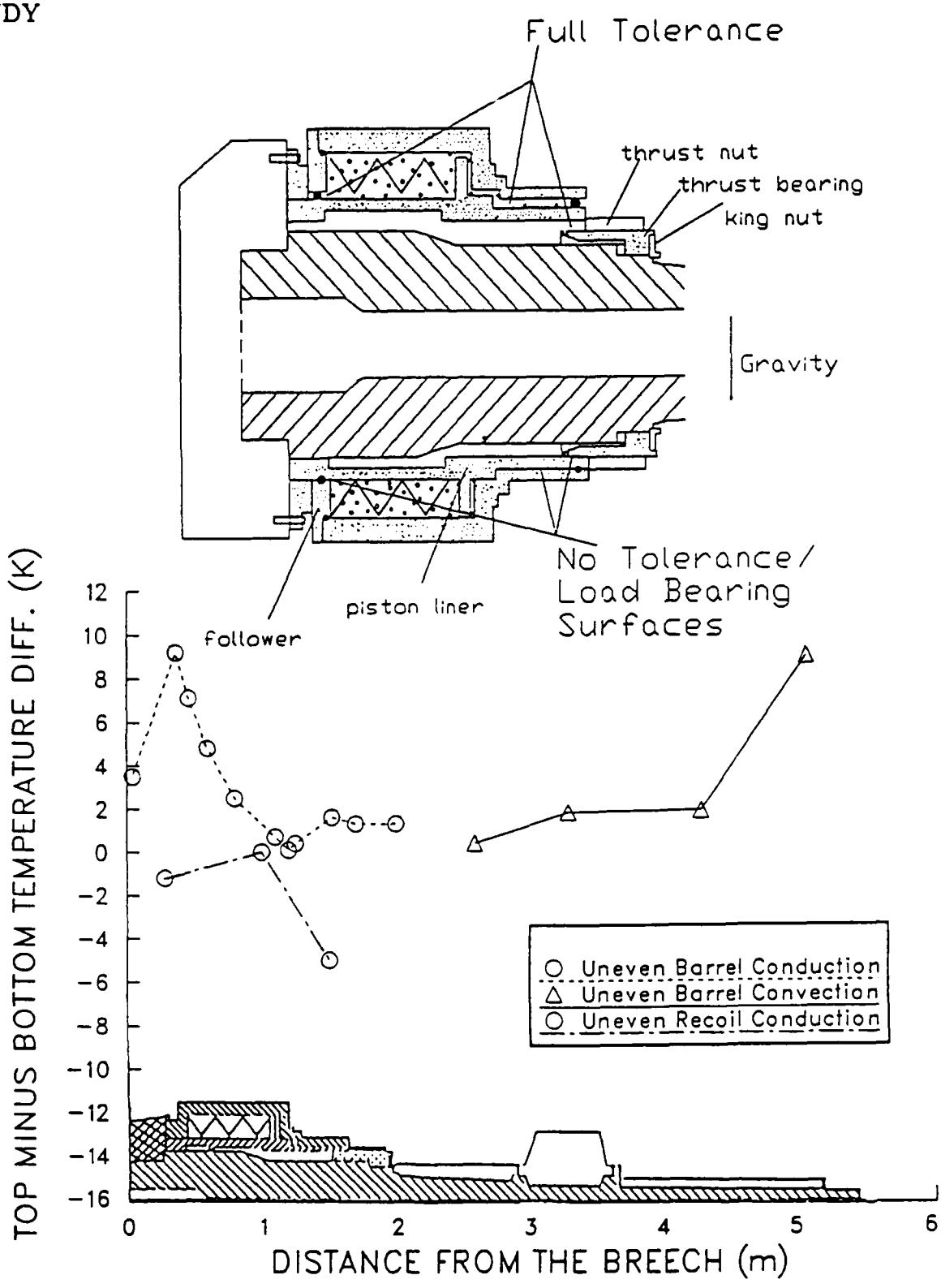

Figure 5. Cross-Barrel and Cross Mount Temperature Differences.

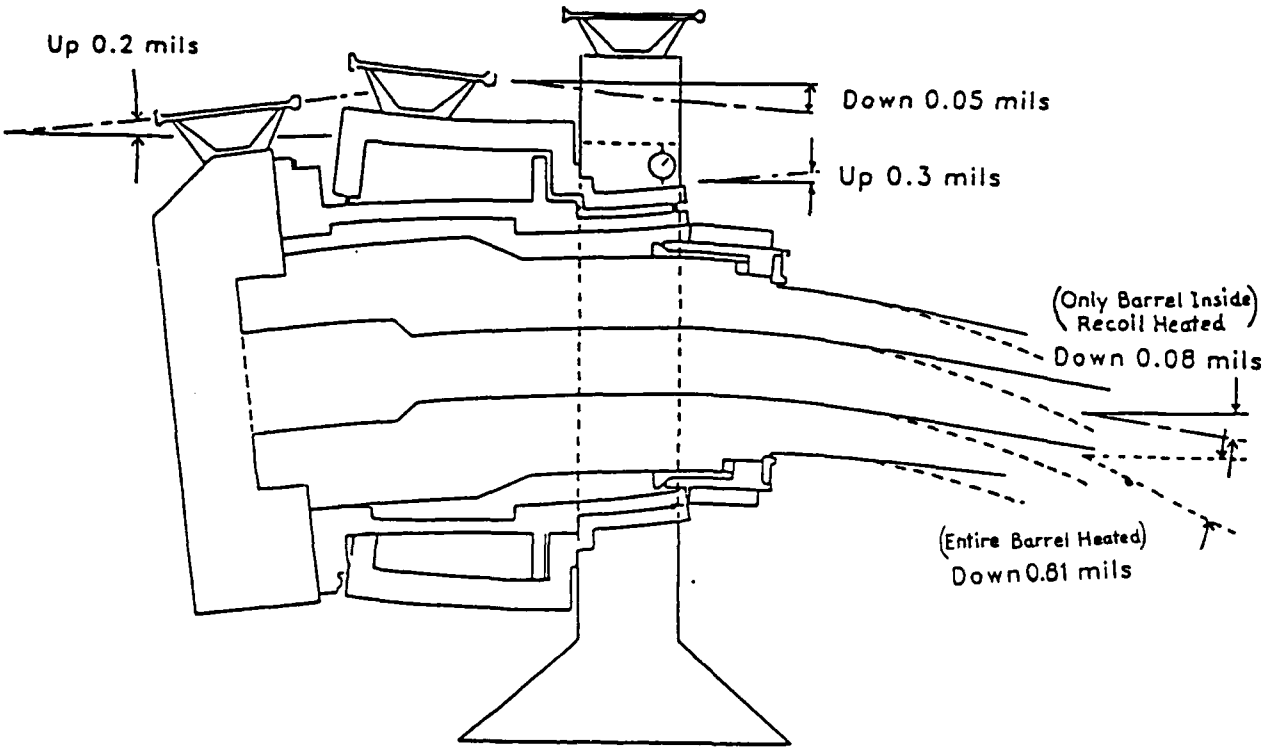

Figure 6. Measured Distortion Angles Due to Uneven Cooling.

FINITE ELEMENT MODELING (FEM)

As a check, and to obtain an estimate of the barrel bend inside the recoil mount, a finite element thermal analysis was performed. The particular modeling program used is called SuperSAP (an offshoot of a much older program called SAP IV, developed in the late 1960's at the University of California at Berkeley, SuperSAP is marketed by Algor Interactive Systems, Inc (4)).

The recoil mount consists of an outer recoil cradle, which remains stationary when the barrel recoils, and a recoil piston liner, which recoils with the barrel. Briefly (cf. Fig. 5), the barrel is slid through the piston liner and the breech attached. The barrel thrust nut is then turned against the front face of the piston liner, which draws the breech forward until it butts against the rear face of the piston liner. This locks the barrel and piston liner together as a recoiling unit, henceforth abbreviated as the barrel-piston. The recoil cradle, piston liner, and gun barrel were modeled separately, and then grafted together. Left-right symmetry was utilized to model only half of the barrel and mount, with boundary conditions prohibiting mass transfer across the plane of symmetry. The final combined system, consisted of 399 nodes, and 156, 8-node brick elements.

To spatially fix the system, 14 boundary elements were applied in two concentric semicircular arcs, in the area where the recoil cradle would bolt to the trunnion rotor. The stiffness of the boundary elements (essentially) prevented the cradle nodes, to which they were attached, from moving. When the recoil piston liner was grafted to the barrel, adjacent nodes were joined together to form a one-piece barrel-piston system, except where an air gap between the two was physically appropriate. However, in grafting the barrel-piston system into the recoil cradle, nodal joining was prohibited. Because SuperSAP did not have any roller-bearing-like elements to interface between the barrel-piston system and the recoil cradle, two small truss elements were used in the front and rear load bearing areas to loosely fix the barrel-piston system within the recoil cradle. Dimensionally, the truss elements were made physically small to insure that they would have a minimal effect on constraining relative thermal expansion between the barrel-piston and the cradle.

The assignment of nodal temperatures was based on the experimental measurements used to construct Fig. 5. Interpolation and extrapolation were used to make temperature assignments where experimental data were not available. Thermal expansion was computed/predicted based on the prescribed temperature distribution. For ease of visualization, the thermal distortion (magnified 1000 times) is shown in Fig. 7 at an oblique angle for each of the three recoil system components, viz., the cradle, piston liner, and barrel, as well as the combination. Figure 8 shows the computed angular changes, along with the corresponding observed angular changes, from Fig. 6. The predicted and observed values are within the experimental error at all positions except where the dial indicator was used. At this position, the measured value is about three times as large as that predicted. However, finite element analysis reveals that 55% of the dial indicator deflection should be attributed to radial thermal expansion. If only 45%, or 0.14 mils, is due to mount bending, then this is much closer to the FEM prediction of 0.10 mils.

CONCLUSIONS

Conventional gun mounts support the weight of the barrel from below, leaving on top the diametrical tolerance necessary to remove the barrel from the mount. This leads to asymmetric conduction of firing-generated heat out of the barrel and into the mount through the lower, load bearing surfaces. This, in turn, produces cross-barrel and cross-mount temperature differences, which lead to uneven thermal expansion that distorts both the barrel and mount.

The barrel distortion directly affects the projectile trajectory by changing the muzzle pointing angle. It indirectly affects the trajectory by changing the barrel centerline, which is known to change the projectile jump. The barrel distortion also effects any breech-mounted barrel sight, such as the gunner's quadrant. Likewise, but to a lesser degree, the mount distortion will affect recoil-mounted barrel sights, like the gunner's auxiliary sight, or the recoil-mounted Wye Scope (used in fixed-mount tests). To minimize these trajectory and sight-line disturbances, a thermally symmetric recoil mount is needed, such as one that supports the weight of the barrel from the sides.

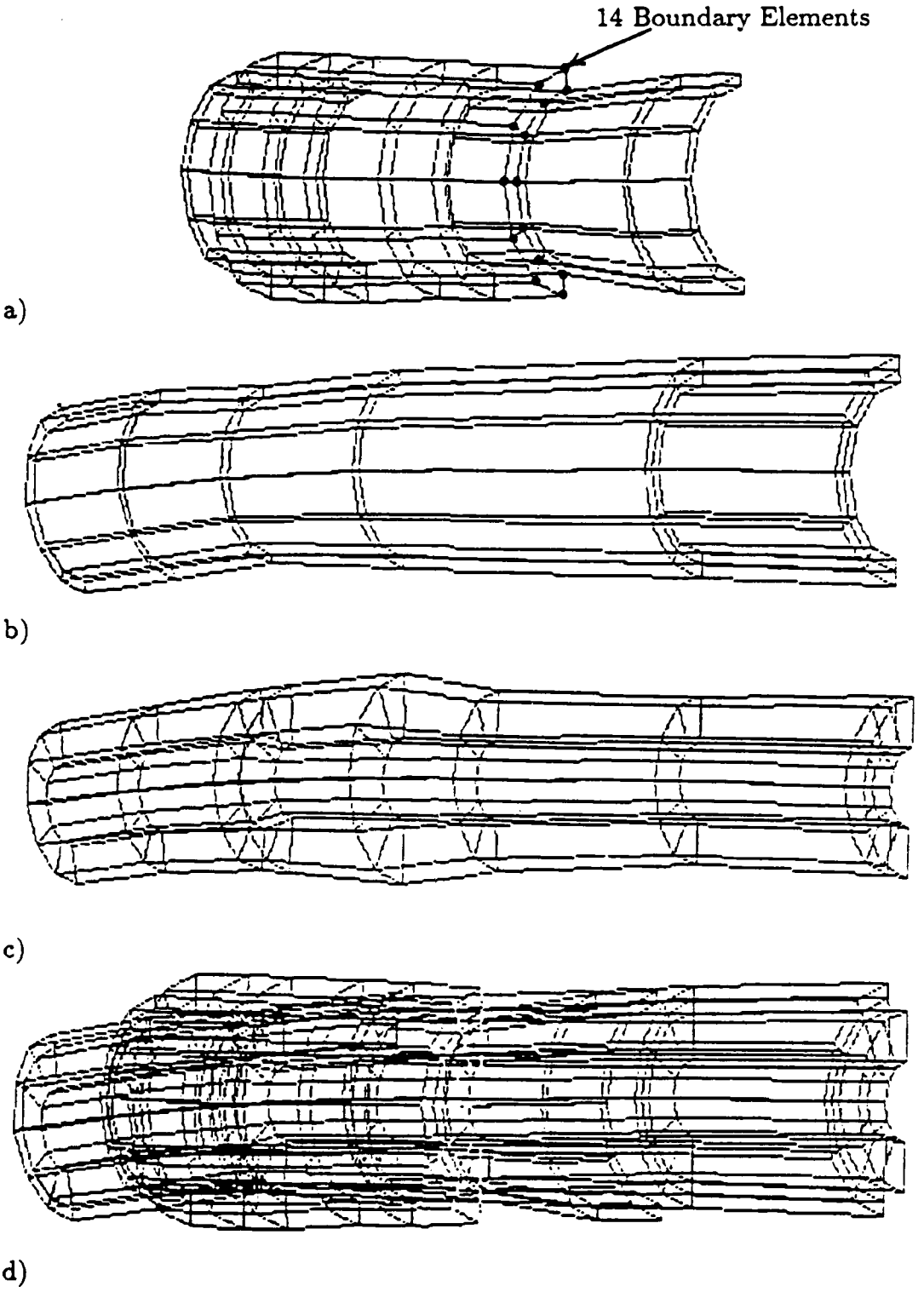

Figure 7. Thermal Distortion of a) Recoil Cradle (Showing Location of Boundary Elements); b) Piston Liner; c) Gun Barrel; and d) Combined System.

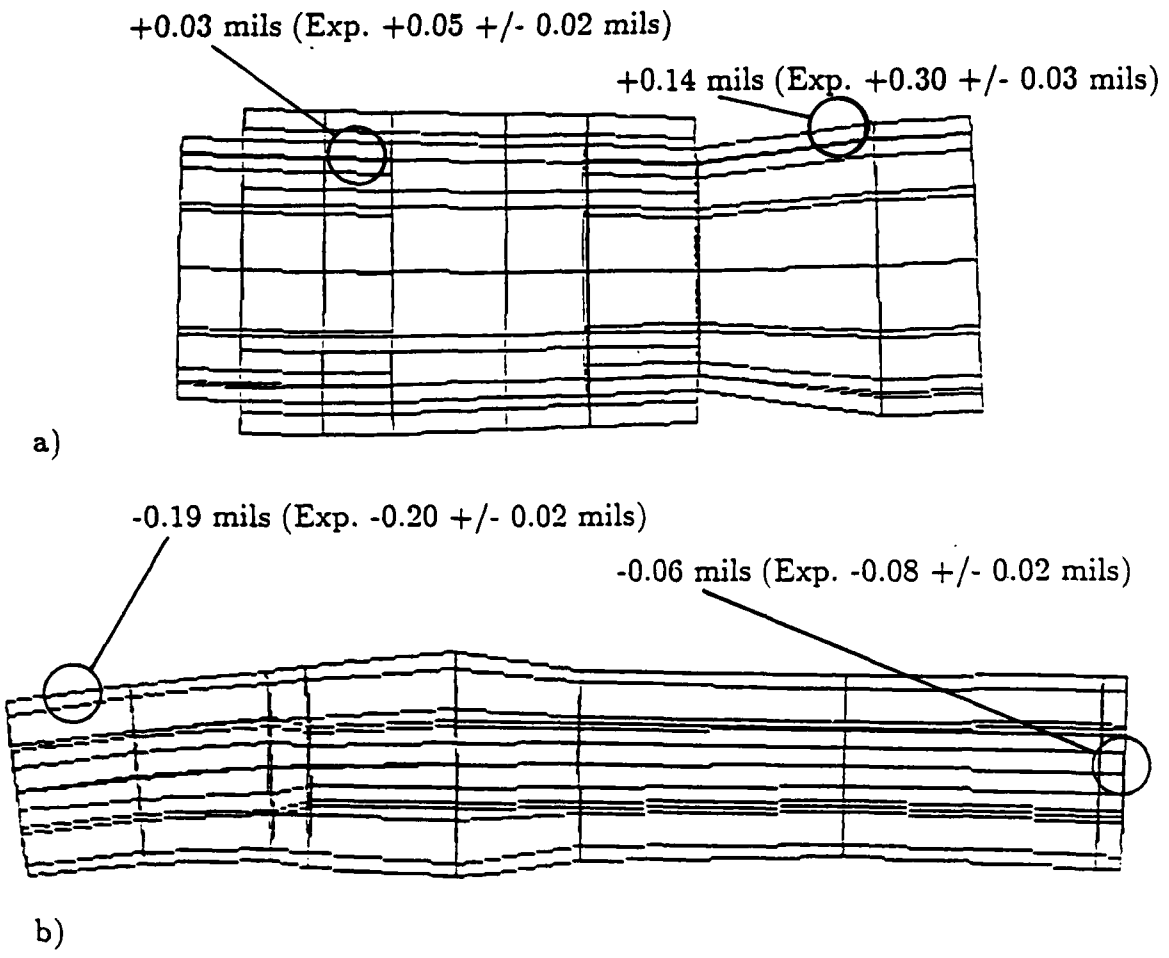

Figure 8. Comparison of FEM Computed Thermal Distortion With Experimental Observations (From Fig. 6), Along a) the Recoil Cradle, and b) the Barrel

REFERENCES

(1) Bundy, M.L., "Gun Barrel Cooling and Thermal Droop Modeling," U.S. Army Ballistic Research Laboratory Report (To be Published), Aberdeen Proving Ground, MD. (1990).

(2) Bundy, M.L., "Non-Firing Tests for Thermal Evaluation of Tank Cannon Components," Proceedings of the Test Technology Symposium III (To be Published), sponsored by U.S. Army Test and Evaluation Command, Aberdeen Proving Ground, MD. (1990).

(3) Bundy, M.L., "Barrel Heating Model," Proceedings of the 12th International Symposium on Ballistics (To be Published), sponsored by American Defense Preparedness Association, Arlington, VA. (1990).

(4) Algor Interactive Systems, Inc., Essex House, Essex Square, Pittsburgh, Pa., 15206.

SESSION III:

THE MOTION OF GUN TUBES - THEORY

KINGSBURY and TSAY

TITLE: Mode Coupling of Gun Tubes Caused by Space Curvature and Initial Twist

Herbert B. Kingsbury and Huoy-Shyi Tsay
Department of Mechanical Engineering
University of Delaware, Newark, DE 19711

ABSTRACT:

This paper formulates the equations of motion for a gun tube with arbitrary space curvature and cross section geometry and presents results showing the effects of curvature, torsion, and cross section shape on natural frequencies and mode shapes.

Expressions for the kinetic and potential energy functions of a curved and twisted tube are formulated in terms of centerline displacements and cross section rotations. These expressions are first used to derive the equations of motion and natural boundary conditions using Hamilton's Principle. The equations of motion are then specialized for various variations of centerline curvature, torsion and corss section shape along the tube axis.

Next, the kinetic and potential energy functions are used to formulate a Rayleigh-Ritz solution for the mode shapes and natural frequencies of helical tubes with fixed-free ends. The effects of space curvature and torsion and of cross section out-of-roundness on frequencies and mode shapes are examined.

The natural frequencies and mode shapes of tubes are found to be significantly affected by even a slight change in values of the curvature and torsion parameters. The fundamental frequencies and the degree of coupling among the displacement variables in natural modes always increased when either curvature parameter was increased. Out-of-roundness also introduces coupling among the displacement variables in the natural modes.

BIOGRAPHY:

PRESENT ASSIGNMENT:

Professor, Department of Mechanical Engineering,
University of Delaware, Newark, DE.

PAST EXPERIENCE:

Assistant Professor, Pennsylvania State University, State College, PA (1966-1968), Engineer with General Electric Company, Missile and Space Division, Philadelphia, PA (1964-1966), Scientist with Dyna-Structures Inc., Springfield, PA (1961-1964).

DEGREES HELD:

B.S.M.E., University of Connecticut (1958).
M.S.M.E., University of Pennsylvania (1960).
Ph.D. E.M., University of Pennsylvania (1964).

MODE COUPLING OF GUN TUBES CAUSED BY SPACE CURVATURE AND INITIAL TWIST

Herbert B. Kingsbury*
Huoy-Shyi Tsay
Department of Mechanical Engineering
University of Delaware, Newark, Delaware 19716

INTRODUCTION

In this study, a gun tube is modeled as a rod of arbitrary cross section with three dimensional space curvature. The problem of vibration of rods curved in a plane, especially circular arcs, has been the subject of a large number of investigations. This type of curvature results in mode shapes in which lateral, out-of-plane, motion is coupled with twisting and in which in-plane axial and transverse displacements are coulped.

One of the seminal treatments of the derivation of equations on the motion of rods with initial curvature appears in the text on elasticity by Love [1]. Although restrictive forms of Love's equations are used directly or are re-derived by subsequent investigators [2-5] for small amplitude vibration of rods curved in circular arcs, there are deficiencies in Love's work which render his strain-displacement equations unsuitable as the starting point for a general examination of the motion of rods with space curvature.

Love's displacement was recently re-examined by Kingsbury [6], who employed a completely general set of small strain but large displacement and rotation strain-displacement equations with no a priori assumptions regarding the structural action or mode of deformation of a gun tube. Thus, the functional form of the displacement components was unspecified. Kingsbury's technical theory of a curved gun tube thus provides the starting point for this study.

LINEARIZED STRAIN-DISPLACEMENT EQUATIONS

Linearized strain-displacement equations for a general curved and twisted gun tube are presented in a paper by Kingsbury [6]. These equations were based on the assumptions employed in the strength of material formulations for the bending and twisting of a curved and twisted gun tube. It was assumed that a typical cross section would be unchanged in size and shape after the structure was deformed, and each cross section was assumed to undergo a small rotation around each of the three coordinate axes while its centroid was displaced along each of

these axes; the resulting linearized strain-displacement equations are

$$\varepsilon_{xx}=\varepsilon_{yy}=\varepsilon_{xy}=0 \quad , \tag{1a}$$

$$\varepsilon_{zz}=\frac{\partial w_o}{\partial z}-x\frac{\partial \alpha_y}{\partial z}-y\frac{\partial \alpha_x}{\partial z}-\kappa_o(u_o-y\phi) \quad , \tag{1b}$$

$$2\varepsilon_{xz}=\frac{\partial u_o}{\partial z}-\alpha_y-\lambda_o v_o+\kappa_o w_o+y\left(\kappa_o\alpha_x-\frac{\partial \phi}{\partial z}\right)-x(\lambda_o\phi+\kappa_o\alpha_y) \quad , \tag{1c}$$

$$2\varepsilon_{yz}=\frac{\partial v_o}{\partial z}+\lambda_o u_o+\alpha_x+x\frac{\partial \phi}{\partial z}-y\lambda_o\phi \quad . \tag{1d}$$

In Equation (1), u_o, v_o, and w_o are the displacement components at a point on the centroidal curve (the origin of the local x, y and z coordinates); λ_o and κ_o are the initial torsion and curvature (Appendix B) of the centroidal axes, while α_x, α_y and ϕ are small angles of rotation of the cross sections about the x, y and z axes respectively as shown in Figure 1.

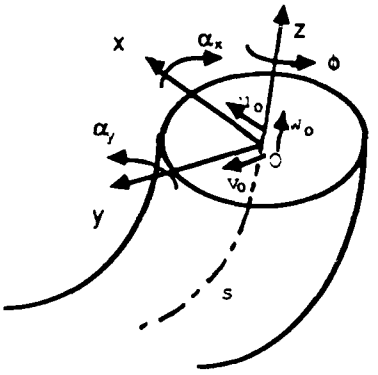

Figure 1: Displacement and rotation components.

STRAIN ENERGY OF A GENERAL CURVED AND TWISTED GUN TUBE WITH SYMMETRICAL CROSS SECTION

The strain-displacement equations introduced will be used for the derivation of the strain energy function of a gun tube. Assuming the material constituting the gun tube to be linear elastic, the strain energy for this gun tube can be expressed by

$$U=\frac{1}{2}\int_V \varepsilon^T\sigma\, dV \quad . \tag{2}$$

The stress and strain vectors in the above expression are

$$\sigma^T=[\sigma_{xx},\sigma_{yy},\sigma_{zz},\sigma_{xy},\sigma_{yz},\sigma_{xz}]\ ,\ \varepsilon^T=[\varepsilon_{xx},\varepsilon_{yy},\varepsilon_{zz},\varepsilon_{xy},\varepsilon_{yz},\varepsilon_{xz}]\ . \tag{3}$$

The applicable stress-strain relations for an isotropic material are

$$\sigma_{zz}=E\,\varepsilon_{zz},\ \sigma_{xz}=2\,G\varepsilon_{xz},\ \text{and}\ \sigma_{yz}=2\,G\varepsilon_{yz} \tag{4}$$

where E is the modulus of elasticity, and G is the modulus of elasticity in shear.

Upon substituting Equations (1) and (4) into Equation (2), the following expression for the strain energy is obtained:

$$U=\int_V (P_1 x\,y+P_2 y\,y+P_3 x\,x+P_4+P_5 x+P_6 y)\,dV \tag{5}$$

where the quantities P_1, P_2, P_3, and P_4 are presented in Appendix A. Since the centroidal axis is the origin of the coordinate system, the P_5 and P_6 terms vanish. Hence, the strain energy is simplified to the following expression:

$$U=\int_0^{\xi} (P_1 I_{xy}+P_2 I_{xx}+P_3 I_{yy}+P_4 A)\,dz \tag{6}$$

where ξ the length of the gun tube, A the cross sectional area, and I_{ij} the second moments and products of area.

The total kinetic energy of the system is defined by

$$T=\int_0^{\xi} \frac{1}{2}\rho\{A[(\dot{u}_o)^2+(\dot{v}_o)^2+(\dot{w}_o)^2]+(I_{xx}+I_{yy})(\dot{\phi})^2\}\,dz \tag{7}$$

where a superscript "dot" indicates differentiation with respect to time (t), and ρ represents the mass density.

In the above expressions for U and T, it has been assumed that the transverse shear strains vanish at the centroidal axes, or in the average over the cross section. With the use of Equations (1c) and (1d), this assumption yields the relations for α_x and α_y to the remaining displacement variables. It is noted that the moments of inertia, area, torsion, curvature, and the tensile and shear moduli may arbitrarily vary with z, the coordinate along the curve. Although the average transverse shear strain has been set equal to zero, the extension of the centroidal curve is still retained.

THE EQUATIONS OF MOTION AND NATURAL BOUNDARY CONDITIONS

Applying Hamilton's Principle for the undamped free vibration problem, yields the following Euler-Lagrange equations as well as the natural boundary conditions for the system.

$$\frac{\partial^2}{\partial z^2}\frac{\partial F}{\partial u_o''} - \frac{\partial}{\partial z}\frac{\partial F}{\partial u_o'} + \frac{\partial F}{\partial u_o} - \frac{\partial}{\partial t}\frac{\partial F}{\partial \dot{u}_o} = 0 \quad , \tag{8a}$$

$$\frac{\partial^2}{\partial z^2}\frac{\partial F}{\partial v_o''} - \frac{\partial}{\partial z}\frac{\partial F}{\partial v_o'} + \frac{\partial F}{\partial v_o} - \frac{\partial}{\partial t}\frac{\partial F}{\partial \dot{v}_o} = 0 \quad , \tag{8b}$$

$$-\frac{\partial}{\partial z}\frac{\partial F}{\partial w_o'} + \frac{\partial F}{\partial w_o} - \frac{\partial}{\partial t}\frac{\partial F}{\partial \dot{w}_o} = 0 \quad , \tag{8c}$$

$$-\frac{\partial}{\partial z}\frac{\partial F}{\partial \phi'} + \frac{\partial F}{\partial \phi} - \frac{\partial}{\partial t}\frac{\partial F}{\partial \dot{\phi}} = 0 \quad . \tag{8d}$$

Here, a superscript "prime" indicates differentiation with respect to z, and $F = T - U$. The boundary conditions at $z=0$ and $z=\xi$ are found to be

$$\text{either } u_o' \text{ is specified or } \frac{\partial F}{\partial u_o''} = 0 \quad ,$$

$$\text{either } u_o \text{ is specified or } \frac{\partial}{\partial z}\frac{\partial F}{\partial u_o''} - \frac{\partial F}{\partial u_o'} = 0 \quad ,$$

$$\text{either } v_o' \text{ is specified or } \frac{\partial F}{\partial v_o''} = 0 \quad ,$$

$$\text{either } v_o \text{ is specified or } \frac{\partial}{\partial z}\frac{\partial F}{\partial v_o''} - \frac{\partial F}{\partial v_o'} = 0 \quad ,$$

$$\text{either } w_o \text{ is specified or } \frac{\partial F}{\partial w_o'} = 0 \quad ,$$

$$\text{either } \phi \text{ is specified or } \frac{\partial F}{\partial \phi'} = 0 \quad .$$

The Euler-Lagrange equations for a gun tube with space curvature is presented explicitly in terms of the tube displacement functions, torsion, curvature, section properties, and their derivatives in Reference [7].

RAYLEIGH-RITZ SOLUTION FOR THE CLAMPED-FREE GUN TUBE

In the following, the general form of the governing equations and the strain energy function are specialized for the gun tube which has constant torsion and curvature. The strain energy function for this gun tube is then employed with the Rayleigh-Ritz method to formulate

approximate solutions for natural frequencies and mode shapes for a clamped-free gun tube with a uniform cross section.

In the clamped-free case, the boundary conditions at the fixed end, $z=0$, are $u'_o=0$, $u_o=0$, $v'_o=0$, $v_o=0$, $w_o=0$, $\phi=0$ and with reference to the relations between moments, forces, and displacements presented in Reference [6], the natural boundary conditions at the free end ($z=\xi$) are found to be expressed in terms of moment and force resultants in the following manner:

$$\frac{\partial F}{\partial u_o''} = M_y = 0 \quad , \tag{9a}$$

$$\frac{\partial F}{\partial v_o''} = -M_x = 0 \quad , \tag{9b}$$

$$\frac{\partial F}{\partial w_o'} = V_x + \kappa_o M_y = 0 \quad , \tag{9c}$$

$$\frac{\partial F}{\partial \phi'} = M_z = 0 \quad , \tag{9d}$$

$$\frac{\partial}{\partial z}\frac{\partial F}{\partial u_o''} - \frac{\partial F}{\partial u_o'} = 0 \equiv -V_x \quad , \tag{9e}$$

$$\frac{\partial}{\partial z}\frac{\partial F}{\partial v_o''} - \frac{\partial F}{\partial v_o'} = 0 \equiv -V_y \quad . \tag{9f}$$

Since the forces and moments are zero at the free end ($z=\xi$), the normal mode functions of a clamped-free straight beam, which are admissible trial functions, are employed to obtain approximate solutions. As obtained from Young and Felger [8], the normal mode functions for the straight clamped-free beam are

$$u_o = \xi \sin(\varpi t) \sum_{n=1}^{2} a_n \left\{ \cosh\left(\frac{k_n z}{\xi}\right) - \cos\left(\frac{k_n z}{\xi}\right) - m_n \left[\sinh\left(\frac{k_n z}{\xi}\right) - \sin\left(\frac{k_n z}{\xi}\right) \right] \right\} \quad , \tag{10a}$$

$$v_o = \xi \sin(\varpi t) \sum_{n=1}^{2} b_n \left\{ \cosh\left(\frac{k_n z}{\xi}\right) - \cos\left(\frac{k_n z}{\xi}\right) - m_n \left[\sinh\left(\frac{k_n z}{\xi}\right) - \sin\left(\frac{k_n z}{\xi}\right) \right] \right\} \quad , \tag{10b}$$

$$w_o = \xi \sin(\varpi t) \sum_{n=1}^{2} c_n \sin\left[\frac{(2n-1)\pi z}{2\xi}\right] \quad , \tag{10c}$$

$$\phi = \sin(\varpi t) \sum_{n=1}^{2} d_n \sin\left[\frac{(2n-1)\pi z}{2\xi}\right] \quad . \tag{10d}$$

where a_n, b_n, c_n and d_n are coefficients to be determined, $k_1=1.875104$, $k_2=4.694091$, $m_1=0.734095$, $m_2=1.018467$, and ϖ is a natural frequency of free vibration.

Upon the substitution of these displacements into the strain energy function Equation (6) and the kinetic energy function Equation (7), an expression for the total energy for a gun tube undergoing free vibration is obtained but not presented explicitly in this paper because of its excessive length. The total energy is then minimized with respect to each of the eight unknown coefficients to yield a system of algebraic equations represented as

$$(\mathbf{M}_e - \psi \mathbf{M}_f)\,\mathbf{C} = 0 \qquad (11)$$

where $\mathbf{C}^T$ = [a1, a2, b1, b2, c1, c2, d1, d2] , ψ = ($\rho \xi^2 \varpi^2$) / E, and $\mathbf{M_e}$ and $\mathbf{M_f}$ are matrices of coefficients. Since the elements of the column matrix $\mathbf{C}$ cannot be trivial, the characteristic equations are then obtained by requiring the coefficient determinent of $\mathbf{C}$ in Equation (11) vanish. The characteristic equations are presented in Reference [7].

RESULTS AND DISCUSSION

The Rayleigh-Ritz formulation for clamped-free gun tubes is next used to examine the effects of slenderness, curvature, torsion, cross section shape and orientation of cross section principal axes on the natural frequencies and mode shapes of a gun tube with an elliptical cross section. In all cases the material of the gun tube is assumed to have a Poisson's ratio 0.3 (G/E=0.4).

Figures 2 and 3 show the effects of slenderness, torsion, and curvature on the fundamental frequency of a gun tube with a circular cross section. As expected, the fundamental frequency increases with decreasing LD (length / radius of cross section). It is seen that the fundamental frequency is insensitive to changes in the curvature (LK = length x curvature) and torsion (LL = length x torsion) parameters for extremely small values of these parameters. These effects are explored in more detail in Figure 3 which plots frequency in a linear rather than logarithmic scale. It is seen that the fundamental frequency becomes noticeably dependent upon curvature and torsion when each of these parameters reaches the value of 10^{-2}.

The effects of changes of curvature and torsion on the fundamental mode shape are explored in Table I. At small values of both torsion and curvature, the transverse displacement v_o dominates the mode shape. As the curvature is increased, for a constant small torsion, the displacements u_o and w_o become coupled as do v_o and ϕ. On the other hand, as the torsion parameter is increased with small curvature (moving down the left hand column) the lateral displacements u_o and v_o become coupled and approach the same magnitude. If both parameters are

increased, then all of the variables approach the same magnitude. Significant coupling among the displacement variables seems to begin to occur at about the same values of the curvature and torsion parameters when frequency changes become noticeable.

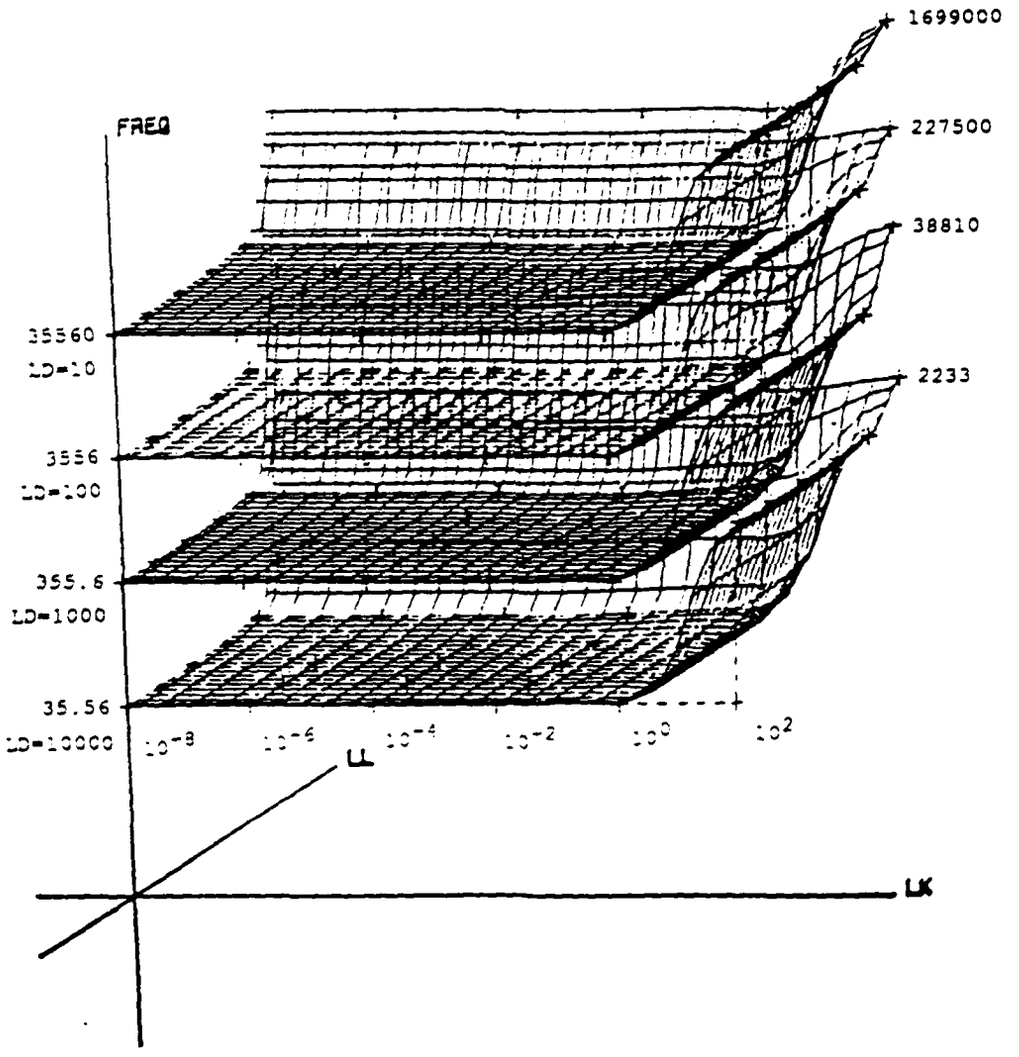

Figure 2: Fundamental frequencies of clamped-free gun tubes ($LD=10^1$ to $LD=10^4$)

(LL=length x λ_o, LK=length x κ_o, LD=length / cross section radius).

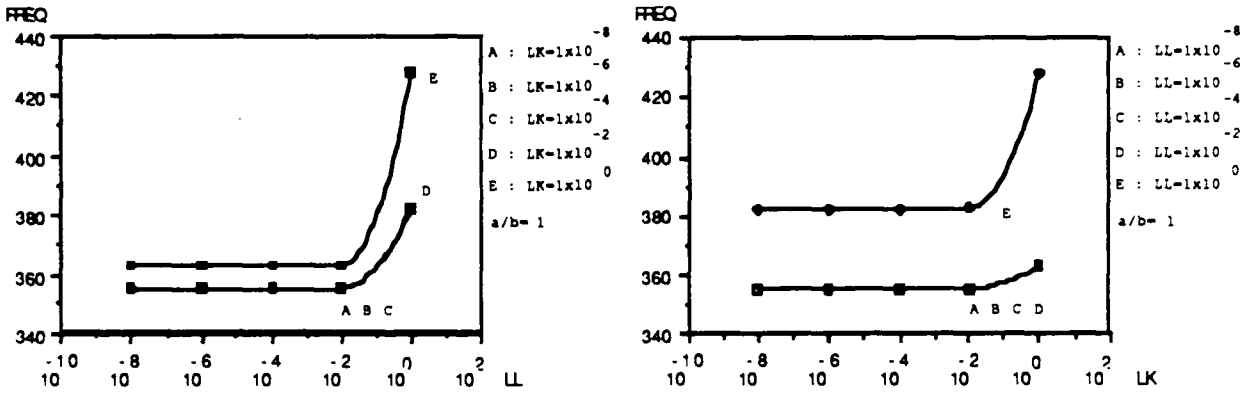

Figure 3: Fundamental frequencies of clamped-free gun tubes ($LD=10^3$).

Table I: Fundamental frequencies and mode shapes of clamped-free gun tubes ($LD=10^3$).

*LL	0.10E-07				
LK	0.10E-07	0.10E-05	0.10E-03	0.10E-01	0.10E+01
FREQ	355.6	355.6	355.6	355.6	363.1
U	0.10E+01	0.10E+01	0.10E+01	0.10E+01	0.10E+01
V	-0.32E+08	-0.11E+10	-0.12E+10	-0.12E+10	-0.15E+12
W	0.43E-08	0.89E-06	0.91E-04	0.91E-02	0.91E+00
Φ	-0.13E+00	-0.47E+03	-0.48E+05	-0.49E+07	-0.51E+11
*LL	0.10E-05				
LK	0.10E-07	0.10E-05	0.10E-03	0.10E-01	0.10E+01
FREQ	355.6	355.6	355.6	355.6	363.1
U	0.10E+01	0.10E+01	0.10E+01	0.10E+01	0.10E+01
V	-0.13E+08	-0.12E+08	-0.12E+08	-0.12E+08	-0.15E+10
W	0.99E-08	0.90E-06	0.91E-04	0.91E-02	0.91E+00
Φ	-0.54E-01	-0.48E-01	-0.48E+03	-0.49E+05	-0.51E+09
*LL	0.10E-03				
LK	0.10E-07	0.10E-05	0.10E-03	0.10E-01	0.10E+01
FREQ	355.6	355.6	355.6	355.6	363.1
U	0.10E+01	0.10E+01	0.10E+01	0.10E+01	0.10E+01
V	-0.11E+06	-0.12E+06	-0.12E+06	-0.12E+06	-0.15E+08
W	0.87E-08	0.91E-06	0.91E-04	0.91E-02	0.91E+00
Φ	-0.44E-03	-0.48E-01	-0.48E+01	-0.49E+03	-0.51E+07
*LL	0.10E-01				
LK	0.10E-07	0.10E-05	0.10E-03	0.10E-01	0.10E+01
FREQ	355.6	355.6	355.6	355.6	363.1
U	0.10E+01	0.10E+01	0.10E+01	0.10E+01	0.10E+01
V	-0.13E+04	-0.12E+04	-0.12E+04	-0.12E+04	-0.15E+06
W	0.98E-08	0.91E-06	0.91E-04	0.91E-02	0.91E+00
Φ	-0.55E-05	-0.48E-03	-0.48E+01	-0.49E+01	-0.51E+05
*LL	0.10E+01				
LK	0.10E-07	0.10E-05	0.10E-03	0.10E-01	0.10E+01
FREQ	382.2	382.2	382.2	382.7	427.7
U	0.10E+01	0.10E+01	0.10E+01	0.10E+01	0.10E+01
V	-0.12E+02	-0.12E+02	-0.12E+02	-0.12E+02	-0.16E+04
W	0.91E-08	0.91E-06	0.91E-04	0.91E-02	0.91E+00
Φ	-0.59E-07	-0.59E-05	-0.59E-03	-0.60E-01	-0.50E+03

In order to examine the effects of out-of-roundness on a gun tube motion, the cross section of the gun tube is changed from circular to elliptical while keeping the cross section area as a constant. The configuration is shown in Figure 4. The product of inertia (I_{xy}) is then systematically varied by rotating the principal axes of the cross section configurations while the torsion (LL) and curvature (LK) parameters are varied for each value of orientation of the principal axes of the cross section.

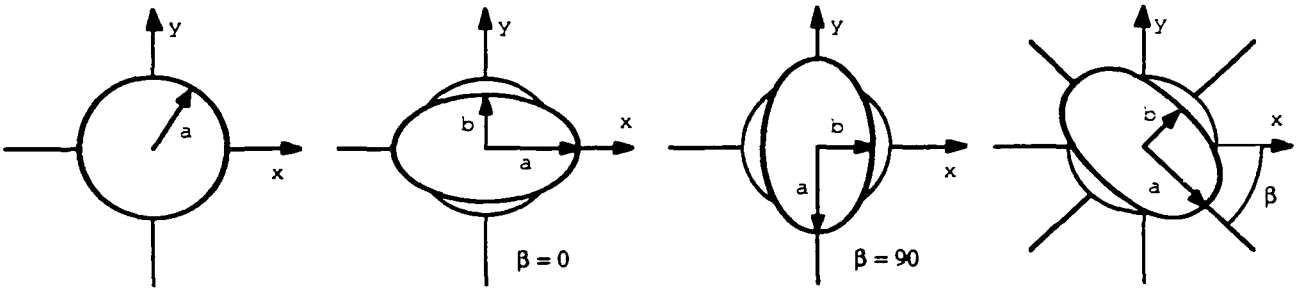

Figure 4: Deformation of the cross section.

Figures 5 and 6 show the effects on the fundamental frequency of changing the ratio of major to minor axes while keeping the rotation angle $\beta = 0$ ($I_{xy}=0$). It is seen that the effect of out-of-roundness is not symmetrical since the direction of the major axis substantially affects the manner in which the fundamental frequency is affected by the changes of the torsion and curvature parameters.

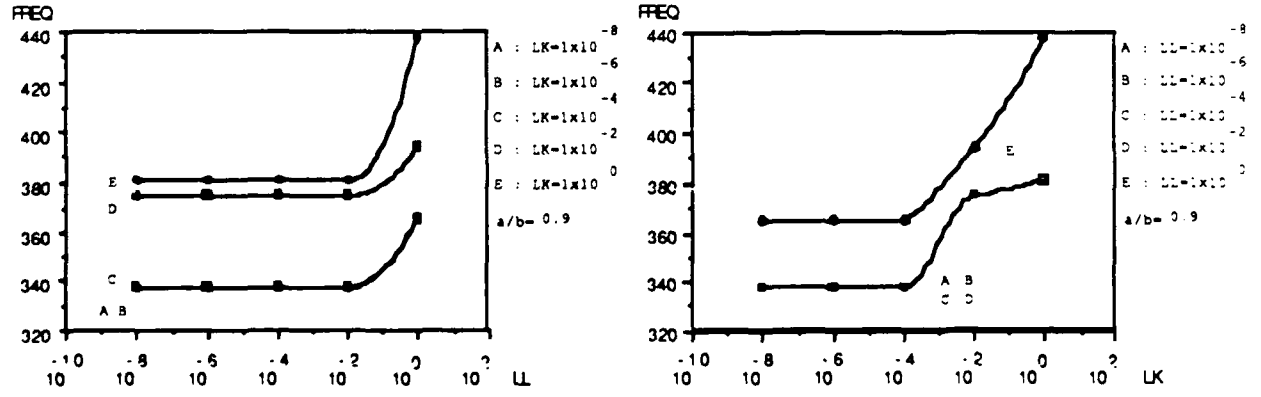

Figure 5: Effects of non-circular cross section on tne fundamental frequency (a/b=0.9, b=0 or a/b=1.1, b=90).

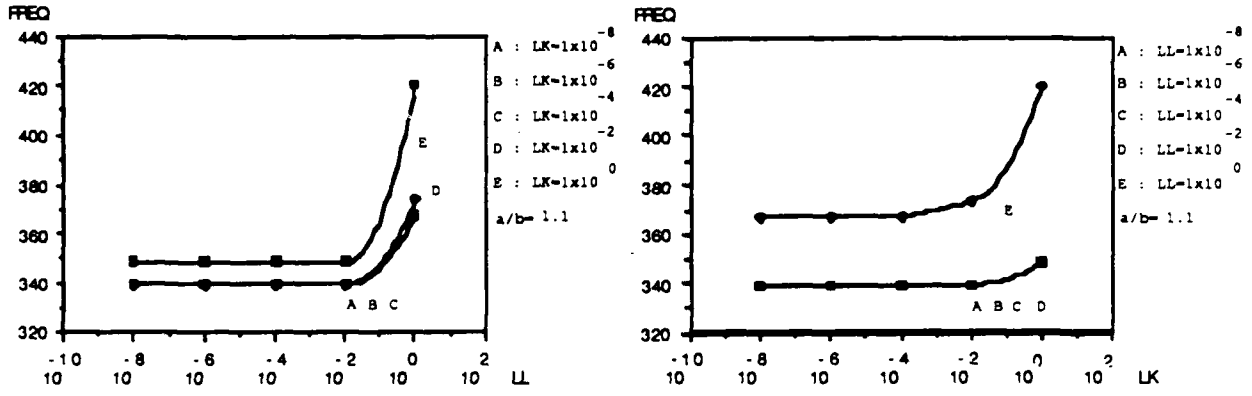

Figure 6: Effects of non-circular cross section on the fundamental frequency (a/b=1.1, b=0).

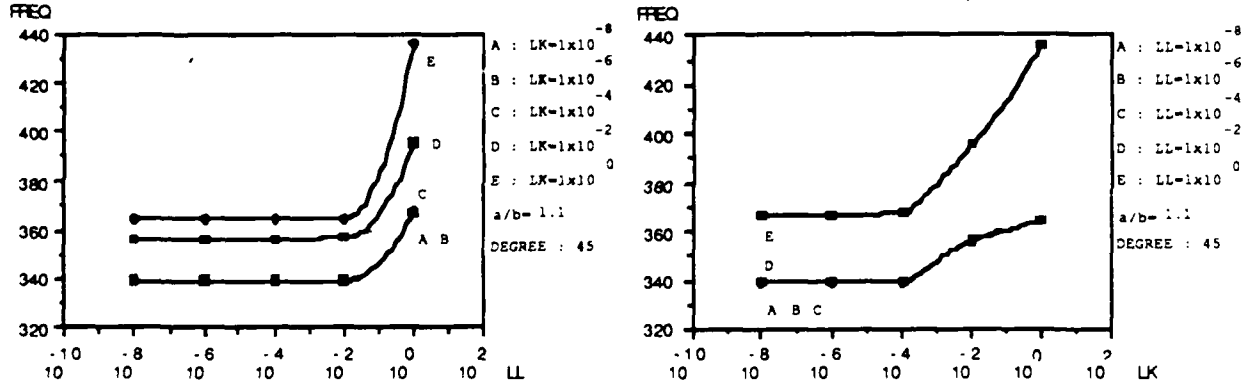

Figures 7: Effects of non-circular cross section on the fundamental frequency (a/b=1.1, b=45).

Figures 5, 6, and 7 illustrate the effects of cross section rotation on the fundamental frequency. Again, it is noted that rotating the cross section of fixed geometry changes the manner in which the curvature and torsion parameters affect the frequency.

The displacement coupling caused by the non-axisymmetric cross section is examined and explored in Tables II, III, and IV. It is found that for the almost straight gun tube ($LL=LK=10^{-8}$) the dominant displacement remains in the direction of the minor axis as the cross section is rotated. For higher values of curvature and torsion, rotation of the cross section is seen to change the relative values and phase of the four displacement components to certain manner.

Finally, it is noted that when $LD=1000$, LK and LL are smaller than 10^{-4} and a/b is in the range of 1.1 to 1, then the fundamental frequencies are essentially independent of the rotation angle β and also

lower than the frequencies of a gun tube with circular cross section.

Table II. Effects of Non-Circular Cross Section on the Fundamental Frequency and Mode Shape (a/b=1.1, β=0)

*LL	0.10E-07				
LK	0.10E-07	0.10E-05	0.10E-03	0.10E-01	0.10E+01
FREQ	339.1	339.1	339.1	339.1	347.9
U	0.10E+01	0.10E+01	0.10E+01	0.10E+01	0.10E+01
V	0.33E+09	0.33E+09	0.33E+09	-0.13E+10	-0.15E+12
W	0.87E-08	0.26E-06	0.25E-04	0.94E-02	0.91E+00
ϕ	0.12E+01	0.12E+03	0.12E+05	-0.50E+07	-0.44E+11
*LL	0.10E-05				
LK	0.10E-07	0.10E-05	0.10E-03	0.10E-01	0.10E+01
FREQ	339.1	339.1	339.1	339.1	347.9
U	0.10E+01	0.10E+01	0.10E+01	0.10E+01	0.10E+01
V	0.33E+07	0.33E+07	0.33E+07	-0.13E+08	-0.15E+10
W	0.24E-08	0.25E-06	0.25E-04	0.94E-02	0.91E+00
ϕ	0.12E-01	0.12E+01	0.12E+03	-0.50E+05	-0.44E+09
*LL	0.10E-03				
LK	0.10E-07	0.10E-05	0.10E-03	0.10E-01	0.10E+01
FREQ	339.1	339.1	339.1	339.1	347.9
U	0.10E+01	0.10E+01	0.10E+01	0.10E+01	0.10E+01
V	0.33E+05	0.33E+05	0.33E+05	-0.13E+06	-0.15E+08
W	0.25E-08	0.25E-06	0.25E-04	0.94E-02	0.91E+00
ϕ	0.12E-03	0.12E-01	0.12E+01	-0.50E+03	-0.44E+07
*LL	0.10E-01				
LK	0.10E-07	0.10E-05	0.10E-03	0.10E-01	0.10E+01
FREQ	339.1	339.1	339.1	339.1	347.9
U	0.10E+01	0.10E+01	0.10E+01	0.10E+01	0.10E+01
V	0.33E+03	0.33E+03	0.33E+03	-0.13E+04	-0.15E+06
W	0.25E-08	0.25E-06	0.25E-04	0.94E-02	0.91E+00
ϕ	0.12E-05	0.12E-03	0.12E-01	-0.50E+01	-0.44E-05
*LL	0.10E+01				
LK	0.10E-07	0.10E-05	0.10E-03	0.10E-01	0.10E+01
FREQ	366.9	366.9	366.9	373.3	420.3
U	0.10E+01	0.10E+01	0.10E+01	0.10E+01	0.10E+01
V	0.26E+01	0.26E+01	0.26E+01	-0.14E+02	-0.15E+04
W	0.29E-08	0.29E-06	0.29E-04	0.95E-02	0.91E+00
ϕ	0.11E-07	0.11E-05	0.11E-03	-0.64E-01	-0.46E+03

Table III. Effects of Non-Circular Cross Section on the Fundamental Frequency and Mode Shape (a/b=1.1, β=45)

*LL	0.10E-07				
LK	0.10E-07	0.10E-05	0.10E-03	0.10E-01	0.10E+01
FREQ	339.1	339.1	339.2	356.2	364.0
U	0.10E+01	0.10E+01	0.10E+01	0.10E+01	0.10E+01
V	0.10E+01	0.10E+01	0.10E+01	0.94E+02	0.31E+05
W	0.39E-08	0.39E-06	0.39E-04	0.54E-02	0.90E+00
ϕ	0.38E-08	0.38E-06	0.38E-04	0.39E+00	0.10E+05
*LL	0.10E-05				
LK	0.10E-07	0.10E-05	0.10E-03	0.10E-01	0.10E+01
FREQ	339.1	339.1	339.2	356.2	364.0
U	0.10E+01	0.10E+01	0.10E+01	0.10E+01	0.10E+01
V	0.10E+01	0.10E+01	0.10E+01	0.94E+02	0.31E+05
W	0.39E-08	0.39E-06	0.39E-04	0.54E-02	0.90E+00
ϕ	0.38E-08	0.38E-06	0.38E-04	0.39E+00	0.10E+05
*LL	0.10E-03				
LK	0.10E-07	0.10E-05	0.10E-03	0.10E-01	0.10E+01
FREQ	339.1	339.1	339.2	356.2	364.0
U	0.10E+01	0.10E+01	0.10E+01	0.10E+01	0.10E+01
V	0.10E+01	0.10E+01	0.10E+01	0.95E+02	0.31E+05
W	0.39E-08	0.39E-06	0.39E-04	0.54E-02	0.90E+00
ϕ	0.38E-08	0.38E-06	0.38E-04	0.39E+00	0.10E+05
*LL	0.10E-01				
LK	0.10E-07	0.10E-05	0.10E-03	0.10E-01	0.10E+01
FREQ	339.1	339.1	339.2	356.4	364.1
U	0.10E+01	0.10E+01	0.10E+01	0.10E+01	0.10E+01
V	0.99E+00	0.99E+00	0.10E+01	0.10E+03	0.39E+05
W	0.39E-08	0.39E-06	0.39E-04	0.51E-02	0.89E+00
ϕ	0.38E-08	0.38E-06	0.38E-04	0.43E+00	0.13E+05
*LL	0.10E+01				
LK	0.10E-07	0.10E-05	0.10E-03	0.10E-01	0.10E+01
FREQ	366.9	366.9	367.1	395.6	436.2
U	0.10E+01	0.10E+01	0.10E+01	0.10E+01	0.10E+01
V	0.44E+00	0.44E+00	0.45E+00	-0.14E+02	-0.17E+04
W	0.38E-08	0.38E-06	0.38E-04	0.94E-02	0.91E+00
ϕ	0.19E-08	0.19E-06	0.19E-04	-0.78E-01	-0.67E+03

Table IV. Effects of Non-Circular Cross Section on the Fundamental Frequency and Mode Shape (a/b=1.1, β=90)

*LL	0.10E-07				
LK	0.10E-07	0.10E-05	0.10E-03	0.10E-01	0.10E+01
FREQ	339.1	339.1	339.3	373.0	379.0
U	0.10E+01	0.10E+01	0.10E+01	0.10E+01	0.10E+01
V	-0.47E-07	-0.47E-07	-0.47E-07	-0.51E+09	-0.11E+12
W	0.39E-08	0.39E-06	0.39E-04	0.71E-02	0.90E+00
ϕ	0.56E-16	-0.17E-13	-0.17E-11	-0.23E+07	-0.40E+11
*LL	0.10E-05				
LK	0.10E-07	0.10E-05	0.10E-03	0.10E-01	0.10E+01
FREQ	339.1	339.1	339.3	373.0	379.0
U	0.10E+01	0.10E+01	0.10E+01	0.10E+01	0.10E+01
V	-0.35E-06	-0.35E-06	-0.35E-06	-0.10E+08	-0.16E+10
W	0.39E-08	0.39E-06	0.39E-04	0.87E-02	0.91E+00
ϕ	-0.11E-14	-0.90E-13	-0.92E-11	-0.47E+05	-0.57E+09
*LL	0.10E-03				
LK	0.10E-07	0.10E-05	0.10E-03	0.10E-01	0.10E+01
FREQ	339.1	339.1	339.3	373.0	379.0
U	0.10E+01	0.10E+01	0.10E+01	0.10E+01	0.10E+01
V	-0.31E-04	-0.31E-04	-0.31E-04	-0.10E+06	-0.16E+08
W	0.39E-08	0.39E-06	0.39E-04	0.87E-02	0.91E+00
ϕ	-0.74E-13	-0.74E-11	-0.75E-09	-0.47E+03	-0.58E+07
*LL	0.10E-01				
LK	0.10E-07	0.10E-05	0.10E-03	0.10E-01	0.10E+01
FREQ	339.1	339.1	339.3	373.0	379.0
U	0.10E+01	0.10E+01	0.10E+01	0.10E+01	0.10E+01
V	-0.31E-02	-0.31E-02	-0.31E-02	-0.10E+04	-0.16E+06
W	0.39E-08	0.39E-06	0.39E-04	0.87E-02	0.91E+00
ϕ	-0.74E-11	-0.74E-09	-0.75E-07	-0.47E+01	-0.58E+05
*LL	0.10E+01				
LK	0.10E-07	0.10E-05	0.10E-03	0.10E-01	0.10E+01
FREQ	366.9	366.9	367.1	393.1	436.6
U	0.10E+01	0.10E+01	0.10E+01	0.10E+01	0.10E+01
V	-0.38E+00	-0.38E+00	-0.39E+00	-0.11E+02	-0.16E+04
W	0.42E-08	0.42E-06	0.42E-04	0.87E-02	0.91E+00
ϕ	-0.14E-08	-0.14E-06	-0.14E-04	-0.56E-01	-0.54E+03

SUMMARY AND CONCLUSIONS

The primary purpose of the work presented in this paper was to examine the effects of curvature in three dimensional space and of cross section out-of-roundness on the vibrations of gun tubes with special attention to gun tubes which are nearly straight.

Although the derived governing equations apply to a gun tube with general space curvature, the mode shapes and natural frequencies of a free vibration curve were calculated for a gun tube whose centroidal axis was a helix. For this case, both the curvature and torsion were constants rather than position dependent. Natural frequencies and mode shapes were obtained using admissible trial functions with the Raleigh-Ritz method.

It was found that the introduction of even slight space curvature,

as characterized by the curvature and torsion parameters, introduced significant changes on the gun tube's natural frequencies and especially on mode shapes compared to those of a straight gun tube. Increasing either curvature parameter always changes the fundamental frequency and increases the degree of coupling among the displacement variables in the natural modes.

The effects of out-of-roundness were examined by calculating the natural frequencies and mode shapes of a gun tube of an ellipitical cross section and varying the orientation of the principal axes of the ellipse with respect to the natural coordinates of space curvature of the gun tube center line. It was found that the orientation of the cross section had a pronunced effect on the coupling of the displacement variables on any given natural mode of free vibration, and that the out-of-roundness changed the manner in which changes of the torsion and curvature parameters affected the gun tube's natural frequencies and mode shapes.

REFERENCES

[1] A. E. H. Love, *A Treatise on the Mathematical Theory of Elasticity*, Dover Publications (1927).

[2] S. Timoshenko, D. H. Young and W. Weaver Jr., *Vibration Problems in Engineering*, John Wiley & Sons Inc. (1974).

[3] J. P. Den Hartog, "The Lowest Natural Frequency of Circular Arcs", *Phil. Mag. S.7* No.28 (1928).

[4] I. Chang and E. Volterra, "Upper and Lower Bounds of Frequencies of Elastic Arcs", *Journal of Acoustical Society of America* 46, 1165-1174 (1969).

[5] S. S. Rao, "Effects of Transverse Shear and Rotatory Inertia on the Coulped Twist-Bending Vibrations of Circular Rings", *Journal of Sound and vibration* 16, 551-556 (1971).

[6] Herbert B. Kingsbury, "A Reexamination of the Equations of Motion of a Curved and Twisted Gun Tube", *Proceeding of the Fouth U.S. Army Symposium on Gun Dynamics*, I1-I21 (1985).

[7] Huoy-Shyi Tsay, "On the Vibrations of Helical Rods", Dept. of Mechanical Eng., University of Delaware, thesis (1986).

[8] D. Young and R. P Felgar Jr., "Tables of Characteristic Function Representing Normal Modes of Vibration of a Beam", *Bureau of Engr. Research* , Engr. Res. Series No. 44 (1949).

APPENDIX A

P_1, P_2, P_3 and P_4 appearing in Equation 5 are given by

$$P_1 = E\kappa v'' w' + E\kappa\lambda u' w' + E\kappa\lambda' u w' - E\kappa^2\phi w' + E\kappa' v'' w + G\kappa^3 v' w + E\kappa'\lambda u' w + E\kappa'\lambda' u w + G\kappa^3\lambda u w + G\kappa^2\phi' w - E\kappa\kappa'\phi w - E\lambda v' v'' - E\lambda' v v'' + E u'' v'' - G\kappa^2\lambda v v' - E\lambda^2 u' v' + G\kappa^2 u' v' - E\lambda\lambda' u v' + G\kappa\lambda\phi v' + E\kappa\lambda\phi v' - E\lambda\lambda' u' v - E(\lambda')^2 u v - G\kappa^2\lambda^2 u v - G\kappa\lambda\phi' v + E\kappa\lambda'\phi v + E\lambda u' u'' + E\lambda' u u'' - E\kappa\phi u'' + G\kappa^2\lambda u u' + G\kappa\phi' u' + G\kappa\lambda^2\phi u,$$

$$P_2 = (1/2)[E(v'')^2 + Gk2(v')^2 + E\lambda^2(u')^2 + E(\lambda')^2 u^2 + G\kappa^2\lambda^2 u^2 + G(\phi')^2 + G\lambda^2\phi^2 + E\kappa^2\phi^2] + E\lambda u' v'' + E\lambda' u v'' - E\kappa\phi v'' + G\kappa^2\lambda u v' + G\kappa\phi' v' + E\lambda\lambda' u u' - E\kappa\lambda\phi u' + G\kappa\lambda\phi' u - E\kappa\lambda'\phi u,$$

$$P_3 = (1/2)[E\kappa^2(w')^2 + E(\kappa')^2 w^2 + G\kappa^4 w^2 + E\lambda^2(v')^2 + E(l')^2 v^2 + G\kappa^2\lambda^2 v^2 + E(u'')^2 + G\kappa^2(u')^2 + G(\phi')^2 + G\lambda^2\phi^2] + E\kappa\kappa' w w' - E\kappa\lambda v' w' - E\kappa\lambda' v w' + E\kappa u'' w' - E\kappa'\lambda v' w - E\kappa'\lambda' v w - G\kappa^3\lambda v w + E\kappa' u'' w + G\kappa^3 u' w + G\kappa^2\lambda\phi w + E\lambda\lambda' v v' - E\lambda u'' v' - E\lambda' u'' v - G\kappa^2\lambda u' v - G\kappa\lambda^2\phi v + G\kappa\lambda\phi u',$$

$$P_4 = (1/2)[E(w')^2 + E\kappa^2 u^2] - E\kappa u w'.$$

APPENDIX B

In this paper, the space curvature of the rod centroidal axis is characterized by the torsion (λ_o) and curvature (κ_o) parameters. These are related to the rate of change of the space curve tangent ($\boldsymbol{k}$), normal ($\boldsymbol{i}$), and binormal ($\boldsymbol{j}$) unit vectors through the Serret-Frenet formulas by

$$d\mathbf{k}/ds = \kappa_o \mathbf{i} \quad , \quad d\mathbf{j}/ds = -\lambda_o \mathbf{i} \quad , \quad d\mathbf{i}/ds = \lambda_o \mathbf{j} - \kappa_o \mathbf{k} . \qquad (B1)$$

SHICK AND TIERSTEN

TITLE: A VARIATIONAL ANALYSIS OF RESONANCE IN GUN TUBES WITH ECCENTRIC BORES

D.V. Shick and H.F. Tiersten
Rensselaer Polytechnic Institute
Troy, NY 12180-3590

ABSTRACT:

An analysis of the steady-state vibrations of gun tubes with eccentric bores is performed entirely within the framework of three-dimensional linear elasticity. The dispersion curves for the eccentric cylindrical tube are obtained by satisfying the differential equations and boundary conditions on the external cylindrical surface exactly and the boundary conditions on the eccentric inner cylindrical surface variationally. The resulting solutions clearly exhibit the coupling between the extensional and flexural motions. The forced vibrations are treated by satisfying the continuity conditions at the interface of the step in bore pressure using a variational principle in which all conditions, i.e., those of both constraint- and natural-type, appear as natural conditions. The calculations reveal the existence of resonance at critical velocities and increasing coupling to flexural motions with increasing eccentricities.

A VARIATIONAL ANALYSIS OF RESONANCE IN GUN TUBES WITH ECCENTRIC BORES

D.V. Shick and H.F. Tiersten
Rensselaer Polytechnic Institute
Troy, NY 12180-3590

1. INTRODUCTION

Unusually high strain data was obtained during the test firing of a lightweight 120 mm gun tube at Aberdeen Proving Grounds during 1985. Motivated by this data Simkins[1] found that there is a critical propagation speed, at which a resonance type phenomenon occurs with accordingly high strains, and that this had been treated earlier by others[2-4] for purposes other than resonance in gun tubes. Subsequent careful experimental investigation showed that the high amplitude strain with appropriate frequency existed at a projectile velocity very close to the aforementioned "critical velocity."

In his investigation Simkins extended the existing critical velocity theory of thin-walled cylinders to thick-walled cylinders using the Mirsky-Herrmann equations[5]. He also showed that the theory very accurately accounts for the experimental observations. Simkins further pointed out that the critical velocity would be more accurately predicted using the three-dimensional theory of elasticity rather than the two-dimensional Mirsky-Herrmann equations and showed that there was a difference. In order to model the nonuniformity of the wall thickness, or eccentricity of the bore, Simkins[6] assumed an angular distribution of mass density around the cross-section of the tube, which resulted in the coupling of the axisymmetric, i.e., extensional, mode with the lowest nonaxially symmetric, i.e., flexural mode. This time Simkins used the simplified two-dimensional equations of Flugge[7] which contain the essence of the phenomena. Although this treatment accounts for the angular variation in inertia, it does not account for the angular variation in stiffness.

In this work we treat the problem of a uniformly moving pressure step on the interior of a cylindrical gun tube with an eccentric cylindrical bore using the equations of three-dimensional linear elasticity throughout. Since the cylindrical hole has a small eccentricity with respect to the outer cylindrical surface of the tube, the axisymmetric and nonaxially symmetric waves, which exist in the case of concentric cylinders, are coupled in the modes for the case of eccentric inner and outer cylinders. In the treatment the geometry of the eccentric inner cylinder is expressed in terms of the geometry of a concentric inner cylinder of the same diameter and an expansion is made to lowest order in the eccentricity. The solution functions are referred to the cylindrical coordinates for the concentric case and are chosen to satisfy the

differential equations and boundary conditions on the outer cylindrical surface exactly. The boundary conditions on the inner eccentric cylindrical surface, which are not satisfied by the solution functions, are satisfied variationally by means of the appropriate variational principle of linear elasticity[8]. Since the solution functions satisfy the differential equations and boundary conditions on the outer surface exactly, all that remains in the variational principle is the integral over the eccentric inner cylindrical surface. The resulting system of homogeneous linear algebraic equations yields the transcendental equation which gives the dispersion curves for the tube with the eccentric hole. When the eccentricity is taken to vanish the transcendental equation uncouples and reduces to the well-known ones for the case of concentric cylinders[9] and, hence, the dispersion curves become the well-known ones for the cylindrical tube[10].

When the pressure step is included in the forced vibration problem, the solution consists of the sum of the static pressure solution in the projectile coordinate system and the appropriate coupled waves behind the step and only the appropriate coupled waves ahead of the step. Since there is a discontinuity in the steady-state solution functions on each side of the interface at the step in pressure and these interface conditions cannot be satisfied exactly, they are satisfied variationally. Since the solution functions employed can satisfy no a priori conditions at the interface, a variational principle in which all conditions, i.e., those of both natural- and constraint-type appear as natural conditions[11,12] is employed. Since the input functions satisfy the differential equations and some of the boundary conditions exactly and the others variationally, the variational principle yields an integral across the discontinuity interface, which results in a linear algebra for the amplitudes of the coupled waves on each side of the interface in terms of the magnitude of the pressure step. Results are presented as a function of projectile velocity and for a few velocities as a function of distance from the step.

2. PRELIMINARY CONSIDERATIONS

The problem we are concerned with consists of a uniform pressure step moving along the interior cylindrical surface of a gun tube at constant velocity V as shown in Fig.1. The outside cylindrical surface of the gun tube is traction-free and we are interested in determining the steady-state solution in an intertial coordinate system moving with the constant projectile velocity V.

The stress equations of motion in the absence of body forces may be written in the invariant form

$$\underset{\sim}{\nabla} \cdot \underset{\sim}{\tau} = \rho \ddot{\underset{\sim}{u}}, \tag{2.1}$$

where $\underset{\sim}{\nabla}$ denotes the gradient operator, $\underset{\sim}{\tau}$ the symmetric stress tensor, $\underset{\sim}{u}$ the displacement vector and ρ the mass density, and we have introduced the convention that a dot over a variable denotes partial differentiation with respect

to time. The linear stress-displacement-gradient relations for an isotropic elastic solid may be written in the invariant form

$$\underset{\sim}{\tau} = \lambda \underset{\sim}{\nabla} \cdot \underset{\sim}{u}\, \underset{\sim}{I} + \mu(\underset{\sim}{\nabla}\underset{\sim}{u} + \underset{\sim}{u}\underset{\sim}{\nabla}), \tag{2.2}$$

where λ and μ are the Lamé constants and $\underset{\sim}{I}$ denotes the idemfactor (or identity). The substitution of (2.2) into (2.1) yields the displacement equations of motion in the form

$$\mu\nabla^2\underset{\sim}{u} + (\lambda+\mu)\underset{\sim}{\nabla}\underset{\sim}{\nabla}\cdot\underset{\sim}{u} = \rho\ddot{\underset{\sim}{u}}. \tag{2.3}$$

When the vector $\underset{\sim}{u}$ is expressed in terms of scalar and vector potentials φ and $\underset{\sim}{H}$ in the form

$$\underset{\sim}{u} = \underset{\sim}{\nabla}\varphi + \underset{\sim}{\nabla}\times\underset{\sim}{H}, \tag{2.4}$$

where $\underset{\sim}{\nabla}\cdot\underset{\sim}{H}$ is arbitrary, the solutions of (2.3) may be obtained from

$$\nabla^2\varphi = \frac{1}{V_1^2}\ddot{\varphi}, \quad \nabla^2\underset{\sim}{H} = \frac{1}{V_2^2}\ddot{\underset{\sim}{H}}, \tag{2.5}$$

where

$$V_1^2 = (\lambda+2\mu)/\rho, \quad V_2^2 = \mu/\rho, \tag{2.6}$$

and V_1 and V_2 are the speeds of dilatational and equivoluminal waves, respectively.

Since we are concerned with a cylindrical geometry, we need the equations in cylindrical coordinates. In cylindrical coordinates r, θ, z the stress equations of motion take the form

$$\begin{aligned}
&\frac{\partial\tau_{rr}}{\partial r} + \frac{(\tau_{rr}-\tau_{\theta\theta})}{r} + \frac{1}{r}\frac{\partial\tau_{r\theta}}{\partial\theta} + \frac{\partial\tau_{rz}}{\partial z} = \rho\ddot{u}_r,\\
&\frac{1}{r}\frac{\partial\tau_{r\theta}}{\partial\theta} + \frac{\partial\tau_{rz}}{\partial z} + \frac{\partial\tau_{\theta r}}{\partial r} + \frac{2\tau_{r\theta}}{r} = \rho\ddot{u}_\theta,\\
&\frac{\partial\tau_{zz}}{\partial z} + \frac{\partial\tau_{zr}}{\partial r} + \frac{\tau_{zr}}{r} + \frac{1}{r}\frac{\partial\tau_{z\theta}}{\partial\theta} = \rho\ddot{u}_z.
\end{aligned} \tag{2.7}$$

The linear stress-displacement-gradient relations may be written in the form

$$\tau_{rr} = \lambda\Delta + 2\mu\frac{\partial u_r}{\partial r}, \quad \tau_{\theta\theta} = \lambda\Delta + 2\mu\left(\frac{1}{r}\frac{\partial u_\theta}{\partial\theta} + \frac{u_r}{r}\right),$$

$$\tau_{zz} = \lambda\Delta + 2\mu\frac{\partial u}{\partial z}\,,\quad \tau_{r\theta} = \mu\left(\frac{1}{r}\frac{\partial u_r}{\partial\theta} + \frac{\partial u_\theta}{\partial r} - \frac{u_\theta}{r}\right),$$

$$\tau_{\theta z} = \mu\left(\frac{\partial u_\theta}{\partial z} + \frac{1}{r}\frac{\partial u_z}{\partial\theta}\right),\quad \tau_{zr} = \mu\left(\frac{\partial u_z}{\partial r} + \frac{\partial u_r}{\partial z}\right), \tag{2.8}$$

where

$$\Delta = \underset{\sim}{\nabla}\cdot\underset{\sim}{u} = \frac{\partial u_r}{\partial r} + \frac{u_r}{r} + \frac{1}{r}\frac{\partial u_\theta}{\partial\theta} + \frac{\partial u_z}{\partial z}\,. \tag{2.9}$$

In cylindrical coordinates the relations between the displacement fields and the potentials take the form

$$u_r = \frac{\partial\varphi}{\partial r} + \frac{1}{r}\frac{\partial H_z}{\partial\theta} - \frac{\partial H_\theta}{\partial z}\,,$$

$$u_\theta = \frac{1}{r}\frac{\partial\varphi}{\partial\theta} + \frac{\partial H_r}{\partial z} - \frac{\partial H_z}{\partial r}\,,$$

$$u_z = \frac{\partial\varphi}{\partial z} + \frac{\partial H_\theta}{\partial r} + \frac{H_\theta}{r} - \frac{1}{r}\frac{\partial H_r}{\partial\theta}\,, \tag{2.10}$$

and the wave equations (2.5) take the component form

$$\frac{\partial^2\varphi}{\partial r^2} + \frac{1}{r}\frac{\partial\varphi}{\partial r} + \frac{1}{r^2}\frac{\partial^2\varphi}{\partial\theta^2} + \frac{\partial^2\varphi}{\partial z^2} = \frac{1}{V_1^2}\ddot{\varphi}\,,$$

$$\frac{\partial^2 H_r}{\partial r^2} + \frac{1}{r}\frac{\partial H_r}{\partial r} + \frac{1}{r^2}\left(\frac{\partial^2 H_r}{\partial\theta^2} - 2\frac{\partial H_\theta}{\partial\theta} - H_r\right) + \frac{\partial^2 H_r}{\partial z^2} = \frac{1}{V_2^2}\ddot{H}_r,$$

$$\frac{\partial^2 H_\theta}{\partial r^2} + \frac{1}{r}\frac{\partial H_\theta}{\partial r} + \frac{1}{r^2}\left(\frac{\partial^2 H_\theta}{\partial\theta^2} + 2\frac{\partial H_r}{\partial\theta} - H_\theta\right) + \frac{\partial^2 H_\theta}{\partial z^2} = \frac{1}{V_2^2}\ddot{H}_\theta\,,$$

$$\frac{\partial^2 H_z}{\partial r^2} + \frac{1}{r}\frac{\partial H_z}{\partial r} + \frac{1}{r^2}\frac{\partial^2 H_z}{\partial\theta^2} + \frac{\partial^2 H_z}{\partial z^2} = \frac{1}{V_2^2}\ddot{H}_z\,. \tag{2.11}$$

Since we are interested in the steady-state solution, we may eliminate the rigid motion Vt of the step in pressure by introducing the transformation

$$\zeta = z - Vt\,, \tag{2.12}$$

which is then employed in all the equations. When this is done $\partial/\partial z$ is replaced by $\partial/\partial\zeta$ and $\partial/\partial t$ is replaced by $-V\partial/\partial\zeta$ in all the equations, which

are then independent of time. In the cylindrical coordinate system r, θ, ζ we have the boundary conditions

$$T_{rr} = 0, \; T_{r\theta} = 0, \; T_{r\zeta} = 0, \tag{2.13}$$

on the outer cylindrical surface r = b of the gun tube for all ζ and

$$T_{rr} = -p, \; T_{r\theta} = 0, \; T_{r\zeta} = 0, \tag{2.14}$$

on the inner cylindrical surface (when the eccentricity is neglected) for $\zeta < 0$ and

$$T_{rr} = 0, \; T_{r\theta} = 0, \; T_{r\zeta} = 0, \tag{2.15}$$

on the inner cylindrical surface (when the eccentricity is neglected) for $\zeta > 0$.

Since we have different boundary conditions for $\zeta < 0$ and $\zeta > 0$, we will obtain the solution by satisfying the differential equations and boundary conditions (either exactly or approximately) for $\zeta > 0$ and $\zeta < 0$ separately, which means that we then should satisfy the continuity of $T_{\zeta\zeta}$, $T_{\zeta r}$, $T_{\zeta\theta}$, u_r, u_θ and u_ζ across the interface at $\zeta = 0$. However, since the solution functions we employ satisfy the differential equations and boundary conditions as mentioned above, they cannot satisfy the continuity conditions across the interface at $\zeta = 0$ exactly. Nevertheless, the remaining continuity conditions at the interface can be satisfied approximately by satisfying the proper form of the appropriate variational principle of linear elasticity, in which all conditions, i.e., of both natural and constraint-type, appear as natural conditions. When this is done all that remains in the variational principle is an integral over the surface of discontinuity in the input functions at $\zeta = 0$ because all other terms in that form of the variational principle vanish on account of the equations and conditions satisfied by the solution functions employed. The form of the variational principle of interest here is given in Eq.(6.44) of Ref.12, which we reproduce here for the configuration shown in Fig.2 in the invariant form

$$\sum_{m=1}^{2}\Big[\int_{V^{(m)}}(\nabla\cdot\underset{\sim}{T}^{(m)} - \rho^{(m)}\ddot{\underset{\sim}{u}}^{(m)})\cdot\delta\underset{\sim}{u}^{(m)}\,dV + \int_{S_N^{(m)}}(\bar{\underset{\sim}{t}}^{(m)} - \underset{\sim}{n}^{(m)}\cdot\underset{\sim}{T}^{(m)})\cdot\delta\underset{\sim}{u}^{(m)}\,dS$$

$$+ \int_{S_C^{(m)}}\underset{\sim}{n}^{(m)}\cdot(\underset{\sim}{u}^{(m)} - \bar{\underset{\sim}{u}}^{(m)})\cdot\delta\underset{\sim}{T}^{(m)}\,dS\Big] + \frac{1}{2}\int_{S^{(d)}}\underset{\sim}{n}^{(d)}\cdot[(\underset{\sim}{T}^{(2)} - \underset{\sim}{T}^{(1)})\cdot(\delta\underset{\sim}{u}^{(1)}$$

$$+ \delta\underset{\sim}{u}^{(2)}) + (\underset{\sim}{u}^{(1)} - \underset{\sim}{u}^{(2)})\cdot(\delta\underset{\sim}{T}^{(1)} + \delta\underset{\sim}{T}^{(2)})]\,dS = 0, \tag{2.16}$$

where $S^{(d)}$ denotes the surface of discontinuity separating region 1 from region 2, and $S_N^{(m)}$ and $S_C^{(m)}$ denote the portions of the mth surface on which natural- and constraint-type conditions, respectively, are prescribed. We note that $S_N^{(m)}$ and $S_C^{(m)}$ refer to different portions of the surface for different terms in the boundary sums depending on each actual condition at a point. In (2.16) $\underset{\sim}{n}^{(m)}$ denotes the outwardly directed unit normal to the mth surface, $\underset{\sim}{n}^{(d)}$ denotes the unit normal to the surface of discontinuity directed from region 1 to region 2, $\underset{\sim}{\bar{t}}^{(m)}$ and $\underset{\sim}{\bar{u}}^{(m)}$ denote the prescribed tractions and displacements for the mth surface and the meaning of the remaining quantities in (2.16) is known from earlier discussion. The variational condition (2.16) for the simplest configuration, which is shown in Fig.2, makes clear how to apply the variational condition to other configurations. Consequently, it is not worthwhile writing the general variational equivalent of (2.16) for each configuration because it can become too cumbersome and the actual useful condition can be obtained from (2.16) for any configuration. Furthermore, in any given application what is taken as a surface of discontinuity for application of the variational principle (2.16) is not clear from the figure itself, but depends on what conditions the approximating functions satisfy.

Since the inner cylinder, i.e., the bore, is eccentric with respect to the outer cylindrical surface and we are employing cylindrical coordinates in which r = b defines the outer cylindrical surface, we introduce a concentric inner cylindrical surface on which r = a and which has the center displaced by a small distance Δ from the center of the cylindrical bore of radius r = a as shown in Fig.3. In Fig.3 we have introduced two polar coordinate systems separated by the distance Δ along the x-axis. Then a point on the surface of the bore has coordinates r, θ in the concentric coordinate system and a, φ in the bore coordinate system. From Fig.3 it is clear that for any point on the surface of the bore we have the relations

$$r\cos\theta = a\cos\varphi + \Delta, \quad r\sin\theta = a\sin\varphi, \tag{2.17}$$

and we note that for the purposes of this work it is convenient to introduce the difference angle α which is defined by

$$\alpha = \varphi - \theta. \tag{2.18}$$

Dividing $(2.17)_1$ by $r\sin\theta$, substituting from $(2.17)_2$ and (2.18), expanding and retaining terms of order α, we obtain

$$\alpha = \Delta \sin\theta/a. \tag{2.19}$$

Substituting from (2.18) into either of (2.17), expanding, retaining terms of order α and substituting from (2.19), we obtain

$$r = a + \Delta \cos \theta . \tag{2.20}$$

In the sequel we will need the relation between the unit base vectors normal, $\hat{\underset{\sim}{e}}_a$, and tangential, $\hat{\underset{\sim}{e}}_\varphi$, to the surface of the bore and the unit base vectors $\underset{\sim}{e}_r$ and $\underset{\sim}{e}_\theta$ in the concentric polar coordinate system, which are shown in Fig.4. From Fig.4, we have

$$\hat{\underset{\sim}{e}}_a = \cos \alpha \underset{\sim}{e}_r + \sin \alpha \underset{\sim}{e}_\theta , \quad \hat{\underset{\sim}{e}}_\varphi = - \sin \alpha \underset{\sim}{e}_r + \cos \alpha \underset{\sim}{e}_\theta , \tag{2.21}$$

from which for small α, we obtain

$$\hat{\underset{\sim}{e}}_a = \underset{\sim}{e}_r + \alpha \underset{\sim}{e}_\theta , \quad \hat{\underset{\sim}{e}}_\varphi = - \alpha \underset{\sim}{e}_r + \underset{\sim}{e}_\theta . \tag{2.22}$$

We will also need the relation between the displacement components $\hat{u}_a$, $\hat{u}_\varphi$ and $\hat{u}_\zeta$ and u_r, u_θ and u_ζ referred to the concentric cylindrical coordinate system. From the transformation of the components of a vector for small α we obtain

$$\hat{u}_a = u_r + \alpha u_\theta , \quad \hat{u}_\varphi = - \alpha u_r + u_\theta , \quad \hat{u}_\zeta = u_\zeta . \tag{2.23}$$

Similarly, we will need the relation between the components $\hat{\tau}_{aa}$, $\hat{\tau}_{a\varphi}$, $\hat{\tau}_{a\zeta}$ of the traction vector on the surface of the bore and the stress components, τ_{rr}, $\tau_{r\theta}$, $\tau_{\theta\theta}$, $\tau_{r\zeta}$ and $\tau_{\theta\zeta}$. From the transformation of the components of a second rank tensor for small α we obtain

$$\hat{\tau}_{aa} = \tau_{rr} + 2\alpha\tau_{r\theta} , \quad \hat{\tau}_{a\varphi} = \tau_{r\theta} + \alpha(\tau_{\theta\theta} - \tau_{rr}) , \quad \hat{\tau}_{a\zeta} = \tau_{r\zeta} + \alpha\tau_{\theta\zeta} . \tag{2.24}$$

Since in the variational approximation for the determination of the dispersion curves for the case of the eccentric bore we integrate the traction around the surface of the bore and we have the solution functions in the concentric cylindrical coordinate system, we need the expressions

$$\begin{aligned}
\hat{\tau}_{aa} &= \tau_{rr}\Big)_a + \frac{\partial \tau_{rr}}{\partial r}\Big)_a \Delta \cos \theta + 2\alpha\tau_{r\theta}\Big)_a , \\
\hat{\tau}_{a\varphi} &= \tau_{r\theta}\Big)_a + \frac{\partial \tau_{r\theta}}{\partial r}\Big)_a \Delta \cos \theta + \alpha\Big[\tau_{\theta\theta}\Big)_a - \tau_{rr}\Big)_a\Big] , \\
\hat{\tau}_{a\zeta} &= \tau_{r\zeta}\Big)_a + \frac{\partial \tau_{r\zeta}}{\partial r}\Big) \Delta \cos \theta + \alpha\,\tau_{\theta\zeta}\Big)_a ,
\end{aligned} \tag{2.25}$$

to lowest order in Δ. For similar reasons we need the expressions

$$\hat{u}_a = u_r\Big)_a + \frac{\partial u_r}{\partial r}\Big)_a \Delta\cos\theta + \alpha\, u_\theta\Big)_a ,$$

$$\hat{u}_\varphi = -\alpha u_r\Big)_a + u_\theta\Big)_a + \frac{\partial u_\theta}{\partial r}\Big)_a \Delta\cos\theta ,$$

$$\hat{u}_\zeta = u_\zeta\Big)_a + \frac{\partial u_\zeta}{\partial r}\Big)_a \Delta\cos\theta . \tag{2.26}$$

Furthermore, in the angular integrals along the surface of the bore we have $ds = a\,d\varphi$ and employing (2.18) and (2.19), we obtain

$$ds = (a + \Delta\cos\theta)\,d\theta . \tag{2.27}$$

3. DISPERSION RELATIONS

In this section we determine the phase velocity - wavenumber dispersion relations for the cylindrical tube with an eccentric cylindrical bore. To this end we first write the solutions of (2.11) in the form[13]

$$\varphi = f(r)\cos n\theta\, e^{i\gamma\zeta},\quad H_r = h_r(r)\sin n\theta\, e^{i\gamma\zeta},$$

$$H_\theta = h_\theta(r)\cos n\theta\, e^{i\gamma\zeta},\quad H_\zeta = h_\zeta(r)\sin\theta\, e^{i\gamma\zeta}, \tag{3.1}$$

which satisfy (2.11) provided

$$f'' + \frac{1}{r}f' + \left(\eta^2 - \frac{n^2}{r^2}\right)f = 0,\quad h_\zeta'' + \frac{1}{r}h_\zeta' + \left(\beta^2 - \frac{n^2}{r^2}\right)h_\zeta = 0,$$

$$h_r'' + \frac{1}{r}h_r' + \frac{1}{r^2}(-n^2 h_r + 2nh_\theta - h_r) + \beta^2 h_r = 0,$$

$$h_\theta'' + \frac{1}{r}h_\theta' + \frac{1}{r^2}(-n^2 h_\theta + 2nh_r - h_\theta) + \beta^2 h_\theta = 0, \tag{3.2}$$

where

$$\eta^2 = \gamma^2[(V^2/V_1^2) - 1],\quad \beta^2 = \gamma^2[(V^2/V_2^2) - 1]. \tag{3.3}$$

First subtracting and then adding $(3.2)_3$ and $(3.2)_4$, we obtain, respectively,

$$h_1'' + \frac{1}{r}h_1' + \left[\beta^2 - \frac{(n+1)^2}{r^2}\right]h_1 = 0,$$

$$h_2'' + \frac{1}{r} h_2' + \left[\beta^2 - \frac{(n-1)^2}{r^2}\right] h_2 = 0, \tag{3.4}$$

where

$$2h_1 = h_r - h_\theta, \quad 2h_2 = h_r + h_\theta. \tag{3.5}$$

Since in the calculation region of primary interest in this work both η^2 and β^2 are negative, we write the solutions of each of Bessel's differential equations $(3.2)_{1-2}$ and (3.4) in the form

$$f^{(n)} = A_2^{(n)} I_n(\tilde{\eta} r) + B_2^{(n)} K_n(\tilde{\eta} r), \quad h_3^{(n)} = A_3^{(n)} I_n(\tilde{\beta} r) + B_3^{(n)} K_n(\tilde{\beta} r), \tag{3.6}$$

$$h_1^{(n)} = A_1^{(n)} I_{n+1}(\tilde{\beta} r) + B_1^{(n)} K_{n+1}(\tilde{\beta} r), \tag{3.7}$$

$$h_2^{(n)} = A_4^{(n)} I_{n-1}(\tilde{\beta} r) + B_4^{(n)} K_{n-1}(\tilde{\beta} r), \tag{3.8}$$

where $h_3 = h_\zeta$ and

$$\tilde{\eta} = -i\eta, \quad \tilde{\beta} = -i\beta. \tag{3.9}$$

We now observe, as did Gazis[9], that since $\nabla \cdot \underset{\sim}{H}$ is arbitrary, we may eliminate one of the h_i without any loss in generality. Hence we set $h_2 = 0$, which with (3.5) yields

$$h_r = h_1, \quad h_\theta = -h_1, \tag{3.10}$$

which enables the displacement field to be written in the form

$$\begin{aligned} u_r &= \left(f' + \frac{1}{r} n h_3 + i\gamma h_1\right) \cos n\theta \, e^{i\gamma\zeta}, \\ u_\theta &= \left(-\frac{n}{r} f + i\gamma h_1 - h_3'\right) \sin n\theta \, e^{i\gamma\zeta}, \\ u_\zeta &= \left[i\gamma f - h_1' - \frac{(n+1)}{r} h_1\right] \cos n\theta \, e^{i\gamma\zeta}, \end{aligned} \tag{3.11}$$

which with

$$\Delta = -(\eta^2 + \gamma^2) f \cos n\theta \, e^{i\gamma\zeta}, \tag{3.12}$$

enables the expressions for the stresses to be obtained from (2.8). For each n we may now satisfy the boundary conditions (2.13). Substituting from (2.8), (3.6), (3.7), (3.11) and (3.12) into (2.13) and rearranging terms, we obtain

$$A_1^{(n)} 2i\gamma\left[\tilde{\beta} I_n(\tilde{\beta}b) - \frac{(n+1)}{b} I_{n+1}(\tilde{\beta}b)\right] + A_2^{(n)} 2\left[\left(\frac{n(n-1)}{b^2} + \gamma^2 + \tilde{\beta}^2\right) I_n(\tilde{\eta}b)\right.$$

$$\left. - \frac{\tilde{\eta}}{b} I_{n+1}(\tilde{\eta}b)\right] + A_3^{(n)} 2n\left[\frac{(n-1)}{b^2} I_n(\tilde{\beta}b) + \frac{\tilde{\beta}}{b} I_{n+1}(\tilde{\beta}b)\right] - B_1^{(n)} 2i\gamma\left[\tilde{\beta} K_n(\tilde{\beta}b)\right.$$

$$\left. + \frac{(n+1)}{b} K_{n+1}(\tilde{\beta}b)\right] + B_2^{(n)} 2\left[\left(\frac{n(n-1)}{b^2} + \gamma^2 + \tilde{\beta}^2\right) K_n(\tilde{\eta}b) + \frac{\tilde{\eta}}{b} K_{n+1}(\tilde{\eta}b)\right]$$

$$B_3^{(n)} 2n\left[\frac{(n-1)}{b^2} K_n(\tilde{\beta}b) - \frac{\tilde{\beta}}{b} K_{n+1}(\tilde{\beta}b)\right] = 0,$$

$$A_1^{(n)} i\gamma\left[\tilde{\beta} I_n(\tilde{\beta}b) - \frac{2(n+1)}{b} I_{n+1}(\tilde{\beta}b)\right] - A_2^{(n)} 2n\left[\frac{(n-1)}{b^2} I_n(\tilde{\eta}b)\right.$$

$$\left. + \frac{\tilde{\eta}}{b} I_{n+1}(\tilde{\eta}b)\right] + A_3^{(n)} 2\left[\left(\frac{n(n-1)}{b^2} - \tilde{\beta}^2\right) I_n(\tilde{\beta}b) + \frac{\tilde{\beta}}{b} I_{n+1}(\tilde{\beta}b)\right]$$

$$- B_1^{(n)} i\gamma\left[\tilde{\beta} K_n(\tilde{\beta}b) + 2\frac{(n+1)}{b} K_{n+1}(\tilde{\beta}b)\right] - B_2^{(n)} 2n\left[\frac{(n-1)}{b^2} K_n(\tilde{\eta}b)\right.$$

$$\left. - \frac{\tilde{\eta}}{b} K_{n+1}(\tilde{\eta}b)\right] + B_3^{(n)}\left[\left(\frac{2n(n-1)}{b^2} - \tilde{\beta}^2\right) K_n(\tilde{\beta}b) - \frac{2\tilde{\beta}}{b} K_{n+1}(\tilde{\beta}b)\right] = 0,$$

$$- A_1^{(n)}\left[\frac{n\tilde{\beta}}{b} I_n(\tilde{\beta}b) + (\tilde{\beta}^2 + \gamma^2) I_{n+1}(\tilde{\beta}b)\right] + A_2^{(n)} 2i\gamma\left[\frac{n}{b} I_n(\tilde{\eta}b)\right.$$

$$\left. + \tilde{\eta} I_{n+1}(\tilde{\eta}b)\right] + A_3^{(n)} \frac{i\gamma n}{b} I_n(\tilde{\beta}b) + B_1^{(n)}\left[\frac{n\tilde{\beta}}{b} K_n(\tilde{\beta}b) - (\tilde{\beta}^2\right.$$

$$\left. + \gamma^2) K_{n+1}(\tilde{\beta}b)\right] + B_2^{(n)} 2i\gamma\left[\frac{n}{b} K_n(\tilde{\eta}b) - \tilde{\eta} K_{n+1}(\tilde{\eta}b)\right] + B_3^{(n)} \frac{i\gamma n}{b} K_n(\tilde{\beta}b) = 0. \tag{3.13}$$

Equations (3.13) constitute a system of three linear homogeneous equations in six amplitudes $A_1^{(n)}$, $A_2^{(n)}$, $A_3^{(n)}$, $B_1^{(n)}$, $B_2^{(n)}$ and $B_3^{(n)}$ for each n, which may readily be solved for the $B_i^{(n)}$ in terms of the $A_j^{(n)}$ to obtain

$$B_i^{(n)} = \sum_{j=1}^{3} G_{ij}^{(n)}(b) A_j^{(n)}, \quad B_i^{(0)} = \sum_{j=1}^{2} G_{ij}^{(0)}(b) A_j^{(0)}, \tag{3.14}$$

where the $G_{ij}^{(n)}(b)$ are a consequence of the inversion and are too cumbersome to write here and provide no additional insight.

As noted in the Introduction the homogeneous boundary conditions on the eccentric cylindrical hole (bore),

$$\hat{\tau}_{aa} = 0, \ \hat{\tau}_{a\varphi} = 0, \ \hat{\tau}_{a\zeta} = 0, \tag{3.15}$$

cannot be satisfied exactly and must be satisfied approximately. Since the solution functions we employ satisfy the differential equations and boundary conditions on the external cylindrical surface exactly and all boundary conditions are natural conditions and there are no surfaces of discontinuity, all that remains of (2.16) is

$$\int_{S_N} (\underset{\sim}{\bar{t}} - \underset{\sim}{n} \cdot \underset{\sim}{\tau}) \cdot \delta \underset{\sim}{u} \, dS = 0 , \tag{3.16}$$

where in this case S_N represents the eccentric interior cylindrical surface. Furthermore, since the surface of the bore is traction-free, $\bar{t} = 0$ and (3.16) yields

$$\int_S (\hat{\tau}_{aa} \delta \hat{u}_a + \hat{\tau}_{a\varphi} \delta \hat{u}_\varphi + \hat{\tau}_{a\zeta} \delta \hat{u}_\zeta) \, ds = 0, \tag{3.17}$$

which is the equation we employ to satisfy the conditions on the eccentric inner cylindrical surface approximately. Although Eq.(3.17) will in general couple all the concentric solution functions we have obtained, when the expansion introduced in Section 2, which retains terms only linear in the eccentricity Δ, is employed only the concentric solutions for $n = 0$ and $n = 1$ remain coupled. Consequently, as the approximate solution satisfying (3.17) we take

$$\begin{aligned} u_r = e^{i\gamma\zeta}\Big\{ & i\gamma\Big[A_1^{(0)} I_1(\hat{\beta}r) + \Big(\sum_{k=1}^{2} G_{1k}^{(0)} A_k^{(0)}\Big) K_1(\hat{\beta}r)\Big] \\ & + \tilde{\eta}\Big[A_2^{(0)} I_1(\tilde{\eta}r) - \Big(\sum_{k=1}^{2} G_{2k}^{(0)} A_k^{(0)}\Big) K_1(\tilde{\eta}r)\Big] \\ & + \cos\theta\Big(i\gamma\Big[A_1^{(1)} I_2(\hat{\beta}r) + \Big(\sum_{k=1}^{3} G_{1k}^{(1)} A_k^{(1)}\Big) K_2(\hat{\beta}r)\Big] \\ & + \frac{1}{r}\Big[A_2^{(1)} I_1(\tilde{\eta}r) + \Big(\sum_{k=1}^{3} G_{2k}^{(1)} A_k^{(1)}\Big) K_1(\tilde{\eta}r)\Big] \\ & + \tilde{\eta}\Big[A_2^{(1)} I_2(\tilde{\eta}r) - \Big(\sum_{k=1}^{3} G_{2k}^{(1)} A_k^{(1)}\Big) K_1(\tilde{\eta}r)\Big] \end{aligned}$$

$$+\frac{1}{r}\left[A_3^{(1)}I_1(\tilde{\beta}r)+\left(\sum_{k=1}^{3}G_{3k}^{(1)}A_k^{(1)}\right)K_1(\tilde{\beta}r)\right]\Big\},$$

$$u_\theta = e^{i\gamma\zeta}\sin\theta\Big\{i\gamma\Big[A_1^{(1)}I_2(\tilde{\beta}r)+\left(\sum_{k=1}^{3}G_{1k}^{(1)}A_k^{(1)}\right)K_2(\tilde{\beta}r)\Big]$$

$$-\frac{1}{r}\left[A_2^{(1)}I_1(\tilde{\eta}r)+\left(\sum_{k=1}^{3}G_{2k}^{(1)}A_k^{(1)}\right)K_1(\tilde{\eta}r)\right]$$

$$+\frac{1}{r}\left[A_3^{(1)}I_1(\tilde{\beta}r)+\left(\sum_{k=1}^{3}G_{3k}^{(1)}A_k^{(1)}\right)K_1(\tilde{\beta}r)\right]$$

$$+\tilde{\beta}\left[A_3^{(1)}I_2(\tilde{\beta}r)-\left(\sum_{k=1}^{3}G_{3k}^{(1)}A_k^{(1)}\right)K_2(\tilde{\beta}r)\right]\Big\},$$

$$u_\zeta = e^{i\gamma\zeta}\Big\{-\tilde{\beta}\Big[A_1^{(0)}I_o(\tilde{\beta}r)-\left(\sum_{k=1}^{2}G_{1k}^{(0)}A_k^{(0)}\right)K_o(\tilde{\beta}r)\Big]$$

$$+i\gamma\Big[A_2^{(0)}I_o(\tilde{\eta}r)+\left(\sum_{k=1}^{2}G_{2k}^{(0)}A_k^{(0)}\right)K_o(\tilde{\eta}r)\Big]$$

$$+\cos\theta\Big[-\tilde{\beta}\Big[A_1^{(1)}I_1(\tilde{\beta}r)-\left(\sum_{k=1}^{3}G_{1k}^{(1)}A_k^{(1)}\right)K_1(\tilde{\beta}r)\Big]$$

$$+i\gamma\Big[A_2^{(1)}I_1(\tilde{\eta}r)+\left(\sum_{k=1}^{3}G_{2k}^{(1)}A_k^{(1)}\right)K_1(\tilde{\eta}r)\Big]\Big\}, \quad (3.18)$$

which solution functions contain the five unknown amplitudes $A_1^{(0)}$, $A_2^{(0)}$, $A_1^{(1)}$, $A_2^{(1)}$, $A_3^{(1)}$.

Substituting from (3.18) into (2.8) with (2.9) and then into (2.25) and employing (2.26) and (2.27) in (3.17) and performing the integration, we obtain

$$\sum_{j=1}^{2}\Big[\sum_{i=1}^{2}A_i^{(0)}f_{ij}^{00}+\Delta\sum_{i=1}^{3}A_i^{(1)}f_{ij}^{01}\Big]\delta A_j^{(0)}+$$

$$\sum_{j=1}^{3}\Big[\Delta\sum_{i=1}^{2}A_i^{(0)}f_{ij}^{10}+\sum_{i=1}^{3}A_i^{(1)}f_{ij}^{11}\Big]\delta A_j^{(1)}=0, \quad (3.19)$$

where the expressions for f_{ij}^{00}, f_{ij}^{01}, f_{ij}^{10} and f_{ij}^{11} are much too cumbersome to present here[14]. Since the variations $\delta A_j^{(0)}$ and $\delta A_j^{(1)}$ are arbitrary, we obtain

$$\sum_{i=1}^{2} A_j^{(0)} f_{ij}^{00} + \Delta \sum_{i=1}^{3} A_i^{(1)} f_{ij}^{01} = 0, \quad j = 1,2,$$

$$\Delta \sum_{i=1}^{2} A_i^{(0)} f_{ij}^{10} + \sum_{i=1}^{3} A_i^{(1)} f_{ij}^{11} = 0, \quad j = 1,2,3. \tag{3.20}$$

Equations (3.20) constitute a system of five linear homogeneous algebraic equations in $A_i^{(0)}$ and $A_i^{(1)}$, which yield nontrivial solutions when the determinant of the coefficients vanishes. For a given b, a, Δ and V, the resulting equation yields values of γ that determine[15] the two dispersion curves shown in Fig.5 for two distinct values of $\epsilon = \Delta/(b - a)$. The modes associated with the dispersion curves consist of coupled extensional and flexural motions for which the amplitude ratios $A_1^{(0)}:A_2^{(0)}:A_1^{(1)}:A_2^{(1)}:A_3^{(1)}$ can be obtained from any four of the five consistent equations in (3.20). It should be noted that when the eccentricity Δ vanishes, the determinantal equation uncouples into two equations, one for n = 0 and the other for n = 1. These equations correspond to the exact solutions obtained by Gazis for the concentric cylindrical tube. As already noted, when the solutions for $n > 1$ are included, they all uncouple and produce the aforementioned exact solutions for $n > 1$ for the concentric cylindrical tube. The dispersion curves for $n \leq 6$ are shown in Fig.6 for an intermediate value of $\epsilon = \Delta/(b - a)$.

4. FORCED VIBRATIONS OF GUN TUBES

We now treat the problem of a uniformly moving pressure step on the interior of the eccentric bore of a cylindrical gun tube in the inertial coordinate system moving with the velocity of the pressure step. As already noted the steady-state solution behind the step consists of the static solution due to the pressure plus the coupled waves for the case of the eccentric bore obtained in Section 3, while the solution ahead of the step consists only of the waves. Although we can readily include the influence of the eccentricity of the bore in the static portion of the solution, we do not bother to do so because we do not consider it worth the effort since it introduces only a small correction to the static inhomogeneous forcing term, and the important dynamic effect in the waves has already been included. Consequently, for the static pressure portion of the solution we take the usual Lamé solution in the form

$$u_r^o = \frac{pa^2}{2(b^2 - a^2)} \left(\frac{r}{\lambda + \mu} + \frac{b^2}{\mu r} \right). \tag{4.1}$$

The wave solutions are given in (3.18) for each of the dispersion curves shown in Fig.5 for two distinct values of $\varepsilon = \Delta/(b-a)$. For the value of Δ of actual interest we have the dispersion curves shown in Fig.7. It can be seen from Fig.7 that in the velocity range of interest, i.e., between the points labeled A and B in the figure there are always five waves. At values of V near A the waves are all real and since the group velocity $V_g = V + \gamma\, dV/d\gamma$, all waves are moving in the direction of the pressure step. The waves with negative $dV/d\gamma$ are behind the step and those with positive $dV/d\gamma$ are in front of the step. As noted in all the earlier work, as $dV/d\gamma \to 0$ a form of resonance arises since the energy stays with the step and grows. At values of V near B there is one real wave ahead of the step and four complex waves, two of which are ahead of the step and two behind, because the solutions must decay and not grow with distance from the step. In between the two points at which $dV/d\gamma = 0$ there is a range of V in which there are three real waves, two of which are ahead and one of which is behind the step.

From the foregoing discussion and Fig.7 it is clear that we always have five waves, two of which are behind and three of which are ahead of the step. Since the solution functions we employ satisfy the differential equations and boundary conditions on the outside cylindrical surface exactly and the boundary conditions on the eccentric inner cylindrical surface approximately, i.e., variationally, to great accuracy all that remains of (2.16) is

$$\frac{1}{2}\int_{S^{(d)}} \underset{\sim}{n}^{(d)} \cdot \Big[(\underset{\sim}{\tau}^{(2)} - \underset{\sim}{\tau}^{(1)}) \cdot (\delta\underset{\sim}{u}^{(1)} + \delta\underset{\sim}{u}^{(2)}) + (\underset{\sim}{u}^{(1)} - \underset{\sim}{u}^{(2)}) \cdot (\delta\underset{\sim}{\tau}^{(1)} + \delta\underset{\sim}{\tau}^{(2)}) \Big]\, dS = 0, \tag{4.2}$$

where $S^{(d)}$ represents the surface of discontinuity at the pressure step and region 2 is in front of and 1 behind the step. In the problem being treated here Eq.(4.2) yields

$$\int_0^{2\pi} d\theta \int_a^b \Big[(\tau_{\zeta r}^{(2)} - \tau_{\zeta r}^{(1)})(\delta u_r^{(1)}) + \delta u_r^{(2)} + (\tau_{\zeta\theta}^{(2)} - \tau_{\zeta\theta}^{(1)})(\delta u_\theta^{(1)} + \delta u_\theta^{(2)}) + (\tau_{\zeta\zeta}^{(2)} - \tau_{\zeta\zeta}^{(1)})(\delta u_\zeta^{(1)} + \delta u_\zeta^{(2)}) + (u_r^{(1)} - u_r^{(2)})(\delta\tau_{\zeta r}^{(1)} + \delta\tau_{\zeta r}^{(2)}) + (u_\theta^{(1)} - u_\theta^{(2)})(\delta\tau_{\zeta\theta}^{(1)} + \delta\tau_{\zeta\theta}^{(2)}) + (u_\zeta^{(1)} - u_\zeta^{(2)})(\delta\tau_{\zeta\zeta}^{(1)} + \delta\tau_{\zeta\zeta}^{(2)}) \Big]_{\zeta=0} r\,dr = 0, \tag{4.3}$$

which is the equation we employ to satisfy the conditions on the surface $\zeta = 0$ approximately. We now note that for the same convenience achieved in employing only the Lamé solution for the static pressure portion of the problem, which ignores the eccentricity of the bore, we ignore the eccentricity of the bore in performing the integrations in (4.3). This causes little error since the important influence of the eccentricity on the waves has already been included.

In accordance with the foregoing discussion we take the solution of the steady-state forced vibration problem in the form

$$\tilde{u}_r^{(1)} = \sum_{i=1}^{2} K_1 u_r^i + u_r^o, \quad \tilde{u}_\theta^{(1)} = \sum_{i=1}^{2} K_i u_\theta^i, \quad \tilde{u}_\zeta^{(1)} = \sum_{i=1}^{2} K_i u_\zeta^i, \qquad \zeta < 0,$$

$$\tilde{u}_r^{(2)} = \sum_{i=3}^{5} K_i u_r^i, \quad \tilde{u}_\theta^{(2)} = \sum_{i=3}^{5} K_i u_\theta^i, \quad \tilde{u}_\zeta^{(1)} = \sum_{i=3}^{5} K_i u_\zeta^{(i)}, \qquad \zeta > 0, \tag{4.4}$$

where u_r^i, u_θ^i and u_ζ^i are the known solution functions given in (3.18) for each of the appropriate five dispersion curves shown in Fig.7 for a particular value of V in accordance with the above discussion. Substituting from (4.4) into (4.3) with the aid of (4.1), (3.18), (2.8) and (2.9) and performing the integration using a 10-point Newton-Cotes procedure[16], we obtain

$$\sum_{j=1}^{5} \sum_{i=1}^{5} (K_i h_{ij} - q_j) \delta K_j = 0, \tag{4.5}$$

where the expressions for the h_{ij} and q_j are too cumbersome to present here and are not terribly revealing. Since the variations δK_j are arbitrary, we obtain

$$\sum_{i=1}^{5} K_i h_{ij} = q_j, \quad j = 1, 2 \ldots 5, \tag{4.6}$$

which constitute a system of five linear inhomogeneous algebraic equations for the five K_i, the inversion of which yields the response as a function of V.

Calculations have been performed for the values of b and a near those of the gun tube used in the test firings at Aberdeen Proving Grounds for the Δ used in calculating the dispersion curves in Fig.7. The dynamic amplification, i.e., the ratio of the dynamic u_r at r = a to the static (Lamé) u_r at r = a is plotted as a function of V for that value of ζ for which it is a maximum in Fig.8. The figure clearly shows the onset of resonance as V approaches the region of the critical velocities, i.e., the velocities corresponding to the points at which dV/dγ = 0. Since there are two such points, one for each curve, two resonance peaks appear with slight separation in Fig.8. In Figs.9a-c, we plot the amplification vs ζ for a point C slightly above the upper resonance[17], for which all waves are real, for (a) the entire disturbance, (b) the axisymmetric (extensional) portion and (c) the nonaxisymmetric (flexural) portion. It can be seen from the figures that an appreciable portion of the motion is flexural as a result of the eccentricity and that all waves are are traveling waves without decay. In Figs.10a-c we plot the amplification

vs ζ for a point D slightly below the lower resonance, for which only one wave ahead of the step does not decay and in which a, b and c have the same meaning as in Fig.9. Again the figures show that an appreciable portion of the motion is flexural. They also show that all waves behind decay and that most of the disturbance ahead of the step decays and only a small portion travels. In Figs.11a-c we plot the amplification vs ζ for a point E in between the two resonance points, for which only one wave ahead of the step and one wave behind the step decay. Again the figures show that an appreciable portion of the motion is flexural. They also exhibit the decaying and traveling portions of the disturbance. Calculations not presented here indicate that the amount of flexural motion increases with eccentricity.

Acknowledgements

This work was supported in part by Benet Laboratories, Watervliet Arsenal under U.S. Army Contract No. DAAA22-89-C-7007.

REFERENCES

1. T.E. Simkins, "Resonance of Flexural Waves in Gun Tubes," U.S. Army Armament Research, Development and Engineering Center, Close Combat Armaments Center, Benet Weapons Laboratory, Watervliet, NY 12189-4050, Technical Report ARCCB-TR-87008, July 1987.

2. H. Reismann, "Response of a Prestressed Cylindrical Shell to Moving Pressure Load," Developments in Mechanics, Solid Mechanics - Proceedings of the Eighth Midwest Mechanics Conference, Part II, Vol.2 (Pergamon Press, Ltd., 1965), pp.349-363.

3. S. Tang, "Dynamic Response of a Tube Under Moving Pressure," Journal of the Engineering Mechanics Division, Proceedings of the ASCE, Part I, 91, 97 (1965).

4. J.P. Jones and P.G. Bhuta, "Response of Cylindrical Shells to Moving Loads," J. Appl. Mech., 31, 105 (1964).

5. J. Mirsky and G. Herrmann, "Axially Symmetric Motions of Thick Cylindrical Shells," J. Appl. Mech., 25, 97 (1958).

6. T.E. Simkins, "Wave Coupling and Resonance in Gun Tubes," Proceedings of the 59th Shock and Vibration Symposium, Vol.III, Sandia Laboratories, Albuquerque, New Mexico, 1988, pp.271-285.

7. A.W. Leissa, "Vibration of Shells," NASA SP-288, Washington, DC, 1973, pp.32-34.

8. A.E.H. Love, A Treatise on the Mathematical Theory of Elasticity (Cambridge University Press, Cambridge, England, 1927), 4th ed. (reprinted by Dover Publications, Inc., New York, 1944), Secs.69 and 115.

9. D.C. Gazis, "Three-Dimensional Investigation of the Propagation of Waves in Hollow Cylinders. I. Analytical Foundations," J. Acoust. Soc. Am., 31, 568 (1959).

10. D.C. Gazis, "Three-Dimensional Investigation of the Propagation of Waves in Hollow Circular Cylinders. II. Numerical Results," J. Acoust. Soc. Am., 31, 573 (1959).

11. H.F. Tiersten, "Natural Boundary and Initial Conditions from a Modification of Hamilton's Principle," J. Math. Phys., 9, 1445 (1968).

12. H.F. Tiersten, Linear Piezoelectric Plate Vibrations (Plenum Press, New York, 1969), Chap.6, Sec.4.

13. The solution functions in θ could readily have been with a different phase angle than used in defining the eccentricity in Sec.2. However, since the range of integration is 2π, it would have no influence.

14. All terms arise from angular integrals of products of trigonometric functions over 2π. Consequently, only those arising from the double angle terms survive. All others vanish as a result of the periodicity. The resulting forms are very cumbersome and not particularly revealing.

15. H.A. Scarton, "Double Precision Fortran Subroutines to Compute Both Ordinary and Modified Bessel Functions of the First Kind and of Integer Order with Arbitrary Complex Argument: $J_n(x+jy)$ and $I_n(x+jy)$," J. Comp. Phys., 8, 295 (1971). An extended version of these subroutines by H.A. Scarton and P. Liang was kindly provided.

16. P.J. Davis and I. Polonsky, "Numerical Interpolation, Differentiation and Integration," in Handbook of Mathematical Functions, M. Abramowitz and I.O. Stegun, Eds. (Dover Publications, Inc., New York, 1965), pp.877-899, Formula 25.4.19.

17. It is of interest to note from Figs.9 - 11 to what extent the continuity of the radial displacement $u_r(a)$ at the pressure step ($\zeta = 0$) has been satisfied since the continuity of u_r, u_ζ and u_θ across the interface has not been imposed by the variational principle employed, in which all conditions appear as natural conditions. Consequently, the degree of continuity is indicative of the accuracy of the solution.

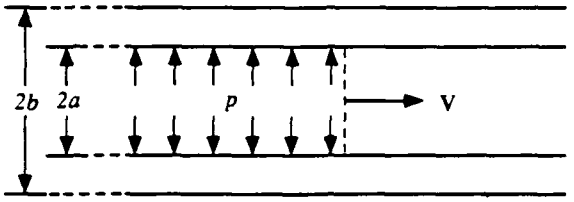

Figure 1 Cross-Section of Gun Tube Showing Pressure Step

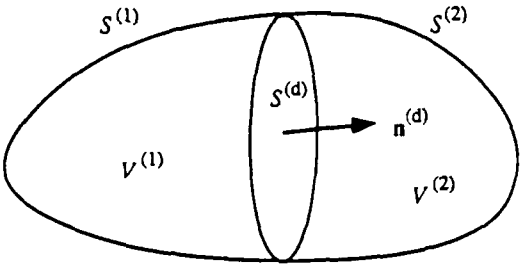

Figure 2 Diagram of a Bounded Region Containing an Internal Surface of Discontinuity

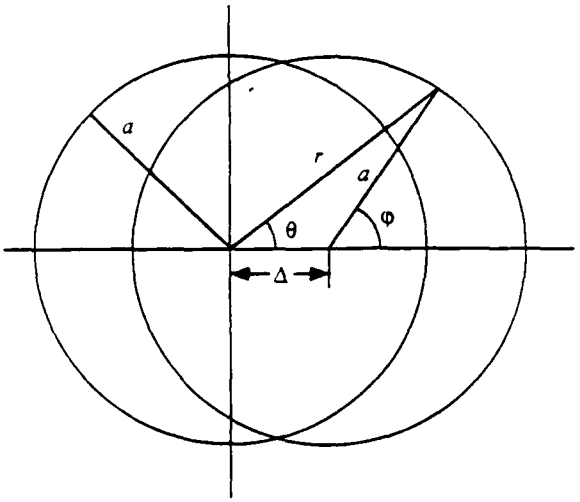

Figure 3 Diagram Relating Geometry of Eccentric Cylindrical Hole to Concentric Polar Coordinate System

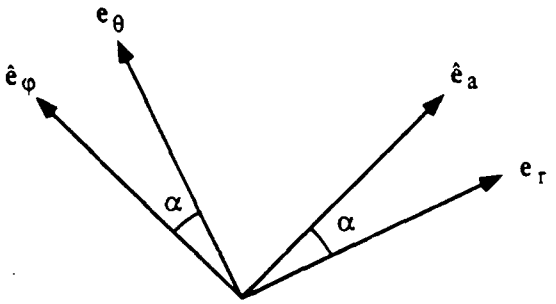

Figure 4 Diagram Showing the Relation Between Orthogonal Unit Vectors Referred to the Bore Surface and Orthogonal Unit Vectors in the Concentric Coordinate System

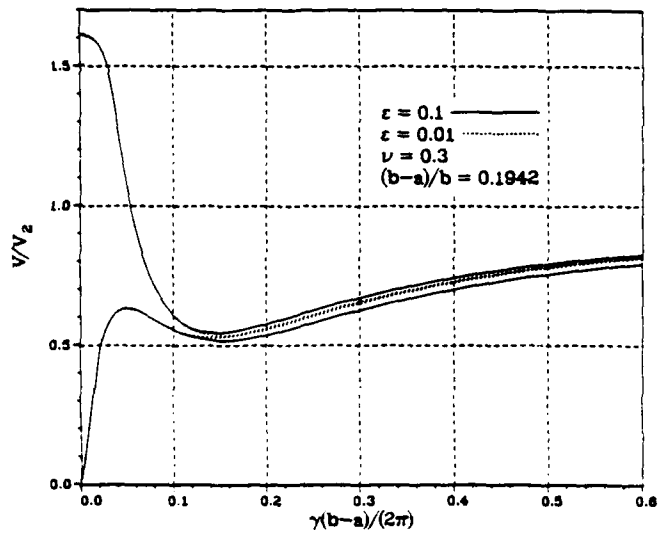

Figure 5 Phase Velocity Dispersion Curves for the Two Lowest Coupled Extensional and Flexural Modes for Two Distinct Eccentricity Ratios

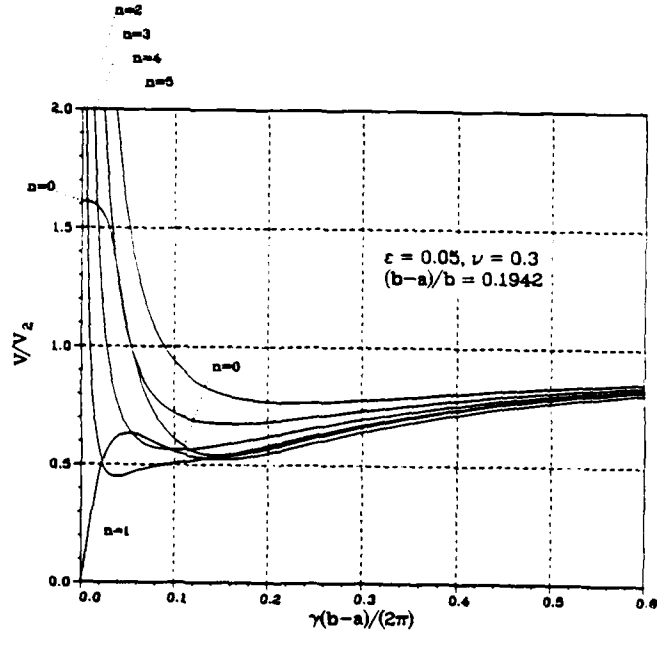

Figure 6 Phase Velocity Dispersion Curves for the Six Lowest Modes for an Intermediate Eccentricity Ratio

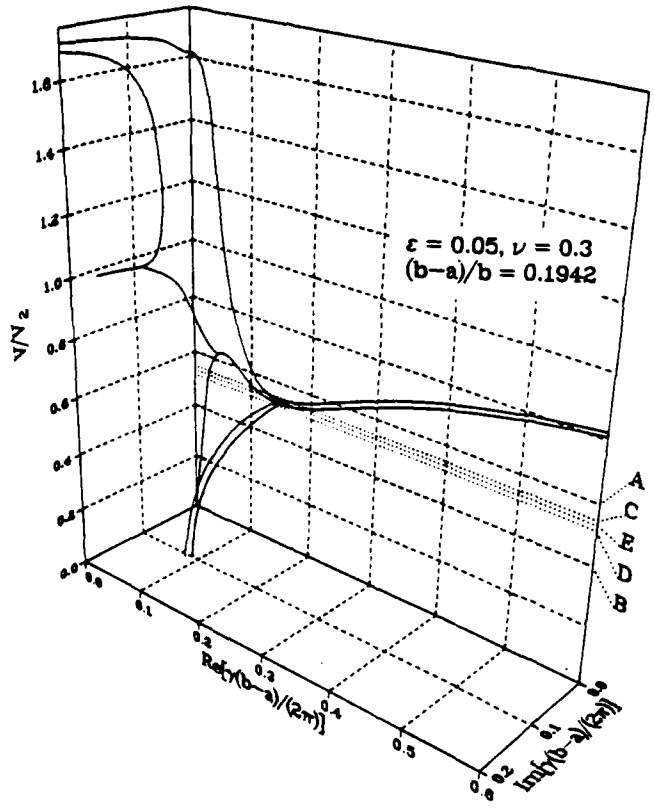

Figure 7 Phase Velocity Dispersion Curves for the Modes of Interest for the Eccentricity Used in the Forced Vibration Problem

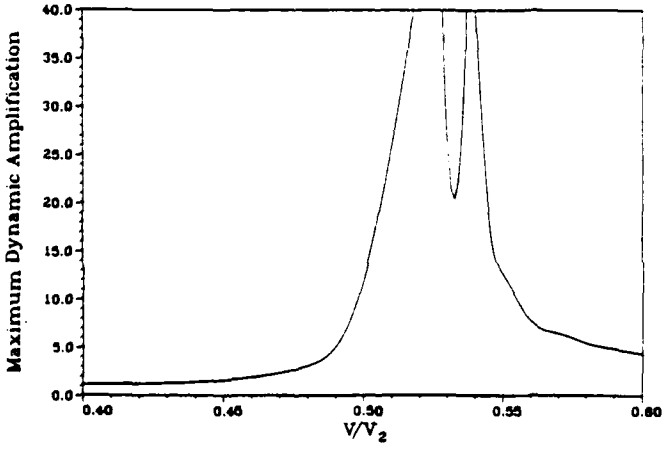

Figure 8 Dynamic Amplification Versus Projectile Velocity

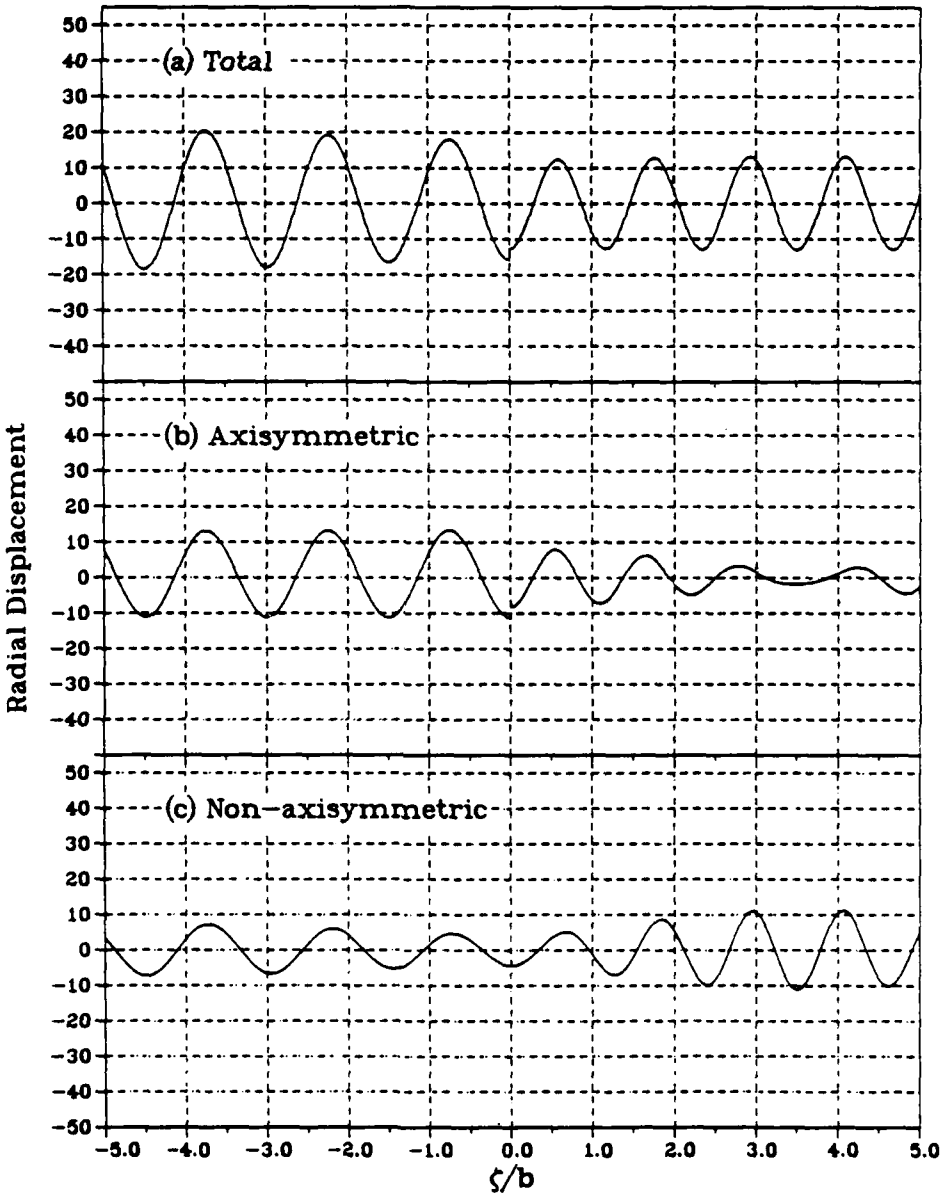

Figure 9 Radial Displacement Ratio (Amplification) Versus Distance from Pressure Step for the Projectile Velocity C for (a) the Entire Disturbance $\theta = \pi$, (b) the Axisymmetric Portion, (c) the nonaxisymmetric Portion

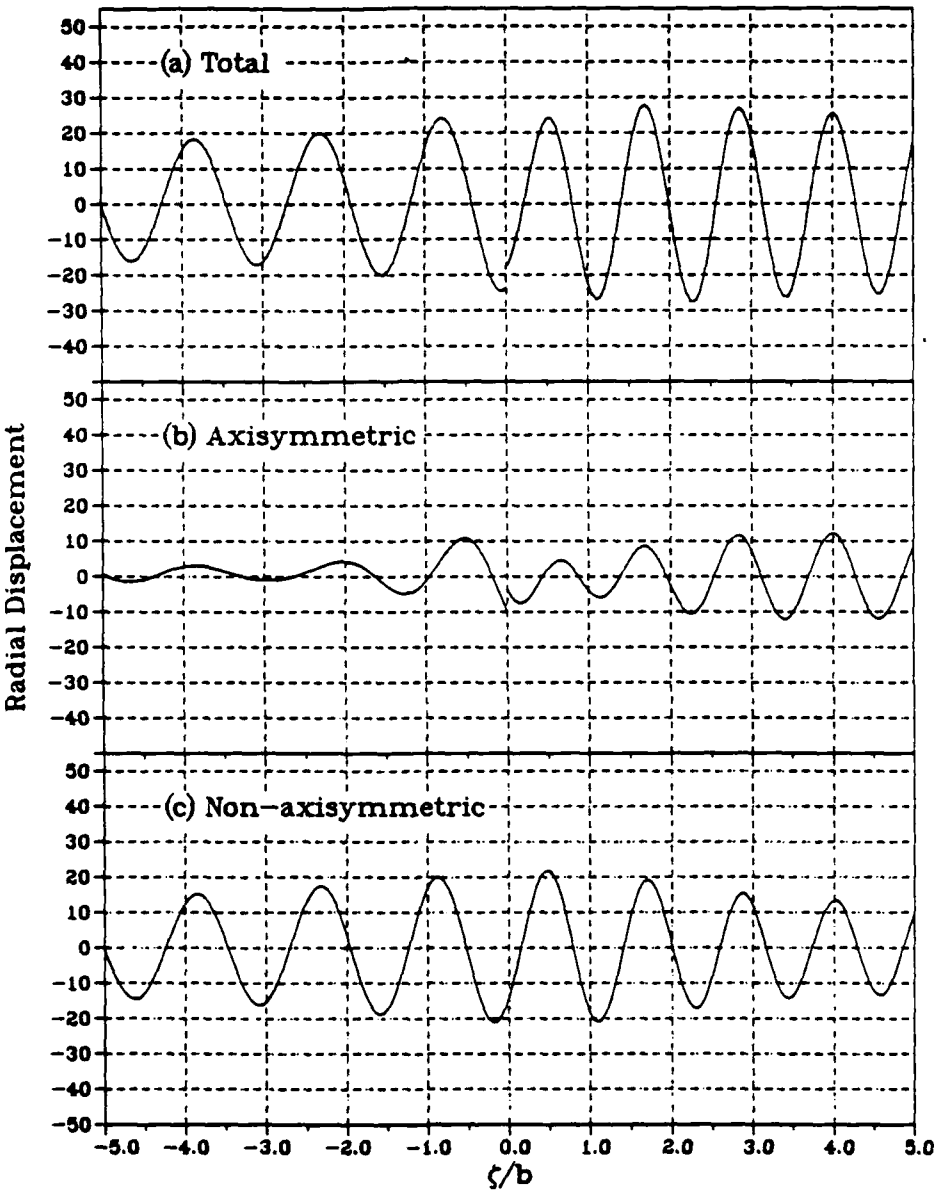

Figure 10 Contains the Same Information for the Projectile Velocity D as Figure 9 does for the Projectile Velocity C, (a) $\theta = 0$

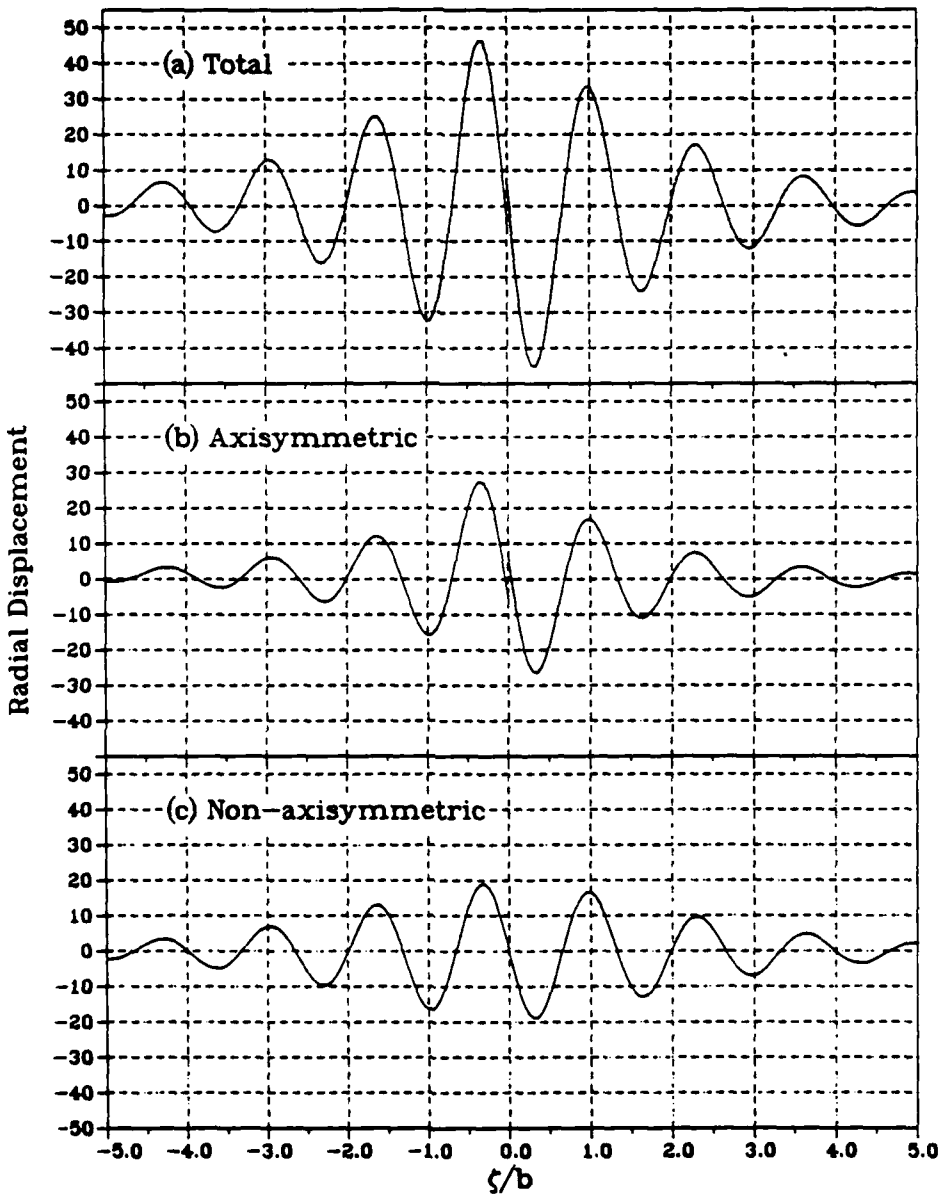

Figure 11 Contains the Same Information for the Projectile Velocity E as Figure 9 does for the Projectile Velocity C, (a) $\theta = 0$

TITLE: TRANSIENT VIBRATIONS AND INSTABILITY IN FLEXIBLE GUNS

IRADJ G. TADJBAKHSH[1], YUAN-AN SU[2]
DEPARTMENT OF CIVIL ENGINEERING
TROY, NEW YORK

ABSTRACT:

The gun tube is modeled as a flexible cylindrical shell with the effects of transverse shear and rotary inertia included. The projectile is modeled as a rigid body which rides on the gun. The interaction is assumed frictionless. This gives rise to forces acting on the projectile that depend on the deformation of the tube. The reaction on the cylinder is a travelling force whose position and magnitude depend upon the position of the projectile. The problem is nonlinear in the context of small deformation theory of shells. Numerical solution shows the wave-like nature of the vibrations and occurrence of instability for high velocities.

BIOGRAPHY: (1) and (2) Industrial and Educational backgrounds
PRESENT ASSIGNMENT: (1) Professor, (2) Graduate Research Assistant

PAST EXPERIENCE: (1) Industrial and Academic Research and Teaching, (2) Industrial Design and Research

DEGREES HELD: (1) B.S., M.S., Ph.D., (2) B.S., M.S., Ph.D. Candidate

I. INTRODUCTION

A complex dynamical system consists of a long flexible high–caliber gun tube firing projectiles propelled by the adiabatic expansion of explosive gases. Theoretically muzzle velocities of 12 km/s can be achieved. According to Charters (1987) even higher velocities lie in the realm of possibility if some design modifications of the gas reservoir and the breech mechanism are carried out.

The development of modern nigh velocity guns took a quantum jump when it was discovered that muzzle velocities of 7km/s can be achieved by using low molecular weight propellants such as hydrogen or helium. Earlier guns using nitrocellulose propellants are capable of achieving velocities of the order of 3 km/s. Employment of techniques that maintain constant pressure at the base of the projectile promises even greater muzzle velocities in the near future (Curtis, 1962). The combination of high internal pressure, hypervelocity projectile, and flexible gun tubes provides the mechanism for transfer of a large amount of the released energy to the gun and thus causing excessive vibrations and dynamic instability.

The problem of a moving pressure front and a projectile on a flexible tube is the important part of the dynamics of a gun. The moving mass and the moving load problems have been considered by many investigators in connection with the dynamics of bridges and cable–supported trolley cars. Achenbach and Sun (1965) considered the response of a Timoshenko–Rayleigh beam supported by an elastic foundation when subjected to a moving load. Their study pertains to the steady state situation in which a wave front moves with the speed of the load. Their results show the existence of certain critical speeds that when exceeded unbounded solutions may result.

In a later study Steele (1968) analyzed the response of a semi–infinite Timoshenko–Rayleigh beam on an elastic foundation under a step load that travels with a constant velocity. The author shows the existence of a singly "truly" critical speed and the impossibility of the occurrence of a steady state. He points out that the transients never die out but continue to linger in the vicinity of the front of the advancing load.

The moving mass problem introduces a more complex interaction with the supporting structure. Thus Ting, Genin and Ginsberg (1974) consider the effect of convective acceleration terms that were previously not included. This same effect has been recognized for pipes supporting moving fluids. This latter class of problems has been considered by Chen and Jendrzekczul (1985), Paidousis and Issid (1974).

Also Alexandridis, Dowell and Moon (1978) treated the dynamic interaction problem between a spring–mass–damper element and its supporting rail modeled as a prestressed continuously supported infinitely long beam. Their results indicate existence of critical velocity above which the system is dynamically unstable.

The history of developments in the problem of a hollow cylinder or a cylindrical shell with an expanding internal pressure is less crowded. In a basic early study Herrmann and Mirsky [1956] treated the problem of axisymmetric free vibration of a cylindrical shell

of infinite length. Their main result is the dispersion relations determining the axial phase velocity as a function of the wave length. In particular they point out the existence of a certain minimum phase velocity for the smaller wave lengths that would require use of shell bending theory. In a subsequent study the same authors (1958) consider the same problem in the light of refinements that take into account the effect of transverse normal stresses appropriate to thick shells. In their study of the nonaxially symmetric motion (1957) they show that bending or beam type motions are coupled with axial and radial components. Also existence of maximum and minimum phase velocities for certain wave lengths is observed. In this connection the study by Gazis (1959) of the three–dimensional wave propagation in hollow cylinders should be pointed out. This study, carried out within the general theory of linear elasticity, serves as a benchmark against which the results of the approximate shell theories can be checked.

The problem of the steady state response of an infinitely long cylindrical shell subjected to a concentrated ring load that moves with constant velocity was considered by Jones and Bhuta (1964). They show that bending resonances can occur at lower critical velocities than previously had been expected. In a similar study Tang (1985) considers a constant internal pressure that travels with a constant velocity. His results indicate the existence of a number of critical velocities, resonance and non–uniqueness of the solutions. These phenomena occur when the velocity of the advancing front falls in certain ranges delineated by the critical velocities.

The foregoing studies have had an impact on the understanding of the resonant vibrations of gun tubes during firing. Accurate recent measurements of dynamic strains corroborate the implications of the critical velocity theories of moving loads (Simkins, 1985). Noting that in the linear range transient vibrations are particular superpositions of free modes of vibrations the relevance of free vibrations analyses becomes apparent. Furthermore, as stated by Simkins (1987), energy of vibrations travel with the group velocity implying that certain high–frequency waves travel ahead of the moving pressure wave. This phenomenon gives rise to amplification of flexural vibrations.

In this study the gun tube is modeled as a flexible cylindrical shell with the effects of transverse shear and rotary inertia retained in the theoretical description. The projectile is modeled as a rigid body which rides on the gun tube and is driven by the expanding pressure front. Each body is governed separately by the laws of motion and the reaction forces that act between them. The interaction is considered to be that of two bodies that exert forces upon each other that are normal to the surface of contact. This type of interaction gives rise to forces acting on the projectile that depend upon the deformation of the cylinder. The reaction on the cylinder may be thought of as a traveling force whose magnitude, as well as position, depend upon the deformation. Thus the problem is nonlinear even in the context of linear shell theory.

The solution is sought by employing Galerkin procedure and reducing the problem to a nonlinear finite dimensional dynamical system. Of crucial importance to the convergence of the solution is the number of coordinate functions in the Galerkin procedure. This number must be large enough for these functions to accurately represent the spatial variations of the displacement field that accompany the high–frequency, short–wave length waves that are generated during firing. Therefore a wave dispersion

relationship, for free vibrations of the shell, was also carried out to obtain the necessary information relating the wave lengths to the speed of wave propagation.

Our numerical results show that except at the muzzle the bending effects are relatively unimportant for higher velocities. Vibrations are wave–like and depend upon the the speed of arrival of the pressure wave. When this speed exceeds a critical value, large amplitude and high frequency vibrations set in.

II. PROJECTILE IN A SMOOTH BORE

A cylindrical shell of length $\bar{\ell}$, thickness $\bar{h}$ and radius a is considered. As shown in Fig. 1 a Cartesian coordinate system x_i, i = 1, 2, 3 is selected such that x_1 is along the axis of the bore and x_1, x_3 is the vertical plane. For tilted firing, x_1–axis will be inclined with respect to the horizon by an angle θ. Also a cylindrical coordinate system α_1 $(=x_1)$ and α_2 $(=\alpha)$, denoting the polar angle, is selected to describe positions on the shell. A right handed triad of unit vectors $\underset{\sim}{n}_i$, i = 1, 2, 3, is selected with $\underset{\sim}{n}_1$ and $\underset{\sim}{n}_2$ drawn in the direction of increasing α_1 and α_2 respectively. The time–dependent components of displacements in directions of $\underset{\sim}{n}_i$ are denoted by $\bar{u}_i(x_1, \alpha, \bar{t})$ with $\bar{u}_3$ being the outward radial displacement.

The projectile of mass M is confined to the smooth bore. It is assumed that the motion of M takes place in the vertical x_1, x_3 plane. Thus the position $\underset{\sim}{r}_M$ of the projectile is given by

$$\underset{\sim}{r}_M = \bar{x}_0(\bar{t})\underset{\sim}{e}_1 + \bar{u}_3(x_1, 0, \bar{t})\underset{\sim}{e}_3 \tag{1}$$

where $\underset{\sim}{e}_1$, $\underset{\sim}{e}_2$, $\underset{\sim}{e}_3$ are the unit vectors of the Cartesian frame and $\bar{x}_0(t)$ represents the displacement of the projectile in the x_1 direction. The origin of α is placed on the x_3 axis so that the radial displacement $\bar{u}_3$ at $\alpha = 0$ is the displacement of the tube in the x_3 direction. The acceleration of the projectile is in the vertical plane and, expressed in terms of derivatives of the shell displacements, contains convective terms

$$\underset{\sim}{a}_M = a_1\underset{\sim}{e}_1 + a_3\underset{\sim}{e}_3 \equiv \frac{d^2\bar{x}_0}{d\bar{t}^2}\underset{\sim}{e}_1 + \left[\frac{\partial^2\bar{u}_3}{\partial x_1^2}\left(\frac{d\bar{x}_0}{d\bar{t}}\right)^2 + \frac{\partial\bar{u}_3}{\partial x_1}\frac{d^2\bar{x}_0}{d\bar{t}^2} + 2\frac{\partial^2\bar{u}_3}{\partial x_1\partial\bar{t}}\frac{d\bar{x}_0}{d\bar{t}} + \frac{\partial^2\bar{u}_3}{\partial\bar{t}^2}\right]\underset{\sim}{e}_3 \tag{2}$$

We now consider equation of motion of the projectile. As stated above this motion is assumed to take place in the x_1, x_3 plane, Fig. 2a. Account is taken of the deflected shape of the axis of the tube. The tangent to the deflected axis makes an angle γ with the $\underline{e}_1'$ direction. The unit tangent and the unit normal to the deflected axis are denoted by $\underline{e}_1'$ and $\underline{e}_3'$. Therefore we have

$$M\underline{a}_M = \bar{p}\, A_b\, \underline{e}_1' - Mg(\underline{e}_1 \sin\theta + \underline{e}_3 \cos\theta) - N\underline{e}_3' \tag{3}$$

where $\bar{p}$ is the pressure of the propellant gases, A_b is the base area of the projectile and g is the acceleration of gravity. The distributed reaction of the smooth tube on the projectile can be represented by $r(\alpha, \bar{t})\, \underline{n}_3'$ with $\underline{n}_3'$ being the radial unit normal to the tube in the deflected position and r assumed to be symmetric in α i.e. $r(\alpha, \bar{t}) = r(-\alpha, \bar{t})$. As shown in Fig. 2b, the reaction r acts over the semi circle of contact represented by $-\pi \leq \alpha \leq \pi$. Due to symmetry of r the resultant of the distributed reactions is in the vertical plane and can be represented by

$$\int_{-\pi}^{\pi} r\, \underline{n}_3'\, a\,d\alpha = \int_{-\pi}^{\pi} r(\sin\alpha\, \underline{e}_2' + \cos\alpha\, \underline{e}_3')\, a\,d\alpha = (a \int_{-\pi}^{\pi} r\cos\alpha\, d\alpha)\underline{e}_3' \equiv N\underline{e}_3' \tag{4}$$

Eq. (3) can be solved for N by doting it with $\underline{e}_3'$. The result is

$$N = -Mg\cos(\theta + \gamma) - M(-a_1 \sin\gamma + a_3 \cos\gamma) \tag{5}$$

The second term on the right in (5) is the contribution of acceleration of the projectile to the resultant of the reaction that acts on the projectile by the tube. Simkins has noted that this term, when considered for finite γ, does not contain the slope of the gun tube $\partial\bar{u}_3/\partial x_1$. To show this, one needs to note that $\partial\bar{u}_3/\partial x_1 = \tan\gamma$ and hence

$$-\frac{d^2\bar{x}_0}{d\bar{t}^2}\sin\gamma + \frac{\partial\bar{u}_3}{\partial x_1}\left[\frac{d^2\bar{x}_0}{d\bar{t}^2}\right]\cos\gamma = 0$$

Consequently these same terms drop from (5). Also for the first term in (5) one can make the approximation $\cos\gamma \approx 1$, $\sin\gamma \approx \partial\bar{u}_3/\partial x_1$. Therefore

$$N = -Mg\left[\cos\theta - \sin\theta\left[\frac{\partial\bar{u}_3}{\partial x_1}\right]\right] - M\left[\frac{\partial^2\bar{u}_3}{\partial\bar{t}^2} + 2\frac{\partial^2\bar{u}_3}{\partial x_1\partial\bar{t}}\left[\frac{d\bar{x}_0}{d\bar{t}}\right] + \frac{\partial\bar{u}_3}{\partial x_1^2}\left[\frac{d\bar{x}_0}{d\bar{t}}\right]^2\right] \tag{6}$$

The forces that act on the cylindrical shell consist of its own weight, the pressure of the expanding gases behind the projectile $\bar{p}$ and the reaction of the projectile upon the shell. Expressing these as a distributed vector–valued function, we have

$$\underset{\sim}{q} = -mg\,(\sin\theta\,\underset{\sim}{e}_1 + \cos\theta\,\underset{\sim}{e}_3) + \bar{p}\,\underset{\sim}{n}_3\,H(\bar{x}_0 - x_1) + N\,\underset{\sim}{e}_3'\,\delta(a\alpha)\,\delta(x_1 - \bar{x}_0) \tag{7}$$

where H is the unit step function, equal to unity for positive arguments and zero otherwise, and δ is the Dirac delta function. Noting that $\underset{\sim}{e}_3' = \cos\gamma\,\underset{\sim}{e}_3 - \sin\gamma\,\underset{\sim}{e}_1$, we retain only the linear terms in $\underset{\sim}{u}_i$ in the product $N\underset{\sim}{e}_3'$. Expressing the result in terms of components in directions $\underset{\sim}{n}_i$ we have

$$\begin{aligned}\underset{\sim}{q} = {} & [-mg\sin\theta + Mg\cos\theta\,S^*\cdot\delta(a\alpha)\,\delta(x_1-\bar{x}_0)]\underset{\sim}{n}_1 + \\ & \{mg\cos\theta + M[g\cos\theta - g\sin\theta\cdot S^* + R^*]\,\delta(a\alpha)\,\delta(x_1-\bar{x}_0)\}\sin\alpha\cdot\underset{\sim}{n}_2 + \\ & \{\bar{p}H(\bar{x}_0-x_1) + [-mg\cos\theta + M(-g\cos\theta + g\sin\theta\cdot S^* - R^*)\,\delta(a\alpha)\,\delta(x_1-\bar{x}_0)]\cos\alpha\}\underset{\sim}{n}_3\end{aligned} \tag{8}$$

where

$$R^* = \frac{\partial^2\bar{u}_3}{\partial\bar{t}^2} + 2\frac{\partial^2\bar{u}_3}{\partial x_1\partial\bar{t}}\frac{d\bar{x}_0}{d\bar{t}} + \frac{\partial^2\bar{u}_3}{\partial x_1^2}\left[\frac{d\bar{x}_0}{d\bar{t}}\right]^2$$

$$S^* = \frac{\partial\bar{u}_3}{\partial x_1} \tag{9}$$

Thus the reaction of the projectile on the cylinder is represented as a concentrated traveling load that acts on the x_1, x_3 plane ($\alpha = 0$). The equation of balance of linear momentum for the shell will be

$$\frac{\partial \underline{F}_1}{\partial x_1} + \frac{1}{a}\frac{\partial \underline{F}_2}{\partial \alpha} + \underline{q} = m\frac{\partial^2 \underline{u}}{\partial \bar{t}^2} \tag{10}$$

wherein m is mass per unit area of shell and $\underline{F}_1$ and $\underline{F}_2$ represent the force per unit area acting on cross sections x_1 = const. and α = const., respectively. The force vector $\underline{q}$ is given by (8).

The dot product of (3) with $\underline{e}_1$ yields the equation of motion of the projectile along the axis of the tube

$$M\frac{d^2\bar{x}_0}{d\bar{t}^2} = \bar{p}\,A_b\cos\gamma - Mg\sin\theta + N\sin\gamma \tag{11}$$

Using the approximation for small γ and using (7), but retaining only linear terms in shell displacements, (11) becomes

$$M\frac{d^2\bar{x}_0}{d\bar{t}^2} = \bar{p}\,A_b - Mg\left[\sin\theta + \cos\theta\left[\frac{\partial \bar{u}_3}{\partial x_1}\right]_{\alpha_2 = 0, \alpha_1 = \bar{x}_0}\right] \tag{12}$$

The gas pressure $\bar{p}$ in general depends upon the thermodynamic laws that govern its behavior or may be programmed, by injections through the breech, to follow a prescribed path. In this paper we consider only constant values for $\bar{p}$.

III. THE CYLINDRICAL TUBE

We shall assume that the linear theory of deformation of cylindrical shells is adequate for the description of the behavior of the tube. We shall however, take account of transverse shear deformations in order to allow for thick–walled cylinders. The equations of balance of angular momentum of the shell are

$$\begin{aligned}\frac{\partial M_{11}}{\partial x_1} + \frac{1}{a}\frac{\partial M_{12}}{\partial \alpha} - N_{13} &= \frac{m\bar{h}^2}{12}\frac{\partial^2 \beta_1}{\partial \bar{t}^2}\\ \frac{\partial M_{21}}{\partial x_1} + \frac{1}{a}\frac{\partial M_{22}}{\partial \alpha} - N_{23} &= \frac{m\bar{h}^2}{12}\frac{\partial^2 \beta_2}{\partial \bar{t}^2}\end{aligned} \tag{13}$$

where M_{ij}, i,j = 1,2, are the bending and twisting moments in the shell, N_{13} and N_{23} are

the radial stress resultants and β_1, β_2 are the shear strains on cross sections x_1 = const. and α = const. respectively.

Equations (10) and (13) form a single matrix equations describing the behavior of the shell. With E and ν denoting Young's modulus and Poisson's ratio, we define dimensionless variables and parameters

$$u_i = \bar{u}_i/\bar{h},\ i = 1, 2, 3;\ U = (U_1, U_2, U_3, U_4, U_5)^T \equiv (u_1, u_2, u_3, \beta_1, \beta_2)^T$$

$$t = \sqrt{\frac{E\bar{h}}{ma^2(1-\nu^2)}}\,\bar{t},\ x = \frac{x_1}{a},\ x_0 = \frac{\bar{x}_0}{a},\ h = \frac{\bar{h}}{a},\ \ell = \frac{\bar{\ell}}{a} \tag{14}$$

$$p = \frac{a^2(1-\nu^2)}{E\bar{h}^2}\,\bar{p} \equiv c\bar{p}.\ \rho_m = \frac{mga^2(1-\nu^2)}{E\bar{h}^2},\ \rho_M = \frac{Mg(1-\nu^2)}{E\bar{h}^2},\ \rho_r = \frac{M}{ma^2}$$

and multiply (10) by c and (13) by $c/\bar{h}$. The result is

$$\underline{L}\underline{U} + \underline{Q} = \underline{J}\ddot{\underline{U}} \quad , \quad (\cdot = \frac{\partial}{\partial t}) \tag{15}$$

where

$$\underline{J} = \text{diag}\left[1, 1, 1, \frac{1}{12}, \frac{1}{12}\right] \tag{16}$$

$$\underline{Q} = (Q_1, Q_2, Q_3, 0, 0)^T = (c\,\underline{q}^T, 0, 0)^T$$

We separate $\underline{Q}$ into regular and singular parts and further separate the latter into the part due to weight and the part due to interaction of the projectile with the cylinder. Then

$$\underline{Q} = \underline{Q}^1 + (\underline{Q}^2 + \underline{Q}^3)\delta(\alpha)\delta(x - x_0) \tag{17}$$

where

$$\underline{Q}^1 = (-\rho_m \sin\theta,\ \rho_m \cos\theta \sin\alpha,\ pH\,(x_0 - x) - \rho_m \cos\theta \cos\alpha,\ 0,\ 0)^T$$

$$\underline{Q}^2 = \rho_M \cos\theta\,(0, \sin\alpha, -\cos\alpha, 0, 0)^T \tag{18}$$

$$\underset{\sim}{Q}^3 = (\rho_M \cos\theta\, h\, \dot{s},\ (-\rho_M \sin\theta\, h\dot{s} + \rho_r \hat{R}) \sin\alpha,\ (\rho_M \sin\theta\, h\dot{s} - \rho_r \hat{R}) \cos\alpha,\ 0,\ 0)^T$$

Here the delta functions have been transformed according to $\delta(a\alpha) = a^{-1}\ \delta(\alpha)$ and $\delta(x_1 - x_0) = a^{-1}\ \delta(x - x_0)$ and $\hat{R}$ and $\hat{S}$ stand for

$$\hat{R}(x,\alpha,t) = \ddot{U}_3 + 2\dot{U}_3' \dot{x}_0 + U_3'' (\dot{x}_0)^2$$
$$\hat{S}(x,\alpha,t) = U_3' \tag{19}$$

The operator $\underset{\sim}{L}$ in (13) is a 5x5 symmetric, second order differential operator that is based upon the elastic behavior of thick shells (presented in the Appendix).

We shall assume that the gun tube is totally fixed at the breech end which implies

$$\underset{\sim}{U} = \underset{\sim}{0} \qquad \text{at} \qquad x = 0 \tag{20}$$

The condition of zero traction, $\underset{\sim}{F}_1 = M_{11} = M_{12} = 0$, at the muzzle end can be written in the matrix form

$$\underset{\sim}{U}' + \underset{\sim}{B}\underset{\sim}{U} = 0 \qquad \text{at} \qquad x = \ell \tag{21}$$

where $\underset{\sim}{B}$ is a constant 5x5 matrix defined in the Appendix.

IV. THE GALERKIN SOLUTION

With prescribed loading given in (17) one can seek solutions for the displacement of the shell that consists of rotationally symmetric part and the part that described its bending. For the former the components u_2 and u_5 $(=\beta_2)$ vanish. For the latter u_2 and u_5 will be antisymmetric.

Consistent with these symmetries we seek solutions of the following type

$$\begin{aligned}
u_1 &= u_{10}(x,t) + u_{11}(x,t)\cos\alpha \\
u_2 &= \qquad\quad + u_{21}(x,t)\sin\alpha \\
u_3 &= u_{30}(x,t) + u_{31}(x,t)\cos\alpha \\
u_4 &= u_{40}(x,t) + u_{41}(x,t)\cos\alpha \equiv \beta_1 \\
u_5 &= \qquad\quad + u_{51}(x,t)\sin\alpha \equiv \beta_2
\end{aligned} \tag{22}$$

In the matrix form this can be represented by

$$\underline{U} = \hat{\underline{I}}_0 \underline{U}^0(x,t) + \hat{\underline{I}}_1 \underline{U}^1(x,t) \tag{23}$$

where

$$\begin{aligned} \hat{\underline{I}}_0 &= \text{diag}\,[1,0,1,1,0] \\ \hat{\underline{I}}_1 &= \text{diag}\,[\cos\alpha, \sin\alpha, \cos\alpha, \cos\alpha, \sin\alpha] \end{aligned} \tag{24}$$

and

$$\begin{aligned} \underline{U}^0 &= (u_{10}, 0, u_{30}, u_{40}, 0)^T \\ \underline{u}^1 &= (u_{11}, u_{21}, u_{31}, u_{41}, u_{51})^T \end{aligned} \tag{25}$$

Thus $\underline{U}^0$ is the rotationally symmetric part of the solution and $\underline{U}^1$ is the part of the solution that accounts for bending of the tube. The matrices $\hat{\underline{I}}_0$ and $\hat{\underline{I}}_1$ are matrices of coordinate functions that characterize the dependence of the solution upon α.

The boundary conditions (17) and (18) translate into

$$\begin{aligned} \underline{U}^0 &= \underline{0} \quad , \quad x = 0 \\ \underline{\dot{U}}^0 + \underline{B}^0\underline{U}^0 &= 0 \quad , \quad x = \ell \end{aligned} \tag{26}$$

for $\underline{U}^0$ and

$$\begin{aligned} \underline{U}^1 &= 0 \quad , \quad x = 0 \\ \underline{\dot{U}}^1 + \underline{B}^1\underline{U}^1 &= 0 \quad , \quad X = \ell \end{aligned} \tag{27}$$

where $\underline{B}^0$ and $\underline{B}^1$ are constant matrices of order 5x5 and are given in the Appendix. For the coordinate functions in the x–direction we assume

$$\underset{\sim}{U}^0 = \sum_{i=1}^{N_0} \underset{\sim}{\beta}^i(x)\underset{\sim}{Y}^i(t) \equiv \underset{\sim}{\beta}(x)\underset{\sim}{Y}(t)$$

$$\underset{\sim}{U}^1 = \sum_{i=1}^{N_1} \underset{\sim}{\gamma}^i(x)\underset{\sim}{Z}^i(t) \equiv \underset{\sim}{\gamma}(x)\underset{\sim}{Z}(t) \tag{28}$$

where $\underset{\sim}{\beta}^i$, $\underset{\sim}{\gamma}^i$ are 5x5 matrices given by

$$\underset{\sim}{\beta}^i = V_i(x)\cos\frac{i\pi x}{\ell}\,\underset{\sim}{I} - \frac{\ell}{i\pi}\sin\frac{i\pi x}{\ell}\,\underset{\sim}{B}^0, \quad i = 1, 2, 3, \ldots N_0$$

$$\underset{\sim}{\gamma}^i = V_i(x)\cos\frac{i\pi x}{\ell}\,\underset{\sim}{I} - \frac{\ell}{i\pi}\sin\frac{i\pi x}{\ell}\,\underset{\sim}{B}^1, \quad i = 1, 2, 3, \ldots N_1 \tag{29}$$

Here $\underset{\sim}{I}$ is the unit matrix and N_0 and N_1 are selected large enough to ensure convergence for the two parts of the solution. The scalars $V_i(x)$ are selected such that

$$V_i(0) = V_i'(\ell) = 0 \quad , \quad V_i(\ell) = 1, \quad i = 1, 2, \ldots\ldots \tag{30}$$

and consequently the boundary conditions (20) – (21) are satisfied for each i as may be verified by direct substitution. In the work reported here it was expedient to select all ν_i's as equal and equal to

$$V = \sin\frac{\pi x}{2\ell} \tag{31}$$

Also in (27) we have defined

$$\underset{\sim}{\beta} = \left[\underset{\sim}{\beta}^1, \underset{\sim}{\beta}^2, \ldots\underset{\sim}{\beta}^{N_0}\right] \quad , \qquad \underset{\sim}{Y} = (\underset{\sim}{Y}^{1T}, \underset{\sim}{Y}^{2T}, \ldots, \underset{\sim}{Y}^{N_0T})^T$$

$$\underset{\sim}{\gamma} = \left[\underset{\sim}{\gamma}^1, \underset{\sim}{\gamma}^2, \ldots\underset{\sim}{\gamma}^{N_1}\right] \quad , \qquad \underset{\sim}{Z} = (\underset{\sim}{Z}^{1T}, \underset{\sim}{Z}^{2T}, \ldots, \underset{\sim}{Z}^{N_1T})^T \tag{32}$$

For future use it is noted that $\underset{\sim}{\beta}$ and $\underset{\sim}{\gamma}$ may also be written as

$$\underline{\beta} = \begin{bmatrix} \underline{\beta}_1 \\ \underline{\beta}_2 \\ \vdots \\ \underline{\beta}_5 \end{bmatrix} \quad , \quad \gamma = \begin{bmatrix} \underline{\gamma}_1 \\ \underline{\gamma}_2 \\ \vdots \\ \underline{\gamma}_5 \end{bmatrix} \tag{33}$$

where $\underline{\beta}_1 \ldots \underline{\beta}_5$ and $\underline{\gamma}_1 \ldots \underline{\gamma}_5$ are $1*N_0$ and $1*5N_1$ row matrices of $\underline{\beta}$ and $\underline{\gamma}$ respectively.

To implement the Galerkin procedure we substitute (28) into (15) and make the result orthogonal to $\underline{I}_0\,\underline{\beta}$ and $\underline{I}_1\underline{\gamma}$. Thus we have

$$\int_0^{\ell} \int_{-\pi}^{\pi} \underline{\beta}^T \hat{\underline{I}}_0^T \left[\left[\underline{J} \frac{\partial^2}{\partial t^2} - \underline{L} \right] \left[\hat{\underline{I}}_0 \underline{\beta}\, \underline{Y} + \hat{\underline{I}}_1 \underline{\gamma}\, \underline{Z} \right] - \underline{Q} \right] d\alpha dx = \underline{0} \tag{34}$$

$$\int_0^{\ell} \int_{-\pi}^{\pi} \underline{\gamma}^T \hat{\underline{I}}_1^T \left[\left[\underline{J} \frac{\partial^2}{\partial t^2} - \underline{L} \right] \left[\hat{\underline{I}}_0 \underline{\beta}\, \underline{Y} + \hat{\underline{I}}_1 \underline{\gamma}\, \underline{Z} \right] - \underline{Q} \right] d\alpha dx = 0 \tag{35}$$

In the reduction of these equations one notes that

$$\int_{\pi}^{\pi} \hat{\underline{I}}_0^T \underline{J}\, \hat{\underline{I}}_1 d\alpha = \int_{\pi}^{\pi} \hat{\underline{I}}_1^T \underline{J}\, \hat{\underline{I}}_0 d\alpha = \int_{\pi}^{\pi} \hat{\underline{I}}_0^T \underline{L}\, \hat{\underline{I}}_1 d\alpha = \int_{\pi}^{\pi} \hat{\underline{I}}_1^T \underline{L}\, \hat{\underline{I}}_0 d\alpha = 0 \tag{36}$$

for in each case the matrix of integrals are diagonals with elements that are proportional to either $\cos\alpha$ or $\sin\alpha$. Also

$$\begin{aligned} &\int_{\pi}^{\pi} \hat{\underline{I}}_0^T \underline{J}\, \hat{\underline{I}}_0 d\alpha = 2\pi \underline{J}_0 \equiv 2\pi\, \mathrm{diag}\left[1,0,1,\tfrac{1}{12},0\right] \\ &\int_{\pi}^{\pi} \hat{\underline{I}}_1^T \underline{J}\, \hat{\underline{I}}_1 d\alpha = \pi \underline{J} \end{aligned} \tag{37}$$

Dividing (34) by 2π and (35) by π we can write the result in the following form

$$\underline{M}^0\ddot{\underline{Y}} + \underline{K}^0\underline{Y} + \Delta\underline{M}^0 \cdot \ddot{\underline{W}} + \Delta\underline{C}^0 \cdot \dot{\underline{W}} + \Delta\underline{K}^0\,\underline{W} = \underline{F}^0 \tag{38.1}$$

$$\underline{M}^1\ddot{\underline{Z}} + \underline{K}^1\underline{Z} + \Delta\underline{M}^1 \cdot \ddot{\underline{W}} + \Delta\underline{C}^1 \cdot \dot{\underline{W}} + \Delta\underline{K}^1\,\underline{W} = \underline{F}^1 \tag{38.2}$$

where $\underline{W} = (\underline{Y}^T, \underline{Z}^T)^T$ and the primary mass and stiffness matrices are constants given by the following definitions

$$\begin{aligned}
\underline{M}^0 &= \frac{1}{2\pi}\int_0^{\ell}\int_{-\pi}^{\pi} \underline{\beta}^T\,\hat{\underline{I}}_0^T\,\underline{J}\,\hat{\underline{I}}_0\,\underline{\beta}\,d\alpha\,dx = \int_0^{\ell} \underline{\beta}^T\,\underline{J}_0\,\underline{\beta}\,dx \\
\underline{K}^0 &= -\frac{1}{2\pi}\int_0^{\ell}\int_{-\pi}^{\pi} \underline{\beta}^T\,\hat{\underline{I}}_0^T\,\underline{L}\,\hat{\underline{I}}_0\,\underline{\beta}\,d\alpha\,dx = -\int_0^{\ell} \underline{\beta}^T\,\underline{L}_0\,\underline{\beta}\,dx \\
\underline{M}^1 &= \frac{1}{\pi}\int_0^{\ell}\int_{-\pi}^{\pi} \underline{\gamma}^T\,\hat{\underline{I}}_0^T\,\underline{J}\,\hat{\underline{I}}_1\,\underline{\gamma}\,d\alpha\,dx = \int_0^{\ell} \underline{\gamma}^T\,\underline{J}\,\underline{\gamma}\,dx \\
\underline{K}^1 &= -\frac{1}{\pi}\int_0^{\ell}\int_{-\pi}^{\pi} \underline{\gamma}^T\,\hat{\underline{I}}_1^T\,\underline{L}\,\hat{\underline{I}}_1\,\underline{\gamma}\,d\alpha\,dx = -\int_0^{\ell} \underline{\gamma}^T\,\underline{L}^1\,\underline{\gamma}\,dx
\end{aligned} \tag{39}$$

where:

$$\begin{aligned}
\underline{L}^0 &= \hat{\underline{I}}_0^T\,\underline{L}\,\hat{\underline{I}}_0 \\
\underline{L}^1 &= \frac{1}{\pi}\int_{-\pi}^{\pi} \hat{\underline{I}}_1^T(\alpha)\,\underline{L}\,\hat{\underline{I}}_1(\alpha)\,d\alpha
\end{aligned} \tag{40}$$

The remaining matrices in (38) arise from the integrals of $\underline{Q}^3$ in (34) – (35). These matrices are non stationary and couple the two systems. Recalling the definition of $\dot{R}$ and $\hat{S}$ from (19) we note that

$$\hat{R}(x,0,t) = \underline{\delta}^T\ddot{\underline{W}} + 2\dot{x}_0\,\underline{\delta}^{T'}\dot{\underline{W}} + \dot{x}_0^2\underline{\delta}^{T''}\underline{W}$$

$$\hat{S}(x,0,t) = \underset{\sim}{\delta}^{T'}\ \underset{\sim}{W} \tag{41}$$

where $\underset{\sim}{\delta} = [\underset{\sim}{\beta}_3,\ \underset{\sim}{\gamma}_3]$. Therefore the integrals of $\underset{\sim}{Q}^3$ in (34) – (35) became

$$-\frac{1}{2\pi}\int_0^{\ell}\int_{-\pi}^{\pi} \underset{\sim}{\beta}^T\ \hat{\underset{\sim}{I}}_0^T\ \underset{\sim}{Q}^3\ \delta(\alpha)\delta(x-x_0)d\alpha\,dx = -\frac{\rho_M h\cos\theta}{2\pi}\ \underset{\sim}{\beta}_1^T(x_0)\ \hat{S}(x_0,0,t)$$

$$-\frac{\underset{\sim}{\beta}_3^T(x_0)}{2\pi}\left[\rho_M \sin\theta\, h\, \hat{S}(x_0,0,t) - \rho_r\, \hat{R}(x_0,0,t)\right]$$

$$= \Delta\ \underset{\sim}{M}^0\ \ddot{\underset{\sim}{W}} + \Delta\ \underset{\sim}{C}^0\ \dot{\underset{\sim}{W}} + \Delta\underset{\sim}{K}^0\ W$$

$$-\frac{1}{\pi}\int_0^{\ell}\int_{-\pi}^{\pi} \underset{\sim}{\gamma}^T\ \hat{\underset{\sim}{I}}_1^T\ \underset{\sim}{Q}^3\ \delta(\alpha)\delta(x-x_0)d\alpha\,dx = -\frac{\rho_M h\cos\theta}{\pi}\ \underset{\sim}{\gamma}_1^T(x_0)\ \hat{S}(x_0,0,t) \tag{42}$$

$$-\frac{\underset{\sim}{\gamma}_3^T(x_0)}{\pi}\left[\rho_M \sin\theta\, h\, \hat{S}(x_0,0,t) - \rho_r\, \hat{R}(x_0,0,t)\right]$$

$$= \Delta\ \underset{\sim}{M}^1\ \ddot{\underset{\sim}{W}} + \Delta\ \underset{\sim}{C}^1\ \dot{\underset{\sim}{W}} + \Delta\underset{\sim}{K}^1\ \underset{\sim}{W}$$

specifically we have for the incremental matrices

$$\Delta\underset{\sim}{M}^0 = \frac{\rho_r}{2\pi}\left[\underset{\sim}{\beta}_3^T(x_0)\ \underset{\sim}{\delta}(x_0)\right], \qquad \Delta\underset{\sim}{M}^1 = \frac{\rho_r}{\pi}\left[\underset{\sim}{\gamma}_3^T(x_0)\ \underset{\sim}{\delta}(x_0)\right]$$

$$\Delta\underset{\sim}{C}^0 = \frac{\rho_r \dot{x}_0}{\pi}\left[\underset{\sim}{\beta}_3^T(x_0)\ \underset{\sim}{\delta}'(x_0)\right], \qquad \Delta\underset{\sim}{C}^1 = \frac{2\rho_r \dot{x}_0}{\pi}\left[\underset{\sim}{\gamma}_3^T(x_0)\ \underset{\sim}{\delta}'(x_0)\right] \tag{43}$$

$$\Delta\underset{\sim}{K}^0 = \frac{\rho_r \dot{x}_0^2}{2\pi}\left[\underset{\sim}{\beta}_3^T(x_0)\underset{\sim}{\delta}''(x_0)\right] - \frac{\rho_M h}{2\pi}\left\{\cos\theta\cdot\left[\underset{\sim}{\beta}_1^T(x_0)\underset{\sim}{\delta}'(x_0)\right] + \sin\theta\left[\underset{\sim}{\beta}_3^T(x_0)\ \underset{\sim}{\delta}'(x_0)\right]\right\}$$

$$\Delta\underset{\sim}{K}^1 = \frac{\rho_r \dot{x}_0^2}{\pi}\left[\underset{\sim}{\gamma}_3^T(x_0)\underset{\sim}{\delta}''(x_0)\right] - \frac{\rho_M h}{\pi}\left\{\cos\theta\cdot\left[\underset{\sim}{\gamma}_1^T(x_0)\underset{\sim}{\delta}'(x_0)\right] + \sin\theta\left[\underset{\sim}{\gamma}_3^T(x_0)\ \underset{\sim}{\delta}'(x_0)\right]\right\}$$

The integrals of $\underset{\sim}{Q}^1$ and $\underset{\sim}{Q}^2$ in (34) – (35) lead to the forcing vectors $\underset{\sim}{F}^0$ and $\underset{\sim}{F}^1$. We have

$$\underset{\sim}{F}^0 = -\rho_m \sin\theta \int_0^{\ell} \underset{\sim}{\beta}_1^T(x)\,dx + p \int_0^{x_0} \underset{\sim}{\beta}_3^T(x)\,dx - \frac{\rho_M \cos\theta}{2\pi}\,\underset{\sim}{\beta}_3^T(x_0) \tag{44}$$

$$\underset{\sim}{F}^1 = \rho_m \cos\theta \int_0^{\ell} \underset{\sim}{\gamma}_2^T(x)dx - \rho_m \cos\theta \int_0^{\ell} \underset{\sim}{\gamma}_3^T(x)dx - \frac{\rho_M \cos\theta}{\pi}\,\underset{\sim}{\gamma}_3^T(x_0) \tag{45}$$

Finally if we define

$$\underset{\sim}{F} = \begin{bmatrix} \underset{\sim}{F}^0 \\ \underset{\sim}{F}^1 \end{bmatrix}, \qquad \underset{\sim}{M} = \begin{bmatrix} \underset{\sim}{M}^0, & \Delta\underset{\sim}{M}^0 \\ \Delta\underset{\sim}{M}^1, & \underset{\sim}{M}^1 \end{bmatrix}, \qquad \underset{\sim}{C} = \begin{bmatrix} \Delta\underset{\sim}{C}^0 \\ \Delta\underset{\sim}{C}^1 \end{bmatrix}, \qquad K = \begin{bmatrix} \underset{\sim}{K}^0, & \Delta\underset{\sim}{k}^0 \\ \Delta\underset{\sim}{K}^1, & \underset{\sim}{K}^1 \end{bmatrix} \tag{46}$$

then (38) can be written in the standard form

$$\underset{\sim}{M}\,\ddot{\underset{\sim}{W}} + \underset{\sim}{C}\,(\dot{x}_0, x_0)\,\dot{\underset{\sim}{W}} + \underset{\sim}{K}\,(\dot{x}_0, x_0)\,\underset{\sim}{W} = \underset{\sim}{F}\,(x_0) \tag{47}$$

Finally it is noted that in problem (38.1), the rotationally symmetric part of the solution is of a lower dimension than the problem of (38.2). This is observed from (25) in which $\underset{\sim}{U}^0$ has only three non–zero components. Consequently $\underset{\sim}{Y}$ and $\underset{\sim}{F}^0$ have dimension $3N_0$ while $\underset{\sim}{M}^0$ and $\underset{\sim}{K}^0$ are $3N_0 * 3N_0$. Also $\underset{\sim}{W}$ has $3N_0 + 5N_1$, elements while $\Delta\underset{\sim}{M}^0$, $\Delta\underset{\sim}{c}^0$and $\Delta\underset{\sim}{k}^0$ are $3N_0*(3N_0 + 5N_1)$ matrices. The equations (12) for axial motion of the projectile becomes

$$\ddot{x}_0 = \frac{\pi h}{\rho_r} p - \rho_m h\,[\sin\theta + h\,\underset{\sim}{\delta}^{T'}(x_0)\,\underset{\sim}{W}\,(t)] \tag{48}$$

The system consisting of (47) – (48) is nonlinear due to dependence of coefficients in (47) upon $x_0(t)$ with the latter depending upon $\underset{\sim}{W}$ as indicated by (48). This nonlinearity arises within the linear shell theory and is due to frictionless normal reaction of the projectile on the barrel.

The initial condition of the combined system is the deflected gun tube due to its own weight, and can be given by

$$Y(0) = (\underset{\sim}{K}^0)^{-1}[-\rho_m \sin\theta \int_0^{\ell} \underset{\sim}{\beta}_1^T(x)dx] \tag{49}$$

$$Z(0) = (\underset{\sim}{K}^1)^{-1}\{-\rho_m \cos\theta \int_0^{\ell} [\underset{\sim}{\gamma}_2^T(x) - \underset{\sim}{\gamma}_3^T(x)]\, dx\} \tag{50}$$

V. THE NUMERICAL SOLUTION

The selection of the number N_0 of the Galerkin coordinate functions to achieve numerical accuracy of rotationally symmetric waves is of paramount importance. This number is the number of harmonics required to represent the spatial variations of the displacement field. Since in a firing, waves of very short wave lengths (very high frequency) are generated, the number N_0 must be large enough to provide sufficient resolution in the expansion. Similarly the number N_1 must be large enough to ensure convergence of the bending part of the solution.

Considering first the rotationally symmetric vibrations we note that, in general, such vibrations are superpositions of free travelling waves in the medium. Therefore we consider the wave dispersion relationship for the dimensionless wave equation

$$\underset{\sim}{L}^0 \underset{\sim}{U}^0 = \underset{\sim}{J}^0 \ddot{\underset{\sim}{U}}^0 \tag{51}$$

The displacement field is assumed to be of the form

$$\underset{\sim}{U}^0 = \hat{U} \exp in(x-vt) \tag{52}$$

where v is the constant velocity and n is the wave number. The dispersion relationship takes the form

$$n^2(An^4 - 2Bn^2 + C) = 0 \tag{53}$$

where

$$A = (v^2-1)^2\,(v^2-k)$$

$$B = \tfrac{1}{2}(v^2-1)\,[(1 - \frac{12k}{h^2})v^2 - (1-\nu^2)]$$

$$C = \frac{12k}{h^2}\,[v^2 - (1-\nu^2)] \tag{54}$$

and, v is a dimensionless velocity defined by

$$v = \frac{\bar{v}}{\bar{v}_d} \tag{55}$$

in which $\bar{v}$ is the constant moving velocity of the wave front travelling along the tube, $\bar{v}_d$ is the dilational wave velocity of the shell as given by

$$\bar{v}_d = \sqrt{\frac{E}{\rho(1-\nu^2)}} \tag{56}$$

Two of the roots n in Eq. (51) are zero which represent the rigid body modes in axial direction, the other four roots are given by

$$n = \pm\left[\frac{1}{A}\left(B \pm \sqrt{B^2-AC}\right)\right]^{\frac{1}{2}} \tag{57}$$

Here, n may be real, complex, or pure imaginary. The real parts of n represent the wave number of the system, which is defined as the number of cycles in a length of $x = 2\pi$. The imaginary part of n is the attenuation number which is the number of times a decaying exponential is multiplied by e^{-1} in the unit length. The typical wave dispersion curves are shown in Fig. 3 in which the dimensionless thickness h is 0.20 and the shear stress factor of cross section k^* is 2/3. The solid curves denote the wave number and the dashed curves represent the attenuation number for each case. When the velocity v is smaller than v_a, which is given by

$$v_a = \frac{1}{\left(\frac{12k}{h^2}-1\right)}\left\{(1-\nu^2)\left(1-\frac{12k}{h^2}\right) - \frac{24k^2}{h^2}\left(1-\left[(1-\nu^2)\left(\frac{12}{h^2}\,\frac{1}{k}\right)+1\right]^{\frac{1}{2}}\right)\right\}^{\frac{1}{2}} \tag{58}$$

then the roots n are two pairs of complex conjugates of which share opposite signs and the response of the system consists of a decaying sinusoidal wave.

All roots n are real when v falls between v_a and $\sqrt{k}$. Two sinusoidal waves comprise the response of the system. One of these waves is an advancing wave which travels in the positive x–direction. The other wave travels in the negative x–direction and with a lower velocity. For a finite length tube, one can express N_0 by equating the wave number in a harmonic distribution to the wave number of the advancing wave, i.e.

$$N_0 = \frac{\ell}{\pi} n \tag{59}$$

In a firing, the velocity of pressure wave front is zero at the breech and reaches its peak when the projectile emerge from the muzzle. Hence the minimum for N_0, denoted by N_{min}, can be obtained from the wave number corresponding to zero velocity and is determined to be

$$N_{min} = \frac{\ell}{\pi}\left[\frac{1}{h}\sqrt{3(1-\nu^2)} - \frac{1}{4k}(1-\nu^2)\right]^{\frac{1}{2}} \tag{60}$$

The required number of terms, denoted by N_ℓ, can be approximately given by

$$N_\ell = \frac{\ell}{\pi} n_\ell \tag{61}$$

where n_ℓ is the wave number for the velocity of the pressure front being equal to projectile exit velocity. The latter can be shown to be given by

$$v(\ell) = \dot{x}_0(\ell) \approx \sqrt{2\ell\left(\frac{\pi h p}{\rho_r} - \rho_m h \sin\theta\right)} \tag{62}$$

For purpose of comparison with results of previous investigators, we also define

$$\lambda = \frac{m\bar{x}_0^2(\ell)}{2}\sqrt{\frac{a^2}{E\bar{h}D}} \tag{63}$$

which in terms of dimensionless quantities can be shown to be

$$\lambda = \frac{\dot{x}_0^2(\ell)}{h}\sqrt{\frac{3}{1-\nu^2}} \approx \frac{2\ell}{h}\left(\frac{\pi h p}{\rho_r} - \rho_m h \sin\theta\right) \tag{64}$$

We note that Reismann (1965) has shown that rotationally symmetric waves, moving axially with constant velocity in a "thin" shell of infinite extent, become unbounded when $\lambda = 1$.

Now, consider a gun with the following properties

$$\ell = 30,\ h = 0.20,\ k = 0.2333,\ \theta = 0,$$

$$\rho_m = 1.15 \times 10^{-7},\ \rho_r = 15,\ \nu = 0.30,\ \rho_M = 0 \tag{65}$$

Only the rotationally symmetric mode is considered, i.e., a cylindrical shell subjected to a constant moving pressure front p travelling with constant acceleration as determined from a simplified form of (48) as

$$\ddot{x}_0 = \frac{\pi h p}{\rho_r} - \rho_m h \sin\theta \tag{66}$$

Then the equation of motion of the system can be taken to be from (38.1)

$$\underset{\sim}{M}^0 \ddot{\underset{\sim}{Y}} + \underset{\sim}{K}^0 \underset{\sim}{Y} = \underset{\sim}{F}^0 \tag{67}$$

For the parameter values selected above $v_a = 0.30449$ and the corresponding value of N_0, denoted by N_a is 45. For λ equal to 1 and 1.25, the values of N_0's are 70 and 96 respectively. The radial response, normalized by dividing by the Lamé constant $w_L = (1-\nu^2)/p$, is denoted by w. Thus

$$w = U_{30}/w_L \tag{68}$$

Fig. (4) shows the maximum radial expansion of the cylinder for $\lambda_\ell = 1.25$, where λ_ℓ refers to value of λ at $x = \ell$. The results show that accuracy is acceptable for all $N_0 \geq 70$. Thus numerical convergence can be achieved for $\lambda_\ell \geq 1$ by using the N_0 that corresponds to $\lambda = 1$. The small discrepancy in results between values corresponding to $N_0 = 45$ and $N_0 = 70$ is attributable to the missing advancing waves in the range $45 > N_0 > 70$. Therefore (61) can be used to find appropriate N_0 for any λ and maximum N_0, denoted by N_{max}, corresponds to $\lambda = 1$ even when $\lambda_\ell > 1$.

Regarding N_0 as a function of the velocity $v(\ell)$, one can construct the range of values of N_0 for the h values that occur in practice and this is shown in Fig. 5 where the length of the tube is 100. The number of terms between N_a and N_{max} in Fig. 5 represent the necessary terms to account for the effect of the advancing waves.

Moving on to the convergence consideration for the bending mode we note that a critical case exists for a beam supporting a mass that moves with a constant velocity. Ting, Genin and Ginsburg (1974) show the existence of a critical velocity that is proportional to the first fundamental frequency of flexural vibrations. This relationship takes the form

$$v_{cr} = \frac{\ell}{\pi}\omega_1 \tag{69}$$

where ω_1 is the first flexural frequency in radians per second. Therefore, the lower indexed terms of Galerkin coordinate functions (29) play a major role in the analysis of flexural vibrations of the shells. Typically we find that a much smaller number N_1, independent of the moving pressure wave velocity, will provide accurate results.

The test for convergence of bending mode on the physical model consisting of a cylindrical shell with a self–propelling and constantly accelerating projectile. Thus the effect of the internal pressure was removed. The governing equations are the same as in (38) with the term involving p removed in the definition of $\underset{\sim}{F}^0$ in (44). The pressure term $\pi hp/\rho_r$ in (48) is retained as the motive force on the projectile. The results show that convergence can be achieved for $N_1 = 15$.

VI. RESPONSE CHARACTERISTICS

To investigate the response characteristics of the system we begin with an investigation of the bending behavior. The results for the maximum bending deflection over time at any location x/ℓ is shown in Fig. 6. The bending deflections is the radial deflection w at $\alpha = 0$ and is denoted by w_b. Two sets of values for $\lambda_\ell = 1.25$ and $\lambda_\ell = 10$ and in each case ρ_r is given the two values $\rho_r = 4$ and $\rho_r = 40$. Based on data of Charters (1987) the range $4 \leq \rho_r \leq 40$ are the values encountered in modern hypervelocity guns.

The results show that the bending response is dominated by the mass of projectile, which is represented by the relative mass ratio ρ_r. From Fig. 6, the resonant behavior of the bending mode clearly show up in the heavy mass cases but with deflections that are of order of $10^{-5}\,\ell$. These values are neglible for practical considerations.

Next we consider a long gun similar to 120 mm × M25 for which $\ell = 100$ and the remaining parameter are taken to be $\rho_r = 15$, $h = 0.2$, $\theta = 0$ and $\lambda_\ell = 1.25$. Based on the necessary criteria for convergence the values $N_0 = 230$ and $N_1 = 15$ are selected. In Fig. 7 the numerical results for the rotationally symmetric mode based on (67) are shown in dotted line. The results for the full or the complete system, eqs (38), are shown in solid lines. The numerical integration for the complete system can be carried out until the projectile reaches $0.99546\,\ell$. Beyond this the solution diverges abruptly. Since the solution should be continuous, the integration was considered complete at this point. The two sets of results are in complete agreement in the interval $0 \leq x \leq 0.78$ L. At $x = 0.78\ell$, λ becomes approximately 0.975 and the radial expansion reaches the value 3.70. Between this point and the muzzle discrepancy appears between the two sets of solutions which is negligible up to nearly $x = 0.97$L and thereafter becomes significant. These two solutions

are presented in Fig. 8 as waves viewed by an observer at $x = 0.9\ell$. The wave character of the solutions, being calm before the arrival of the projectile and rapid high amplitude vibrations thereafter, is observed.

Noting that for high exit velocities and for most of the length of the gun the effect of bending can be neglected, Fig. 9 shows three different time histories for rotationally symmetric modes at $x = 0.5\ell$. For $\lambda_\ell = 1.25$, the jump in w signifies the arrival of pressure wave. In this case λ at $x = 0.5\ell$ is nearly 0.625 and less than the critical value $\lambda = 1$ predicted by the thin shell theory. Hence no rapid oscillations follow the arrival of the pressure wave. By contrast, when $\lambda_\ell = 3.0$ and λ at $x = 0.5\ell$ is about 1.5 instability sets in immediately upon arrival of the pressure wave. The case when $\lambda_\ell = 10$, can be termed supercritical. The vibrations after passage of projectile are of relatively uniform amplitude and frequency.

The foregoing results show that the response of the system is local, i.e. the response at any point is small before the arrival of the pressure wave. Thereafter the response depends upon the speed of the arrival which appears to be critical at about $\lambda \approx 1$. For $\lambda > 1$ the local vibrations are with large amplitude and high frequency that represent instability and eventually begin to decay. For $\lambda < 1$ the local behavior is stable before and after the arrival of the pressure wave.

From a design point of view a response spectrum which is the envelope of maximum local response as it depends on the local speed of arrival pressure wave v for $\lambda_\ell = 1.25$, 3.0 and 10.0 can be constructed. Such a plot is shown in Fig. 10 and should be compared with plots of dynamic amplification factor with velocity in an infinitely long thin shell with pressure waves that move at constant velocity.

VII. ACKNOWLEDGEMENT

The research reported here was carried out under a grant by U.S. Army Research Office to the Rensselaer Polytechnic Institute. This support is gratefully acknowledged.

VIII. APPENDIX

$\underset{\sim}{L}$ is a 5 × 5 operator matrix which have the following elements.

$L_{11} = \partial_{xx} + ((1-\nu)/2)\,\partial_{\alpha\alpha}$, $L_{12} = ((1+\nu)/2)\partial_{x\alpha}$, $L_{13} = \nu\partial_x$, $L_{14} = L_{15} = 0$
$L_{21} = L_{12}$, $L_{22} = \partial_{\alpha\alpha} + ((1-\nu)/2)\,\partial_{xx} - k$, $L_{23} = (1+k)\partial_\alpha$, $L_{24} = 0$, $L_{25} = k/h$
$L_{31} = -L_{13}$, $L_{32} = -L_{23}$, $L_{33} = k(\partial_{xx} + \partial_{\alpha\alpha}) - 1$, $L_{34} = (k/h)\partial_x$, $L_{35} = (k/h)\partial_\alpha$,
$L_{41} = 0$, $L_{42} = 0$, $L_{43} = -L_{34}$, $L_{44} = (1/12)(\partial_{xx} + ((1-\nu)/2)\partial_{\alpha\alpha}) - (k/h^2)$
$L_{45} = (1/12)((1+\nu)/2)\partial_{x\alpha}$, $L_{51} = 0$, $L_{52} = L_{25}$, $L_{53} = -L_{35}$, $L_{54} = L_{45}$,
$L_{55} = (1/12)[((1-\nu)/2)\partial_{xx} + \partial_{\alpha\alpha})] - (k/h^2)$

Here α_1, α_2 are replaced by x, α respectively and k is defined as $k = ((1-\nu)/2)\,k^*$.

Applying Galerkin's procedure, one can separate $\underset{\sim}{L}$ into $\underset{\sim}{L}^0$ and $\underset{\sim}{L}'$ as shown in Eq. (40), which respectively represent the rotationally symmetric mode and the bending mode of the shell. The elements $\underset{\sim}{L}^0$ and $\underset{\sim}{L}^1$ are as follows

$L^0_{11} = \partial_{xx}$, $L^0_{13} = \nu\partial_x$, $L^0_{14} = 0$, $L^0_{31} = -L^0_{13}$, $L^0_{33} = k\partial_{xx} - 1$, $L^0_{34} = (k/h)\partial_x$
$L^0_{41} = 0$, $L^0_{43} = -L^0_{34}$, $L^0_{44} = (1/12)\partial_{xx} - \dfrac{k}{h^2}$, $L^0_{2j} = 0$, $L^0_{5j} = 0$, $L^0_{i2} = 0$, $L^0_{i5} = 0$
i,j = 1,...5

$L^1_{11} = \partial_{xx} - (1-\nu)/2$, $L^1_{12} = ((1+\nu)/2)\partial_x$, $L^1_{13} = \nu\partial_x$, $L^1_{14} = L^1_{15} = 0$
$L^1_{21} = -L^1_{12}$, $L^1_{22} = ((1-\nu)/2)\,\partial_{xx} - (1+k)$, $L^1_{23} = -(1+k)$, $L^1_{24} = 0$, $L^1_{25} = k/h$
$L^1_{31} = -L^1_{13}$, $L^1_{32} = L^1_{23}$, $L^1_{33} = k(\partial_{xx} - 1) - 1$, $L^1_{34} = (k/h)\partial_x$, $L^1_{35} = k/h$
$L^1_{41} = L^1_{42} = 0$, $L^1_{43} = -L^1_{34}$, $L^1_{44} = (1/12)[\partial_{xx} - ((1-\nu)/2)] - (k/h^2)$,
$L^1_{45} = (1/12)((1+\nu)/2)\partial_x$
$L^1_{51} = 0$, $L^1_{52} = L^1_{25}$, $L^1_{53} = L^1_{35}$, $L^1_{54} = -L^1_{45}$, $L^1_{55} = (1/12)[((1-\nu)/2)\partial_{xx} - 1] - (k/h^2)$

The elements of the matrices $\underset{\sim}{B}$, $\underset{\sim}{B}^0$, and $\underset{\sim}{B}^1$ are listed as follows

$$B_{12} = \nu\partial_\alpha \quad , \quad B_{13} = \nu \quad , \quad B_{21} = \partial_\alpha \quad , \quad B_{34} = h^{-1} \quad , \quad B_{45} = \nu\partial_\alpha \quad , \quad B_{54} = \partial_\alpha$$

$$B^0_{13} = \nu \quad , \quad B^0_{34} = h^{-1}$$

$$B^1_{12} = \nu \quad , \quad B^1_{13} = \nu \quad , \quad B^1_{21} = -1 \quad , \quad B^1_{34} = h^{-1} \quad , \quad B^1_{45} = \nu \quad , \quad B^1_{54} = -1$$

all other elements are zero.

IX. REFERENCES

Achenbach, J.D. and Sun, C.T., "Moving Load on a Flexibly Supported Timoshenko Beam," Int. J. Solids Structures, 1965, Vol. 1, pp. 353–370.

Alexandridis, A.A., Dowell, E.H. and Moon, F.C., "The Coupled Response of a Dynamic Element Riding on a Continuously Supported Beam," Transactions of ASME, J. of Appl. Mech., Vol. 45, Dec. 1978, pp. 864–890.

Charters, A.C., "Development of High–Velocity Gas–Dynamics Gun," Int. J. Impact Engrg., Vol. 5, 1987, pp. 181–203.

Chen, S.S. and Jendrzekczul, J.A., "General Characteristics, Transition and Control of Instability of Tubes Conveying Fluid," J. Acoust. Soc. Am. 77(3), March 1985, pp. 887–895.

Curtis, J.S., "An Accelerated Reservoir Light Gas Gun," NASA TN D–11 04, 1962.

Gazis, D.C., "Three–Dimensional Investigation of the Propagation of Waves in Hollow Cylinders. I. Analytical Foundation: and "II. Numerical Results," J. of the Acoustical Soc. of Am., Vol. 31, No. 5, May 1959, pp. 569–578.

Herrmann, G. and Mirsky, I., "Three–Dimensional and Shell–Theory Analysis of Axially Symmetric Motion of Cylinders," J. Appl. Mech., 1956, 23, pp. 563–568.

Jones, J.P. and Bhuta, P.G., "Response of Cylindrical Shells to Moving Loads," ASME, J. of Appl. Mech., March 1864, pp. 105–111.

Mirsky, I. and Herrmann, G., "Nonaxially Symmetric Motions of Cylindrical Shells," J. Acoust. Soc. Am., Vol. 29, No. 10, 1957, pp. 1116–1124.

Mirsky, I. and Herrmann, G., "Axially Symmetric Motion of Thick Cylindrical Shells," J. Appl. Mech., March 1958, pp. 97–102.

Paidoussis, M.P. and Issid, N.T., "Dynamic Stability of Pipes Conveying Fluid," Journal of Sound and Vibration, 1974, 33(3), pp. 267–294.

Simkins, T.E., Pflegel, G.A. and Scanlon, R.D., "Corroborative Measurements of the Transverse Motion of a Gun Tube During Firing," Proc. 4th U.S. Army Symp. Gun Dyn., 1985.

Simkins, T.E., "Resonance of Flexural Waves in Gun Tubes," U.S. Armament Research, Development and Engineering Center, Watervliet Arsenal, Watervliet, NY, Technical Report ARCCB–TR–87008.

Steels, C.R., "The Timoshenko Beam with a Moving Load," ASME Journal of Applied Mechanics, Sept. 1968, pp. 481–488.

Tang, Sing–Chih, "Dynamic Response of a Tube Under Moving Pressure," ASCE J. Engr. Mech. Div., Vol. 91, No. EM5, 1965, pp. 97–122.

Ting, E.C., Genin, J. and Ginsburg, J.H., "A General Algorithm for Moving Mass Problems," Journal of Sound and Vibrations, 1974, 33(1), pp. 49–58.

Werner, S., "Vibrations of Shells and Plates," Maral Dekker, Inc., New York, 1981.

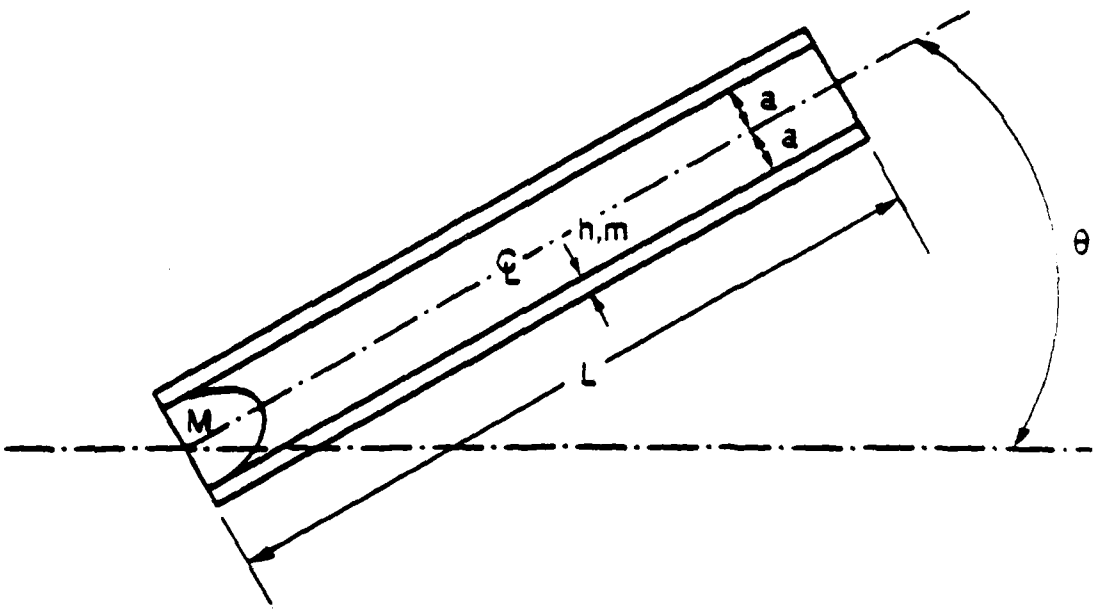

(a) A gas–propelled projectile and gun–tube dynamic system

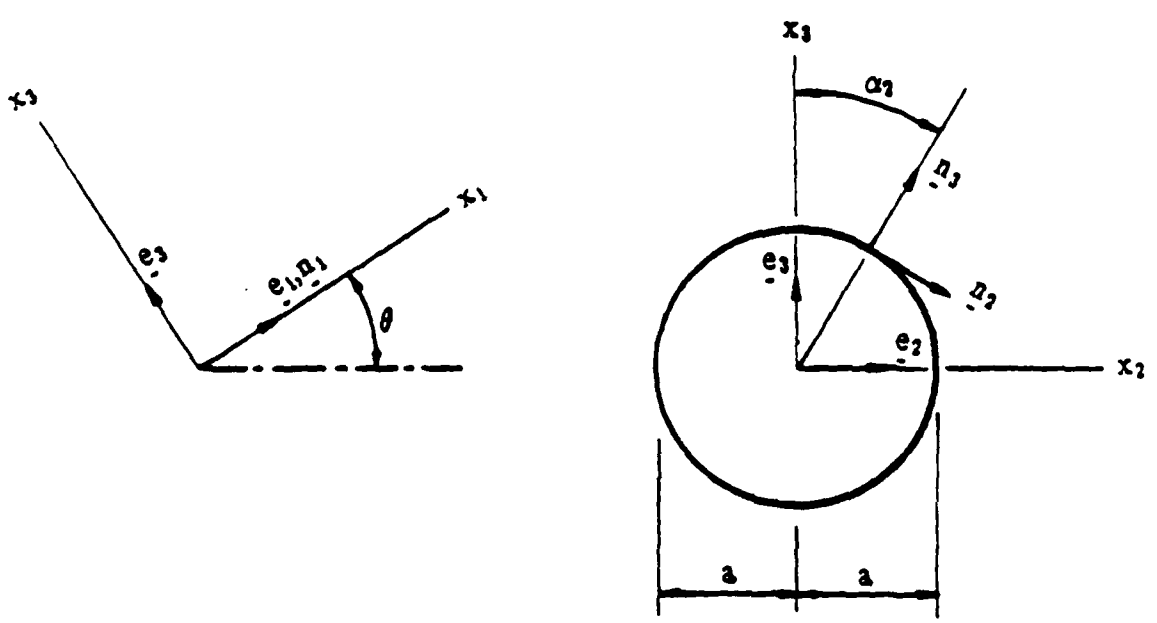

(b) The Cartesian and cylindrical coordinate system

Fig.1 Dynamics of gas–propelled projectile in a smooth bore

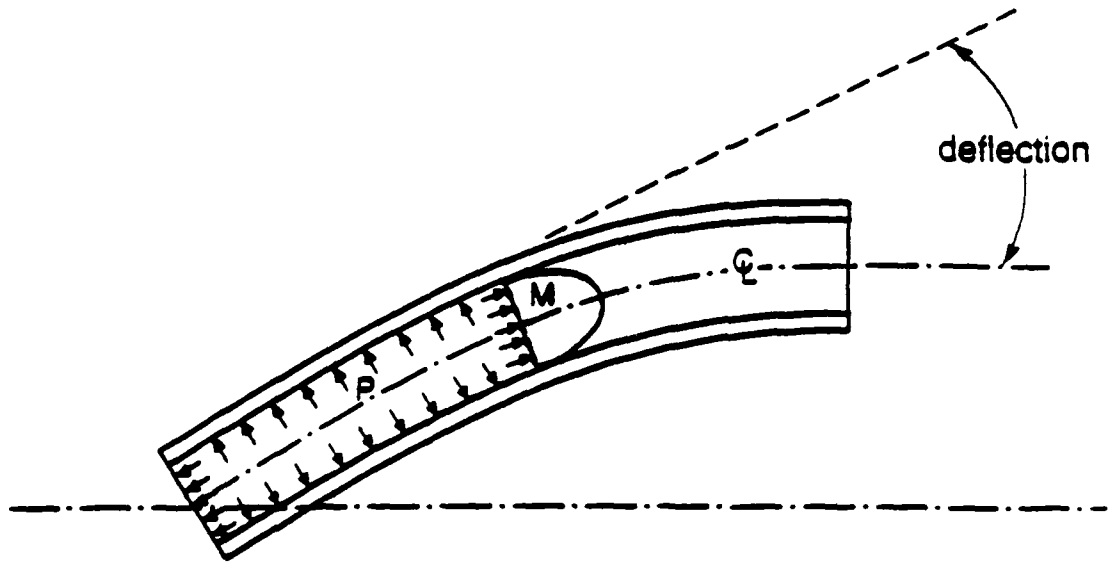

(a) Schematic figure of a deflected gun–tube dynamic system during firing

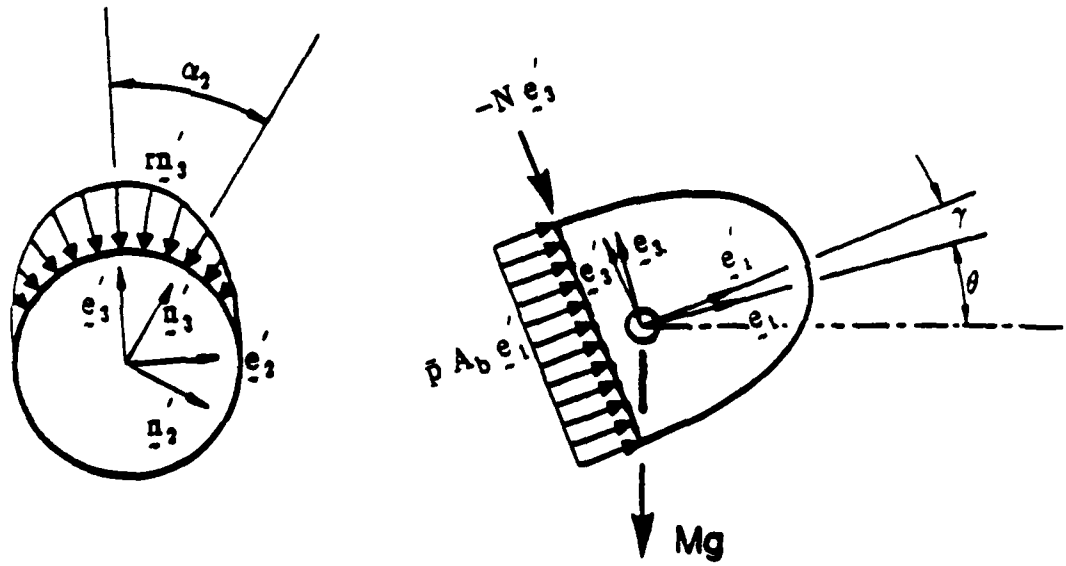

(b) Rigid body diagrams of the projectile

Fig.2 Forces on projectile in frictionless bore

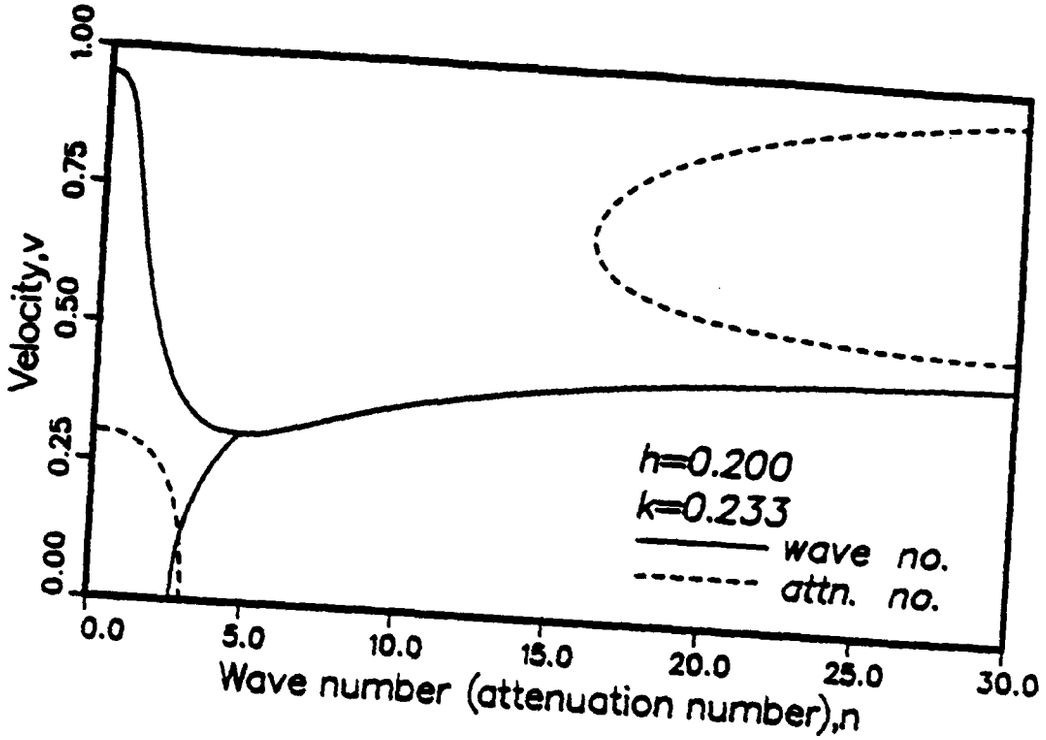

Fig.3 The wave dispersion relation of rotatioanlly symmetric mode

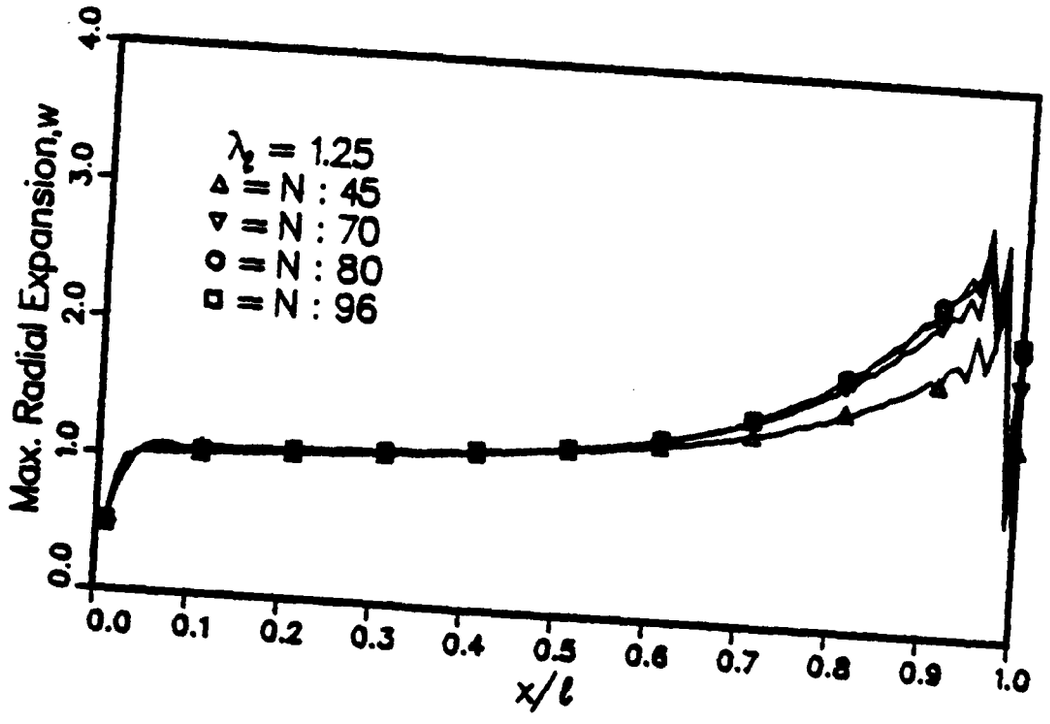

Fig.4 The convergence of Galerkin procedure of the rotationlly symmetric mode

ℓ=30., h=0.2, θ=0., ρ_r=15., λ_ℓ=1.25

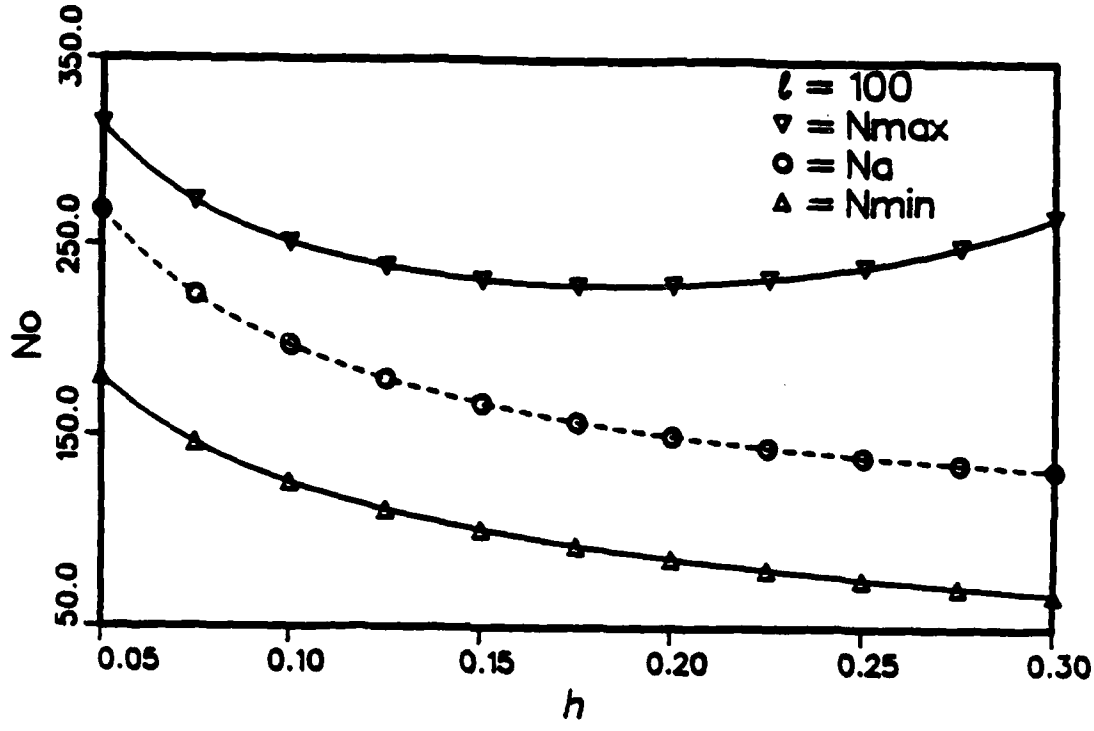

Fig.5 The number of coordinate functions of rotationally symmetric mode

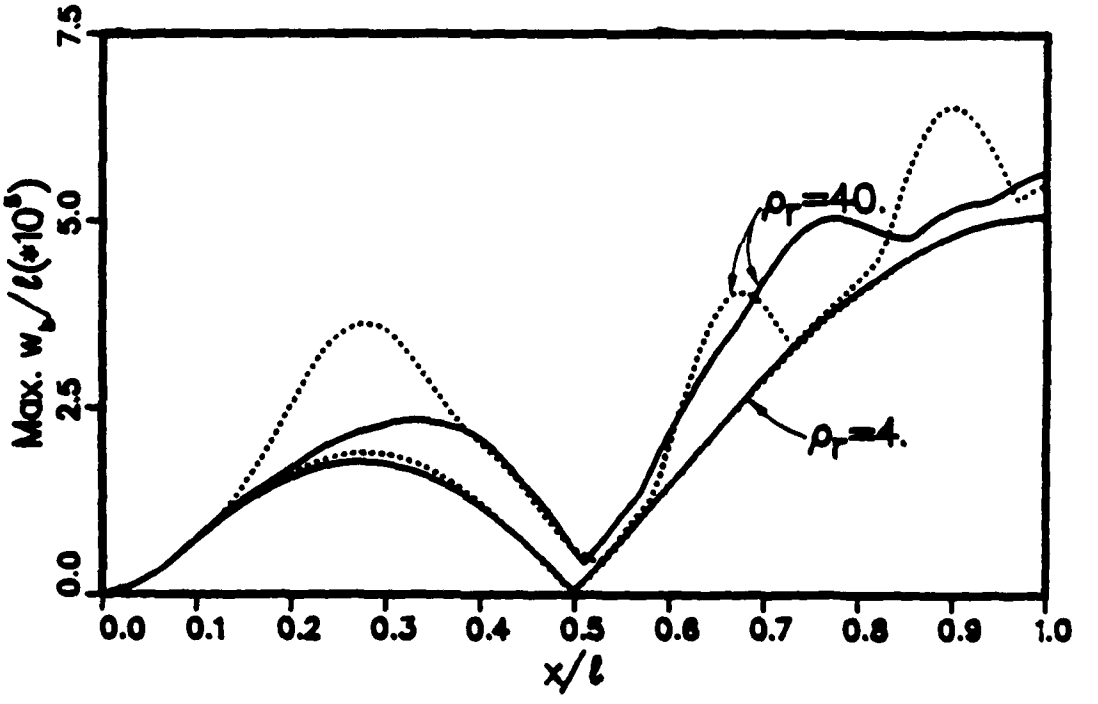

Fig.6 Bending response, ℓ=100., h=0.2, θ=0., solid lines – λ_ℓ=1.25, dotted lines – λ_ℓ= 10.0.

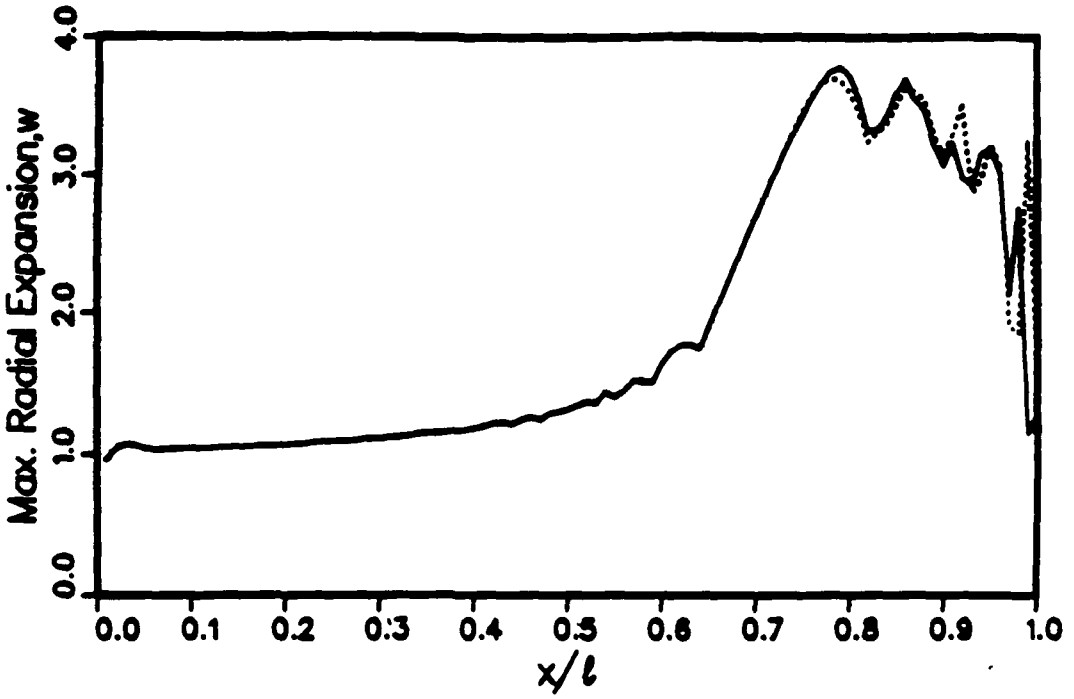

Fig.7 Maximum radial expansion of rotationally symmetric mode, ℓ=100., h=0.2, θ=0., ρ_r=15., λ_ℓ=1.25, solid line – with bending, dotted line – without bending.

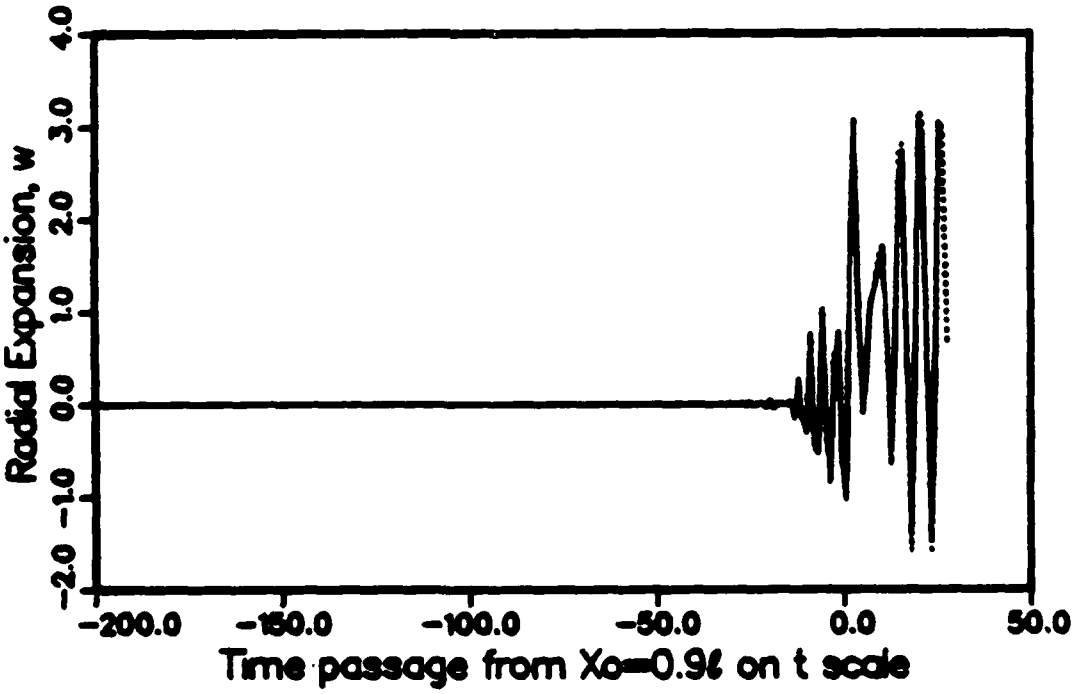

Fig.8 The comparison of radial expansion responses, ℓ=100., h=0.2, θ=0., ρ_r=15., λ_ℓ=1.25, solid line – with bending, dotted line – without bending.

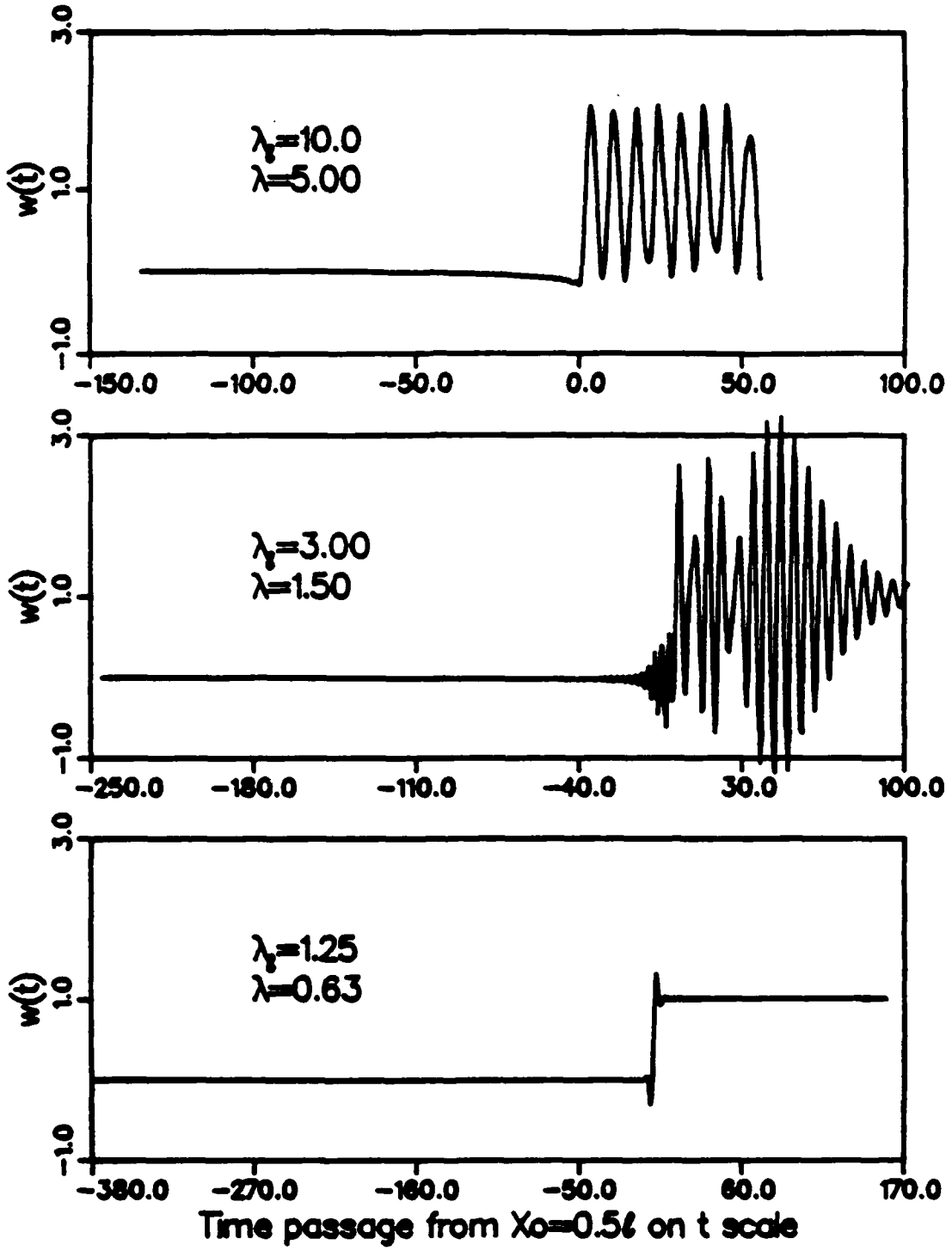

Fig.9 The response time histories of rotationally symmetric modes for λ_ζ=1.25, 3.0, 10.0 ℓ=100., h=0.2, θ=0., ρ_r=15.

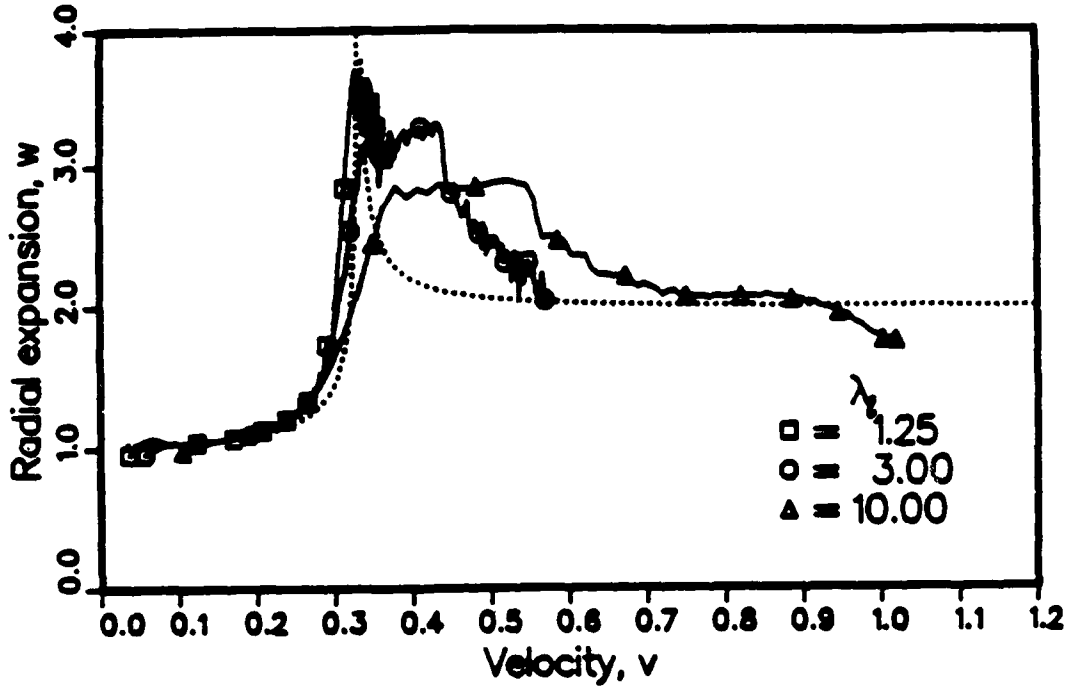

Fig.10 The response spectrum of gas–propelled gun–tube for ℓ=100., h=0.2, θ=0., ρ_r=15, dotted line – theoretical response of thin–walled cylindrical shells to a step pressure moving with constant velocity (Simkins,1987).

GAST

TITLE: THE EFFECT OF BORE CURVATURE ON SHOT ACCURACY IN TANK CANNON

RONALD G. GAST
U.S. ARMY ARMAMENT RESEARCH, DEVELOPMENT, AND ENGINEERING CENTER
CLOSE COMBAT ARMAMENTS CENTER
BENET LABORATORIES
WATERVLIET, NY 12189-4050

ABSTRACT:

In recent years, great strides have been made to isolate the dominant loads which cause transverse flexural vibrations in gun tubes during firing. The loads causing these motions have been identified as interactions with the cannon's supports, eccentrically placed masses recoiling with the cannon (breech, bore evacuator, muzzle brake), and takeup of slack in support and recoil components. Significant muzzle motions have been predicted when these loads are modelled and correlated by testing. Their impact is recognized in tank weaponry and is reflected in the current design of cannon, mount, and recoil system.

A more subtle point involves the bore profile of the gun tube itself. While curvature- and inertia-induced loads due to gravity droop are known to have little effect on gun accuracy, a similar claim in regard to bore straightness cannot be made. Very little analysis or testing has been done to establish these relationships. Since "fleet zero" is imminent for current and future tank systems, it is time to evaluate bore straightness specifications in light of this new calibration policy.

Achievement of this goal requires the use of a gun vibration simulation package within which curvature-induced loads are easily specified and accurately modelled. The gun vibrations model used by the Development Engineering Division of Benet Laboratories is able to simulate these conditions and predict both the flexural motion of the gun tube and the kinematic state of the muzzle ("exit vector") upon shot exit.

BIOGRAPHY:

PRESENT ASSIGNMENT: Mechanical Engineer, Tank Turret Branch, Development Engineering Division, Benet Laboratories (1985 to present).

PAST EXPERIENCE: Mechanical Engineer, Special Projects Section, Benet Laboratories (1971-1985) and Mechanical Engineer, Automatic Weapons Section, Benet Laboratories (1968-1971).

DEGREES HELD: B.S.M.E., Rensselaer Polytechnic Institute, 1968; M.S.M.E., Rensselaer Polytechnic Institute, 1978; Ph.D., Rensselaer Polytechnic Institute, 1988.

THE EFFECT OF BORE CURVATURE ON SHOT ACCURACY IN TANK CANNON

Ronald G. Gast
U.S. Army Armament Research, Development, and Engineering Center
Close Combat Armaments Center
Benet Laboratories
Watervliet, NY 12189-4050

BACKGROUND

In recent years, great strides have been made regarding the isolation of the dominant loads which cause beam-type vibrations in tank cannon during ballistic operation. These motions infringe upon shot accuracy because at projectile disengagement the muzzle's kinematic state may compromise the projectile's intended flight path. The dominant loads causing these motions have been identified as interactions with the cannon's supports and eccentrically applied inertia loads due to non-centered masses attached to the tube (breech, bore evacuator, muzzle brake) or non-symmetric loads due to takeup of slack in support and recoil components. Significant muzzle motions have been modelled [1,2] and reproduced in tests [3] when these conditions exist. Current design philosophy recognizes their impact and is reflected in new designs for the mounting of tank cannon.

A more subtle point involves the bore profile of the gun tube itself. While curvature- and inertia-induced loads due to gravity droop are known to have little effect on gun motions [4,5], a similar claim in regard to center line profile produced by other conditions (manufacturing, thermal flexure, etc.) cannot be made. Very little analysis has been done to establish these relationships, however, firing tests on the 120-mm M256 cannon [3,6] have confirmed that the location of the tube's top vertical center line can have a significant effect upon shot fall. Since a "fleet zero" calibration policy is imminent for current and future tank systems [7], it would be prudent to explore the relationships between tube straightness as related to flexural dynamics and shot fall. Achievement of this goal requires the use of a gun vibration simulation package within which curvature-induced loads are easily specified and accurately modeled. The dedicated gun vibrations model [8] used by the Development Engineering Division of Benet Laboratories is able to simulate these conditions and predict both the flexural motion of the gun tube and its contribution to the initial flight path of the round, as well as the interactive loads induced upon the projectile during in-bore acceleration.

In this paper the following topics are addressed:

1. The relative contribution of gun dynamics to the overall accuracy of various tank rounds.

2. The analytical nature of curvature-induced loads and their modelling representations in Benet's gun vibration model.

3. The effects of various bore profile types on exit conditions for the new lightweight (LW) 120-mm XM291 cannon.

4. A more viable bore profile tolerancing specification for the next generation tank weapons.

ACCURACY ASSESSMENT OF TANK ARMAMENT

Tank armament under development today should serve the needs of the armored units well into the twenty-first century. In the future, as in the present, tank battles require a high degree of first-round kill probability in order to survive and defeat the enemy. This philosophy, along with the "fleet zero" requirement for weapon calibration, places extreme importance on weapon accuracy. Accuracy in this sense is defined as the deviation from the aim direction to the round's impact point on a distant target. Essentially, "fleet zero" states that correction factors are assumed to be a function of round and range only and may be derived from a small percentage of weapon/vehicle combinations. Therefore, tube-to-tube, mount-to-mount, and vehicle-to-vehicle variabilities which are known to infringe upon accuracy must be recognized and minimized for "fleet zero" to be effective.

During the mid-1980s, accuracy tests on the M1A1 tank and its main weapon, the M256 gun, were conducted. The purpose of this testing was to determine the parameters affecting accuracy. The major findings indicate that for the mix of gun tubes and tanks used in this test a strong correlation exists between round impact and tube irrespective of the tank. This is graphically represented in Figure 1, which was derived from data in Reference 6. In this figure, the average values for the center of impact (COI) for two specific round types fired from various M256 tubes are shown. Each tube was mounted on at least three tanks and fired one or more rounds. The actual data points were tightly grouped around the averages. Based upon a statistical analysis of this data by the Ballistic Research Laboratory (BRL), it was suggested that the bore center line profile could be the major cause of the large fluctuations in the COI for each tube. The mechanism entails both tube flexure and the projectiles' transverse dynamics during acceleration and the separation upon exit.

As indicated in the figure, the COI for the high explosive antitank (HEAT) round are closer to the point of aim than for the kinetic energy (KE) round. The explanation for this lies in the type of projectile. The HEAT round is a shell which houses the explosive. It is very stiff structurally, therefore, it

behaves much like a rigid body while in-bore. The excitation forces developed at the projectile/bore interface contribute mostly to tube motion. The COI of such a round will be more strongly governed by motion of the muzzle at exit. On the other hand, the KE round is essentially a subcaliber "dart" encased in a more compliant sabot. Interface loads through the sabot will drive both the tube and projectile. Flexure will result in the tube, while rigid body pitching motions will develop in the projectile. This complicates the projectile's kinematic state at the point of separation, thus infringing upon its accuracy.

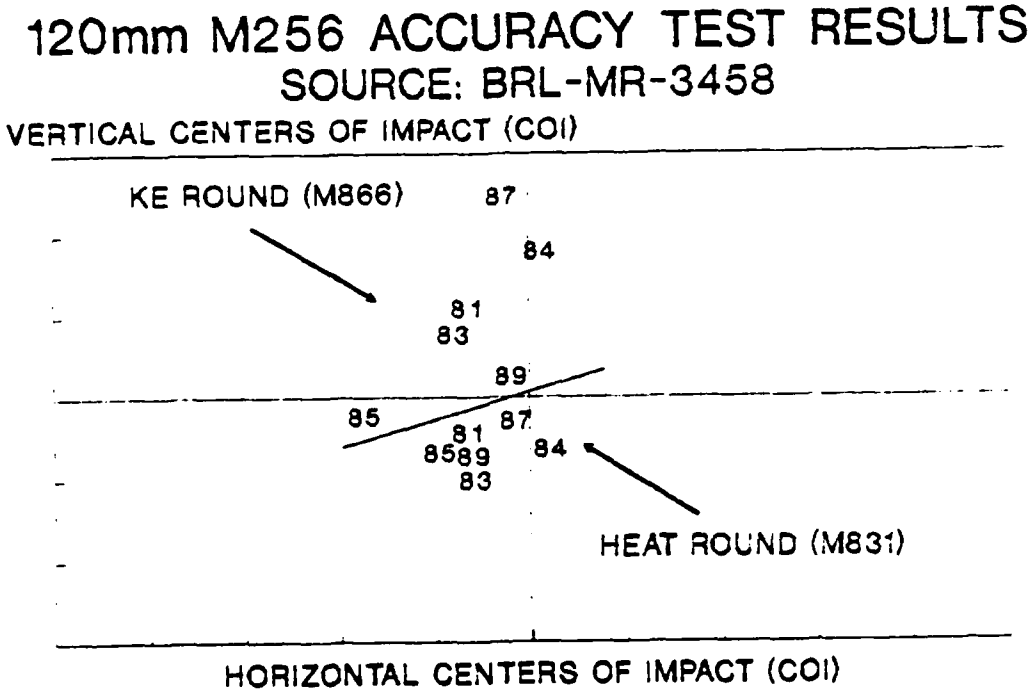

Figure 1. M256 accuracy test results.

In the remaining portions of this paper, the tube's contribution to projectile exit are addressed. The model used to generate the dynamic response treats the projectile as a rigid body, however, projectile loads are recovered along with the tube's dynamic flexure. These loads may provide some insight into the projectile's dynamic state or may be used as driving loads for a separate projectile dynamics study.

ANALYSIS AND MODELLING OF PROFILE-DEPENDENT LOADS

A recoiling tank gun falls into a special class of beam dynamics problems since the loads are applied from within the structure while the structure is being accelerated. Since a tank-mounted cannon is statically similar to a cantilevered beam, it possesses a gravity droop due to its weight. Superimposed upon this is the center line of the bore which may wander about the drooped state due to manufacturing nuances, asymmetric thermal loads, etc. Various researchers [4,5] have identified three load types which are dependent upon the bore center line profile. A brief explanation of these loads and their representative expressions follows.

Recoil Inertia Load

The recoil direction of a gun is a function of the mount within which it resides. Current design philosophy specifies that rail and channel sliding surfaces (similar to artillery pieces) will be a main feature for future tank mount designs. This attenuates gun curvature within the mount maintaining a straight pull which tends to "snap" the overhanging muzzle end of the gun. An inertia couple which is proportional to the slope of the deflection curve and recoil acceleration is produced. This load is expressed as follows:

$$f_r(t,x,y',y'') = \frac{w}{g} a_r[(l-x)y']' \qquad (1)$$

where

f_r = recoil inertia load per unit length
w = $w(x)$ = weight of gun tube per unit length
a_r = $a_r(t)$ = recoil acceleration
g = acceleration of gravity
l = length of gun
x = spatial coordinate
y = $y_t(x,t) = y_d(x,t) + Y_s(x)$ total displacement
y_d = dynamic profile of bore
Y_s = static profile of bore

As can be seen when this load expression is evaluated, the static profile is differentiated along with the dynamic component.

Pressure Curvature Load

Due to the nature of curvature within beam-type structures, diametrically opposite bore surfaces possess differing areas. A pressure load acting within this confined chamber will tend to straighten the chamber because the area of the concave surface is greater than its convex counterpart. This type of load is an axially developing type which travels behind the projectile and is proportional to the second derivative of the deflection curve. The expression for this load function is

$$f_c(x,t,y'') = -F_b y''\{H(x_p-x)\} \quad (2)$$

where

f_c = pressure curvature load per unit length
$F_b(t)$ = gas force within bore
$H\{x_p-x\}$ = step function
H = 1 for $0 < x < x_p$
H = 0 for $x > x_p$
$x_p = x_p(t)$ = axial location of projectile

Projectile Trajectory Load

The accelerating projectile, although of considerably less mass than the tube, can exert a significant transverse force when it is confined to travel along a curved path. This load, which is proportional to the bore's curvature and projectile speed, is modelled as a point load applied at the instantaneous axial location of the projectile and is expressed as follows:

$$f_p(x,t,\dot{y}',y'',\ddot{y}) = -\frac{w_p}{g}[\ddot{y} + 2\dot{x}_p y' + \dot{x}_p^2 y'' + g]\delta(x_p-x) \quad (3)$$

where

f_p = projectile trajectory load per unit length
w_p = projectile weight
$\delta(x_p-x)$ = Dirac delta function
$\delta = 1$ for $x = x_p$
$\delta = 0$ otherwise

Total Transient Solution

The solution model used in this study is called the Uniform Segment Method (USM) and was developed at Benet Laboratories during the mid-1980s [9]. It employs a modal analysis technique in which the gun tube is sectioned into a number of uniform segments within which the Euler beam equation for free vibration is applied. The boundary conditions of the beam are free-free and intersegment continuity of displacement, slope, bending moment, and shear force are preserved at the interfaces. Each segment possesses a unique mode shape function for each natural frequency. These functions satisfy the continuity requirements cited above. The terms of these functions contain the usual trigonometric and hyperbolic forms seen in uniform beam analysis. The natural frequencies and coefficients of the terms are solved from the master system matrix formed from the boundary and intersegment continuity conditions. Loads due to support reactions, non-structural mass (breech, bore evacuator, etc.) are applied as external loads during the transient solution and are not accounted for in the modal analysis portion.

The dynamic profile of the bore center line is expressed as the product of two separable functions as follows:

$$y_d(x,t) = \sum_{i=1}^{N} \phi_{ij}(x) q_i(t) \qquad (4)$$

where

N = number of modes in analysis
$\phi_{ij}(x)$ = mode shape function j-th segment, i-th mode
$q_i(t)$ = displacement amplification coefficient i-th mode

Standard numerical procedures for modal analysis vibration solutions are employed in solving for the amplification coefficients.

DYNAMIC RESPONSE OF XM291 CANNON TO BORE PROFILE VARIATIONS

If the tube's center line were perfectly straight without bends, kinks, or gravity droop, the static contributions from the loads cited previously would vanish. The y's in Eqs. (1) through (3) would contain dynamic terms only. The contributions from these terms are known to be small, therefore, very little motion would result from firing the weapon. Since a perfectly straight bore is impossible, tolerances are routinely assigned to engineering drawings to control the amount of profile deviation. The values used in these tolerancing schemes are somewhat arbitrary in that little testing or analytical work has been done to assess their contribution to tube or projectile dynamics. In this section, a quantification of the effect of bore curvature upon muzzle dynamics is addressed for a tank cannon currently in development. The dependence of muzzle dynamics, especially the muzzle's "exit vector," is tracked as various bore profile functions are applied to the gun tube.

XM291 Cannon and Round Specifications

The XM291 cannon is comprised of a 120-mm smooth bore tube which is 265 ins. long and weighs approximately 3200 lbs. Its breech weighs 1300 lbs and its center of gravity is located approximately 0.03 in. below the bore's center line. A 30-lb bore evacuator is located between 125 and 160 ins. from the rear face of the tube (RFT). The center of gravity is 0.625 in. above the bore's center line. A muzzle reference system (MRS) weighing 12.4 lbs is located 259 ins. from RFT and its center of gravity is 1.35 ins. above the bore's center line. The cannon is supported on a rail system 40 ins. long. Nominal clearance between cannon and support is 0.0075 in. The support is very stiff in the order of 1 million pounds per inch. The specifications for bore profile (excluding gravity droop) require that the overall bend not exceed 0.05 in. for the entire length of the bore or exceed 0.01 in. in any 25-in. span. This requirement is a more significant reduction from that previously accepted for tank cannon. The ballistic loads used in this study are the XM866 KE and the XM831 HEAT. The KE projectile weighs about 12 lbs and exits the muzzle at 5500 feet per second

(fps). Its in-bore time is about 7.00 milliseconds (ms). The HEAT round weighs 30 lbs and exits at 3750 fps at 10.4 ms.

XM291 Free Vibration Frequency Comparison

In the USM model the tube is sectioned into five prismatic segments with axial boundaries and respective diametral dimensions as shown in Table 1.

TABLE 1. XM291 USM TUBE SEGMENTATION (INCHES)

SEGMENT #	AXIAL BOUNDS	INNER DIAMETER	OUTER DIAMETER
1	0 - 55	4.74	12.01
2	55 - 120	"	9.25
3	120 - 165	"	7.50
4	165 - 215	"	6.75
5	215 - 265	"	6.25

The natural vibration frequencies as calculated by the USM are compared with results determined by ABAQUS finite element program. These results are shown in Table 2.

TABLE 2. XM291 USM AND ABAQUS VIBRATION FREQUENCIES (HERTZ)

MODE #	USM VALUE	ABAQUS VALUE	% CHANGE
1	22.90	22.20	3.15
2	65.88	62.90	4.73
3	127.4	120.2	6.00
4	212.9	197.5	7.80
5	330.1	297.9	10.8
6	455.9	403.9	12.9

XM291 Baseline Responses

To establish baseline responses, the model was exercised in the vertical plane with the system parameters set at their nominal values. The profile-dependent loads arose from the natural curvature of the tube due to its weight and additional non-structural components. In this condition, muzzle deflection is about 0.25 in. This plane was chosen since the dynamic response is driven (in theory) by the drooped tube, whereas in the horizontal plane the gun is balanced about the bore's center line, therefore, little motion is expected.

The results for both the HEAT and KE rounds are presented in Figure 2. In this figure muzzle displacements with respect to the static condition are plotted against time and "exit vectors" are plotted against projectile location.

For the HEAT round, the muzzle gradually dips below its static position to about 0.005 in. at projectile exit. The "exit vector" varies as the projectile approaches the muzzle. At exit, it is nearly zero indicating that the combined effect of the muzzle slope and transverse velocity renders a relatively perfect condition for projectile exit. It is highly sensitive, however, since the response varies rapidly prior to exit. If the timing of exit was perturbed slightly (for example, hot or cold rounds), the exit condition would most likely change. For the KE round, the muzzle dips to 0.0015 in. at half of the cycle and nearly returns to its static position at exit. The "exit vector" is 0.050 milli-radian (m-rad) at exit and rather constant throughout the final stages of the shot. These "exit vector" values are not very significant compared with the acceptable dispersion value of 0.25 mil for tank guns. It must be realized that only the tube's contribution to inaccuracy is being reported, while the remaining contributions (disengagement, etc.) may or may not be sensitive to the tube's dynamic state. In subsequent portions of this analysis, these results are compared with those of gun tubes possessing mildly varying profiles added to the static condition.

Parameters Defining Bore Profile Types

Upon a review of actual bore profiles for 120-mm gun tubes (M256 and XM25), a variety of types were uncovered. Some tubes possessed profiles which were isolated to one plane, while others had spiral bends. Some had a single bow along their entire length, while others had bending reversals somewhat like sinusoidal waves. Some were curved more at the muzzle than at the breech. It soon became evident that it would be quite difficult to parameterize bore profiles.

To make the analysis tractable, only sinusoidal profiles of reasonable magnitude which originate at the bore's origin and continue along the tube to the muzzle end were considered. The parameters of this study are the profile's wavelength and its magnitude. By employing this type of strategy, the profile may be made to simulate a bowed condition by choosing a long wavelength (2 times the bore length) or the reversal condition by choosing a short wavelength (0.5 times the bore length). There are two goals to be attained from this portion of the analysis. The first is to determine the sensitivity of muzzle dynamics to loads produced by sinusoidally varying bore profiles. As indicated in the previous section, an interaction exists between the projectile's speed and the local value of the bore's curvature. If this curvature were allowed to vary sinusoidally, the effect on muzzle dynamics may be a strong function of the wavelength and projectile speed. It is hypothesized that certain wavelengths would act like "resonators" causing increased oscillations at the muzzle for very small profile magnitudes. The second goal is to determine the relationship between the magnitude of the bore profile and the muzzle response at any wavelength. If the relationship is nearly linear, the response can be normalized with respect to the profile's magnitude, and estimates of the response could be made upon inspection of the actual profile circumventing the need for detailed dynamic analysis.

XM291 Response to Sinusoidal Profiles of Various Magnitudes

The results of muzzle sensitivity to combinations of these parameters are shown in Figure 3. In this figure the muzzle displacement and "exit vector" at projectile disengagement are plotted against the normalized wavelength (NWL) of the bore's profile with magnitude as the parameter. The response due to the drooped condition, which is called its baseline response, is indicated as a horizontal dotted line at its respective value. The NWL scale runs from 0.40 to 2.00 bore lengths, while the magnitude parameter spans the -0.05 to +0.05-in. range. As indicated in this figure, the responses are, in fact, a non-linear function of wavelength, moreover, the signatures are significantly different for each round. For example, an NWL value which is magnitude-sensitive for the HEAT round is not for the KE round and vice versa. However, the responses are symmetric with respect to baseline values, therefore, if a tube were rotated 180 degrees, its response would rotate as well. This indicates that droop and profile are acting independently in regard to muzzle dynamics. The responses for the combined effects are additive, moreover, the responses are linear with respect to profile magnitude at all wavelengths.

In the upper portion of Figure 3 the responses for the HEAT round are shown. For both the displacement and "exit vector" an "hourglass" shape is shown. The neck of the response is at an NWL value of 0.55 m-rad at which point the "exit vector" deviation from its baseline value is 0.0023 m-rad per milli-inch magnitude. At an NWL value of 1.00, the response is most sensitive to magnitude showing a deviation of 0.0068 m-rad per milli-inch magnitude. Since the baseline "exit vector" for the HEAT round is very close to zero, any additional curvature degrades the gun's performance. Hence, from the standpoint of shot accuracy for the HEAT round, the profile produced by static droop is the best for offsetting all other cannon driving loads.

The situation is somewhat different for the KE round. As with the HEAT round, an "hourglass" response is indicated, however, the neck is actually a crossing point. This neck occurs at an NWL value of 0.87 for muzzle displacement and 1.06 for "exit vector." At these wavelengths the muzzle response is independent of the profile's magnitude yielding projectile exit conditions which are equal to the baseline response. For the "exit vector" there is a local area of high magnitude dependence at an NWL value of 0.62. At this wavelength the deviation from its baseline value is 0.0061 m-rad per milli-inch profile magnitude. Since the baseline "exit vector" is far removed from zero, a number of profiles exist (specified by magnitude and wavelength) which produce a perfect exit. For example, a 0.01-in. profile of 0.53 NWL would produce a perfect exit, as well as the same magnitude at 0.77 NWL. However, when these profiles are indexed by 180 degrees, the resulting "exit vector" deviates greatly with respect to its baseline value.

These results indicate that with the proper orientation of the gun tube, with respect to its static profile, shot accuracy may be improved. This point has been addressed in work done at the Ballistic Research Laboratory [6] on the M256 cannon. The terms "tube indexing" and "ultimate profile" have been coined as a result of these tests and analyses.

Stability of Responses

As shown above, wavelengths exist where the "exit vector" responses are either close to or deviated greatly from the baseline. In this section the transient responses at these "critical" wavelengths are compared to their baseline values to indicate the presence of detrimental conditions during projectile acceleration. This should render insight into the robustness of the exit state if the arrival time of the projectile is perturbated slightly. For example, if the muzzle were vibrating wildy about its baseline condition throughout projectile in-bore time, but just happened to cross its baseline value at exit, the response could not be considered stable since a slight variation in arrival time would result in an exit that is greatly different. For each round, two "critical" wavelengths are studied, namely the two which produced the smallest and greatest deviations from baseline values.

For the HEAT round the NWL value of 0.55 produced "exit vectors" which were least sensitive to profile. The transient responses for a profile magnitude of 0.025 in. at this NWL are shown in Figure 4. As indicated, the muzzle deflection vibrates about its baseline value. The greatest deviation occurs about 8.0 ms at which time the deviation is 0.0027 in. from the baseline. The "exit vector," however, remains relatively stable throughout the final stages of in-bore time, never deviating much from its exit value. At an NWL value of 1.00, the "exit vector" response is most sensitive to profile magnitude. In Figure 5 the transient responses at this NWL value are shown. The muzzle displacement tracks its baseline value until 8.0 ms, at which time it diverges to a maximum deviation of 0.0053 in. at exit. The "exit vector" continually diverges with respect to baseline during final stages of projectile acceleration. Although its offset is great, the 'exit vector' is relatively stable during this time.

A "critical" wavelength occurs at 0.62 for the KE round. At this value the exit responses are most sensitive to profile magnitude. In Figure 6 the transient responses at this NWL value are shown. The muzzle deflection remains close to baseline up to 5.0 ms but diverges from this point attaining a maximum value of 0.0034 in. at exit. The "exit vector" is relatively stable, although its deviation is great. In Figure 7 the responses for an NWL value of 1.00 are shown. At this NWL value the responses were shown to be independent of profile, since a crossing point was indicated at exit. The muzzle deflection remains close to baseline for nearly the entire time but diverges greatly after projectile exit. Its maximum deviation is 0.0024 in. immediately after exit. The "exit vector" gradually approaches its baseline value during final stages of in-bore time, never deviating by more than 0.05 m-rad.

The results of this analysis indicate that acceptable profile variations may cause muzzle motions which are on the same order of magnitude as those produced for the naturally drooped condition. Transient muzzle deflections were shown to vary widely for certain profile types, whereas others produced little deviated motion. Although similar results were shown for the "exit vector," its response was relatively stable during the final portion of the projectile's in-bore residency. This is encouraging since the "exit vector" has the greatest impact upon shot accuracy.

RECOMMENDATIONS AND CONCLUSIONS

Summation of Findings

The primary purpose of this analysis was to indicate by computer modelling the dependence of muzzle response on various bore profile types. The next logical step is to utilize this information in gun design, especially for accuracy enhancement in terms of bore profile tolerancing. The term "ultimate profile" (UP) which was mentioned earlier was coined during testing of the 120-mm M256 cannon. Results indicated that the UP need not be a perfectly straight bore. In the spirit of this analysis, UP refers to the profile or profiles which produce a perfect kinematic state at the muzzle during projectile exit. Since the exterior contributions to accuracy (separation, etc.) are not a factor in these calculations, an "exit vector" value of zero is the condition being sought. For the HEAT round, the UP was shown to be the static drooped condition, whereas for the KE round, a number of profiles (specified by wavelength and magnitude) produced a perfect exit.

The assumed premise that the "exit vector" at the muzzle is the response most indicative of the projectile's initial in-flight condition may be in error. Rather, the tube's average dynamic state over some finite length or some other combination of dynamic values may be the key response. In any event, should the projectile's exit be a function of the tube's kinematic state along any axial length, dynamic modelling of the type cited would produce the results needed to evaluate the launch condition.

Use in Gun Design

In principle, the best way to determine the acceptability of a profile is to perform firing tests and measure the accuracy and relate it to the kinematics of the gun. This is an intense venture requiring sophisticated and costly measuring equipment and test hardware. An alternative would be to analyze the performance of individual profiles in a computer model such as the one cited in this paper or any other in which profile deviations are addressed. From a cost standpoint this method is a great improvement over the previous one. A third and least costly method drawing upon the findings of this paper and basic approximation theory could be employed during gun manufacture. The two major points are explained below.

First, since the muzzle response at a given profile wavelength was shown to be a linear function of its magnitude, a single dynamic computation at any magnitude yields all the data needed for a particular wavelength. The response value is simply scaled based upon the profile's magnitude. Second, approximation theory states that any periodic function may be represented by a finite Fourier series of integer multiples of the period. The bore profile can be represented in this manner with the period being the reciprocal of the bore's length. The exit response to the individual terms of the series can be determined beforehand by running the dynamic model at a nominal magnitude for each term (wavelength) in the series. The frequency content of the actual profile may be found by Fourier analysis, therefore, the total exit response can be

determined by scaling and summing the individually calculated responses at the profile frequencies. This type of calculation is not intensive and could be accomplished in real time during bore profile inspection. An immediate decision regarding the acceptability of the tube's profile could be made. In advanced applications "indexing" recommendations could be made regarding the best orientation of the tube to optimize accuracy or suggested locations for straightening.

Ongoing Research in Curvature-Dependent Responses

Over the next two years, testing of curvature-dependent responses on a sub caliber model of the XM291 gun will be conducted in the Gun Dynamics Laboratory at Benet Laboratories. The immediate results from this testing and follow-up analysis will lead to a better understanding of exit dependency on bore profile leading to more viable methods of tube tolerancing and measurement. The tank management community who has sponsored this work is highly attuned to the "fleet zero" tank calibration directives currently in place. Their continued support of this research will reap a bountiful harvest for future large caliber weapon systems.

REFERENCES

1. Erline, T.F. and Kregel, M.D., "Modelling Gun Dynamics with Dominant Loads," paper presented at the Fifth U.S. Army Symposium on Gun Dynamics, Rensselaerville, NY, 23-25 September 1987.

2. Gast, R.G., "Analytical Comparison of the Accuracy of Tank Weapons," ARCCB-TR-89023, Benet Laboratories, Watervliet, NY, November 1989.

3. Schmidt, E., Plostins, P., Haug, B., Bornstein, J., Heaps, C., Brosseau, T., Brandon, F., and Schmidt, J., "Jump From the M1A1 Tank," BRL IMR 868, Ballistic Research Laboratory, Aberdeen Proving Ground, MD, 1987.

4. Simkins, T.E., "Transverse Response of Gun Tubes to Curvature Induced Load Functions," Proceedings of the Second U.S. Army Symposium on Gun Dynamics, ARLCB-SP-78013, Benet Weapons Laboratory, Watervliet, NY, 19-22 September 1978, pp. I-66-I-77.

5. Warken, D., Wolf, K., Heiser, R., Ballman, J., and Pavel, W., "The Effect of Barrel Curvature and Projectile Unbalance on Excitation of Gun Vibations," Proceedings of the Third U.S. Army Symposium on Gun Dynamics, ARLCB-SP-82005, Vol II, Benet Weapons Laboratory, Watervliet, NY, 11-14 May 1982, pp. III-43-III-63.

6. Schmidt, E., Bornstein, J., Thomas, J., and McCloskey, T., "A Method for Indexing Tank Cannon," BRL IMR 912, Ballistic Research Laboratory, Aberdeen Proving Ground, MD, 1988.

7. Brower, J.D. (Major), "New Tank Gun Calibration Policies," Armor, July-August, 1982.

8. Gast, R.G., "Normal Modes Analysis of Gun Vibration by the Uniform Segment Method," ARCCB-TR-87033, Benet Laboratories, Watervliet, NY, November 1987.

XM291 MUZZLE RESPONSES (BASELINE CASE)

DISPLACEMENT & EXIT VECTOR

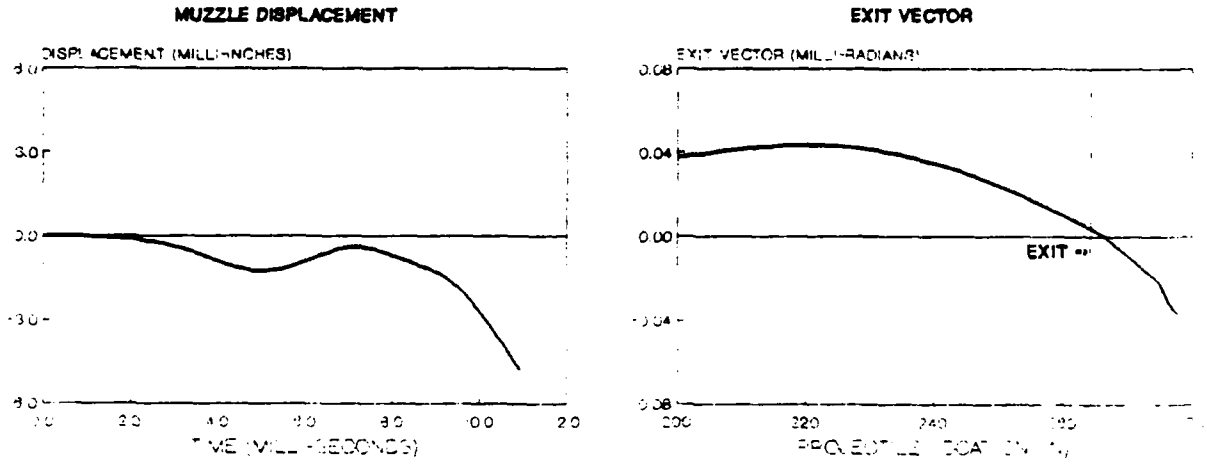

ROUND: HEAT

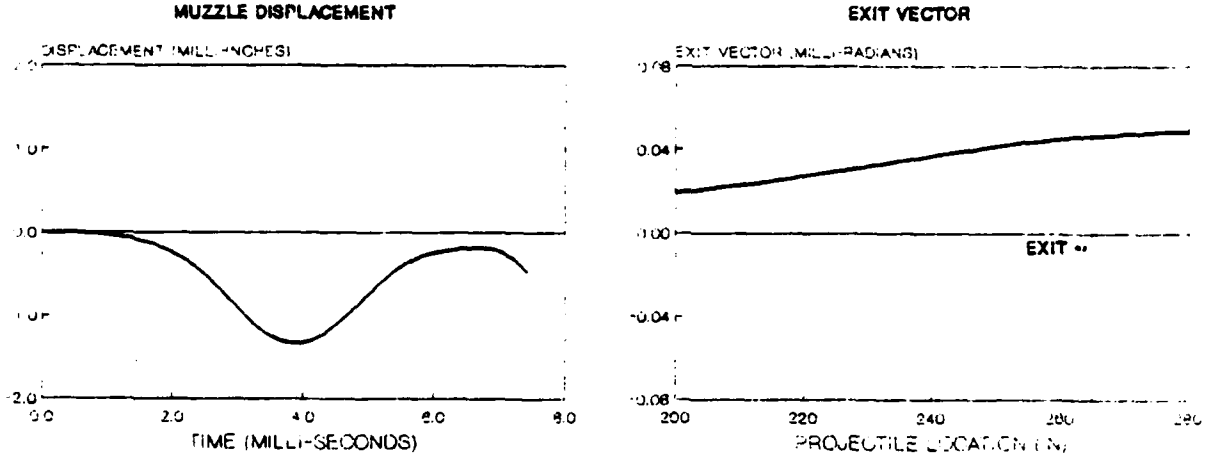

ROUND: KE

Figure 2

XM291 MUZZLE RESPONSES at PROJECTILE EXIT

DISPLACEMENT & EXIT VECTOR vs WAVELENGTH

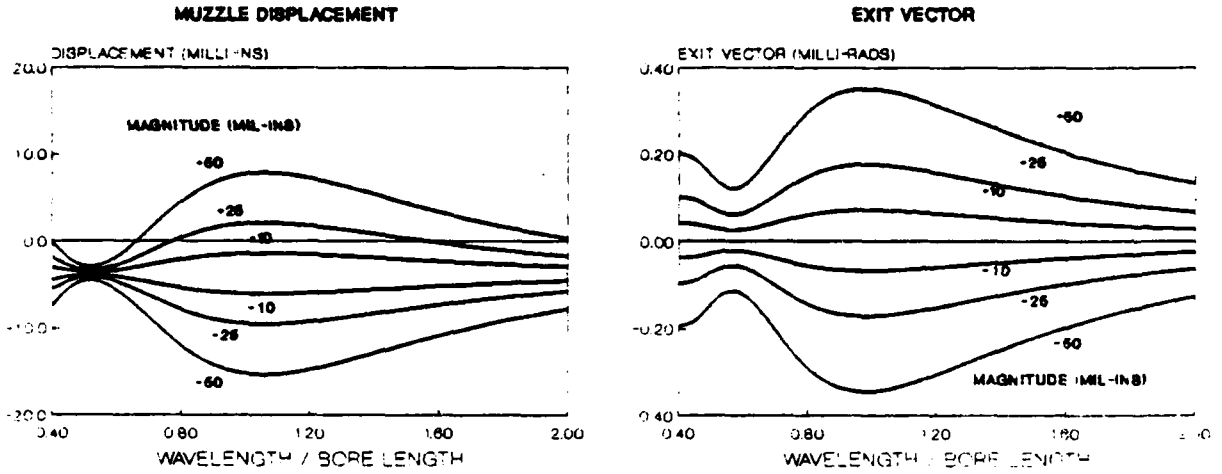

ROUND: HEAT

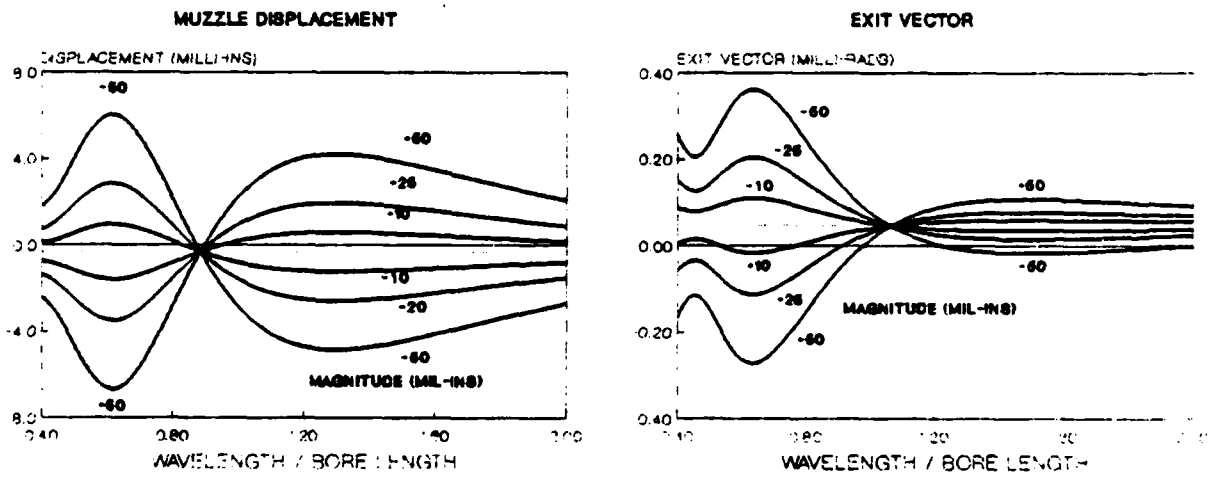

ROUND: KE

Figure 3

XM291 MUZZLE RESPONSES (NWL = .55)

DISPLACEMENT & EXIT VECTOR

ROUND: HEAT

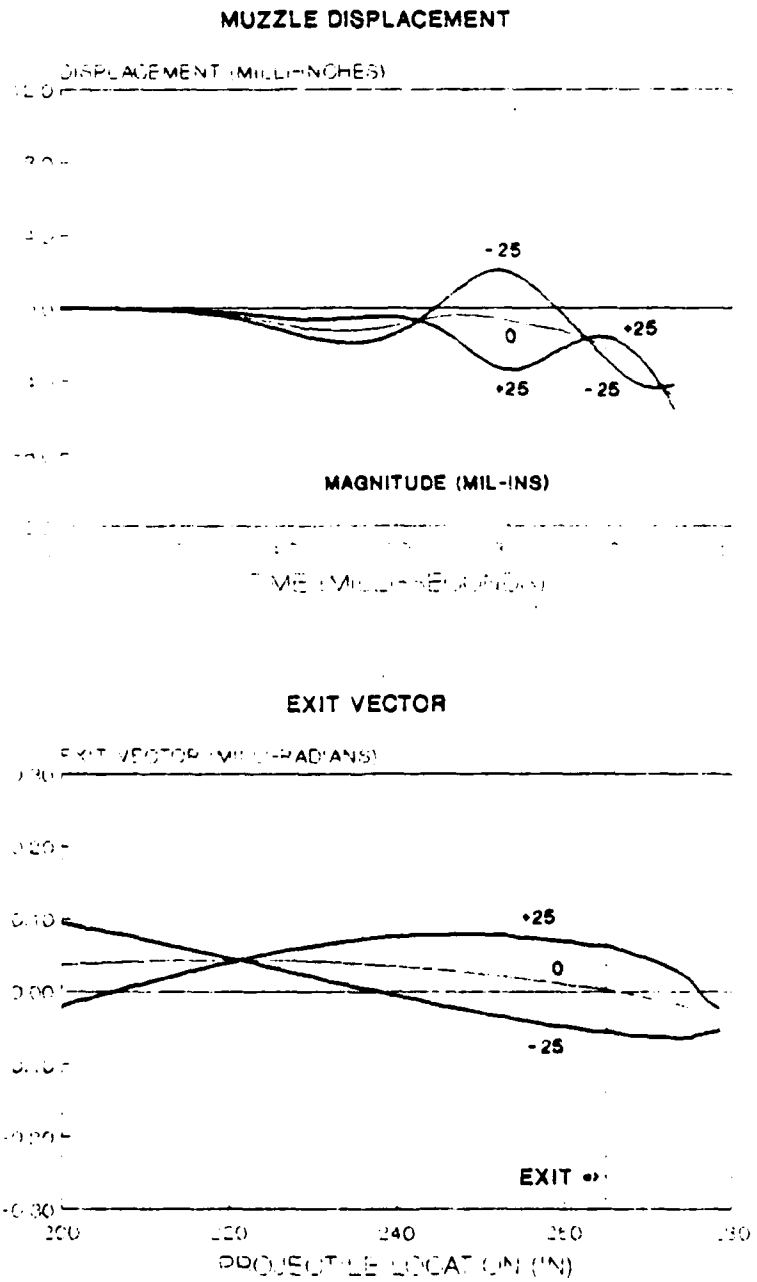

Figure 4

XM291 MUZZLE RESPONSE (NWL = 1.00)

DISPLACEMENT & EXIT VECTOR

ROUND: HEAT

MUZZLE DISPLACEMENT

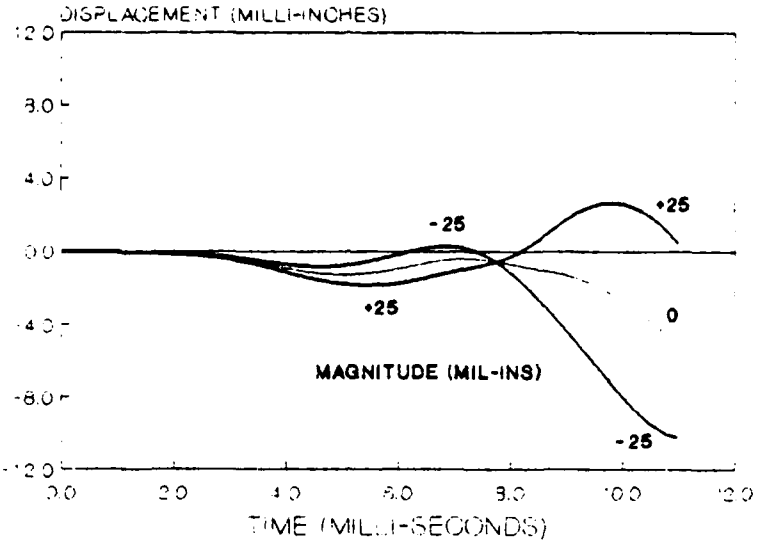

EXIT VECTOR

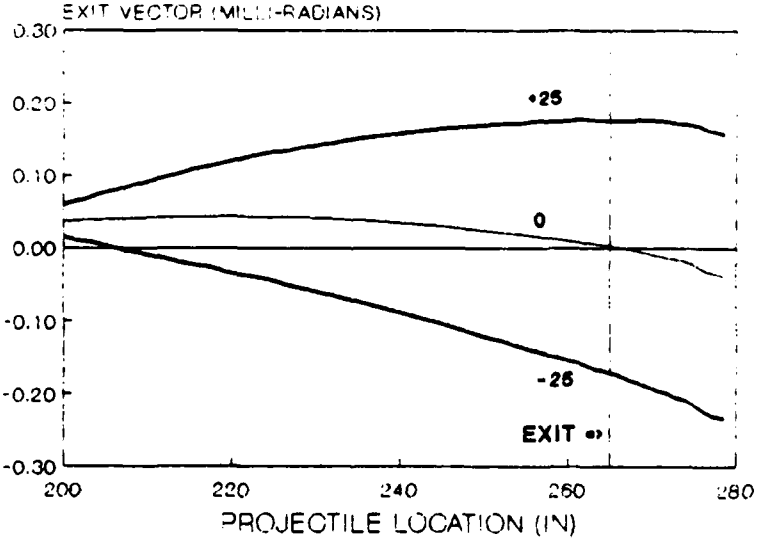

Figure 5

XM291 MUZZLE RESPONSE (NWL = 0.62)

DISPLACEMENT & EXIT VECTOR

ROUND: KE

MUZZLE DISPLACEMENT

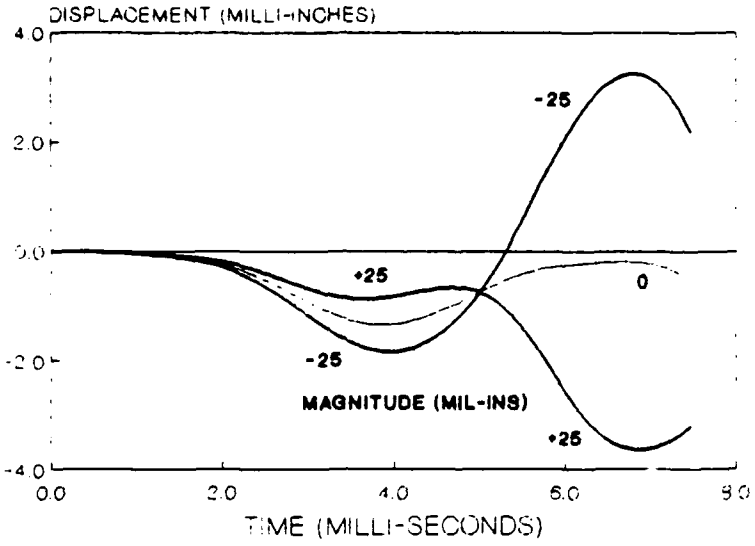

EXIT VECTOR

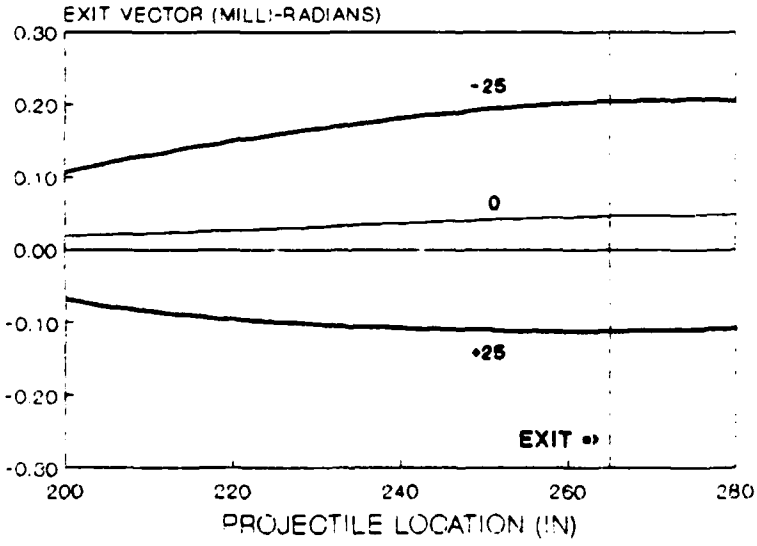

Figure 6

XM291 MUZZLE RESPONSE (NWL = 1.06)

DISPLACEMENT & EXIT VECTOR

ROUND: KE

MUZZLE DISPLACEMENT

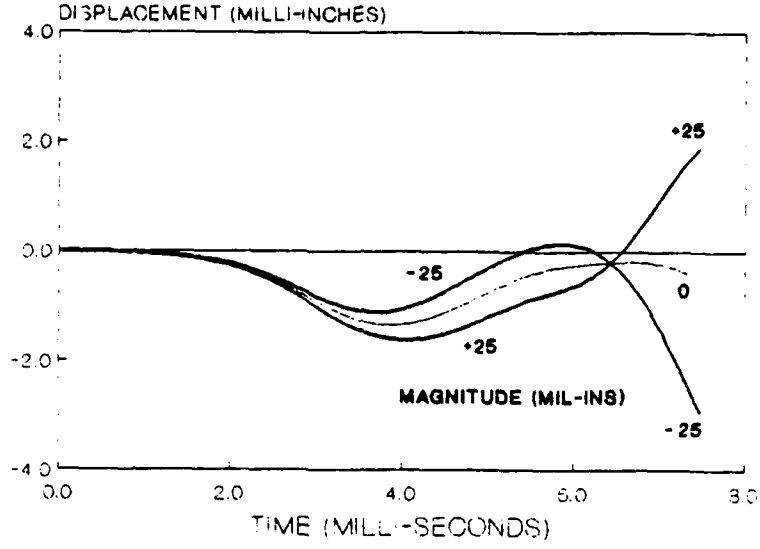

EXIT VECTOR

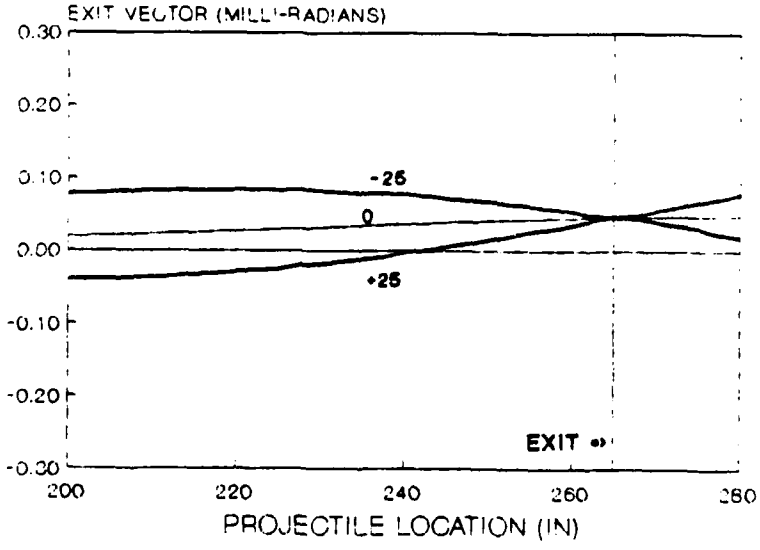

Figure 7

FINLAYSON

TITLE: POINT MASS PROJECTILE FORCES AND MOMENTS ON MOVING GUN TUBES WITH CURVATURE AND TORSION

DAVID F. FINLAYSON
U.S. ARMY ARMAMENT RESEARCH, DEVELOPMENT, AND ENGINEERING CENTER
CLOSE COMBAT ARMAMENTS CENTER
BENET LABORATORIES
WATERVLIET, NY 12189-4050

ABSTRACT

In a recent paper, the author presented a set of general equations in six degrees of freedom for the analysis of the lateral (constraint) forces acting between the projectile and the bore surface of a rifled gun tube for stable (non-balloting) motion of the projectile. Generality is asserted based on the inclusion as parameters of the model: mass eccentricity, misalignment of the principle axis of inertia with the spin axis (tangent to the bore center line), lateral as well as angular velocity and acceleration of the tube, and curvature and torsion of the tube. Additionally, the rotating band engraving force and frictional resistance forces are accounted for.

Since the projectile motion is prescribed by the physical constraints of the tube and the specification of stability, the analytical approach of choice is Newtonian. Kinematical description is facilitated by the definition of moving (translational) and body-fixed coordinate systems in addition to the inertial reference frame. The coupled effects of tube curvature and torsion, lateral and angular velocity and acceleration, and projectile imbalance and misalignment are thus accounted for. Following coordinate transformations, the equations of constraint are developed utilizing Euler's equations along with the equation of motion.

As stated above, the original intent of the analysis was to provide a vehicle for the study of the relative importance of the various anomalies that would occur in gun tube/projectile interface dynamics. Motivation for such a study was provided by the appearance of muzzle wear in some XM199 developmental tubes. Since the wear pattern generally followed a single band (a condition sometimes referred to as "spiral wear"), it was clear that it was the result of stable in-bore projectile motion. More recently a similar phenomenon has appeared in HIP test firings where heavy projectile body engraving has been shown by metallurgical examination to be the result of ablation.

In the aforementioned paper, the general equations are specialized for two cases where the rifling is of constant pitch: the first case being that of an imbalanced and misaligned projectile traveling in a perfectly straight bore, and the second case being that of a perfectly balanced and aligned projectile traveling in a crooked bore. These special equations are currently the basis of numerical models that will be used to study the effects of dimensional variation of tubes and projectiles on the forces of constraint which give rise to muzzle wear and body engraving.

Because of the purpose of the above-mentioned study, the general, as well as the special equations are cast in a form to give the magnitude and direction of the forces produced on the bourrelet(s) and rotating band of the projectile which are, of course, equal and in opposition to the forces of interest on the bore surface of the tube. It has been brought to the attention of the author, however, that if the equations were to be recast in a form to give forces and moments at a point (say the projectile mass centroid), they would have utility in gun tube dynamics analyses providing completeness and rigor to the projectile force input part of the problem heretofore not available.

This paper then is a presentation of the dynamical equations including the features described above from a point mass perspective suitable for inclusion in gun tube dynamics studies.

This paper was not available for printing in this publication.

AUTHOR INDEX

TECHNICAL REPORT INTERNAL DISTRIBUTION LIST

	NO. OF COPIES
CHIEF, DEVELOPMENT ENGINEERING DIVISION	
ATTN: SMCAR-CCB-D	1
-DA	1
-DC	1
-DI	1
-DP	1
-DR	1
-DS (SYSTEMS)	1
CHIEF, ENGINEERING SUPPORT DIVISION	
ATTN: SMCAR-CCB-S	1
-SE	1
CHIEF, RESEARCH DIVISION	
ATTN: SMCAR-CCB-R	2
-RA	1
-RE	1
-RM	1
-RP	1
-RT	1
TECHNICAL LIBRARY ATTN: SMCAR-CCB-TL	5
TECHNICAL PUBLICATIONS & EDITING SECTION ATTN: SMCAR-CCB-TL	3
DIRECTOR, OPERATIONS DIRECTORATE ATTN: SMCWV-OD	1
DIRECTOR, PROCUREMENT DIRECTORATE ATTN: SMCWV-PP	1
DIRECTOR, PRODUCT ASSURANCE DIRECTORATE ATTN: SMCWV-QA	1

NOTE: PLEASE NOTIFY DIRECTOR, BENET LABORATORIES, ATTN: SMCAR-CCB-TL, OF ANY ADDRESS CHANGES.

TECHNICAL REPORT EXTERNAL DISTRIBUTION LIST

	NO. OF COPIES
ASST SEC OF THE ARMY RESEARCH AND DEVELOPMENT ATTN: DEPT FOR SCI AND TECH THE PENTAGON WASHINGTON, D.C. 20310-0103	1
ADMINISTRATOR DEFENSE TECHNICAL INFO CENTER ATTN: DTIC-FDAC CAMERON STATION ALEXANDRIA, VA 22304-6145	12
COMMANDER US ARMY ARDEC	
ATTN: SMCAR-AEE	1
SMCAR-AES, BLDG. 321	1
SMCAR-AET-O, BLDG. 351N	1
SMCAR-CC	1
SMCAR-CCP-A	1
SMCAR-FSA	1
SMCAR-FSM-E	1
SMCAR-FSS-D, BLDG. 94	1
SMCAR-IMI-I (STINFO) BLDG. 59 PICATINNY ARSENAL, NJ 07806-5000	2
DIRECTOR US ARMY BALLISTIC RESEARCH LABORATORY ATTN: SLCBR-DD-T, BLDG. 305 ABERDEEN PROVING GROUND, MD 21005-5066	1
DIRECTOR US ARMY MATERIEL SYSTEMS ANALYSIS ACTV ATTN: AMXSY-MP ABERDEEN PROVING GROUND, MD 21005-5071	1
COMMANDER HQ, AMCCOM ATTN: AMSMC-IMP-L ROCK ISLAND, IL 61299-6000	1
COMMANDER ROCK ISLAND ARSENAL ATTN: SMCRI-ENM ROCK ISLAND, IL 61299-5000	1
DIRECTOR US ARMY INDUSTRIAL BASE ENGR ACTV ATTN: AMXIB-P ROCK ISLAND, IL 61299-7260	1
COMMANDER US ARMY TANK-AUTMV R&D COMMAND ATTN: AMSTA-DDL (TECH LIB) WARREN, MI 48397-5000	1
COMMANDER US MILITARY ACADEMY ATTN: DEPARTMENT OF MECHANICS WEST POINT, NY 10996-1792	1
US ARMY MISSILE COMMAND REDSTONE SCIENTIFIC INFO CTR ATTN: DOCUMENTS SECT, BLDG. 4484 REDSTONE ARSENAL, AL 35898-5241	2
COMMANDER US ARMY FGN SCIENCE AND TECH CTR ATTN: DRXST-SD 220 7TH STREET, N.E. CHARLOTTESVILLE, VA 22901	1
COMMANDER US ARMY LABCOM MATERIALS TECHNOLOGY LAB ATTN: SLCMT-IML (TECH LIB) WATERTOWN, MA 02172-0001	2

NOTE: PLEASE NOTIFY COMMANDER, ARMAMENT RESEARCH, DEVELOPMENT, AND ENGINEERING CENTER, US ARMY AMCCOM, ATTN: BENET LABORATORIES, SMCAR-CCB-TL, WATERVLIET, NY 12189-4050, OF ANY ADDRESS CHANGES.

TECHNICAL REPORT EXTERNAL DISTRIBUTION LIST (CONT'D)

	NO. OF COPIES
COMMANDER US ARMY LABCOM, ISA ATTN: SLCIS-IM-TL 2800 POWDER MILL ROAD ADELPHI, MD 20783-1145	1
COMMANDER US ARMY RESEARCH OFFICE ATTN: CHIEF, IPO P.O. BOX 12211 RESEARCH TRIANGLE PARK, NC 27709-2211	1
DIRECTOR US NAVAL RESEARCH LAB ATTN: MATERIALS SCI & TECH DIVISION CODE 26-27 (DOC LIB) WASHINGTON, D.C. 20375	1 1
COMMANDER AIR FORCE ARMAMENT LABORATORY ATTN: AFATL/MN EGLIN AFB, FL 32542-5434	1
COMMANDER AIR FORCE ARMAMENT LABORATORY ATTN: AFATL/MNF EGLIN AFB, FL 32542-5434	1
METALS AND CERAMICS INFO CTR BATTELLE COLUMBUS DIVISION 505 KING AVENUE COLUMBUS, OH 43201-2693	1

NOTE: PLEASE NOTIFY COMMANDER, ARMAMENT RESEARCH, DEVELOPMENT, AND ENGINEERING CENTER, US ARMY AMCCOM, ATTN: BENET LABORATORIES, SMCAR-CCB-TL, WATERVLIET, NY 12189-4050, OF ANY ADDRESS CHANGES.